Probing Point Defects in Fluorite-Structured Actinide and Analogue Oxides

A Dissertation Presented for the
Doctor of Philosophy
Degree
The University of Tennessee, Knoxville

Raul Irvin Palomares
May 2018

Copyright © 2018 by Raul Irvin Palomares
All rights reserved.

DEDICATION

To my Mom and Kelsa

ACKNOWLEDGEMENTS

This work was made possible through many collaborations with several wonderful colleagues and mentors, most notably: Maik Lang, Jacob Shamblin, Will Cureton, Jason Behrens, Brandon Perlov, Cameron Tracy, Sulgi Park, Dylan Rittman, Fuxiang Zhang, Rod Ewing, Jennifer Szymanowski, Tiankai Yao, Jie Lian, Marshall McDonnell, Matt Tucker, Anna Shelyug, Sarah Finkeldei, Joerg Neuefeind, Christina Trautmann, and Changyong Park. I first thank my primary advisor, Maik Lang, for giving me the freedom to pursue my personal research interests and for providing me with the opportunities to mature into a capable and independent scientist and engineer. I also thank my committee members, Brian Wirth, Steve Zinkle, and Bill Weber, for being excellent role models and mentors. I owe many thanks to my current and former fellow graduate students, Jacob Shamblin, Will Cureton, Jason Behrens, Brandon Perlov, Daniel Shauries, Sulgi Park, and Cameron Tracy for all the assistance and advice. I thank my professional work colleagues, Fuxiang Zhang, Rod Ewing, Jennifer Szymanowski, Marshall McDonnell, Matt Tucker, Anna Shelyug, Sarah Finkeldei, Joerg Neuefeind, Christina Trautmann, and Changyong Park, for all the patience and instruction. Lastly, I'm extremely thankful for my friends, family, and especially Kelsa, for all the love and support.

This research was funded by the Office of Basic Energy Sciences of the U.S. Department of Energy as part of the *Materials Science of Actinides* Energy Frontier Research Center (DE-SC0001089). The research at ORNL's Spallation Neutron Source was sponsored by the Scientific User Facilities Division, Office of Basic Energy Sciences, U.S. Department of Energy. A portion of this work was performed at HPCAT (Sector 16), Advanced Photon Source (APS), Argonne National Laboratory. HPCAT operations are supported by DOE-NNSA under Award No. DE-NA0001974 and DOE-BES under Award No. De-FG02-99ER45775, with partial instrumentation funding by NSF. This research used resources at the Advanced Photon Source, a U.S. Department of Energy (DOE) Office of Science User Facility operated for the DOE Office of Science by Argonne National Laboratory under Contract No. De-AC02-06CH11357. HPCAT beamtime was granted by the Carnegie/DOE Alliance Center (CDAC). I also gratefully acknowledge support from

the U.S. Department of Energy (DOE) National Nuclear Security Administration (NNSA) through the Carnegie DOE Alliance Center (CDAC) under grant number DE-NA-0002006.

ABSTRACT

Lanthanide and actinide oxides, such as CeO_2 [cerium dioxide], ThO_2 [thorium dioxide], and UO_2 [uranium dioxide], are attractive candidates for various energy-related applications such as nuclear fuel and electrolytes for solid oxide fuel cells owing in part to the resiliency of their bulk structures at room temperature up to near-melting temperatures. These materials exhibit broad regimes of phase stability under various extreme conditions including high temperature, pressure, and/or energetic ion irradiation. Upon modification from external perturbation (*e.g.*, ion irradiation) or chemical changes (*e.g.*, doping or oxidation), these fluorite-structured oxides incorporate large concentrations of point defects, which can agglomerate and result in complex microstructures that can severely impact component performance. The final state of defect arrangements is governed by unique interactions among the various vacancies, lanthanides, actinides, oxygens, and dopant atoms. This work investigates short-range atomic disorder in swift heavy ion-irradiated CeO_2 [cerium dioxide] and ThO_2 [thorium dioxide], oxidized UO_2 [uranium dioxide], and lanthanide-doped UO_2 [uranium dioxide] systems in order to understand how changes in local atomic arrangements correlate to bulk structural modifications and degradation of key material properties. Detailed structural analyses revealed that defect complexes, mostly small oxygen clusters, form in all fluorite-structured oxides after high energy ion irradiation, oxidation, and chemical doping. A number of computational studies have shown that these types of defect agglomerates can exhibit diffusion pathways much faster than isolated point defects. Accurate characterization and understanding of defect cluster stability and migration mechanisms will therefore enable better bulk property predictions that are critical to engineering improved fluorite-structured materials for energy applications.

TABLE OF CONTENTS

Introduction 1
Materials, Experimental Methods, and Data Analysis 3
Sample Preparation 3
Starting Materials 3
Ion Irradiation Sample Holders 5
Swift Heavy Ion Irradiation 11
Experimental Characterization 11
Inductively Coupled Plasma Mass Spectrometry 11
Thermogravimetric Analysis 14
X-ray Diffraction 17
X-ray Total Scattering 19
Neutron Total Scattering 22
Raman Spectroscopy 28
Data Modeling and Analysis 29
Rietveld Structural Refinement 29
Small-Box Structural Refinement 30
Large-Box Reverse Monte Carlo Modeling 31
Chapter I: Point Defects in Swift Heavy Ion-Irradiated Ceria and Thoria 33
Abstract 35
Introduction 36
Results and Discussion Part I: Damage Accumulation 42
Neutron and X-ray Diffraction – Average Structure 42
Neutron Total Scattering – Local Structure and Diffuse Scattering 50
Raman Spectroscopy – Local Structure and Vibrational Properties 67
Drop-Solution Calorimetry – Defect Energetics 71
Defect Production Efficiency 80
Results and Discussion Part II: Damage Annealing 84
Neutron and X-ray Diffraction – Average Structure 84
Neutron Total Scattering – Local Structure and Diffuse Scattering 93
Raman Spectroscopy – Local Structure and Vibrational Properties 100
Differential Scanning Calorimetry – Thermodynamic Stability 103
Conclusions and Recommendations 105
Chapter II: Point Defects In Oxidized Uranium Dioxide 110
Abstract 111
Introduction 112
General 112
Overview of UO_2 Oxidation 114
Oxygen Ingress and Defect Clustering 116
Influence of Defect Clustering on Phase Stability 119
The Dilute Limit 123
Results and Discussion 125
Determination of the Oxygen-to-Metal Ratio 125
Pair Distribution Function Simulations 131

Neutron Diffraction – Average Structure 138
Raman Spectroscopy – Local Structure and Vibrational Properties..... 157
Neutron Total Scattering – Local Structure and Defect Clustering..... 163
Conclusions and Recommendations 187
Chapter III: Point Defects in Rare-Earth-Element-Doped Uranium Dioxide..... 189
Abstract..... 190
Introduction..... 191
Results and Discussion 193
Neutron Diffraction – Average Structure 193
Raman Spectroscopy – Local Structure and Vibrational Properties..... 201
Neutron Pair Distribution Function Analysis – Local Structure..... 205
Reverse Monte Carlo Modeling – Defect Clustering 221
Conclusions and Recommendations 228
Conclusions..... 230
References..... 231
Vita..... 248

LIST OF TABLES

Table 1: Sample names and compositions for Nd-doped UO_2 samples 6
Table 2: NOMAD detector bank information..... 26
Table 3: Impurity concentrations in UO_2 samples determined by ICP-MS..... 130
Table 4: Summary of O:M values calculated 132
Table 5: Summary of various defect structure models fit to the local structure of the $UO_{2.07}$ PDFs 170

LIST OF FIGURES

Figure 1: Scanning electron microscopy image of sintered UO_2 pellet. Figure courtesy of Dr. Jie Lian and Tiankai Yao 4
Figure 2: (a) Sequence for preparing samples for synchrotron XRD characterization and (b) images of the samples and sample holders for the ion irradiations. The figure is reproduced from reference [2] 7
Figure 3: Ion irradiation sample holders designed for the neutron scattering experiments. Figure reproduced from reference [6] 10
Figure 4: Linear energy loss vs. ion penetration depth in the neutron scattering samples. Figure reproduced from the supplementary information of reference [6]. 12
Figure 5: Setup used to perform uranium ion exchange for ICP-MS samples 15
Figure 6: auto-sampler used for all ICP-MS measurements 16
Figure 7: LABSYS evo thermogravimetric analysis instrument 18
Figure 8: Schematic of X-ray diffraction setup at 16-BM-D. Figure reproduced from reference [2] 20
Figure 9: Hydrothermal anvil cell setup at 16-BM-D. Figure reproduced from reference [15] 21
Figure 10: NMR tubes loaded with radioactive powders mounted on the NOMAD sample shifter tray for room-temperature neutron scattering measurements 24
Figure 11: Experimental setup for high-temperature measurements performed at the NOMAD beamline. Filled vanadium cans (left) were mounted on a stick (center) that was dropped into the furnace environment (right). The furnace chamber lies under the beamline hutch 25
Figure 12: Energy loss of Au ions in CeO_2 and ThO_2 calculated using the SRIM 2008 code [4]. The dotted grey lines denote the Au ion energies used for ion beam irradiation experiments performed for this work 38
Figure 13: Scanning transmission electron microscopy image of ion track in CeO_2. Image reproduced from reference [51] 40
Figure 14: X-ray diffraction patterns of (a) CeO_2 and (b) ThO_2 before and after irradiation with 2.2 GeV Au Ions. The asterisk denotes the region omitted because it contained a parasitic peak from the sample holder. Figure is from supplemental material of reference [6] 43
Figure 15: Neutron diffraction patterns of (a) CeO_2 and (b) ThO_2 before and after irradiation with 2.2 GeV Au Ions. For brevity, only the diffraction patterns from detector bank 3 are shown. Figure is from supplemental material of reference [6] . 44
Figure 16: (a) X-ray and (b) neutron diffraction patterns of CeO_2 before and after irradiation with 1.1 GeV Au Ions. Only the patterns from neutron detector bank 3 are shown. Figure is from reference [80] 45
Figure 17: Fractional change in unit cell, $\Delta a/a_0$, of CeO_2 and ThO_2 before and after irradiation with 2.2 and 1.1 GeV Au Ions. The data are plotted alongside the Poisson fit (*dashed lines*) derived from the fitting of CeO_2 and ThO_2 data reported in reference [7]. The figure is adapted from supplemental material of reference [6] ... 47
Figure 18: Refined 8*c* oxygen site occupancy from Rietveld analysis of CeO_2 diffraction patterns before and after irradiation 49

Figure 19: Fractional change in isotropic atomic displacement parameters for cations and ions in CeO_2 and ThO_2 before and after irradiation 51
Figure 20: Total scattering function, $S(Q)$, of CeO_2 before irradiation (black) and after irradiation to 5×10^{12} ions/cm^2 (red). The inset shows a zoomed in view of the total scattering function that shows the ingrowth of diffuse scattering peaks after irradiation. The diffuse scattering peaks are denoted by blue asterisks 53
Figure 21: Total Correlation Functions, $T(r)$, of CeO_2 and ThO_2 before and after irradiation with 2.2 GeV Au Ions. Notable interatomic pairs from the pristine fluorite structure are shown above the corresponding peaks. For a description of the difference between the total correlation function and the pair distribution function refer to pg. 34. Figure is from reference [6] 54
Figure 22: Fitted neutron PDFs of (a) CeO_2 and (b) ThO_2 before and after irradiation with 2.2 GeV Au ions. Colored circles represent measured PDF data, red curves represent the fitted fluorite structure model, and the green curves represent the difference between the data and fitted models. The vertical black dotted lines denote the limits used for the boxcar fitting procedure described in the text. Figure is from supplemental material of reference [6] 55
Figure 23: (a) X-ray and (b) neutron pair distribution functions of CeO_2 before and after irradiation with 1.1 GeV Au Ions. All PDFs were fit with the fluorite structure. Figure from ref. [80] 56
Figure 24: Fitted neutron PDFs of CeO2 (left) and ThO2 (right) before and after irradiation with 2.2 GeV Au ions. The blue circles represent the measured PDF data, the red curves represent the fitted fluorite structure model, and the green lines represent the difference between the data and the fitted model. Teal and purple arrows denote peaks with cation-oxygen and oxygen-oxygen contributions, respectively 57
Figure 25: Results from peak fitting of the individual first nearest-neighbor Ce-Ce peak from the X-ray pair distribution functions. Clockwise starting from the top left: the evolution of the full-width at half-max of the peak with increasing fluence, the peak fits for the different PDFs, and the relative change in peak position 59
Figure 26: Results from box-car fitting of the CeO_2 and ThO_2 PDFs. ΔR_w represents the relative change in the goodness-of-fit parameter, R_w, after irradiation. Negative and positive ΔR_w values indicate that the fit was improved or worsened, respectively. The dashed and solid lines are used to guide the eye 61
Figure 27: First-nearest neighbor neutron PDF peak evolution for CeO2 and ThO2 before and after irradiation with 2.2 GeV Au ions. Figure is from reference [6] 63
Figure 28: Evolution of the first-nearest neighbor peaks of CeO_2 in the neutron (left) and X-ray (right) PDFs before and after irradiation with 1.1 GeV Au ions 64
Figure 29: Very short length scales of CeO2 pair distribution functions before and after irradiation with 2.2 GeV Au ions 66
Figure 30: Magnified region of Raman spectrum of CeO_2 before and after irradiation with 1 GeV Au ions. Various defect peaks and radiation damage features are numbered (1-5). The inset shows the full-range Raman spectra. The full-range spectra show decreasing signal-to-noise ratio with increasing ion fluence 68

Figure 31: Schematic of F_{2g} peak modifications based on findings from reference [89]. (a) Pristine CeO_2 shows one F_{2g} peak representative of CeO_8 coordination environment. (b) Replacing Ce^{4+} with Ce^{3+} in the same environment would cause a shorter/stiffer Ce-O and corresponding increase in F_{2g} frequency. (c) Relaxing Ce^{3+} environment by swelling results in a coordination more like that of Ce_2O_3 and decrease in F_{2g} frequency. (d) Irradiation-induced swelling and partial reduction results in asymmetric broadening of F_{2g} peak to lower frequencies indicative of mostly Ce^{4+} with some Ce^{3+} in the structure 70
Figure 32: Relative change in defect band frequency with varying Ce-O coordination environment. The first coordination environment represents a pristine CeO_8 arrangement with a characteristic frequency of ~465 cm^{-1}. A $Ce^{3+}O_7$ arrangement has a characteristic frequency of ~550 cm^{-1}. Defect bands for $Ce^{3+}O_8$ and $Ce^{4+}O_7$ arrangements appear at lower and higher frequencies to the $Ce^{3+}O_7$ defect band, respectively. Frequency predictions based on density functional theory results from reference [89] 72
Figure 33: Change in radiation damage enthalpy with increasing ion fluence for CeO_2 before and after irradiation with 1 GeV and 2 GeV Au ions 74
Figure 34: Schematic of single-impact model. The top panel illustrates an example of how experimental data are represented and the bottom panel shows corresponding frames of how ion tracks (darker patterned circles) are accumulated in the material (lighter matrix). At relatively low ion fluences (region *a*) the damage accumulation is approximately linear in relation to fluence because there is minimal track overlap; each ion track creates new damage. At higher fluences (region *b*) damage accumulation is sub-linear as ion tracks begin to overlap; overlapping regions do not necessarily produce new damage because defects can be annealed or cluster. At the highest fluences (region *c*) damage saturates because ion tracks severely overlap; damage production efficiency is severely lessened. Data showing single-impact Poisson behavior are typically fit with the single-impact model (blue dashed line). Common damage parameters include: unit cell parameters, heterogeneous microstrain, and ion track density 76
Figure 35: Range of electrons in CeO_2 as a function of electron kinetic energy. The calculation was performed with the online ESTAR database [95] and assumes a theoretical density of 7.65 g/cm^3 for CeO_2 79
Figure 36: defect production efficiency calculated using calorimetric absolute energy measurements 82
Figure 37: defect production efficiency normalized by ion fluence as a function of cumulative energy density 85
Figure 38: Example temperature profile for typical isochronal annealing experiment. Figure from reference [98] 87
Figure 39: X-ray diffraction peaks of swift heavy ion irradiated CeO2 before and after high-temperature, post-irradiation annealing 88
Figure 40: Evolution of neutron diffraction pattern of CeO_2 before and after post-irradiation isochronal annealing 89
Figure 41: Fractional change of unit cell parameter of swift heavy ion-irradiated ThO2 before and after isochronal annealing. Figure from reference [98] 90

Figure 42: Fractional changes of unit cell parameters with increasing isochronal annealing temperature. The inset shows the derivative of the fractional change in unit cell parameter. Figure adapted from reference [15] 91
Figure 43: Williamson-Hall plots for CeO2 and ThO2 before and after post-irradiation isochronal annealing. The asterisks denote data points associated with the oxygen sublattice. These points show more scatter compared to points only associated with the cation sublattice. Figure adapted from reference [15]. 94
Figure 44: Total scattering functions of CeO2 and ThO2 before and after isochronal annealing to different temperatures 96
Figure 45: Total scattering functions (top) and normalized total scattering functions of ThO2 before and after isochronal annealing..... 98
Figure 46: Pair distribution functions of swift heavy ion irradiated ThO2 before and after isochronal annealing. Figure is from reference [98]..... 99
Figure 47: Raman spectrum of irradiated ThO2 before and after isochronal annealing. Inset on the left shows the evolution of the F2g peak position. Inset on the right shows a magnified view of F2g peak. Figure is from reference [98] 101
Figure 48: Evolution of Raman spectrum of irradiated ThO2 with absolute intensity. Inset shows the relative change in F2g peak intensity after annealing to different temperatures. Figure is from reference [98] 104
Figure 49: Differential scanning calorimetry measurements of swift heavy ion irradiated CeO_2 performed under flowing air (top) and argon gas (bottom). Positive changes in heat flow (green arrows) denote exothermic events whereas negative changes denote endothermic..... 106
Figure 50: Crystal structure of UO2. The structure is fluorite (space group *Fm*-3*m*) and is composed of interpenetrating FCC uranium (left) and SC oxygen (right) sublattices 118
Figure 51: Various oxygen defect clusters proposed for UO2+x. (a) The 2:2:2 cluster is composed of two oxygen vacancies (Ov), two interstitials oriented along <110> (pink), and two interstitials oriented along <111> (green). (b) The split di-interstitial cluster is formed by three interstitials (*green*) sitting on a 111 plane above an oxygen vacancy. (*c*) The cuboctahedral cluster is formed by twelve oxygen interstitials (*pink*) that form a spherical-like cluster inside of the UO_2 unit cell. Figures are adapted from references [168, 169] 120
Figure 52: The temperature-stoichiometry phase diagram of uranium oxide. (figure from [173])..... 121
Figure 53: Summary of thermogravimetric analysis results for UO_2 and UO_{2+x} samples. Clockwise from the top left: Weight gain *versus* time, weight gain *versus* temperature, heat flow *versus* temperature, and heat flow *versus* time for both samples. The heat flow measurements are compared to a blank alumina crucible to highlight the strong exothermic peaks of the samples..... 128
Figure 54: Simulated pair distribution function of pristine UO_2 with Qmax = 35 $Å^{-1}$... 134
Figure 55: Calculated difference in PDF structure before (black) and after (red) including oxygen interstitials in a Willis 2:2:2 defect configuration..... 136

Figure 56: Calculated PDFs for $UO_{2.0625}$ assuming a split di-interstitial defect configuration (top) and the calculated inter-cluster correlations for the two proposed defect models after optimization 137
Figure 57: Neutron diffraction patterns of UO_2 and UO_{2+x} at different temperatures. Black circles represent measured data, colored lines denote the fits of the refined fluorite structure models, and the green lines signify the difference between the data and the fitted models 139
Figure 58: Comparison of neutron diffraction patterns of UO_2 and $UO_{2.07}$ measured at room temperature and 1000 ºC 141
Figure 59: Comparison of uranium oxide unit cell parameters 142
Figure 60: Measured thermal expansion of UO2 146
Figure 61: Comparison of thermal expansion of UO_2 and UO_{2+x} 148
Figure 62: Evolution of the UO_2 atomic displacement parameters 149
Figure 63: ADPs of UO_2 and UO_{2+x} 151
Figure 64: Temperature evolution of isotropic atomic displacement parameters of UO_2 and $UO_{2.07}$ from Rietveld refinement of high-resolution diffraction patterns 153
Figure 65: Comparison between Rietveld ADP values and Debye predictions 156
Figure 66: Comparison of Raman spectra of UO_2 and UO_{2+x} 159
Figure 67: Peak fit of UO_{2+x} Raman spectrum 162
Figure 68: Small-box refinement fits to the PDFs of UO_2 (left) and $UO_{2.07}$ (right) at all temperatures 165
Figure 69: Comparison of small-box pair distribution function refinement results for UO_2 and $UO_{2.07}$. The top two panels show the evolution of the goodness-of-fit, R_w, with increasing temperature. The bottom plot shows the evolution of the uranium and oxygen isotropic atomic displacement parameters (ADPs; U^{iso}) with varying temperature. The ADPs are compared with predictions based on the Debye model 167
Figure 70: Comparison of goodness-of-fit parameters obtained from fitting different defect models to the PDFs of $UO_{2.07}$ at 600 and 1000 °C 171
Figure 71: RMC fit results for $UO_{2.00}$ data. Experimental data are shown in black, fitted structural models are denoted by the colored lines, and the thin green lines below the data represent the difference between the data and the fitted structural models 174
Figure 72: Partial pair distribution functions (left) and overall fit to the G(r) function for UO_2 data at 25, 500, and 1000 °C. The blue, red, and green partial PDFs represent the U-O, O-O, and U-U partials, respectively 176
Figure 73: Direct comparison of experimental PDFs for UO_2 (black) and $UO_{2.07}$ (red) at ~600 and 1000 °C. The $UO_{2.07}$ sample was measured at 600 °C whereas the UO_2 sample was measured at 625 °C 179
Figure 74: Comparison of RMC model fits to the G(r) function of $UO_{2.07}$ at 600 and 1000 °C (right) and the resultant partial PDFs (left) 181
Figure 75: Examples of the various defect cluster arrangements in the optimized RMC supercells (left) and histograms of defect cluster sizes from RMC results (right). Defect cluster arrangements are shown as viewed along the three principal directions (<100>, <110>, and <111> directions). Each histogram is representative of sampling data from ten 16000-atom supercells 184

Figure 76: Comparison of neutron diffraction patterns of undoped UO_2 (bottom) and Nd-doped UO_2 with the highest Nd loading (top). Both diffraction patterns were fit with the cubic fluorite structure. Both materials are composed of a single cubic phase 194
Figure 77: Evolution of unit cell parameters of UO_2 and Nd-doped UO_2 samples with varying Nd content..... 196
Figure 78: Refined 8*c* site occupancy values vs. Nd content in the UO_2 samples 198
Figure 79: Change in isotropic atomic displacement parameters of the oxygen and cation sites with varying Nd concentration 200
Figure 80: Raman spectra of UO2 and Nd-doped UO2 samples prepared by (a) co-precipitation, (b) sol gel, and (c) acid resin synthesis routes. The values of *x* denote the loading level of Nd in atomic fraction (*e.g.*, $x = 0.017$ is equivalent to 1.7 atom% Nd). The data are shown as grey circles and the colored dotted lines represent fitted peaks. The black lines show the overall fit of the peaks to the data..... 202
Figure 81: Change in normalized peak areas with increasing Nd doping level. Peak areas were derived by peak fitting of the defect bands in the Raman spectra. The shaded region highlights the large discontinuity between the last two data point sets and the dashed lines are included to guide the eye..... 204
Figure 82: Neutron pair distribution functions of all undoped and Nd-doped UO_2 samples 206
Figure 83: Comparison of small-box modeling fit results for the full-range pair distribution function (purple) and for a cropped range (yellow). The cropped PDF corresponds to an R_{min} value of 25 Å whereas the full range PDF corresponds to an R_{min} value of 1 Å. The R_w values listed represent the weighted goodness-of-fit of the fluorite structure model fitted to the data..... 208
Figure 84: Relative change in goodness-of-fit value, R_w, with varying R_{min} value. Note: the data are offset along the *y*-axes. The R_{min} value denotes the lower bound to the fit range for the small-box PDF modeling. The R_{max}, or upper bound to the fit range, was always fixed at 50 Å. The results are separated based on the synthesis route labeled at the top right. The *x* values denote the atomic fraction of Nd in the system and the scale bars show the magnitude for $R_w = 0.005$ 210
Figure 85: Small-box pair distribution function modeling results for the co-precipitation samples. The *x* values at the top denote the atomic fraction of Nd in the samples and the name at the bottom right denotes the sample name. The PDFs were initially fit with the average structure model derived from Rietveld refinement of the neutron diffraction patterns. 212
Figure 86: The unit cell of the fluorite structure (left). The unit on the right shows the tetrahedral coordination environment of a single oxygen atom. The green arrows show schematically how the local coordination environment was disturbed in order to fit 'relaxation' models to the PDFs. Different relaxation models with different displacement directions and magnitudes were used 214
Figure 87: Illustration of minimization scheme for fitting so-called relaxation models to the neutron pair distribution functions (PDFs). Various models were fit to each PDF until the minimum R_w value was attained. The lowest R_w value among the different models corresponds to the model that best fit the data. The location of the minimum also yields the optimal atomic relaxation distance for the model of interest..... 216

Figure 88: Results from fitting various so-called *relaxation* models to the pair distribution functions of Nd-doped UO_2 samples. The R_w is the fit agreement value. The black points represent results for fitting an unperturbed fluorite structure model. The other points represent models with a varying number of cation sites relaxed either towards (↑) or away (↓) from the neighboring anion site. All samples were best fit with relaxation model 7 217
Figure 89: Visual comparison of PDF fits for unperturbed *Fm*-3*m* model (bottom) and relaxation model 7 (top). The relaxation model better models the short-range distortion and also surprisingly better fits higher *r* regions as well (8-10 Å) 219
Figure 90: Optimized atomic relaxation distance *versus* Nd content in the UO_2 samples 220
Figure 91: Summary of RMC modeling results for undoped UO_2 synthesized by the co-precipitation method. Clockwise from top left: the model fit to the diffraction pattern, the fit to the G(r) function, the bond valence sum parameter for the output atom ensemble, and the fit to the D(r) function 224
Figure 92: Final atomic supercell arrangement for UO_2 from reverse Monte Carlo modeling 225
Figure 93: Summary of RMC modeling results for $Nd_{0.133}U_{0.867}O_{2\pm y}$. Clockwise from top left: RMC model fit to the diffraction pattern, fit to G(r), BVS analysis results, and fit to the D(r) 226
Figure 94: Various partial pair distribution functions derived from RMC model of $Nd_{0.133}U_{0.867}O_{2\pm y}$ (left) and two examples of Nd-O polyhedra from the RMC supercell output (right) 227

INTRODUCTION

Fluorite-structured oxides are used in a variety of energy-related applications ranging from nuclear fuels to solid oxide fuel cell (SOFC) electrolytes. One reason for this is the exceptional structural stability that these materials exhibit under a broad range of conditions. The resiliency of these materials is largely attributed to the fluorite structure, which can tolerate the incorporation of very significant amounts of structural and chemical disorder. The type and amount of structural disorder is dependent on the energy application and operating conditions. In nuclear fuel materials, such as uranium dioxide (UO_2), structural disorder is primarily caused by irradiation, off-stoichiometry, and chemical doping.

The work presented here describes studies aimed at understanding atomic-structure modifications of fluorite-structured oxides caused by variants of these three factors, namely: swift heavy ion irradiation, hyper-stoichiometry, and rare-earth element doping. Specifically, this work focuses on elucidating the characteristics and effects of smaller point defects that have been historically challenging to observe and study experimentally. Emphasis is placed on understanding point defect behavior in UO_2, which is the most important nuclear fuel material to date. UO_2 studies are supplemented by swift heavy ion irradiation studies of cerium dioxide (CeO_2) and thorium dioxide (ThO_2), which are isostructural analogues to UO_2. The work is presented in the order that the studies were performed and each chapter acts as a stand-alone section with self-contained abstract, introduction, and conclusion sub-sections.

Chapter I describes studies of swift heavy ion irradiated CeO_2 and ThO_2. The work was initiated with irradiation studies of CeO_2 and ThO_2 for two main reasons. First, these materials exhibit simpler chemistry compared to UO_2, which simplifies defect characterization. Second, swift heavy ion irradiation effects are relatively well-characterized in CeO_2 and ThO_2. The latter enabled the testing and validation of neutron total scattering techniques, which were developed for this work and were ultimately critical to the completion of the subsequent UO_2 studies. The use of total scattering methods for characterizing irradiation effects provided unique insights and improvement to the current

understanding of defect accumulation behavior in CeO_2 and ThO_2. The swift heavy ion irradiation studies also introduce the concept of oxygen point defect clustering, which is vital to understanding the effects of hyper-stoichiometry in UO_2.

The second Chapter describes studies of oxygen defect clustering in hyper-stoichiometric UO_2 (UO_{2+x}). The study of UO_{2+x} draws upon insights gained from the swift heavy ion irradiation studies in regards to point defect clustering and neutron scattering data analysis. Findings from the UO_{2+x} study are considered central to this body of work because they provide the most novel insights into UO_2 point defect behavior. These insights were made possible by applying a unique Reverse Monte Carlo (RMC) interstitial-defect modeling approach that was developed for this study and is described here.

The final chapter, Chapter III, outlines findings from investigations of rare-earth-element-doped UO_2, which aim to emulate certain effects of natural chemical doping by aliovalent rare-earth fission products in spent nuclear fuel. This study combines aspects of the prior two studies (*i.e.*, chemical modifications and RMC modeling) and highlights the current limitations to point defect characterization and modeling in more realistic doped-UO_2 systems. Improvements and implications for future work are discussed.

MATERIALS, EXPERIMENTAL METHODS, AND DATA ANALYSIS

Sample Preparation

Starting Materials

CeO_2 (99.9% purity) and ThO_2 (99.99% purity) samples were produced from microcrystalline powders procured from Alfa Aesar and IBI Labs, respectively. No special care was taken to limit the exposure of these samples to oxygen because CeO_2 and ThO_2 are both stable in air at ambient conditions. High temperature heat treatment of CeO_2 was avoided in order to avoid reduction of CeO_2 to CeO_{2-x}. The typical grain size of these samples as estimated by suppliers was ~1-5 μm.

The UO_2 samples were handled more carefully in order to mitigate the risk of oxidation. All UO_2 materials were handled, packaged, shipped, and prepared in inert argon gas atmosphere. The UO_2 samples were prepared by collaborators at the Rensselaer Polytechnic Institute (RPI). The starting material was obtained in the form of depleted (0.69% U^{235}) UO_2 powder from IBI Labs. Dense pellets of microcrystalline UO_2 were produced at RPI using spark plasma sintering (SPS) following the procedures outlined in [1] and references therein.

The grain size of the sintered pellets was confirmed by scanning electron microscopy (SEM). The SEM images revealed that the two samples exhibited very similar grain structures. An example SEM image is shown in Figure 1. Figure 1 shows that the UO_2 pellets exhibited a dense grain structure with minimal pores and other macroscopic defects. Analysis of the SEM images indicated that the mean grain sizes of the materials were 1-5 μm. Powder samples of uranium dioxide were prepared by grinding the dense UO_2 pellets in inert argon atmosphere using a clean agate mortar and pestle. Preliminary analysis of the lattice parameters determined by laboratory X-ray diffraction indicated that the oxygen-to-metal (O:M) ratios of the two samples were approximately 2.00 and 2.07. Details regarding the O:M determination are presented on page 125.

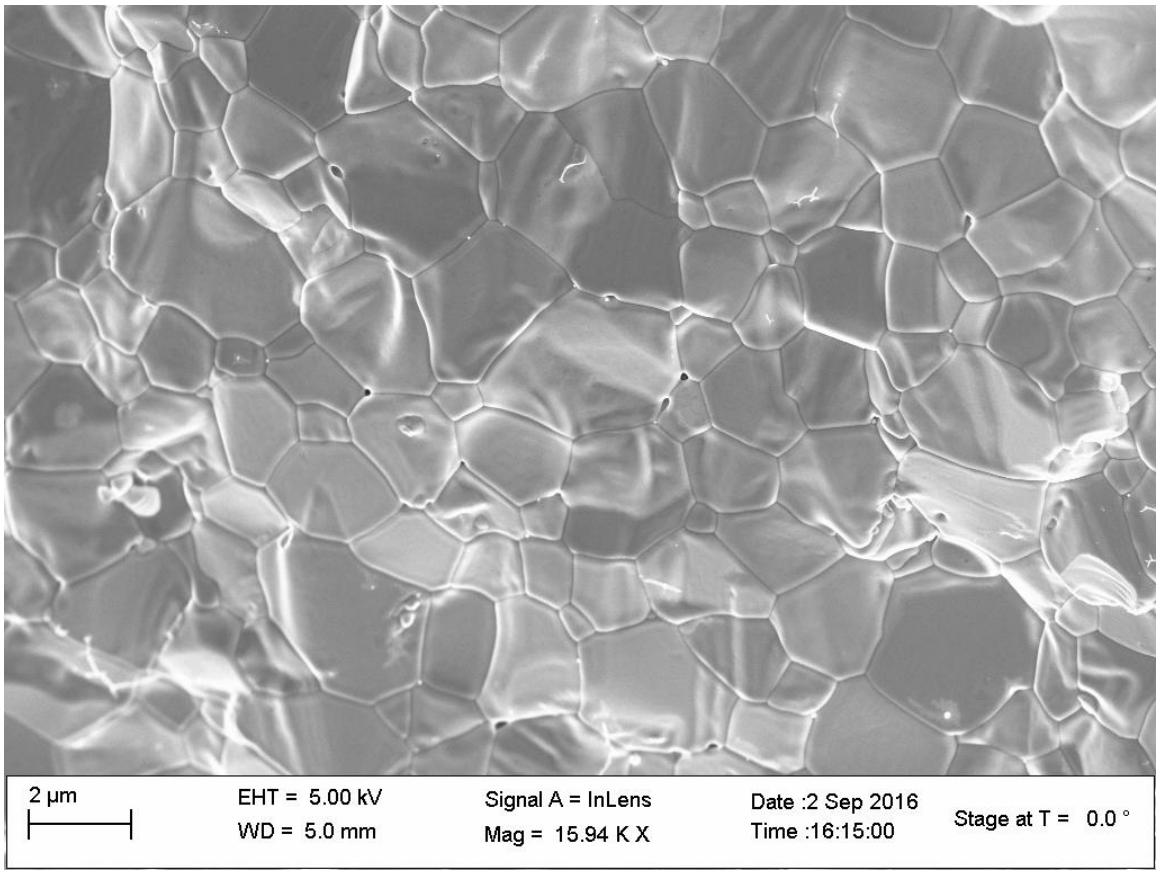


Figure 1: Scanning electron microscopy image of sintered UO_2 pellet. Figure courtesy of Dr. Jie Lian and Tiankai Yao

Neodymium-doped UO_2 samples were prepared by co-precipitation, sol-gel, and acid resin synthesis routes using uranium and neodymium nitrate precursors. All dried powders were ground, pressed into pellets, and sintered in platinum crucibles at 1600 °C under flowing argon gas with 4% hydrogen. After sintering and cooling the samples, powders were handled and shipped in air atmosphere. Therefore, no care was taken to limit oxidation of the samples. Preliminary X-ray diffraction analysis was used to verify the integrity of the sample powders and to verify that all materials exhibited ideal cubic fluorite structures and no superlattice peaks associated with hyper-stoichiometric UO_2 or Nd_2O_3 phases. Analysis based on diffraction results showed that all samples are stoichiometric or slightly sub-stoichiometric. No detailed analysis of oxygen content was performed. The sample identifiers, Nd contents, and synthesis methods for all Nd-doped UO_2 samples are presented in Table 1.

Ion Irradiation Sample Holders

CeO_2 and ThO_2 powders were irradiated with swift heavy ions using specially designed sample holders. Both the synchrotron X-ray diffraction (XRD) and neutron total scattering measurements required unique sample holder systems. The aim in designing the irradiation holders was to maximize the sample surface area exposed to the ion beam while minimizing the sample thickness. This ensured that the energy deposited in the materials by the ion beam was primarily from electronic energy loss with negligible nuclear energy loss. An added benefit to this approach was that the penetration depth of the ion beam exceeded the sample thickness. This ensured that ion implantation was negligible and the change in electronic energy loss throughout the samples was minimal. The change in the electronic energy loss within the bulk of the neutron scattering samples was approximately 40 %. The change in the electronic energy loss was typically much lower in the X-ray diffraction samples (approximately 5 % or less) [2].

The sample preparation method for the synchrotron XRD measurements is described in detail elsewhere [2], but is summarized here. The XRD samples were prepared by pressing loose powders into holes of 200 μm diameter that were drilled into 50 μm-thick stainless steel foils by electric discharge machining (Figure 2). The resulting sample

Table 1: Sample names and compositions for Nd-doped UO_2 samples

Sample identifier	Nd loading (atom %)	Synthesis method
RE-398	0	Co-precipitation
RE-412	0	Sol gel
RE-411	0.014	Sol gel
RE-415	0.017	Co-precipitation
RE-394	0.026	Sol gel
RE-399	0.032	Co-precipitation
RE-402	0.096	Acid resin
RE-416	0.133	Co-precipitation

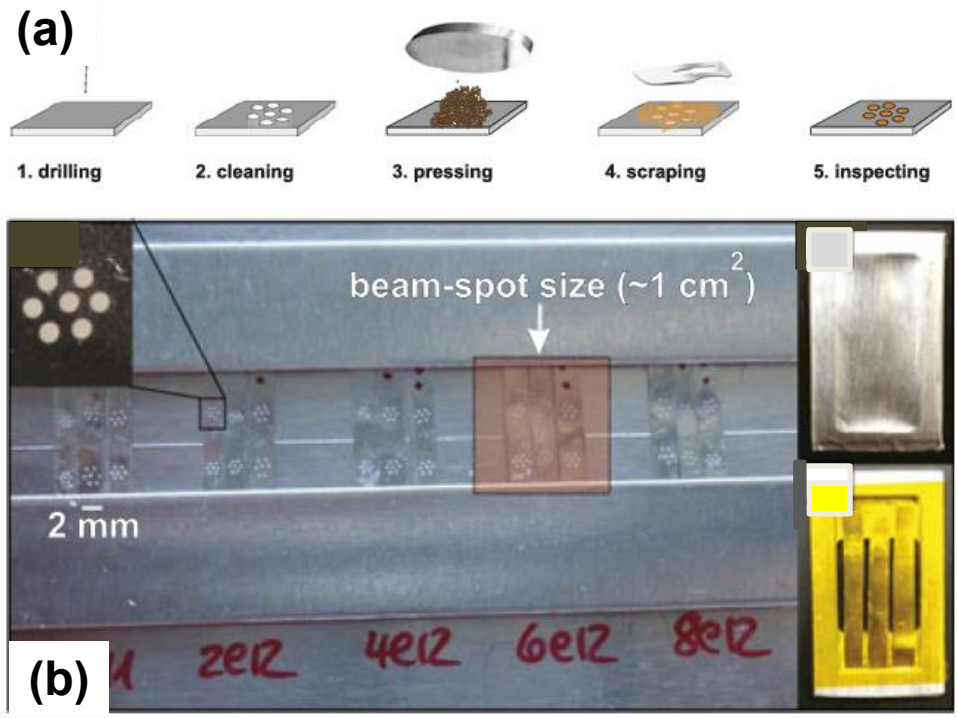


Figure 2: (a) Sequence for preparing samples for synchrotron XRD characterization and (b) images of the samples and sample holders for the ion irradiations. The figure is reproduced from reference [2]

compacts were 40-60 % theoretical density. The density estimates were based on values reported for cold-pressing of isostructural uranium dioxide under similar loads [3]. Two powder types (CeO_2 and ThO_2) were loaded into a single stainless steel foil strip, which was mounted on a rigid aluminum frame [2]. Loading both samples onto a single holder ensured that the samples were irradiated simultaneously under identical beam conditions. The miniscule size of the samples also ensured that the radioactivity of the ThO_2 samples was very low. This allowed the samples to be measured more easily at the synchrotron beamline without the need for bulky sample containment vessels. The projected ranges for 945 MeV Au ions in the ThO_2 and CeO_2 samples were 55 and 58 μm, as calculated by SRIM [4]. Both ranges exceed the thicknesses of the samples.

The sample holders for the neutron scattering experiments were designed with the aim of maximizing the homogeneously irradiated sample volume. Beam intensities from neutron sources are typically much weaker in comparison to the intensities of synchrotron X-ray beams. Therefore, large sample volumes were required for the neutron scattering measurements in order to obtain sufficient signal-to-noise ratio for enabling accurate structural analysis. This requirement has inherently limited the application of neutron scattering for the characterization of ion irradiation effects because the penetration depth of ion beams in metals and ceramics is typically very short. These short penetration depths dictate that homogeneously irradiated sample volumes are very small unless the surface area is greatly increased.

The application of neutron scattering to the characterization of ion irradiation effects in polycrystalline ceramics was made possible by the use of state-of-the-art facilities, such as the Spallation Neutron Source (SNS) at Oak Ridge National Laboratory (ORNL). High-energy (180 MeV – 2.2 GeV) ion beams were used to maximize the homogeneously irradiated sample volume while the use of a high-intensity spallation source minimized the required sample volume for neutron scattering. The combination of these two methods, coupled with uniquely-tailored sample holders, yielded the conditions necessary to obtain suitable signal-to-noise ratios for accurate structural analysis of radiation effects.

Ion range calculations were performed prior to the sample preparation in order to determine the optimal sample geometry. Optimization of the sample geometry was critical for the preparation of the neutron scattering samples and less so for the XRD samples because focused X-ray micro-beams at synchrotron facilities are both highly penetrating and enable the measurement of even the most miniscule of sample sizes. The ion range calculations were performed with the SRIM 2013 code [4] assuming 60% theoretical density. Rather than directly apply a 60% density correction factor in SRIM, the density correction was performed using the procedure outlined by Lang *et al*. [5]. This density correction applies a scaling factor (equal to 1.66 for 60% theoretical density), which scales the ion range values calculated assuming 100% theoretical density in SRIM. This approach was preferred over the SRIM reduced density method because the loose powder compact is modelled as a loosely-packed ensemble of crystallites of theoretical density. The density correction by Lang *et al*. considers that the decrease in *dE/dx* in the empty space in-between crystallites is negligible in comparison to the decrease in *dE/dx* within the individual crystallites of theoretical density.

The projected ion range values for the 2 GeV Au ion irradiations were 83.4 and 82.2 μm in CeO_2 and ThO_2. The calculated ion range of 1 GeV Au in CeO_2 was 48.4 μm. As a result, the samples prepared for the irradiations were made 75 μm thick for the 2.2 GeV Au ion irradiations and 45 μm thick for the 1.1 GeV Au ion irradiations. The sample holders were constructed out of thin aluminum square plates with areas of ~1.5 cm^2. Circular cavities of 1 cm diameter and 75 μm (or 45 μm) thickness were bored into the center of the aluminum plates. Loose powders were scattered and pressed into the cavities using dies in order to yield thin sample platelets of ~1 cm diameter and 75 μm (or 45 μm) thickness (Figure 3). In order to avoid sample powder from penetrating into the aluminum past 75 μm (or 45 μm), the loose powder was weighed prior to loading into the bored cavity. The sample weight was limited to the weight of a platelet of ideal dimensions with 60 % theoretical density. After pressing, the holders were tightly wrapped with thin sheets of aluminum foil in order to prevent sample powder from falling out of the holders. The aluminum foils were 7 and 10 μm thick and the calculated energy loss in the aluminum foils was approximately 0.1 and 0.2 GeV for the 1.1 and 2.2 GeV irradiations, respectively.

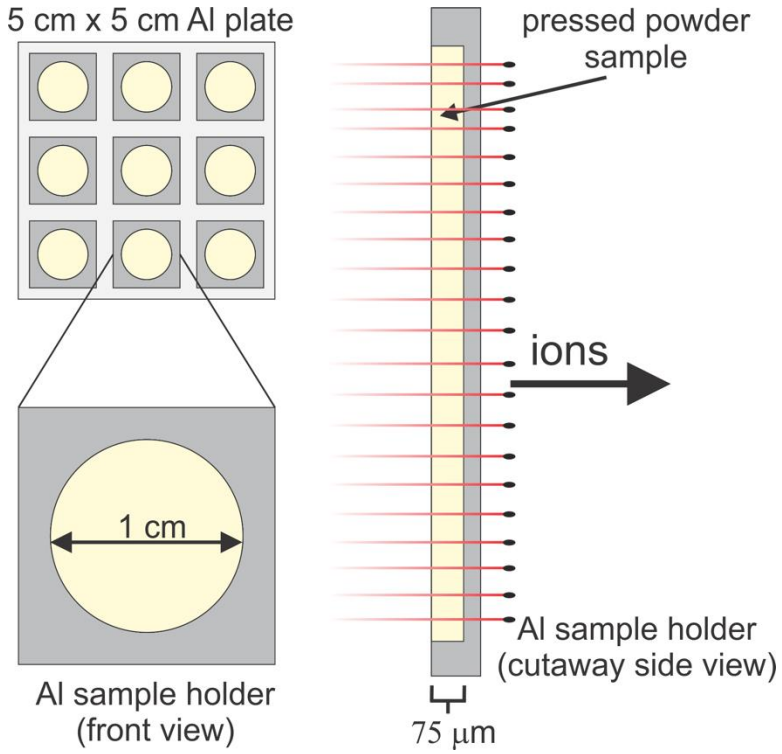


Figure 3: Ion irradiation sample holders designed for the neutron scattering experiments. Figure reproduced from reference [6]

Additional details regarding this sample preparation method are reported elsewhere [6].

Swift Heavy Ion Irradiation

Swift heavy ion irradiations were performed at the GSI Helmholtz Center for Heavy Ion Research in Darmstadt, Germany. All irradiations were performed under vacuum and at room temperature. The samples for synchrotron XRD studies were irradiated with 945 MeV ^{197}Au ions (4.8 MeV/*u*) at beamline M2 of the UNILAC linear accelerator. The samples for neutron scattering studies were irradiated with both 1.1 GeV (5.6 MeV/*u*) and 2.2 GeV (11.2 MeV/*u*) ^{197}Au ions at the X0 beamline. The beam flux at the M2 and X0 beamlines was limited to ~2×10^{9} ions-cm^{-2}-s^{-1} and ~5×10^{8} ions-cm^{-2}-s^{-1}, respectively, in order to avoid sample heating from the ion beam. In all cases, various samples were irradiated to different fluences. The maximum fluence for the neutron scattering samples was 5×10^{12} ions/cm^2 and the maximum fluence for the XRD samples was 1×10^{13} ions/cm^2.

The SRIM code was used to calculate the energy deposited in the samples. The average electronic energy loss per ion across the XRD sample thickness (~50 μm) was approximately 24 keV/nm for both CeO_2 and ThO_2. The corresponding values averaged across the 75 μm (45 μm) neutron scattering sample thickness were 37 keV/nm (27 keV/nm) and 42 keV/nm for CeO_2 and ThO_2, respectively. In all cases the nuclear energy loss was negligible and was orders of magnitude lower than the electronic energy loss. An example of the energy loss vs. ion penetration depth data is shown in Figure 4. Corresponding energy loss diagrams for the 945 MeV irradiations are available in the supplementary figures section of ref. [7]

Experimental Characterization

Inductively Coupled Plasma Mass Spectrometry

Inductively coupled plasma mass spectrometry (ICP-MS) measurements were performed in order to determine impurity concentrations of the UO_2 samples. All sample digestions, sample preparations, and ICP-MS analyses were conducted in class-1000 clean room facilities at the University of Notre Dame. ICP-MS data were collected in medium mass resolution mode ($M/\Delta M$ ~ 3000) using an Attomm (Nu Instruments) high resolution ICP-

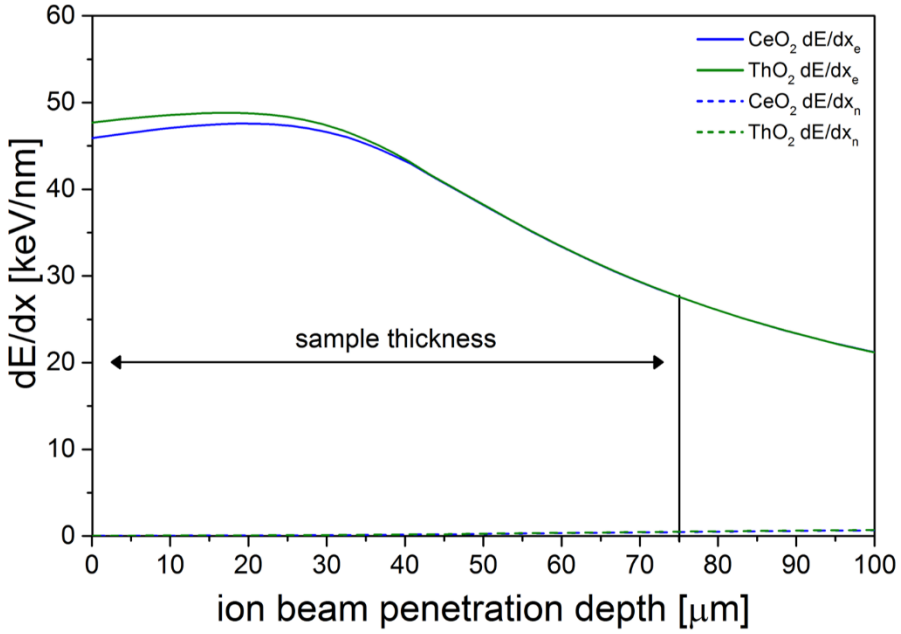


Figure 4: Linear energy loss vs. ion penetration depth in the neutron scattering samples. Figure reproduced from the supplementary information of reference [6]

MS instrument. Generally, an ICP-MS instrument ionizes aerosolized samples and sorts ions using a mass spectrometer in order to determine the distribution of ion species originating from the sample. ICP-MS is routinely used in various fields to quantify elemental concentrations as low as a few parts-per-million (ppm) or parts-per-billion (ppb).

Reported values of non-volatile impurity concentrations in commercial-grade concentration UO_2 are typically only a few ppm at most (see, for example, ref. [8]). Quantification of impurities in such low concentrations is challenging because ICP-MS measurements of UO_2 are dominated by signal intensity from uranium. In order to circumvent this issue, ICP-MS sample solutions were prepared using resins that preferentially separated uranium from the dissolved UO_2 samples in solution.

A few milligrams (10-20 mg) of oxidized uranium oxide powders were individually weighed on a standard laboratory balance and loaded into pre-weighed, empty 15 mL Savillex® Teflon vials. Approximately 3 mL of double-distilled 16N cHNO_3 (concentrated nitric acid) and ~0.5 mL of double-distilled concentrated HF (hydrofluoric acid) was added to each vial, the vials were sealed, and the vials were heated at 150 °C until the samples were completely dissolved. After digestion, the vials were removed from the hot plate and set aside until cooled to room temperature. The vial caps were removed after cooling and the open vials were heated at 110 °C under a fume hood until all liquid evaporated.

Several drops of $CHNO_3$ were added and swirled around in the vials and caps after drying on several occasions (3-5 times) in order to ensure that minimal sample residue remained on the cap and walls of the vials and the samples were as concentrated as possible. The samples were placed on the hot plate after each rinse in order to evaporate all of the added drops of liquid. After complete drying and concentration, the samples were re-dissolved in 0.5 mL of a 8M (8-molar) HNO_3 (nitric acid) + 0.1M HF mixture in preparation for the uranium separations.

Uranium ion exchange was performed using a UTEVA® (100-150 µm mesh) resin, which is typically made with diamyl anylphosphonate sorbed on an inert polymeric support [9]. UTEVA resin preferentially captures uranium with virtually no sorption of any other metals other than some actinides that are not of interest for the present study. Approximately 2 mL of resin was loaded into an Evergreen Scientific 5’’ column (1 per

sample) that was pre-rinsed with ultrapure 18 MQ (milli-Q) water and mounted on a rack (see Figure 5). Prior to separation, the resins were each conditioned (in order) with: 20 mL 18 MQ water, 10 mL 3M HNO_3, and a 20 mL mixture of 8M HNO_3 + 0.1M HF.

Each sample (dissolved in 0.5 mL 8M HNO_3 + 0.1M HF) was deposited into a column and the empty Teflon vials were then rinsed with 1 mL, 0.5 mL, and 10 mL of 8M HNO_3 + 0.1M HF in order to remove residual sample left in the vials. The rinse acids (1 mL, 0.5 mL, and 10 mL quantities) were deposited into each respective resin columns after each rinse cycle. A very similar procedure using UTEVA resin resulted in up to 99.997% capture of uranium from uranium oxide samples [10].

The liquids collected from the columns were dried down in a fume hood in the Teflon vials at 110 °C until completely dry. Once dried, a few drops of cHNO_3 were added and the samples were dried again. This process was repeated 2-3 times and once dried the samples were finally re-suspended in 5 mL of 2% HNO_3 spiked with arsenic (As) internal standard for ICP-MS analysis. The samples, dummy sample standard, and high-purity elemental standards (diluted from ~1000 mg/L solutions) were all measured using an ASX-112FR auto-sampler by CETAC (see Figure 6) and the auto-sampler tip was cleaned with HNO_3 between each measurement. The tabulated ICP-MS results represent averaged values from multiple measurements and the impurity concentrations are expressed as µg per gram of U_3O_8 (see section for further details). The limits of detection were estimated from linear calibration curves with linear regression coefficients better than or equal to 0.99 that were constructed using the high-purity elemental standards in the range 0.005 – 175 µg/L.

Thermogravimetric Analysis

Thermogravimetric analysis (TGA) was employed to measure the weight gain of the UO_2 samples with increasing temperature. The TGA was performed at the University of Notre Dame using a LABSYS evo TGA-DSC instrument. The experimental protocol was modeled after the procedure outlined in ASTM C-1453-00 [11] titled, *Standard Test Method for the Determination of Uranium by Ignition and the Oxygen to Uranium (O/U) Atomic Ratio of Nuclear Grade Uranium Dioxide Powders and Pellets*.

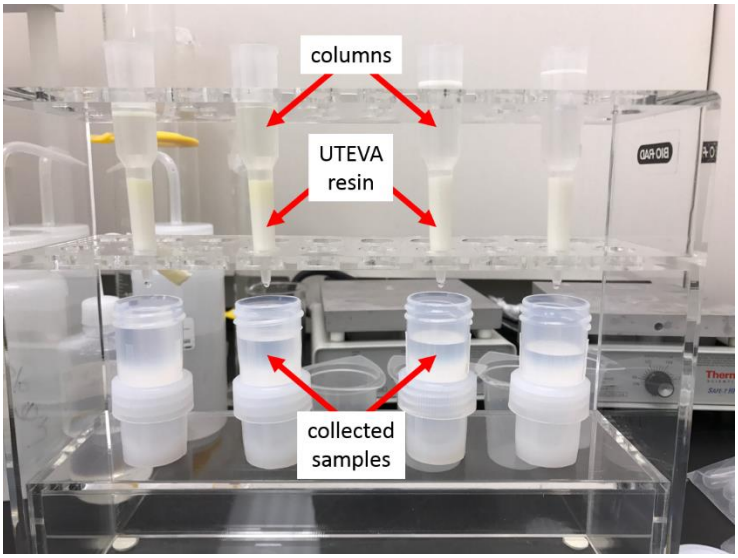


Figure 5: Setup used to perform uranium ion exchange for ICP-MS samples

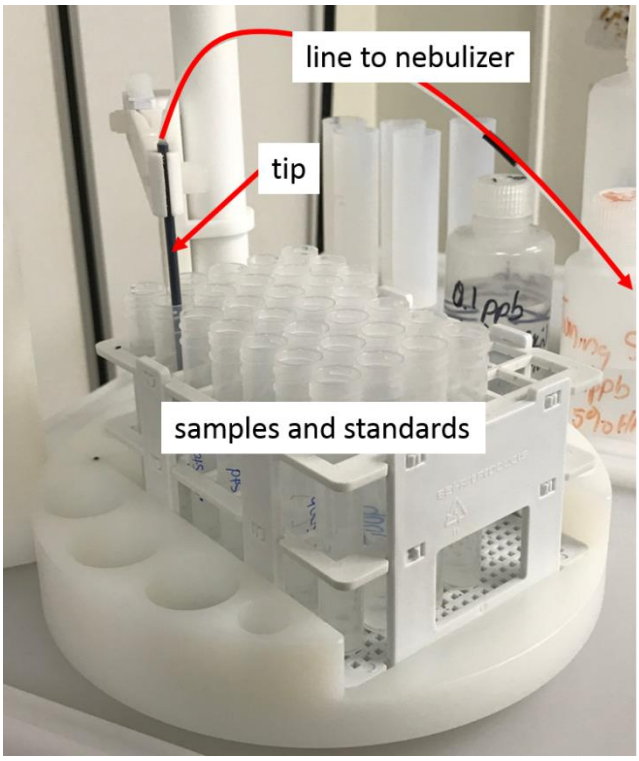


Figure 6: auto-sampler used for all ICP-MS measurements

For each uranium oxide sample, approximately 10-50 mg of powder was loaded into a 100 µL aluminum oxide (Al_2O_3) crucible (see Figure 7 inset). Each filled crucible was mounted onto the TGA balance alongside an empty crucible that was used for weight corrections. Weight changes measured in flowing gas atmosphere are subject to buoyancy forces that result in apparent weight changes. Bouyency effects were corrected by subtracting the results obtained by running two empty crucibles (one as a 'sample' and one as a reference) under identical heating and temperature ramp conditions as the uranium oxide samples.

All samples were heated under a constant flow of 40 mL/min of synthetic air. Each sample was equilibrated at 30 °C for five minutes and the weight was tared prior to ramping to 900 °C with a heating rate of 10 °C/min. The samples were held at 900 °C for 3 hours to allow complete oxidation to U_3O_8. Completion of oxidation processes was confirmed by the negligible weight change with increasing time. The temperature, relative weight change, and heat flow from each sample were measured continuously every 1.2 seconds. The weight precision of the instrument was ±0.01% and the resolution of the instrument was 0.1 µg.

In addition to performing TGA, the instrument also performed the functions of a differential scanning calorimeter (DSC). The simultaneous measurement of heat flow from the sample enabled the identification of exothermic events, such as from phase transformations. Inspection of the exothermic events aided in determining the completion of the oxidation to U_3O_8. However, the DSC measurements were not calibrated to the synthetic air carrier gas used. Thus, the DSC results were only used for qualitative analysis. Omission of a proper DSC carrier gas calibration implies that the exact temperatures of the exothermic events are only approximate and not precise.

X-ray Diffraction

Synchrotron X-ray diffraction measurements were performed at the high-pressure collaborative access team (HPCAT) sector 16-BM-D beamline at the Advanced Photon Source (APS) at Argonne National Laboratory (ANL) [12]. The samples irradiated with 2.2 GeV Au ions were measured in the stainless steel strips using the configuration shown

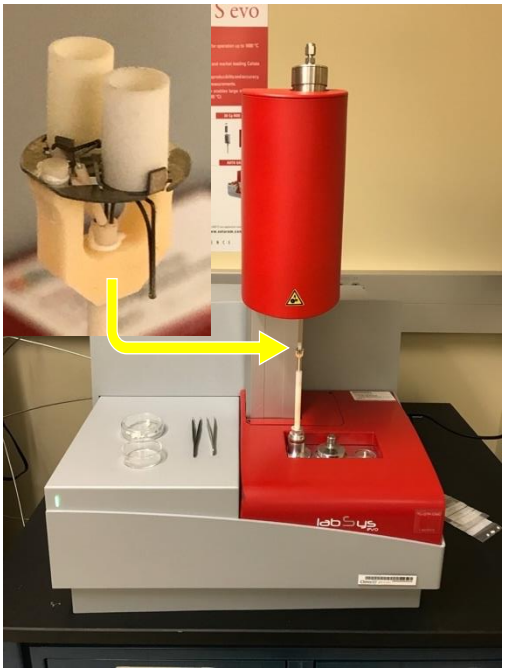


Figure 7: LABSYS evo thermogravimetric analysis instrument

in Figure 8. These measurements were performed in transmission mode at room temperature using a focused beam of 29.2 keV (λ = 0.4246 Å) X-rays.

Isochronal annealing experiments were also performed at the 16-BM-D beamline using a hydothermal diamond anvil cell (HDAC) [13, 14] (see Figure 9) and a beam of 25 keV (λ = 0.4959 Å) X-rays. Two CeO_2 and ThO_2 samples irradiated to a fluence of 1×10^{13} ions/cm^2 were loaded in air into two sample chambers that were drilled into a pre-indented rhenium gasket. The gasket was surrounded by two diamond anvils in order to seal the sample chambers. The thickness of the gasket was made larger than the sample pieces such that the samples were contained in the chambers without pressure.

The HDAC offered several advantages over conventional heating stages. XRD patterns was collected *in situ* with minimal interference from furnace components because the sample is surrounded by X-ray-transparent diamond anvils. The photon beam was directed through the sample chamber and the two diamond anvils, which are fixed on seats that are wrapped with metal wire. The wire provided resistive heating to the diamonds, and the power to each seat/diamond was controlled individually. The HDAC also enabled very rapid heating and quench rates because of the high thermal conductivity of the diamond anvils. Additional details regarding this experimental setup are provided in ref. [15].
Debye Scherrer rings were collected on a two-dimensional (2D) Mar345 image plate detector during both experiments. The sample-to-detector distance was calibrated using the diffraction pattern of a national institute of standards and technology (NIST) CeO_2 powder sample. The 2D detector images were integrated into 1D diffraction patterns using either the Dioptas software [16] or the GSAS-II software [17]. The instrument parameters were derived by refining the peak profile of the XRD pattern of the NIST CeO_2 standard using the GSAS-II software.

X-ray Total Scattering

X-ray total scattering is distinct from X-ray diffraction (XRD) in that the total scattering pattern comprises both diffuse and Bragg scattering components whereas XRD only conveys Bragg structural information. Total scattering patterns are generally obtained by taking into account all sources of absorption and scattering from background sources,

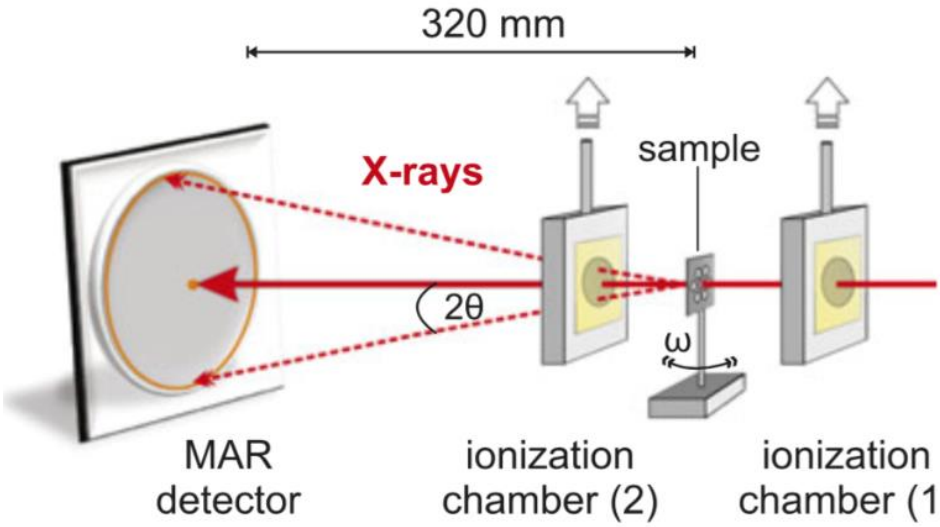


Figure 8: Schematic of X-ray diffraction setup at 16-BM-D. Figure reproduced from reference [2]

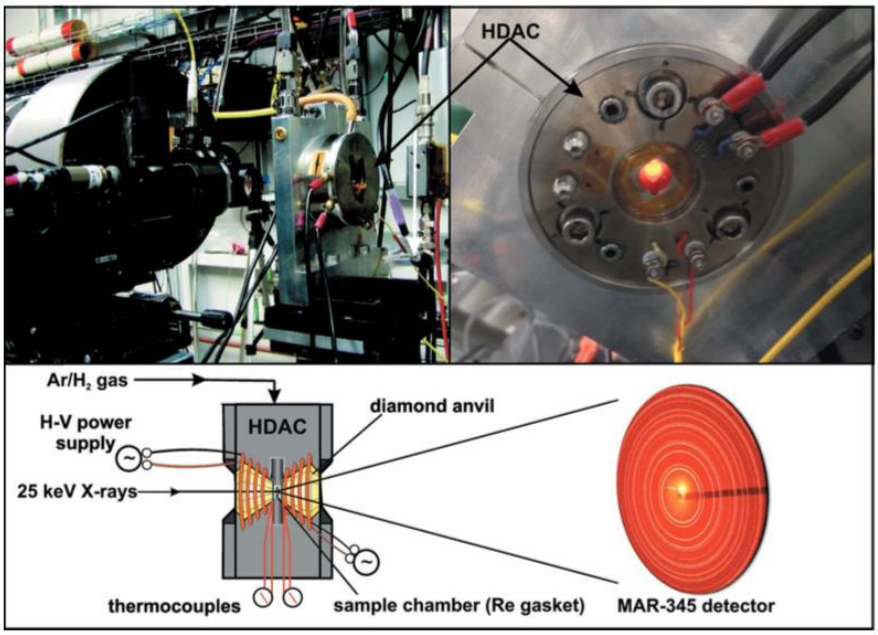


Figure 9: Hydrothermal anvil cell setup at 16-BM-D. Figure reproduced from reference [15]

which are not treated during XRD. X-ray total scattering measurements were performed at the 11-ID-B beamline of the APS at ANL with a beam of 86.7 keV X-rays (0.1430 Å). The irradiated powders were loaded into Kapton tubes of 0.81 mm inner diameter and 10-20 mm length. The ends of the Kapton tube were sealed with epoxy. The loaded Kapton tubes were mounted onto a high-throughput sample shifter that automatically aligned each sample individually. Scattering patterns were collected on a Mar345 image plate camera. The measurement times were minimized to 0.2 seconds to avoid saturation of the detector. Therefore, each X-ray measurement represents the sum of 900 frames, which is equivalent to a total exposure time of 3 minutes.

The detector and diffraction patterns were calibrated using the scattering pattern of a polycrystalline CeO_2 standard. The total scattering patterns were automatically converted into X-ray pair distribution functions (PDFs) using a specialized beamline program called *RAPDFgetX*, which is based on the program *PDFgetX* [18]. The X-ray detector was calibrated with the use of a CeO_2 NIST standard. X-ray structure factors, $S(Q)$, were obtained by subtracting background scattering intensity from the measured scattering pattern of each sample. X-ray pair distribution functions (PDFs), $G(r)$, were calculated by the Fourier transform:

$$G(r) = r\left(A\int_{Q_{min}}^{Q_{max}} Q[S(Q)-1]\sin(Qr)\,dQ\right)$$

where Q is the scattering vector, $Q = 4\pi/\lambda\sin(\theta)$, θ is the scattering angle, λ is the X-ray wavelength, r is distance in real-space, and A is an arbitrary scaling factor. Q_{min} and Q_{max} values were optimized to 0.5 $Å^{-1}$ and 34.0 $Å^{-1}$.

Neutron Total Scattering

Neutron total scattering measurements were performed at the Nanoscale Ordered Materials Diffractometer (NOMAD) beamline (BL-1B) [19] of the Spallation Neutron Source (SNS) at Oak Ridge National Laboratory (ORNL). CeO_2, ThO_2, and UO_2 powders were all measured in quartz tubes. Non-radioactive CeO_2 samples were loaded into thin-walled (0.01 mm) quartz capillaries with 2 mm tube diameters. Radioactive ThO_2 and UO_2

powders were loaded into thicker-walled (0.38 mm) nuclear magnetic resonance (NMR) tubes with ~5 mm tube diameter and low boron continent (< 0.1 ppm) (Figure 10).

Room-temperature measurements of irradiated CeO_2 and ThO_2 were performed using a sample shifter, which could accommodate several tubes and capillaries in a single loading (Figure 10). High temperature measurements were performed using a resistively-heated Institut Laeu-Langevin (ILL)-type vacuum furnace. The furnace comprised a removable sample stick and a furnace chamber in which the sample stick was inserted. Only a single vanadium can was coupled to the bottom of the stick during a given experiment (Figure 11). Radioactive ThO_2 and UO_2 powders were double-encapsulated by loading the samples into NMR tubes and subsequently inserting the NMR tubes into vanadium cans in order to comply with facility safety requirements. All loaded samples were sealed in vanadium cans using boron nitride lids and molybdenum nuts and bolts to prevent the lids from fusing to the cans and/or sample stick.

Prior to each heating cycle, the loaded sample stick was lowered into the furnace chamber, the furnace flange was clamped, and the chamber was evacuated using a turbo pump until a vacuum of ≤ 0.01 mbar was achieved. Heating rates for all experiments were between 4-10 °C/min, depending on the experiment and target temperature, and cooling cycles were performed as fast as possible (*i.e.*, quenching). The initial quench rate was 45-60 °C/min and the cooling rate gradually decreased as the temperature lowered. Once the samples cooled to approximately 200-300 °C, the cooling rate was manually accelerated by continuously pumping and purging the chamber with nitrogen gas.

Scattered neutrons were detected by six detector banks located at different scattering angles. Notable specifications for each detector bank are shown in Table 2. Each detector bank records scattering intensity in a specific *Q*-range such that a single measurement resulted in six unique diffraction patterns. Each detector exhibits different resolution, which depends on the scattering angle. The detectors located at the highest scattering angles (banks 4 and 5) yielded the highest resolution diffraction patterns (smaller ΔQ) and the detectors located at the smaller angles (*e.g.*, bank 1) yielded the worst diffraction resolution. The NOMAD detectors were calibrated using the Bragg peaks from a NIST diamond powder standard. The instrument parameters were derived for each

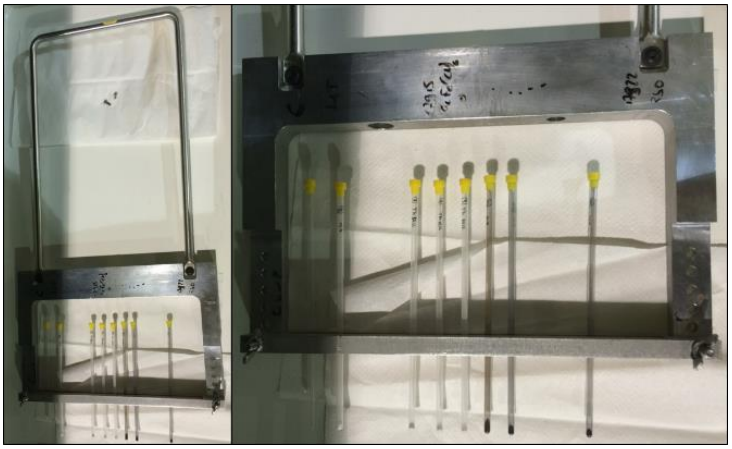


Figure 10: NMR tubes loaded with radioactive powders mounted on the NOMAD sample shifter tray for room-temperature neutron scattering measurements

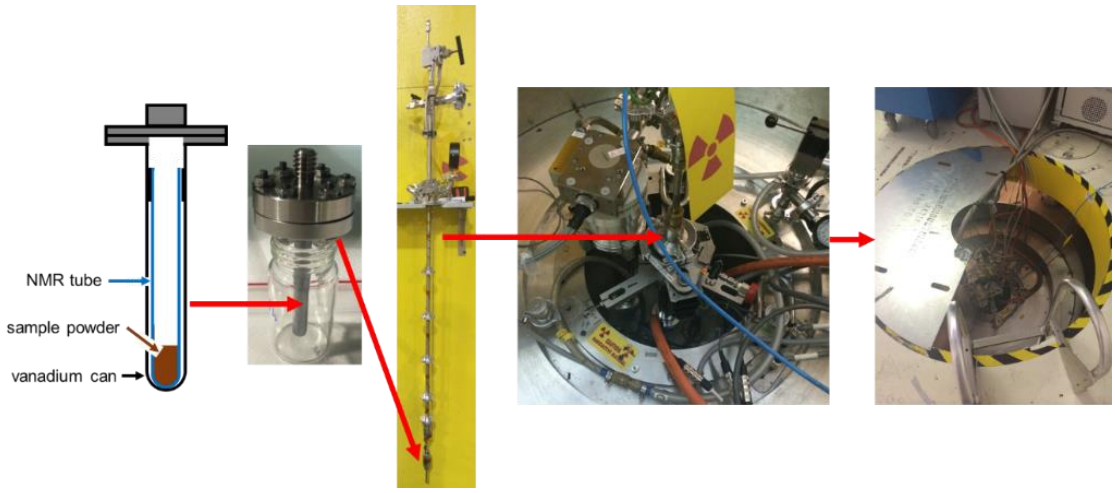


Figure 11: Experimental setup for high-temperature measurements performed at the NOMAD beamline. Filled vanadium cans (left) were mounted on a stick (center) that was dropped into the furnace environment (right). The furnace chamber lies under the beamline hutch

Table 2: NOMAD detector bank information

Detector Bank Number	Total Neutron Flight Path [m]	Two Theta [degrees]
1	21.51	15.1
2	21.18	31.0
3	20.64	65.0
4	20.61	120.40
5	20.29	150.1
6	22.06	8.6

detector bank by refining the peak shape parameters for a NIST Si powder standard using GSAS [20].

Neutron structure factors, $S(Q)$ were obtained by normalizing measured scattering intensity to the scattering intensity from a solid vanadium rod and then subtracting the background scattering intensity. Background scattering intensities were measured using empty quartz tubes in the case of the room-temperature measurements. For the high temperature measurements, the background scattering intensities were measured using an empty NMR tube in a vanadium can. Background measurements were collected at ambient and high temperature to account for temperature-dependent changes in background scattering intensity. Neutron pair distribution functions (PDFs), $G(r)$, were calculated by the Fourier transform:

$$G(r) = r\left(A\int_{Q_{min}}^{Q_{max}} Q[S(Q)-1]\sin(Qr)\,dQ\right)$$

where Q is the scattering vector, $Q = 4\pi/\lambda\sin(\theta)$, θ is the scattering angle, λ is the X-ray wavelength, r is distance in real-space, and A is an arbitrary scaling factor. The Q_{min} and Q_{max} values varied depending on the experiment, but were typically set to 0.1 $Å^{-1}$ and 31.4 $Å^{-1}$, respectively. On occasion, Q_{min} was increased to avoid odd features at low Q values. Q_{max} was also decreased/increased on occasion when the data were of poorer/better quality.

Neutron PDFs were sometimes converted from arbitrary scale (*i.e.*, using an arbitrary scaling factor) to absolute scale. The advantage of using absolute scaling was that the measured area of a PDF peak is equal to the coordination number of the atom pair that contributes to the peak intensity. Absolute scaling was also required for performing Reverse Monte Carlo modeling of the neutron scattering data. Absolute scaling was performed by defining the exact sample composition and density, and applying multiple scattering corrections to the measured data. Two PDF notations were used for absolute scaling. The first was the total correlation function, $T(r)$, which was defined as:

$$T(r) = 4\pi r^2 \rho g(r)$$

where r is real-space distance and ρ is the sample density. The second was the total radiation distribution function as defined by Keen [21], $G(r)_{\text{Keen}}$, which was defined as:

$$G(r)_{Keen} = \sum_{i,j=1}^{n} c_i c_j \bar{b}_i \bar{b}_j \left[g_{ij}(r) - 1\right] = \frac{1}{(2\pi)^3 \rho_0} \int_0^{\infty} 4\pi Q^2 F(Q) \frac{\sin(Qr)}{Qr} dQ$$

where c_i is the concentration of species i in the material, $\bar{b}_i$ is the coherent bound neutron scattering length of species i, g_{ij} is the partial radial distribution function for species i and j, ρ_0 is the average number density of the material in $Å^{-3}$, Q is the scattering vector, r is real-space distance, and $F(Q)$ is the total-scattering structure factor.

Raman Spectroscopy

Confocal micro-Raman spectroscopy studies were conducted at the University of Tennessee with a Horiba Jobin Yvon LabRAM HR evolution instrument. The spectrometer was equipped with red (785 nm), green (532 nm), and blue (473 nm) excitation lasers. The maximum power output values for these lasers were 100, 50, and 25 mW, respectively. Laser power was reduced to anywhere from 0.01-50 % of the max power using an optical filter wheel. Laser radiation was illuminated on the samples through microscope objectives that varied in magnification from 5x to 100x. Raman signals were collected in backscattering geometry using one of two grating types. The first type was a lower-resolution 600 grooves/mm grating with a resolution of approximately 0.8 cm^{-1} with the red laser. The second grating was higher-resolution featuring 1800 grooves/mm and a resolution of approximately 0.4 cm^{-1} with the red laser. In all cases, the resolution was less than 1 cm^{-1}. Back-scattered Raman signals were collected on a liquid-nitrogen-cooled charged couple device (CCD) detector. Calibration of the instrument was performed prior to each experiment by measuring the Raman spectra of a silicon wafer and referencing the ~520 cm^{-1} peak of Si.

Low laser powers (0.05 – 1 mW) were used in all experiments in order to avoid undesired annealing of radiation effects and/or modification of sample composition (e.g., by oxidation). The reported Raman spectra represent an average of multiple measurements (typically 25) collected at different positions in the samples. The collection of spectra at

multiple points ensured that the reported spectra are representative of the bulk sample. Measurements were only collected from one identical position during the isochronal annealing experiments in order to monitor relative changes in the structure. Radioactive UO_2 and ThO_2 samples were contained in a custom-built aluminum box that was equipped with a borosilicate glass window. Borosilicate glass was chosen because it exhibits low optical absorption (<10 %) in the broad range from 0.4-2 μm, which encompasses the visible light range of all three excitation lasers. The instrument and the collection of measurements were controlled by the Horiba LabSpec 6 graphical user interface software. Datlab [22] and Origin softwares were used to extract peak positions, areas, and intensities from the Raman spectra for further analysis.

Data Modeling and Analysis

Rietveld Structural Refinement

Rietveld refinements of X-ray and neutron diffraction patterns were performed using either the *GSAS* [20] or *GSAS-II* [17] software. In general, *GSAS* was typically used for neutron diffraction patterns whereas *GSAS-II* was used for synchrotron XRD data. The diffraction patterns of all of the materials were fit using the fluorite structure model (space group *Fm*-3*m*) in which cations occupy the 4*a* site and oxygens occupy the center of tetrahedra at the 8*c* site.

Typically, only six parameters were refined. These are the background, scale, isometric unit cell parameter, zero-point, isotropic atomic displacement parameter (ADP) of the cation site, and isotropic ADP of the oxygen site. The background was typically fit using a six-coefficient Chebyshev polynomial. The neutron diffraction patterns were fit using *GSAS* profile function #3. In contrast to *GSAS*, *GSAS-II* only offers one profile function, which represents a pseudo-Voigt peak shape. This is advantageous for analyzing the X-ray data because synchrotron XRD patterns are best represented using the pseudo-Voigt function type. On occasion, site occupancies were refined. Oxygen site occupancies were only refined with neutron diffraction data because X-rays are not sensitive to oxygen atoms in the presence of the heavy cations. When analyzing both neutron and X-ray data

sets for a single sample, the oxygen site occupancies from the neutron data refinements were used as fixed input for the X-ray data refinements.

Neutron diffraction was unique from synchrotron XRD in that the NOMAD beamline utilizes six distinct detector banks located at different scattering angles. This means that the scattering from a single sample results in six independent neutron diffraction patterns collected at different scattering angles. Generally, only the diffraction patterns from the highest scattering-angle detector banks (3, 4, and 5) were used for structural refinement. Reported Rietveld refinement results are typically from refinements in which detector banks 3, 4, and 5 were fit simultaneously.

Small-Box Structural Refinement

The structure of a material can be refined using the PDF in a way that is similar to structural refinement performed *via* Rietveld refinement of diffraction patterns. The most popular least-squares refinement method applied to PDFs is commonly performed using the program *PDFgu*i [23]. The method is often referred to as small-box PDF refinement because the PDF is modelled using a small ensemble (*i.e.*, box) of atoms, often the size of a single unit cell. The small ensemble is constructed either manually with *P*1 symmetry or by defining a specific space group symmetry (e.g., *Fm*-3*m*) and designating atoms to special positions (*i.e.*, Wyckoff sites). *PDFgui* calculates the PDF of the constructed atom ensemble (*i.e.*, the starting model), and the model is refined using structure variables until the arrangement of atoms yields a PDF that is in better agreement with the experimental PDF.

The PDFs were fit using the fluorite structure unit cell (space group *Fm*-3*m*) with cations at the 4*a* site and anions at the 8*c* site. Unit cell models contained four cations and eight oxygen atoms. This starting model was refined using 5 parameters: scale, the delta parameter (accounts for short-range correlated atomic motion), isometric unit cell parameter, and the isotropic ADPs for the cations and anions. All four cations were given the same ADP variable because they are all located on the 4*a* site. A single ADP was also applied to all eight oxygen atoms by similar argument.

Small-box fitting of defect structure models to UO_{2+x} and Nd-doped UO_2 data was performed by manually manipulating a simple fluorite structure model (either 1 cell or a 2×2×2 supercell). Defects such as interstitials were inserted manually into the supercells until the desired stoichiometry was achieved. Refinement of these defect structures was very similar to the refinement procedure used for pristine fluorite structures except that changes in interstitial configurations (in the case of UO_{2+x}) or simulated atomic relaxations (in the case of Nd-UO_2) were included.

Large-Box Reverse Monte Carlo Modeling

Monte Carlo-based simulations using larger atom ensembles were employed to compliment the small-box modeling efforts. The method, called Reverse Monte Carlo (RMC), was performed using the *RMCProfile* software [24]. Contrary to conventional Monte Carlo in which the goal is to derive order or patterns from inherently stochastic processes, RMC drives disorder from an initially ordered state. RMC simulations begin with well-ordered systems and aim to maximize the entropy of a system within a set of given constraints. The largest constraints used by *RMCProfile* are the experimental total scattering data, such as the diffraction (Bragg) pattern, absolute-scale PDF $G(r)_{\text{Keen}}$, and arbitrary-scale PDF G(r) (equivalent to the $D(r)$ function defined by Keen [21]). Additional constraints, such as bond-valence-sum (BVS) and distance window constraints are used in order to add chemical and physical restrictions, respectively.

RMC simulation cell sizes can vary. Simulations run in the present study employed 10×10×10 supercells, which comprise 1000 fluorite unit cells and 12000 atoms (4000 cations and 8000 anions). This size was chosen because it provided a reasonable trade-off between minimizing computational power and maximizing counting statistics. The initial atom ensemble composed of cations and anions in perfect fluorite structure arrangement. The parameters for the perfect atomic arrangements (*e.g.*, lattice parameter and atom positions) were obtained from Rietveld refinement (average structure modeling) of the corresponding diffraction pattern for the sample of interest. Identical starting models were run at least 10 times and the final configurations were often averaged in order to improve statistics and to eliminate the possibility of uniqueness problems. The run time for a single

supercell was almost always 12 hrs. This time was chosen as it enabled enough time for entropy optimization while limiting computational resources.

Pair distribution functions, G(r), for RMC were produced at the start of each RMC simulation using the corresponding S(Q) file and the program *STOG*. Various Q_{max} values were tested, but all Q_{max} values were ultimately set to 31.4 $Å^{-1}$ in accordance with the optimized value from the NOMAD beamline. All S(Q) data were corrected for multiple scattering and sample absorption. A Fourier filter was also applied to all PDFs in order to eliminate effects from artificial Fourier ripples at *r* values lower than ~2 Å (the minimum distance of the first PDF peak of UO_2). Extensive testing revealed that no real PDF features exist below this value. Two small peaks were observed in the PDF of UO_{2+x} at ~1.35 and ~1.75 Å. Testing showed that these peaks remain even after varying Q_{max} and varying the SiO_2 signal magnitude. This suggested that the peaks were real PDF features, but these features were also present in the PDF of $UO_{2.00}$ and were therefore attributed to Fourier ripples and eliminated using the Fourier filter. Testing also showed that the application of the Fourier filter did not affect the intensity of any real PDF peak.

All RMC runs for UO_2 systems were run with BVS constraints and minimum distance constraints. The minimum distances were set using the minimum *r* position of the first PDF peak (for U-O, Nd-O, and O-O distances) and the third peak (for U-U, U-Nd, Nd-Nd distances). BVS parameters were based on the latest values reported in ref. [25]. RMC simulations were run with and without BVS constraints in order to test whether the results were influenced or biased by the constraints. The results showed that the converged structures are very similar regardless, but structures with BVS constraints are more chemically-sensible. Valence distributions resulting from RMC runs with BVS constraints showed much tighter valence distributions that are in line with observations made with spectroscopic techniques.

CHAPTER I: POINT DEFECTS IN SWIFT HEAVY ION-IRRADIATED CERIA AND THORIA

Versions of this dissertation chapter were previously published by Raul I. Palomares, Jacob Shamblin, Cameron L. Tracy, Joerg Neuefeind, Rodney C. Ewing, Christina Trautmann, Fuxiang Zhang, Changyong Park, Dmitry Popov, and Maik Lang in the journals: *Journal of Materials Chemistry A*, *Nuclear Instruments and Methods in Physics Research B*, and *Journal of Applied Crystallography*:

R.I. Palomares *et al*., "Defect accumulation in swift heavy ion-irradiated CeO_2 and ThO_2." *J. Mater. Chem. A*, 2017, **5**, 12193

R.I. Palomares *et al*., "Thermal defect annealing of swift heavy ion irradiated ThO_2." *Nucl. Instr. Meth. B* **405** (2017) 15-21

R.I. Palomares *et al*., "*In situ* defect annealing of swift heavy ion irradiated CeO_2 and ThO_2 using synchrotron X-ray diffraction and a hydrothermal diamond anvil cell." *J. Appl. Cryst.* (2015). **48**, 711-717

For these published works, M.L. and R.I.P. conceived of the experiments; R.I.P., C.L.T., and F.Z. prepared the samples; R.I.P., C.L.T., C.T., and M.L. coordinated and/or performed the irradiations; R.I.P., J.S., J.N., C.P., and D.P. coordinated, setup, and/or performed the experiments; R.I.P. performed analysis and interpretation of the experimental data; R.I.P. wrote the manuscripts with input from all co-authors.

A version of this dissertation chapter is also presented in an unpublished manuscript by Anna Shelyug, Raul I. Palomares, Maik Lang, and Alexandra Navrotsky. The manuscript titled, "Defect energetics in fluorite structured oxides exposed to highly ionizing radiation", is currently in preparation for submission to a peer-review scientific journal.

For this currently unpublished work, M.L., R.I.P., and A.N. conceived of the experiments; R.I.P. prepared the samples and coordinated the irradiations; R.I.P. performed the neutron, X-ray, and Raman experiments; A.S. performed the calorimetry experiments; A.S., R.I.P.,

and M.L. performed analysis and interpretation of the experimental data; A.S. and R.I.P. wrote the manuscript with input from all co-authors.

Abstract

Microcrystalline CeO_2 and ThO_2 were irradiated at room temperature with 945 MeV, 1.1 GeV, and 2.2 GeV Au ions in order to characterize effects of electronic energy deposition on atomic structures and structural stability. Atomic structural modifications were characterized using neutron and X-ray diffraction, total scattering, and pair distribution function analysis, and Raman spectroscopy. Energetic destabilization was quantified using drop-solution calorimetry. Structural analyses showed that swift heavy ion irradiation results in the production of primarily oxygen Frenkel defects in CeO_2 and ThO_2 and the two materials show different damage accumulation mechanisms. A large variety of oxygen defect clusters and defect complexes containing Ce^{3+} and oxygen vacancies were observed in CeO_2 after irradiation and were attributed to the redox capability of cerium cations. The stability of irradiation-induced point defects was investigated using isochronal annealing experiments and differential scanning calorimetry. Structural analyses showed that swift heavy ion irradiated CeO_2 and ThO_2 anneal *via* two and one distinct annealing stages within the temperature range studied. The low temperature annealing stage of CeO_2 was strongly influenced by the annealing atmosphere and was attributed to surface or near-surface diffusion mechanisms and/or cation oxidation. Additional low-temperature annealing mechanisms in CeO_2 and ThO_2 were attributed to annihilation of oxygen aggregates. High-temperature annealing stages were attributed to cation vacancy migration in agreement with studies of UO_2. These combined structural and calorimetric studies showed that electronic energy deposition primarily influences the oxygen sublattice and oxygen Frenkel defects are annealed at relatively low temperatures. The observation of oxygen defect clusters and Ce^{3+}/O_V complexes in CeO_2 suggests that cation redox in fluorite structured oxides strongly influences defect clustering. Small oxygen defect clusters can exhibit low migration barriers relative to isolated oxygen interstitials. Therefore, further studies of defect kinetics are needed in order to determine the influence of defect clustering on atomic diffusivity.

Introduction

Fluorite-structured oxides are commonly used as components for a variety of energy applications because they often exhibit both attractive physiochemical properties and high structural durability under a wide range of conditions. Two such materials are cerium dioxide (CeO_2) and thorium dioxide (ThO_2). CeO_2 materials find applications as industrial catalysts [26, 27], oxygen sensors [28], and solid oxide fuel cell (SOFC) electrolytes [29, 30]. CeO_2 is also used as a non-radioactive isostructural analogue to actinide oxides, most notably UO_2 and PuO_2, because CeO_2 has similar density, melting point, and thermal diffusivity and exhibits similar response to UO_2 under most irradiation conditions. There also exist notable differences in electrical, chemical, phase stability, defect migration, and defect clustering properties that can make direct comparisons between CeO_2 and UO_2 challenging [31-33]. Cerium chemistry is most similar to plutonium chemistry and less like uranium chemistry. As a result, CeO_2 is often used as a non-radioactive model system for PuO_2. Studies of mixed oxide (MOX) fuel, for example, have shown that cerium-based MOX analogues exhibit similar compaction, sintering, and thermal properties to plutonium-based materials [34].

ThO_2 is also proposed for a variety of applications ranging from industrial catalysts [35] to nuclear fuels [36]. Interest in thorium-based fuel cycles has historically been limited to countries with high thorium reserves, such as India, but there's been a renewed interest in thorium fuels through the emergence of advanced reactor concepts, such as molten salt reactors. The study of ThO_2-based fuels can also yield valuable insights for the development of advanced fuel concepts regardless of the inherent proliferation risks associated with thorium [37]. For example, ThO_2 is highly refractory (melting point is ~500 °C higher than UO_2 melting point) and chemically durable owing to the fixed valence of thorium (Th^{4+}) in the oxide form. This makes thorium oxide potentially applicable to systems requiring operation under ultra-high temperatures and corrosive environments.

Chemical durability is especially important to consider when evaluating the radiation tolerance of materials because chemical variability is often correlated to phase stability. Nuclear fuels are continuously bombarded with a wide spectrum of alpha, beta, gamma, neutron, and ion radiation in nuclear reactors under normal operating conditions.

Of these types of radiation, structural degradation is typically attributed to alpha, neutron and ion radiation. Neutrons, being particles without charge, interact with materials *via* nuclear interactions. This is in contrast to alpha particles and ions, which can interact by way of both nuclear and electronic interactions. To illustrate this, Figure 12 shows how the energy loss from nuclear and electronic components varies with increasing ion energy.

Effects of neutron and alpha irradiations are generally of interest for nuclear fuel studies because these types of irradiation are most commonly encountered under conventional operation and storage conditions. However, studies of higher-energy ions also hold merit because they aid in understanding effects of fission fragments, which typically have higher mass (*e.g.*, Sr, Xe, I) and higher kinetic energies (*e.g.*., 100-200 MeV). Higher energy ions can exhibit very different nuclear-to-electronic energy loss ratios depending on the incident kinetic energy. This can lead to a diverse range of material modifications owing to the synergistic, competing, or additive radiation effects that can result from nuclear and electronic energy loss components [38].

One means to investigate and de-convolute these complex effects is through the use of swift heavy ion irradiation. Swift heavy ions are loosely defined as particles with kinetic energies greater than or equal to 1 MeV per nucleon (MeV/*u*). Use of this radiation enables the manual variation and optimization of nuclear-to-electronic energy loss ratios, which is valuable for investigating isolated features, such as effects from electronic energy loss alone. Swift heavy ions in this very high energy regime interact much differently than particles that interact primarily *via* elastic collisions.

Swift heavy ions interact primarily through inelastic excitation and ionization events. Several models have attempted to describe the early stages of these interactions [39-47]. The general picture that has emerged is that dense electronic excitations modify interatomic interactions and bonding. Subsequent thermal spikes from electron-phonon coupling induce atomic displacement, which can lead to permanent material modifications when relaxation from the perturbed state is sufficiently rapid, and recovery kinetics are sufficiently slow as to preclude recovery to the initial structure. Atomic disordering in insulators can result in densification [48], phase transformations [49], or amorphization [50], among other modifications. In fluorite-structured oxides, such as CeO_2 and ThO_2,

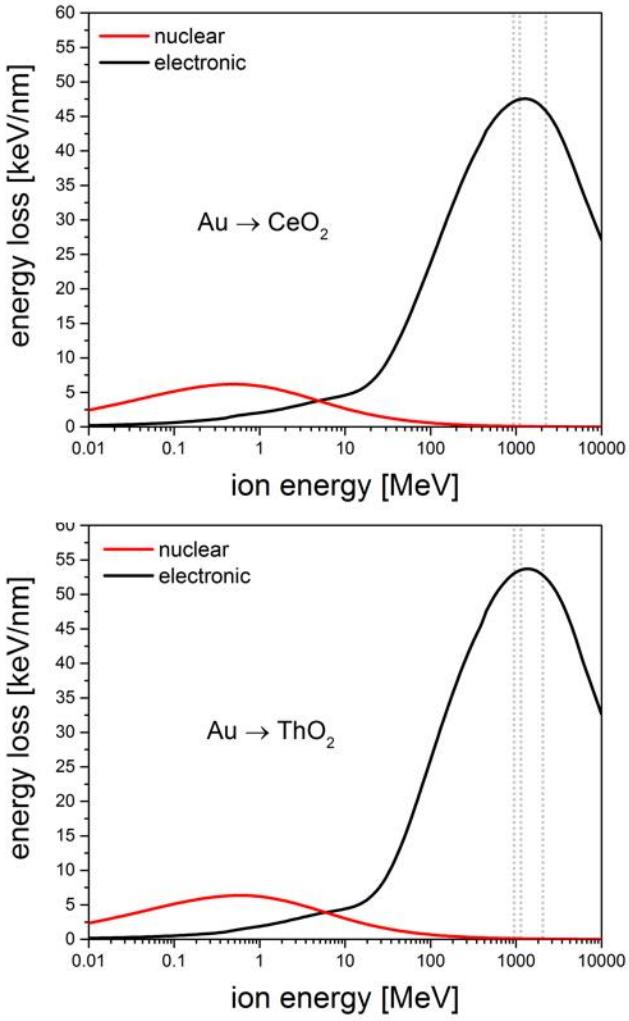


Figure 12: Energy loss of Au ions in CeO_2 and ThO_2 calculated using the SRIM 2008 code [4]. The dotted grey lines denote the Au ion energies used for ion beam irradiation experiments performed for this work

swift heavy ion irradiation does not result in amorphization or phase changes, only minor atomic redistribution and density changes [51, 52].

Several studies have attempted to characterize the early stages of ion-matter interactions [32, 53] and the resultant defective structures [7, 51, 52, 54-67] in CeO_2 and ThO_2 in order to understand how fluorite-structured oxides exhibit such high structural stability under irradiation. Room temperature swift heavy ion irradiation of these materials typically results in the production of Frenkel-type defects that can coalesce to yield clusters [32] and dislocation loops [63], which in turn induce volumetric swelling [68]. The formation of voids is also possible considering the production of vacancy clusters, but voids are scarcely observed as a result of room-temperature swift heavy ion irradiation and/or post-irradiation annealing [69]. Void formation was also absent in CeO_2 irradiated with swift heavy ions at elevated temperatures as high as 800 °C [57].

Beyond the formation of simple point defects and defect agglomerates, swift heavy ion irradiation can also result in the formation of cylindrical damage regions, so-called ion tracks. Formation of ion track structures requires stopping power to exceed a certain threshold [39]. Experimental evidence suggests that the threshold for track formation in CeO_2 is ~15 keV/nm [57]. Molecular dynamics (MD) results are in agreement and suggest a threshold as low as ~12 keV/nm [32]. Investigations of ThO_2 are more limited, but it is possible that energy thresholds are similar for this material considering that ion tracks were observed from lower-energy fission fragment irradiations [67].

Transmission electron microscopy (TEM) studies have yielded detailed microstructural analyses of ion track structures in these materials. Cylindrical ion tracks exhibit a core-shell structure in which the central core region is vacancy-rich and the outer shell, or halo region, is rich in interstitials (see Figure 13) [51, 52]. Vacancies and interstitials in these core and shell regions, respectively, have a tendency to cluster. Analyses have revealed that the anion sublattice is severely disordered, and interstitial clustering in the periphery of ion tracks can result in the growth of dislocation networks and sub-grain formation at high fluences [52].

Cation reduction is also a significant contributor to defect evolution in fluorite-structured oxides, specifically CeO_2 [7]. Cation redox is notably absent in ThO_2 owing to

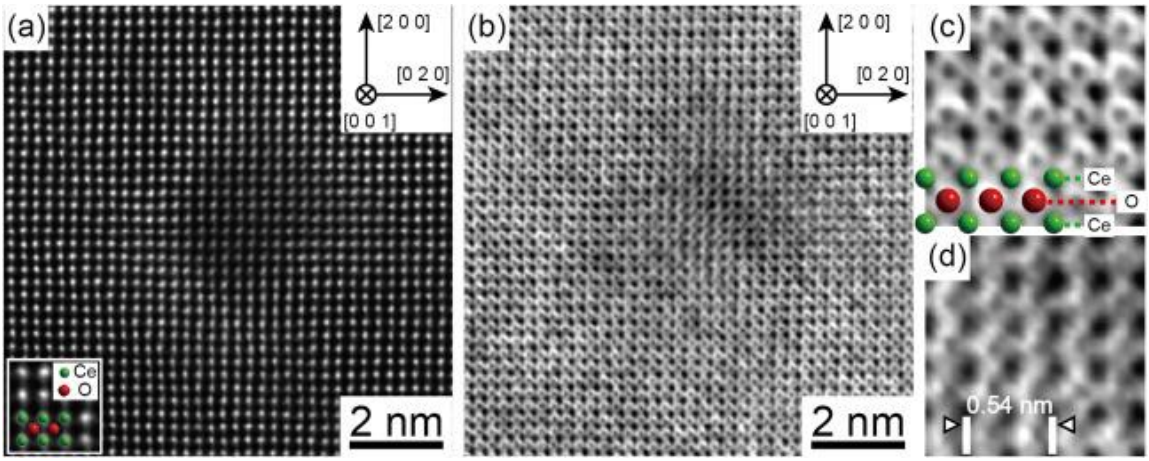


Figure 13: Scanning transmission electron microscopy image of ion track in CeO_2. Image reproduced from reference [51]

the fixed Th^{4+} oxidation state of thorium in the oxide form that results from a presumably high 5th ionization energy [70]. Reduction of cerium from Ce^{4+} to Ce^{3+} is usually concomitant with the incorporation of oxygen vacancies at high temperatures [71]. At room temperature, reduction of cerium can be induced by highly ionizing radiation as confirmed by a number of spectroscopy [7, 56, 58, 72] and magnetic property [62] measurements. It remains unclear if cation redox is primarily driven by initial excitation and ionization processes or the resultant production of oxygen vacancies from swift heavy ion irradiation, *i.e.*, processes occurring on shorter- or longer timescales.

Irradiation-induced redox is important because it proves a means for more efficient defect accumulation schemes. Cerium reduction is an added charge compensation mechanism and enables point defect clustering mechanisms that are potentially forbidden in ThO_2 as a result of the fixed Th^{4+} oxidation state. Density functional theory (DFT) studies of CeO_2 and ThO_2 predict the stability of oxygen defect clusters under hypo- and hyper-stoichiometric conditions [73, 74], such as those found within the core and shell regions of ion tracks, respectively. However, there are certain oxygen defect configurations that are enabled purely as a result of cerium reduction. One example is a bound dimer configuration of two oxygen atoms (one lattice oxygen and one oxygen interstitial). DFT analyses have shown that the covalent bonding of this cluster frees two electrons, which can subsequently localize on cerium atoms and induce reduction [75]. This unique defect mechanism indicates that cerium reduction can result from not only oxygen vacancy formation, but also from defect cluster production. These computational predictions are supported by neutron pair distribution function (PDF) studies of CeO_2 that have revealed the presence of both interstitial- [76] and vacancy-type [77] defect clusters. The aforementioned interstitial clusters are noteworthy because they are analogous to configurations of oxygen interstitials in hyper-stoichiometric UO_2 (UO_{2+x}) [78]. Oxygen interstitial defect clusters in UO_{2+x} can exhibit low kinetic barriers and fast diffusion relative to oxygen vacancies [79], meaning that the stability regimes of these clusters can dictate bulk kinetic and transport properties.

This study aims to elucidate various aspects of point defects in swift heavy ion irradiated CeO_2 and ThO_2, such as:

1. What types of defects are primarily accumulated after swift heavy ion irradiation? (*i.e.*, cation *vs.* oxygen, isolated *vs.* clustered, etc.)
2. How are the bulk and short-range structures modified as a result of defect accumulation? (*e.g.*, are short- and long-range modifications consistent?)
3. What are the thermal stability regimes for defects created by swift heavy ion irradiation?
4. What are the mechanisms for defect annealing in swift heavy ion irradiated oxides?

Defects were produced in microcrystalline CeO_2 and ThO_2 using 1 and 2 GeV Au ion irradiations. Defect production mechanisms were investigated by monitoring structural changes occurring with increasing ion fluence. Defect annealing mechanisms were studied by isochronal annealing experiments. In both cases, structural characterization was performed using neutron total scattering, synchrotron X-ray diffraction, X-ray total scattering, and Raman spectroscopy measurements. Structural studies were complimented by energetics measurements obtained by calorimetric studies performed by collaborators.

Results and Discussion Part I: Damage Accumulation

Neutron and X-ray Diffraction – Average Structure

Analysis of bulk structural modifications was performed using conventional X-ray and neutron diffraction. Diffraction is typically used to quickly perform bulk phase analysis. However, qualitative information is also obtained by inspection of diffraction peaks. For example, peak positions indicate the size of the unit cell parameter, relative peak intensities denote coherency and relative fraction of phase domains, and peak widths indicate phase domain size.

Inspection of the CeO_2 and ThO_2 diffraction patterns (Figure 14, Figure 15, and Figure 16) reveals three main features after irradiation: (1) peaks shift to higher *d*-spacings, (2) peaks broaden, and (3) peak intensities decrease. These features are observed in all diffraction patterns meaning that they are independent of the ion energy used. Peaks shifts indicate that all materials undergo irradiation-induced volumetric swelling as a result of point defect accumulation. Peak broadening and the decrease in peak intensities are consistent with the loss of phase coherency as a result of defect accumulation. Although

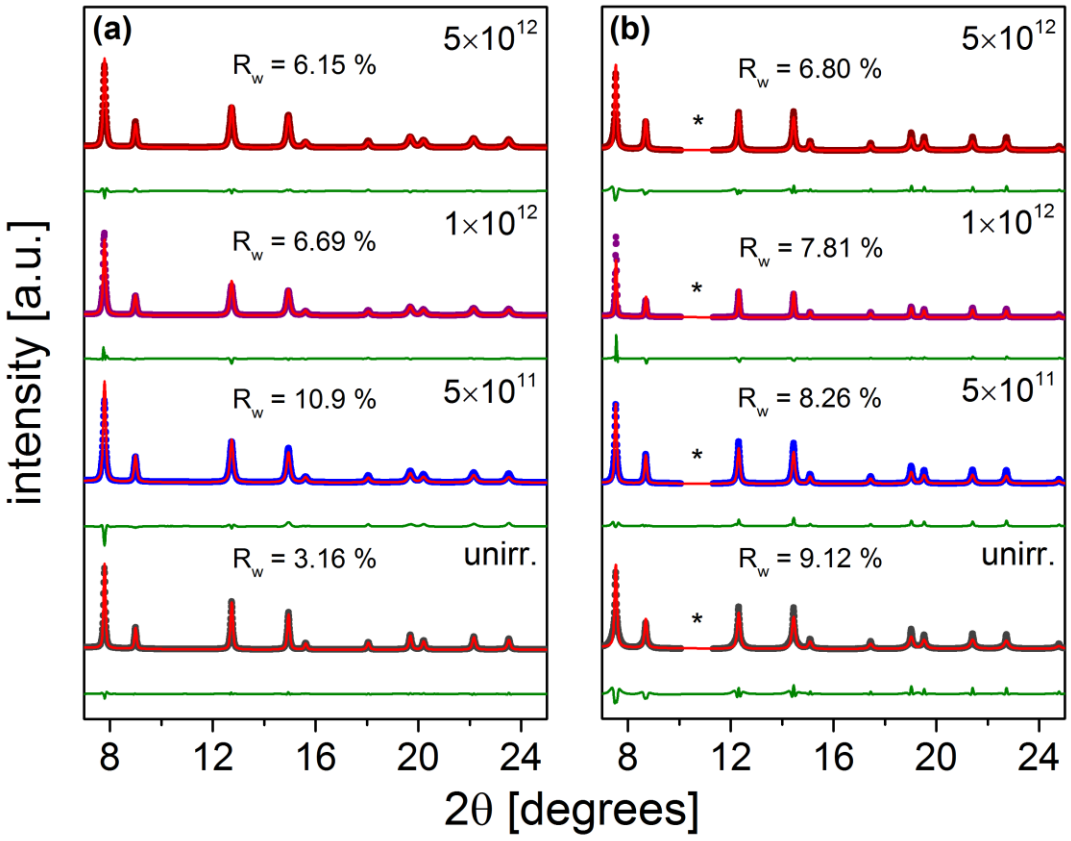


Figure 14: X-ray diffraction patterns of (a) CeO_2 and (b) ThO_2 before and after irradiation with 2.2 GeV Au Ions. The asterisk denotes the region omitted because it contained a parasitic peak from the sample holder. Figure is from supplemental material of reference [6]

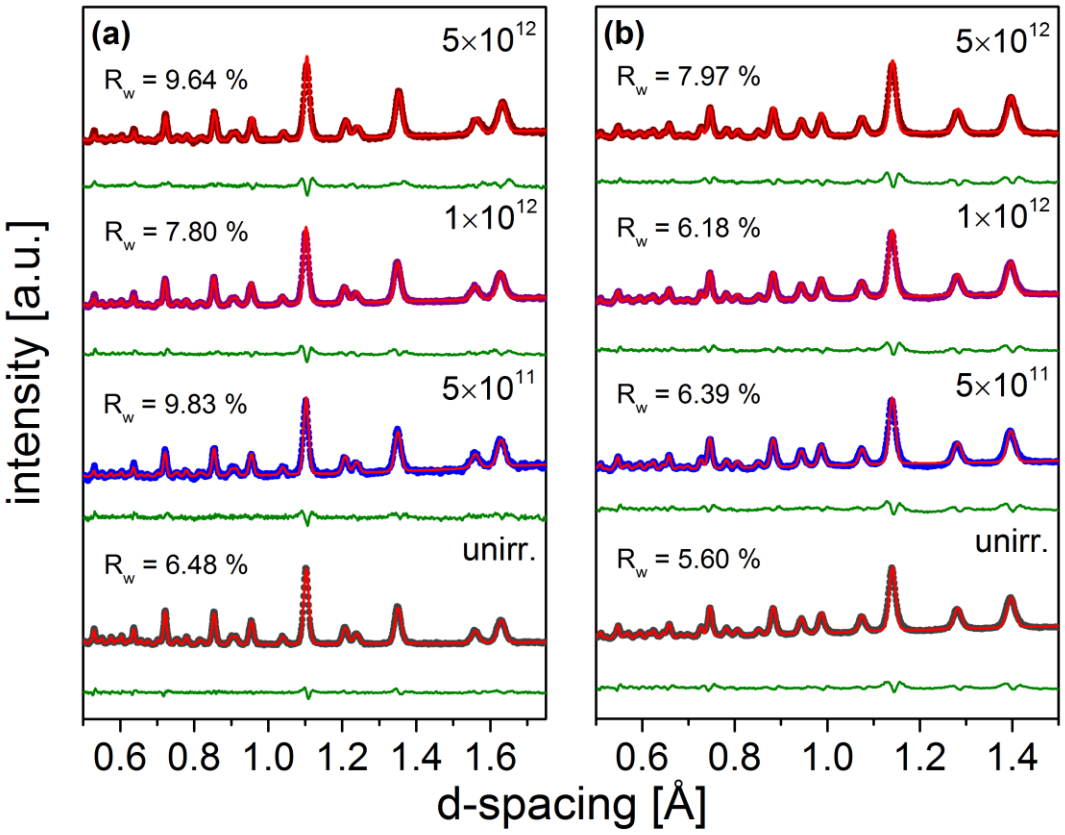


Figure 15: Neutron diffraction patterns of (a) CeO_2 and (b) ThO_2 before and after irradiation with 2.2 GeV Au Ions. For brevity, only the diffraction patterns from detector bank 3 are shown. Figure is from supplemental material of reference [6]

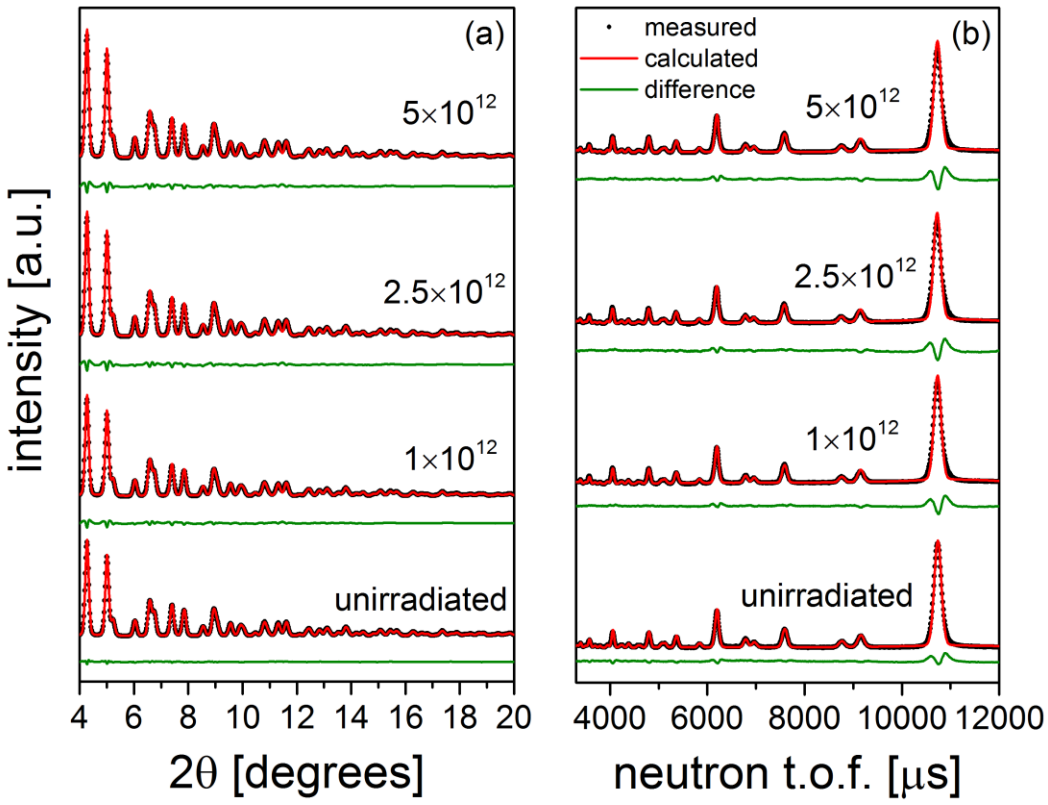


Figure 16: (a) X-ray and (b) neutron diffraction patterns of CeO_2 before and after irradiation with 1.1 GeV Au Ions. Only the patterns from neutron detector bank 3 are shown. Figure is from reference [80]

the neutron diffraction patterns (Figure 15 and Figure 16) exhibit more peaks because of the difference in scattering powers between neutrons and X-rays, the neutron diffraction patterns show the same behavior as X-ray diffraction (XRD) patterns. Neutrons are sensitive to both cation and oxygen sublattices whereas X-rays are primarily sensitive to the cation sublattices.

Quantitative information was extracted from the diffraction patterns by performing Rietveld refinement (see method description on page 29). Structural refinement yields information about unit cell parameters, phase fractions, atomic displacement parameters (ADPs), and atomic positions. The evolution of the unit cell parameters of CeO_2 and ThO_2 after irradiation with 2 GeV and 1 GeV Au ions is shown in Figure 17. After irradiation, the unit cell parameters monotonically increase, but do not saturate at the highest fluence (5×10^{12} ions/cm^2). This is in contrast to findings from other studies [7] and is likely attributable to the relatively low ion fluence achieved in the present study. The onset of saturation of the unit cell typically occurs at around 1×10^{13} ions/cm^2 for CeO_2 and ThO_2 irradiated with swift heavy ions at room temperature [7].

Volumetric swelling of CeO_2 and ThO_2 is attributed to the incorporation of point defects and defect agglomerates, which distort local surroundings and induce an overall swelling of the lattice. Defect accumulation also results in increased heterogeneous microstrain within the material, which partially explains the observed increase in diffraction peak widths after irradiation. Peak broadening is caused by a convolution of instrumental, strain-induced, and crystallite size-induced broadening. Considering that all samples were measured under identical instrument conditions, it's reasonable to assume that the systematic increase in peak broadening results from sample effects (*i.e.*, incorporation of heterogeneous microstrain and/or crystallite size effects). Williamson-Hall analysis of similarly irradiated CeO_2 and ThO_2 samples (950 MeV Au at room temperature) using synchrotron XRD further suggests that peak broadening is likely caused by the heterogeneous microstrain and not changes in crystallite size irradiated [7]. Williamson-Hall analysis is often used to decouple the effects of strain and crystallite size on peak broadening through the evaluation of $\tan(\theta)$ and $\cos^{-1}(\theta)$ peak broadening dependences [81] when performed on data collected with a monochromatic beam.

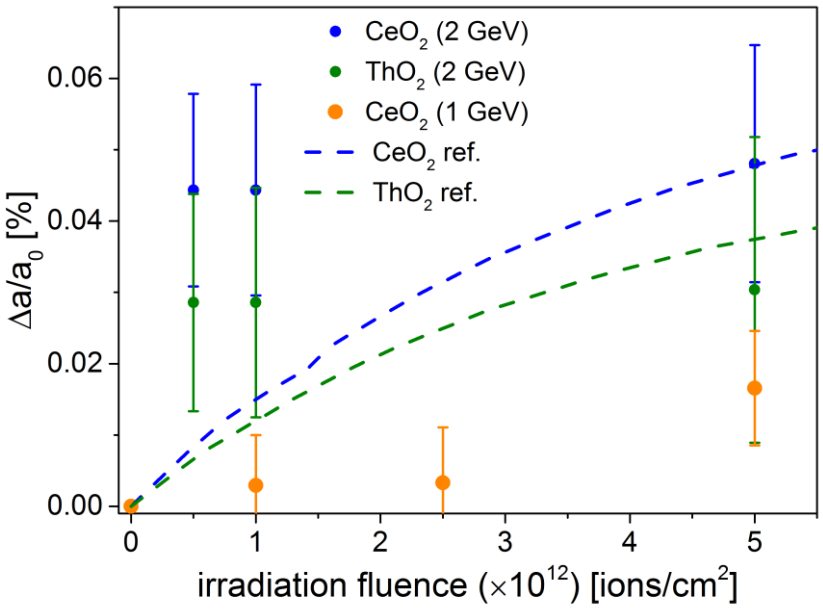


Figure 17: Fractional change in unit cell, $\Delta a/a_0$, of CeO_2 and ThO_2 before and after irradiation with 2.2 and 1.1 GeV Au Ions. The data are plotted alongside the Poisson fit (*dashed lines*) derived from the fitting of CeO_2 and ThO_2 data reported in reference [7]. The figure is adapted from supplemental material of reference [6]

In addition to unit cell parameters, Rietveld analysis can also quantify site occupancy values for the 4*a* cation and 8*c* oxygen sites in the fluorite structure. Refinement of the patterns of the unirradiated samples yielded site occupancy values of unity, meaning that the pristine cation and anion sites are fully occupied prior to irradiation. After irradiation, the occupancy value of the 8*c* oxygen Wyckoff site decreases while all other sites refine to full occupancy within experimental uncertainty. This monotonic decrease in 8*c* site occupancy in the CeO_2 materials (Figure 18) indicates that a significant quantity of oxygen vacancies is formed after irradiation. However, the information from diffraction analysis alone is not sufficient to determine if oxygen interstitials remain in the system as interstitials or leave the material *via* diffusion to grain boundaries.

A clear decrease in the 8*c* site occupancy was only observed in CeO_2 materials and not ThO_2. This difference is attributed to the difference in redox chemistry between CeO_2 and ThO_2. As previously mentioned, thorium only exhibits Th^{4+} oxidation states in the oxide form while cerium takes on both Ce^{3+} and Ce^{4+} oxidation states. The flexible charge state of cerium likely facilitates the incorporation of vacancies in CeO_2 compared to ThO_2. An alternative explanation is that CeO_2 and ThO_2 incorporate different types of oxygen defects. Schottky defects are less likely to be produced in ThO_2 because thorium is much heavier than oxygen. This atomic size difference suggests that anion Frenkel defects are more prevalent. One explanation might be that oxygen point defects more efficiently form dislocations in ThO_2 compared to CeO_2. Rapid dislocation formation would lead to dislocation network formation and eventually grain subdivision at high fluences. This results in a decrease in domain size and within smaller domains, cation and oxygen site occupancies approximate to unity. Evidence for this is presented in the next section. It's also been proposed that charged defects take on a larger role in ThO_2 compared to CeO_2 [74].

Lastly, Rietveld refinement of the fluorite structure yielded quantitative analysis of the cation and oxygen ADPs. The ADPs represent the average displacement or disorder of each Wyckoff site in the structure. The ADPs hereafter are defined as:

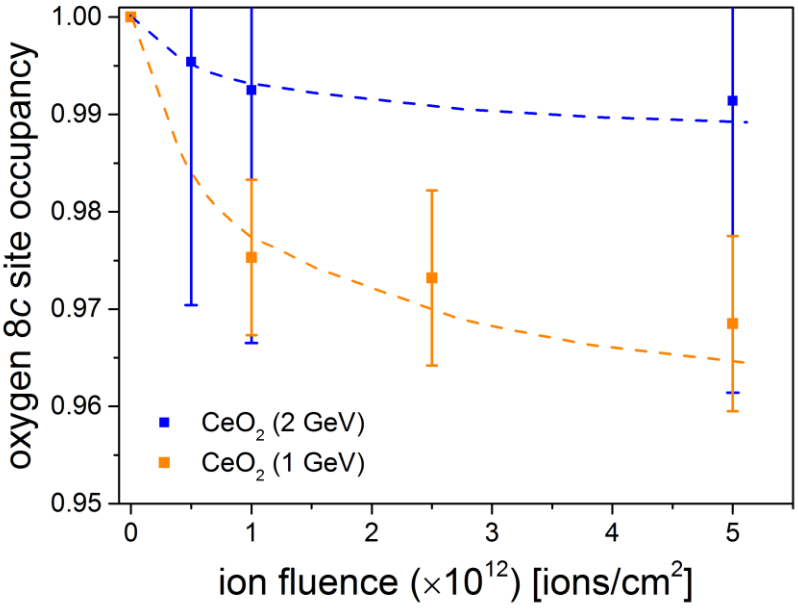


Figure 18: Refined 8*c* oxygen site occupancy from Rietveld analysis of CeO_2 diffraction patterns before and after irradiation

$$U = \langle u^2 \rangle = \frac{B}{8\pi^2}$$

where u is the instantaneous atomic displacement and B is an alternative representation often used by Willis [82, 83], for example. The ADP is often incorrectly referred to as a *temperature factor* or *thermal parameter*. This is not completely accurate because the ADP comprises contributions from both dynamic (*i.e.*, thermal/entropy) and static (*i.e.*, atomic disorder) effects. As a result, a very disordered system will exhibit very high ADPs even though thermal/entropy effects are much lower in comparison.

Figure 19 shows the relative change, $\Delta U/U_0$, in the isotropic ADPs for the cation and oxygen sites in the fluorite structure fitted to the CeO_2 and ThO_2 samples as determined from Rietveld refinement of the diffraction patterns. All ADPs are isotropic based on the symmetry constraints of the fluorite structure (space group *Fm*-3*m*). All ADPs for all atom species increase after irradiation regardless of the ion energy and material. The increases in ADPs are consistent with an increase in static atomic disorder because thermal effects are negligible in comparison at the temperature at which the measurements were performed (~25 °C). Interestingly, the cation ADPs show the largest relative increase after irradiation. This is somewhat counter-intuitive because it's well known that the oxygen sublattice disorders much more easily compared to the cation sublattice [51, 52]. It's noted that although the *relative* changes in cation ADPs are larger, the oxygen ADPs are still larger than the corresponding cation ADPs at all fluences and in all materials. That the cation ADPs have a larger relative change might be attributable to the fact that the magnitude of the cation ADPs are lower to begin with. It may also indicate that oxygen interstitials either cluster or leave the grains at higher fluences, such that microstrain and atomic disorder decreases. The ADPs are sensitive to effects from both microstrain and atomic disorder.

Neutron Total Scattering – Local Structure and Diffuse Scattering

The results presented in the previous section indicate that ion irradiation results in heterogeneous microstrain, atomic disordering, and oxygen vacancies. However, diffraction analysis alone is not sufficient to deduce if interstitials largely leave the systems

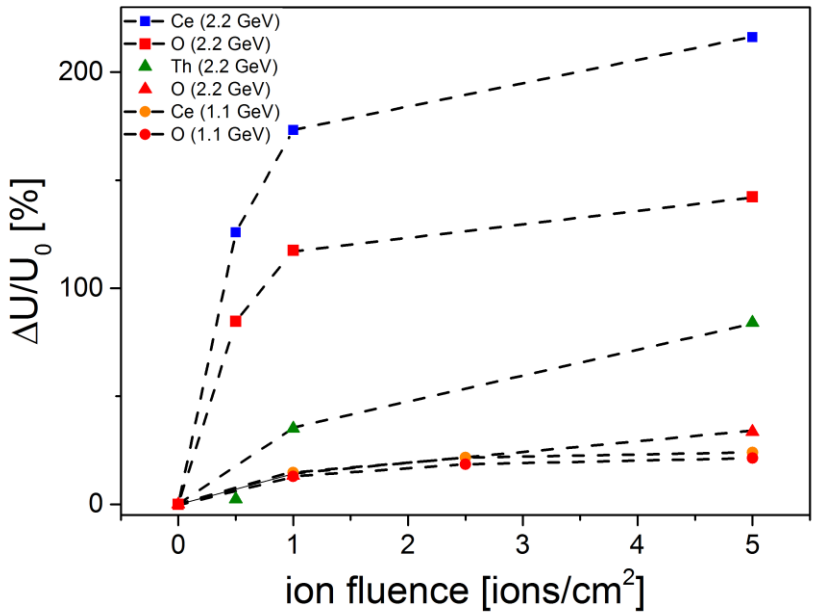


Figure 19: Fractional change in isotropic atomic displacement parameters for cations and ions in CeO_2 and ThO_2 before and after irradiation

via diffusion to grain boundaries or remain in the materials as isolated mono-interstitials, defect clusters, etc. In order to probe local defect arrangements and short-range structural modifications, the materials were further analyzed using total scattering methods.

Total scattering refers to the collection and analysis of both Bragg and diffuse scattering. This is in contrast to diffraction analysis, which only considers Bragg scattering and discards information contained in the diffuse background. Total scattering is complimentary to diffraction (average structure analysis) because the diffuse scattering component conveys information regarding defects and short-range order. The total scattering function, $S(Q)$, comprises scattering intensity from both Bragg and diffuse scattering components and includes corrections for sample absorption, density, and multiple scattering.

A comparison of the total scattering function before and after irradiation (or other material modifications) can give an indication as to the presence of defects or local order, which might be hidden or otherwise undetectable using diffraction analysis. Examples of total scattering function modifications are shown in Figure 20. Before irradiation, the total scattering function of CeO_2 contains mostly sharp Bragg peaks that arise from scattering off atomic planes. After irradiation, broad diffuse scattering peaks emerge. Examples of irradiation-induced diffuse scattering peaks are show in the inset of Figure 20 and are denoted by blue asterisks. Although the total scattering functions show evidence for diffuse scattering, it's not known if the diffuse scattering peaks are caused by defects (*i.e.*, atomic disorder) or short-range atomic ordering. In order to further probe the origin of the broad diffuse scattering peaks, the total scattering functions were converted from reciprocal space to real space using a Fourier transformation, which yielded atomic PDFs.

The atomic PDFs are weighted histograms of interatomic distances in the materials. The PDFs of CeO_2 and ThO_2 before and after irradiation are shown in Figure 21, Figure 22, Figure 23, and Figure 24. Figure 21 shows the PDFs of CeO_2 and ThO_2 before and after irradiation with 2.2 GeV Au ions. Each peak in the PDFs denotes a characteristic interatomic distance in real space, r, and the intensity of a peak is proportional to the relative quantity of that interatomic pair in the material. A PDF peak can represent a single interatomic correlation or multiple interatomic correlations (*i.e.*, a convolution of peaks).

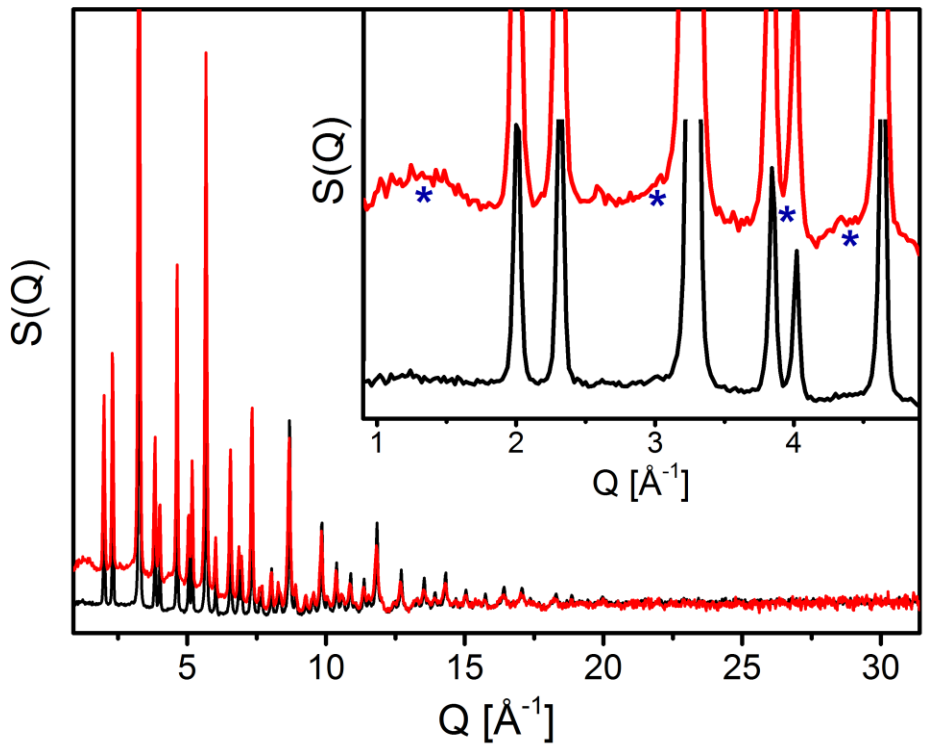


Figure 20: Total scattering function, $S(Q)$, of CeO_2 before irradiation (black) and after irradiation to 5×10^{12} ions/cm^2 (red). The inset shows a zoomed in view of the total scattering function that shows the ingrowth of diffuse scattering peaks after irradiation. The diffuse scattering peaks are denoted by blue asterisks

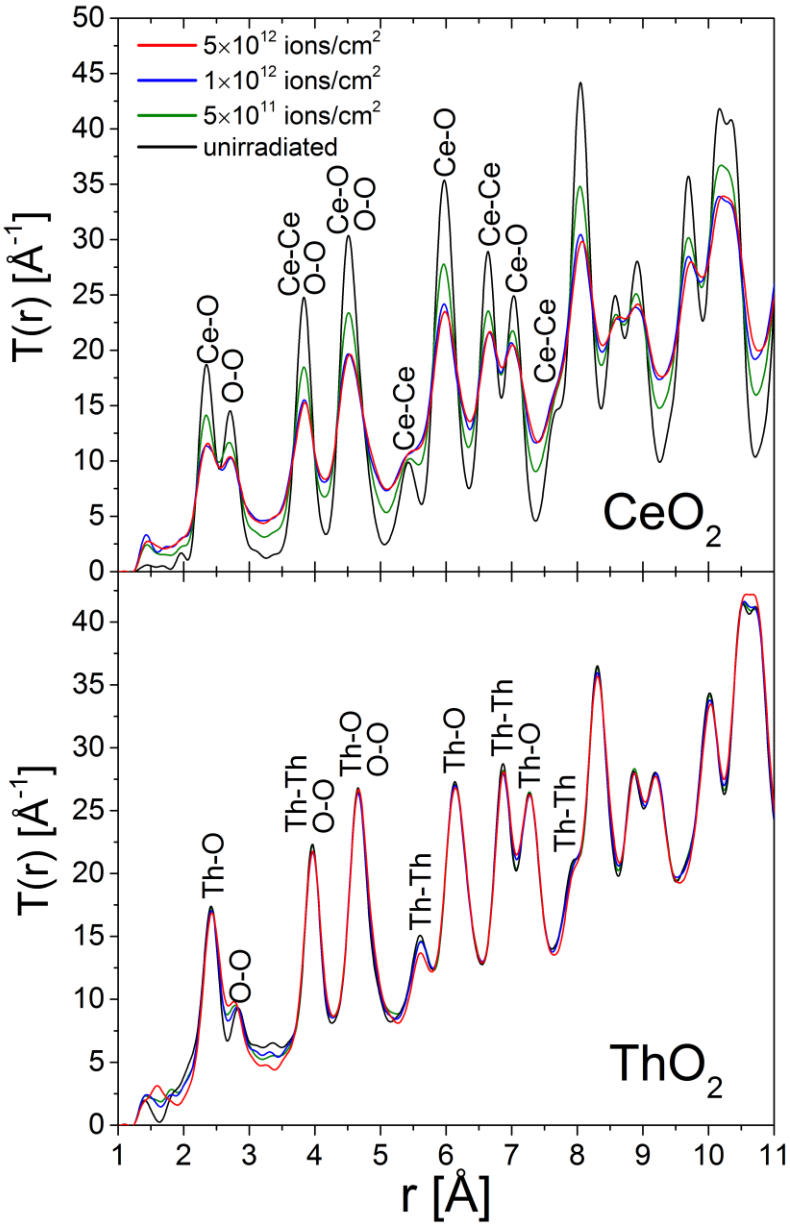


Figure 21: Total Correlation Functions, $T(r)$, of CeO_2 and ThO_2 before and after irradiation with 2.2 GeV Au Ions. Notable interatomic pairs from the pristine fluorite structure are shown above the corresponding peaks. For a description of the difference between the total correlation function and the pair distribution function refer to pg. 22. Figure is from reference [6]

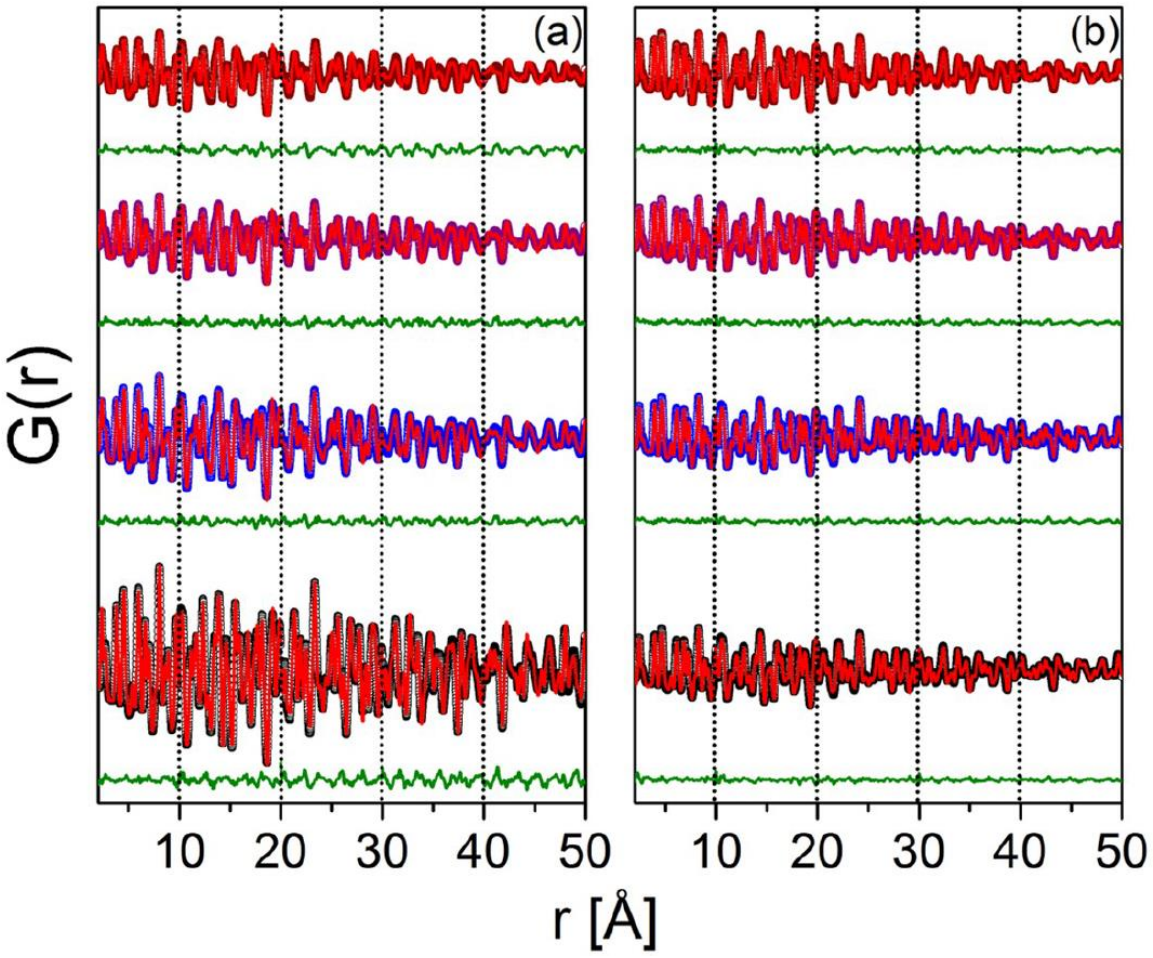


Figure 22: Fitted neutron PDFs of (a) CeO_2 and (b) ThO_2 before and after irradiation with 2.2 GeV Au ions. Colored circles represent measured PDF data, red curves represent the fitted fluorite structure model, and the green curves represent the difference between the data and fitted models. The vertical black dotted lines denote the limits used for the boxcar fitting procedure described in the text. Figure is from supplemental material of reference [6]

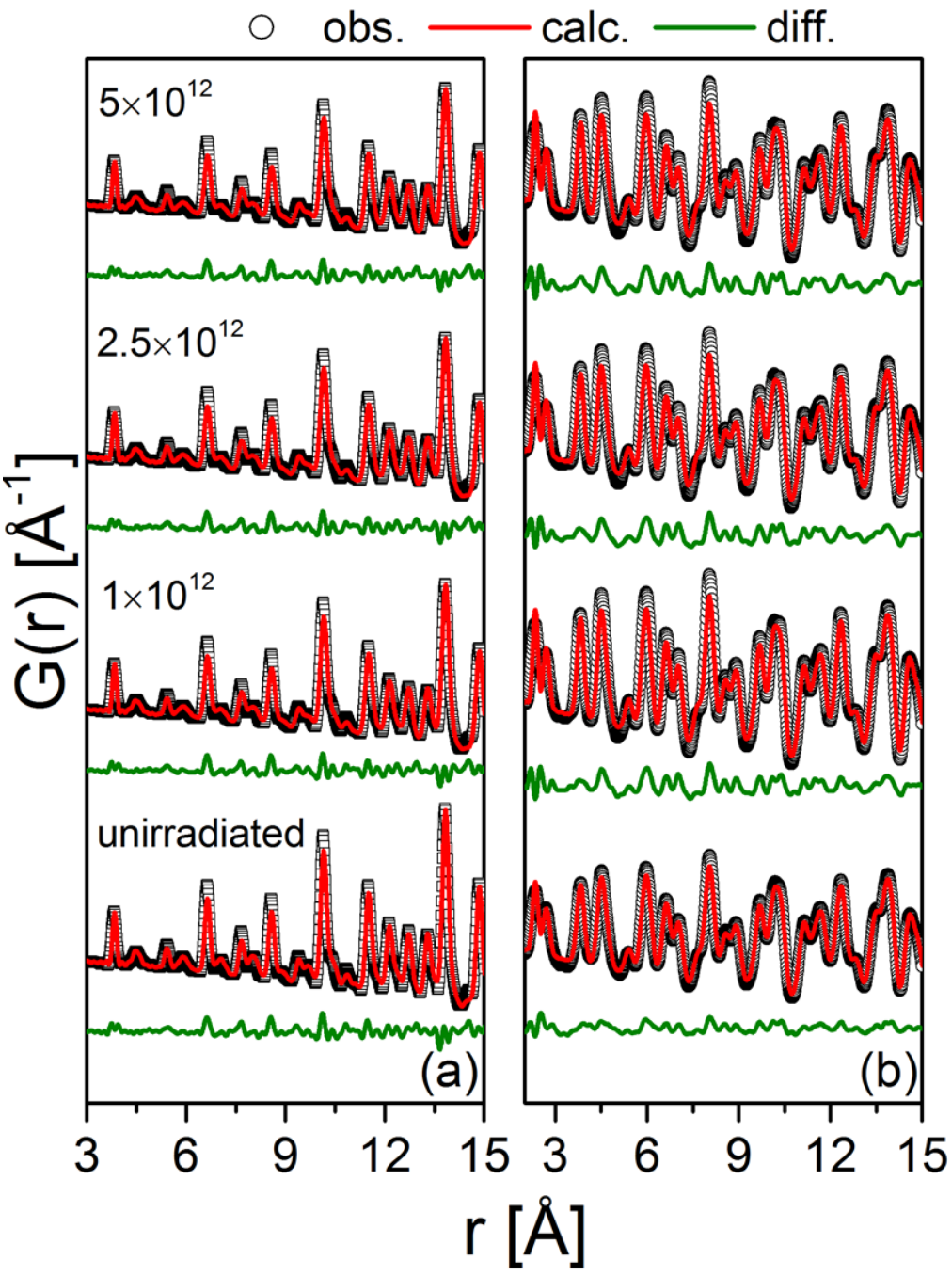


Figure 23: (a) X-ray and (b) neutron pair distribution functions of CeO_2 before and after irradiation with 1.1 GeV Au Ions. All PDFs were fit with the fluorite structure. Figure from ref. [80]

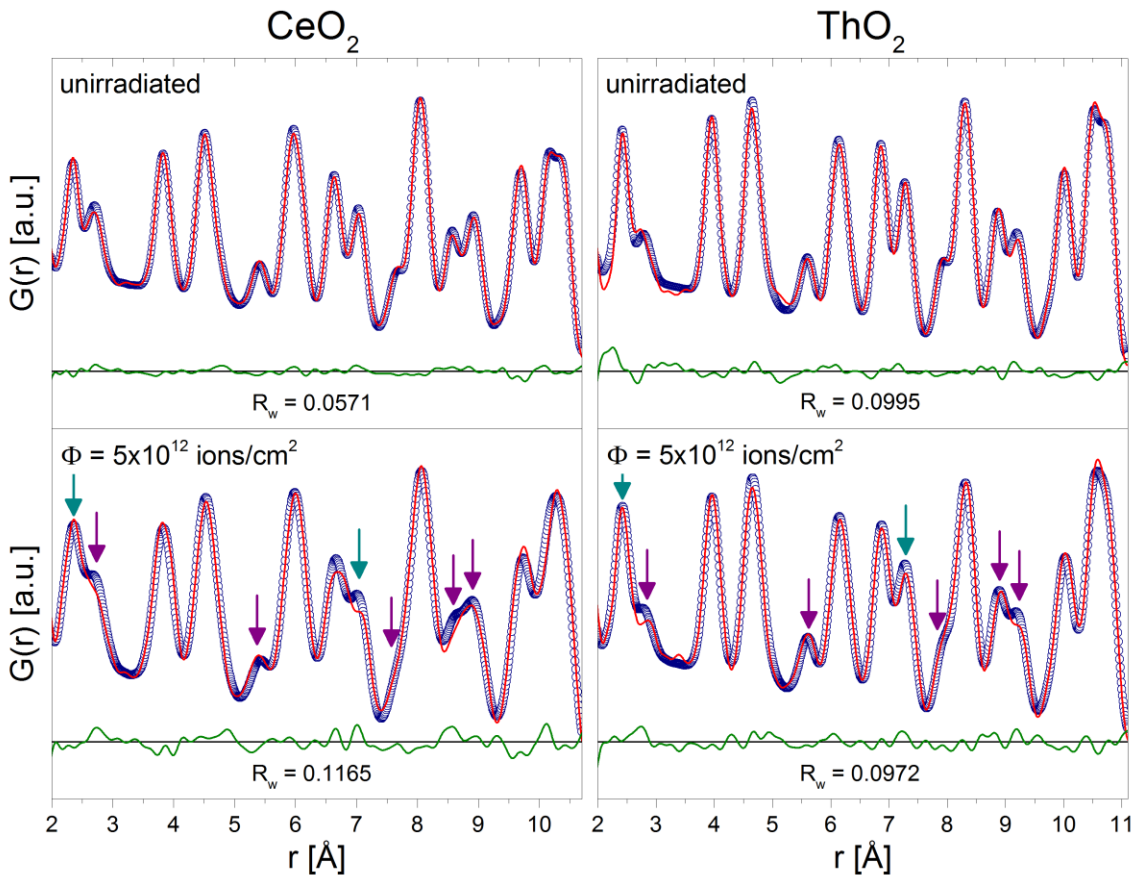


Figure 24: Fitted neutron PDFs of CeO2 (left) and ThO2 (right) before and after irradiation with 2.2 GeV Au ions. The blue circles represent the measured PDF data, the red curves represent the fitted fluorite structure model, and the green lines represent the difference between the data and the fitted model. Teal and purple arrows denote peaks with cation-oxygen and oxygen-oxygen contributions, respectively

Notable interatomic pairs in the pristine fluorite structure are labeled in Figure 21 above the peaks.

Prior to irradiation, the peaks are relatively sharp indicating that the fluorite structure is well-ordered. After irradiation, the peaks broaden, loose intensity, and the incoherent scattering increases. These effects are identical to effects observed in the diffraction patterns and represent similar features. All of the observed features are caused by an increase in the distribution of interatomic distances. There cannot be an absolute loss of intensity unless the atom quantity is decreasing; therefore, the loss of peak intensities is proportional to the increase in peak broadening and scattering intensity in the inter-peak regions. Other than a small peak at ~1.5 Å in the CeO_2 PDFs, the PDFs do not feature any new peaks meaning that all materials retain the fluorite structure after irradiation.

All PDFs were fit with the fluorite structure in order to gauge the amount of structural disorder induced by ion irradiation. Fitting was performed using small-box PDF refinement (see method description on pg. 30). Fitting of the fluorite structure to both neutron and X-ray PDFs of unirradiated and irradiated samples confirmed that the PDFs remain crystalline and do not undergo any phase transformation under swift heavy ion irradiation (Figure 22 and Figure 23). A closer inspection of the fits reveals that many of the misfits are caused by correlations that are influenced by the oxygen sublattice (Figure 24). This is further illustrated in Figure 23 where the X-ray PDFs are fit much better than the corresponding neutron PDFs. The structural changes denoted by the green difference curve in Figure 23 are also larger in the neutron PDFs after irradiation. Neutrons and X-rays are more sensitive to oxygen and cerium, respectively. Therefore, the larger modifications in the neutron PDFs of CeO_2 compared to the X-ray PDFs indicate that structural modifications largely occur on the oxygen sublattice and more minor modifications occur on the cation sublattice.

Individual PDF peak fitting further enabled the measurement of microstrain in the material. Individual peak fitting was only possible with the X-ray PDFs because the scattering contributions from cerium and oxygen are drastically different in the X-ray PDF. This enabled the first nearest-neighbor Ce-Ce peak to be isolated. The first nearest-neighbor Ce-Ce peak was fit with a Gaussian and two variables were examined (Figure 25)

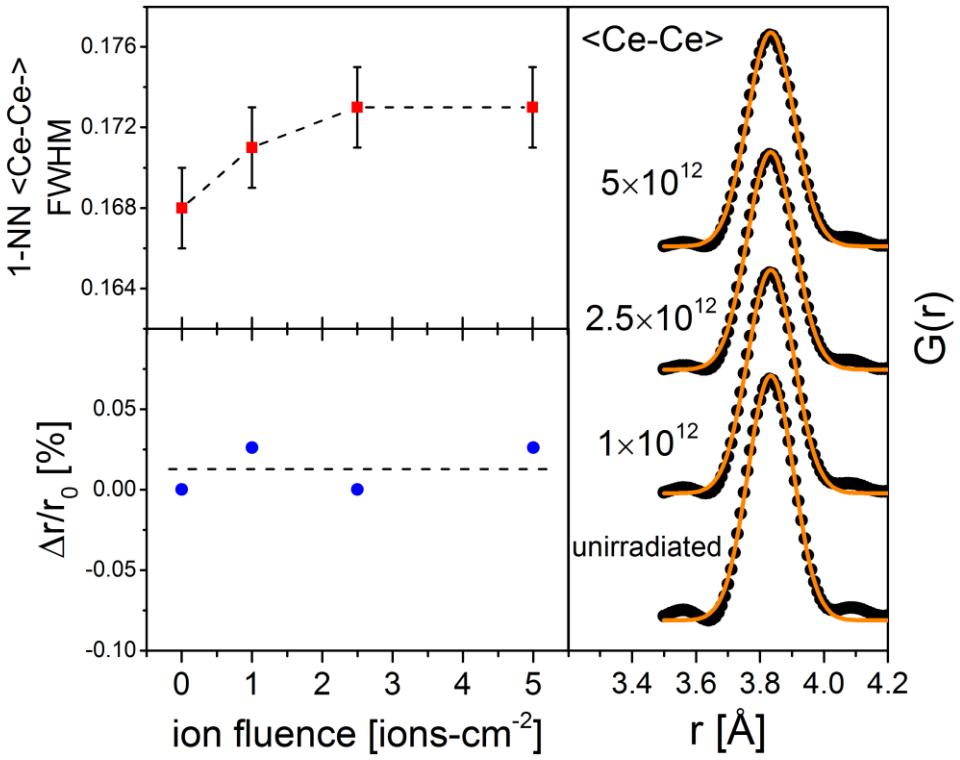


Figure 25: Results from peak fitting of the individual first nearest-neighbor Ce-Ce peak from the X-ray pair distribution functions. Clockwise starting from the top left: the evolution of the full-width at half-max of the peak with increasing fluence, the peak fits for the different PDFs, and the relative change in peak position

: the full-width at half-maximum (FWHM) and the relative change in peak position, $\Delta r/r_0$, which represent heterogeneous and homogeneous strain, respectively. Figure 25 shows that the change in uniaxial strain is negligible after irradiation and the increase in strain is from heterogeneous microstrain. As with the evolution of the ADPs from diffraction analysis (Figure 19), the heterogeneous microstrain appears to saturate at the highest fluences. This in contrast to the evolution of the unit cell parameters, which do not saturate at the highest fluences.

One advantage of small-box refinement is that it can be used to probe different length scales in order to identify the spatial extent of structural modifications. This is typically performed through so-called boxcar refinements in which different regions of a PDF are fitted individually. For the purpose of discussion of boxcar fit results, the terms *short-range structure* and *intermediate-range structure* are hereafter defined as the regions between 0-10 Å and 10-50 Å, respectively. The true definition of the intermediate-range structure of the material is quite vague and is therefore used here only as a bridge between short- and long-range structures.

Boxcar fitting of the PDFs was performed by fitting five ~10 Å intervals of each full PDF. A schematic representation of this is shown in Figure 22 (see figure caption for details). The goodness-of-fit parameters, R_w, corresponding to the different regions were first normalized to the unirradiated sample in order to account for effects from intrinsic material defects. Next, the goodness-of-fit parameters were plotted against bin position for the different fluences (Figure 26). The results show that CeO_2 and ThO_2 accommodate disorder in very different ways. CeO_2 exhibits disorder primarily in the short-range structure (1-10 Å) at the intermediate fluences whereas ThO_2 features structural changes primarily in the more intermediate range structure (20-50 Å). In addition to the changes in intermediate range structure, it appears that irradiation causes structural relaxation of the very short-range structure in ThO_2. At the highest fluence, the disorder is accommodated more homogeneously throughout the short- and intermediate-range structures of CeO_2.

It's speculated here that the stark differences in damage accumulation between CeO_2 and ThO_2 can again be attributed to differences in redox chemistry. As shown from Rietveld refinement of the diffraction patterns, CeO_2 incorporates a significant

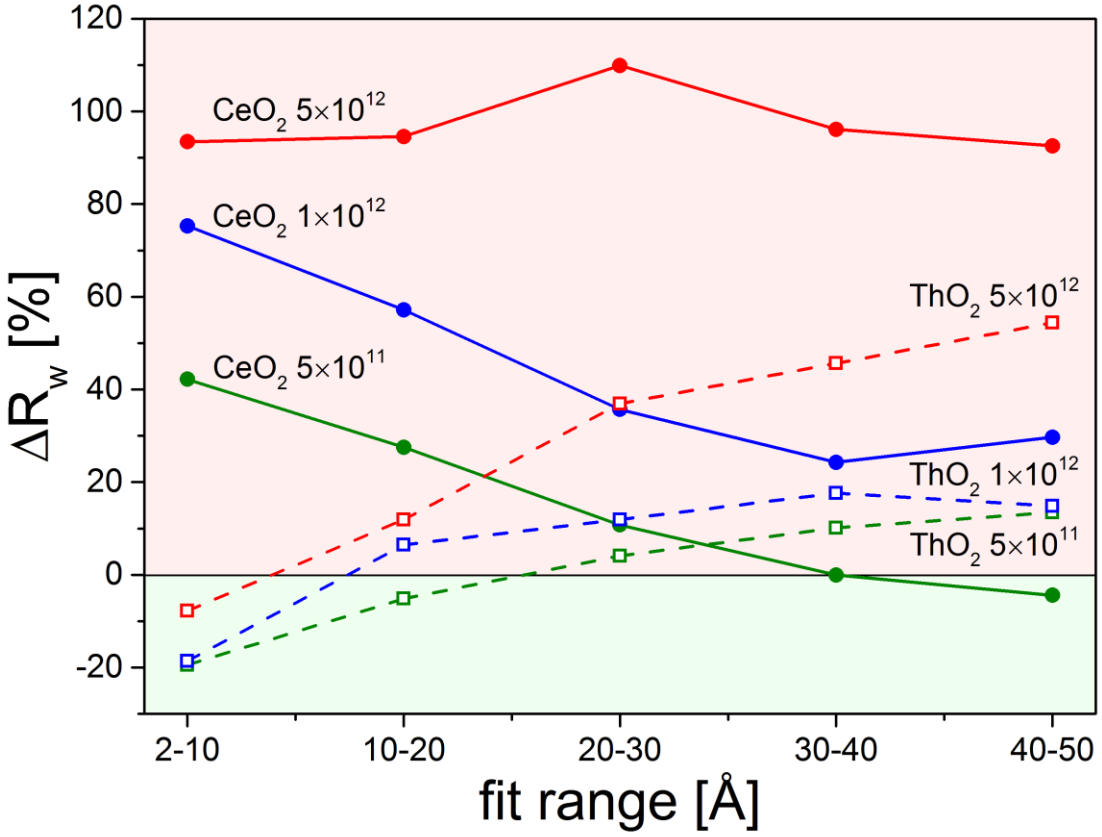


Figure 26: Results from box-car fitting of the CeO_2 and ThO_2 PDFs. ΔR_w represents the relative change in the goodness-of-fit parameter, R_w, after irradiation. Negative and positive ΔR_w values indicate that the fit was improved or worsened, respectively. The dashed and solid lines are used to guide the eye

concentration of oxygen vacancies after irradiation, which likely result in the reduction of some cerium atoms to Ce^{3+} [7, 56, 58, 62, 75]. In the previous section it was speculated that efficient dislocation formation or charged defects are responsible for the negligible change in the 8*c* oxygen site occupancy in ThO_2 after irradiation and that the formation of dislocation defects might result in a decrease in domain size. Figure 26 suggests that this is true because preferential changes to the long- and intermediate range structure are indicative of changes in domain size. Therefore, the picture that emerges is that damage accumulation from swift heavy ion irradiation is primarily driven by cation redox and point defects in CeO_2 and changes in domain size in ThO_2. Changes in domain size result from the incorporation of dislocations, dislocation networks, and subsequent sub-grain boundary formation. Dislocation networks are often observed at high fluences and were observed in near-surface areas of CeO_2 after swift heavy ion irradiation [64]. It's possible that these effects are more prevalent in ThO_2 and enhanced by the thin sample geometry of the samples used in the present study.

Examination of the first-nearest neighbor (1-NN) peaks in the PDFs provides clues as to how atoms disorder and further highlights differences in damage accumulation mechanisms between CeO_2 and ThO_2. The evolution of the 1-NN peaks in the neutron and X-ray PDFs of CeO_2 and ThO_2 before and after irradiation with 1 and 2 GeV Au ions are shown in Figure 27 and Figure 28. A comparison of all the 1-NN peaks shows that nearly all peaks lose intensity and the peak intensities saturate at the highest fluences. The only exception is the 1-NN O-O peak of ThO_2. The saturation behavior is more clearly illustrated in the insets of Figure 28. This evolution is analogous to the saturation behavior observed for heterogeneous microstrain and likely indicates that heterogeneous microstrain is coupled to the atomic disordering mechanism that drives the changes in PDF peak intensities. Considering that the unit cell parameter does not saturate at the highest fluence achieved, it appears that volumetric swelling is perhaps driven more by redox effects.

Figure 27 shows that the changes in CeO_2 are much more drastic compared to the changes in ThO_2. Regardless, both materials show similar PDF peak evolution with the exception of the O-O peaks. In CeO_2, the 1-NN O-O peak shows an overall increase in interatomic distance. The 1-NN O-O peak in ThO_2 shows an overall decrease in distance.

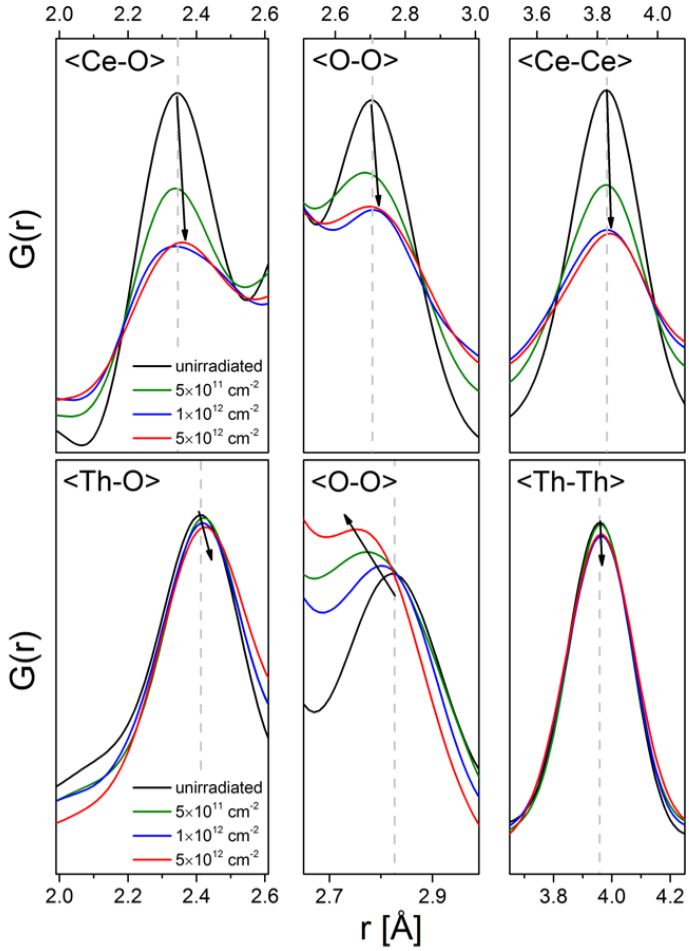


Figure 27: First-nearest neighbor neutron PDF peak evolution for CeO2 and ThO2 before and after irradiation with 2.2 GeV Au ions. Figure is from reference [6]

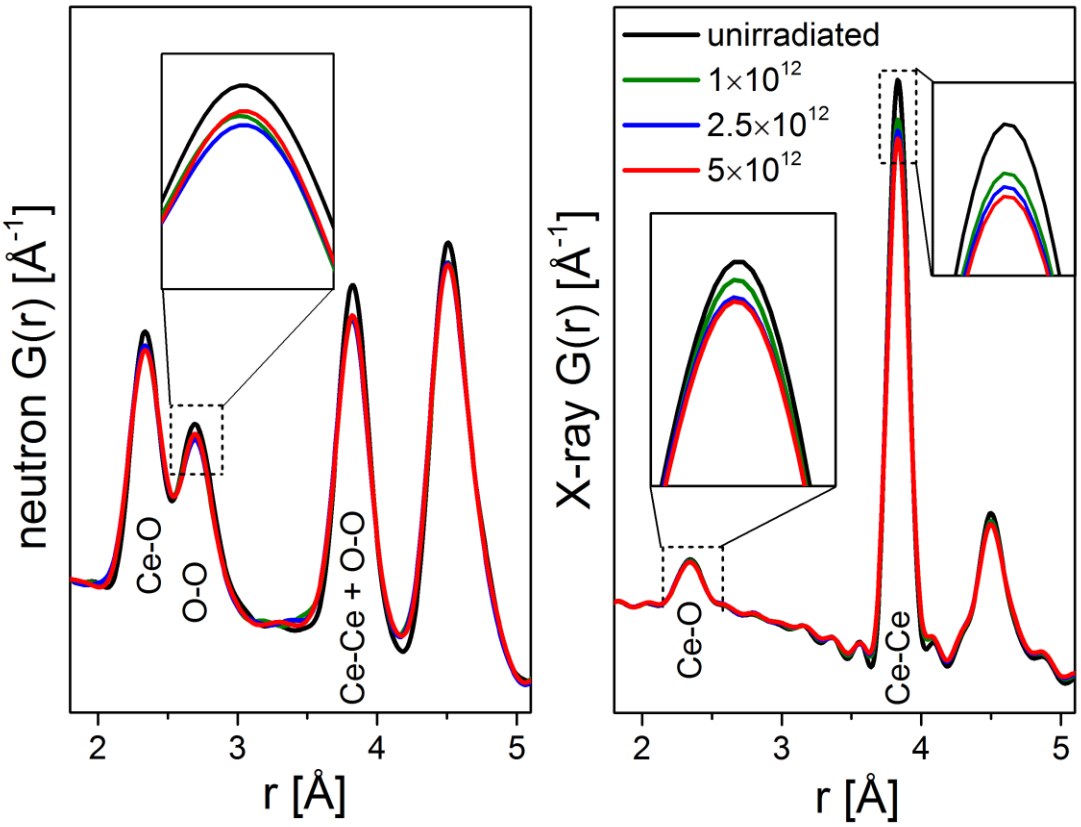


Figure 28: Evolution of the first-nearest neighbor peaks of CeO_2 in the neutron (left) and X-ray (right) PDFs before and after irradiation with 1.1 GeV Au ions

All other peaks show an overall increase in peak position in agreement with the diffraction data that demonstrated increasing volumetric swelling after irradiation. The relative changes provide insights into how certain point defects are incorporated into the fluorite structure.

The incorporation of an oxygen vacancy into CeO_2 causes loss of the attractive interaction between cations one of the eight nearest oxygens. This loss in turn causes the relaxation of the other nearest-neighbor oxygens towards the central cation. The result is a shorter cation–oxygen distance. Contractions of the mean Ce–O distance can also be explained by non-counterpoised forces [84]. Similar concepts show that the O–O distance should also increase. The magnitude of relaxation of 1-NN oxygens surrounding an oxygen vacancy is larger than the magnitude of relaxation of second nearest-neighbor (2-NN) oxygens. The O–O distance among 1-NNs decreases while the O–O distance between 1-NNs and 2-NNs increases. Since 2-NN oxygens outnumber 1-NN oxygens at a ratio of 2:1, the O–O distance will increase overall. Lastly, the increases of the 1-NN cation-cation distances are consistent with the incorporation of reduced cerium atoms and volumetric swelling. The counter-intuitive decrease in the 1-NN O-O distance of ThO_2 after irradiation is attributed to either non-cubic distortions, defect clustering, or charged defects. Non-cubic distortions are proposed because the O-O distance decreases with a minimal change in Th-O distance. However, it's more likely that the unique O-O evolution is caused by defect clustering or charged defects on account of the diffraction and PDF refinement results showing minimal change in Th:O ratio and decreasing domain size with increasing ion fluence.

Finally, close inspection of the very short-range structure of the materials revealed that oxygen dimer-type defects are produced in CeO_2 after swift heavy ion irradiation. Figure 29 shows the very short length scales of the CeO_2 PDFs. After irradiation, a small correlation emerges at ~1.5 Å. The correlation was attributed to an oxygen-oxygen correlation based on how short interatomic distance is. DFT studies have predicted several oxygen dimer-type defects in CeO_2 and ThO_2 with O-O distances between ~1.35-1.45 Å [74]. The small correlation was only confirmed for CeO_2 materials. A small increase in intensity was also observed in the ThO_2 PDFs in the same region; however, the ThO_2 PDFs

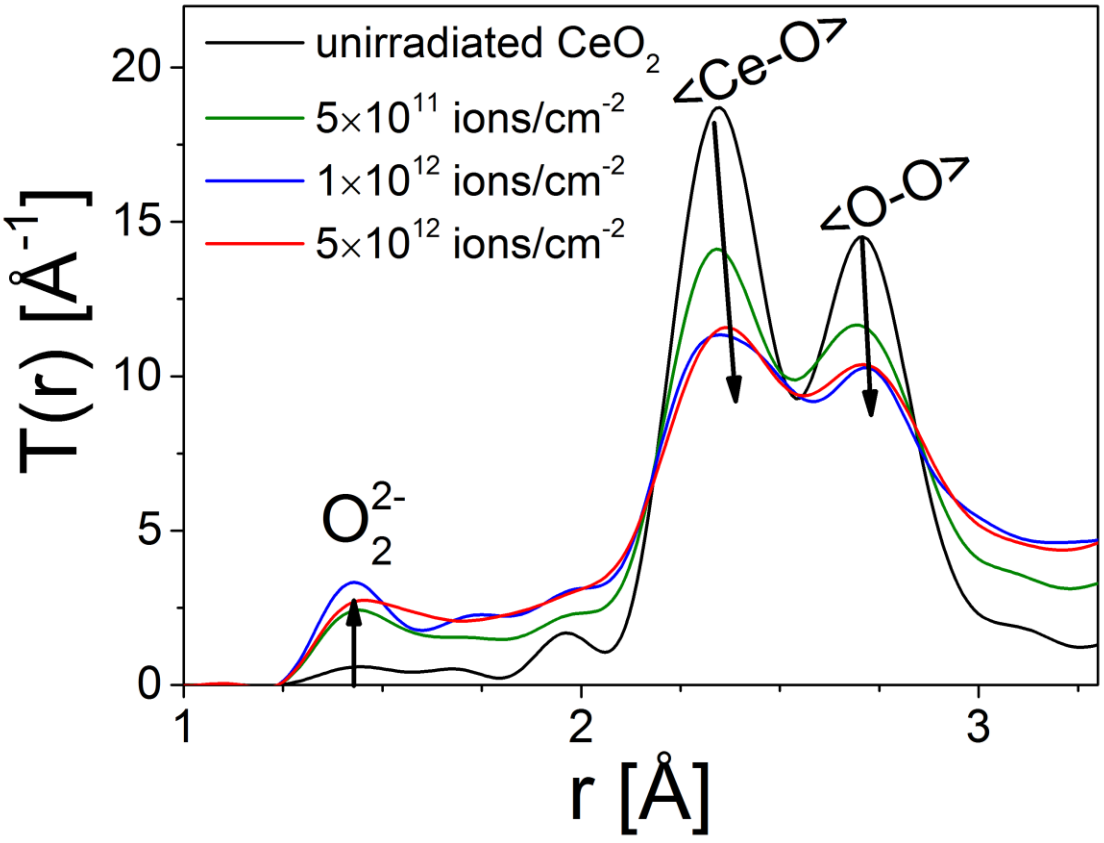


Figure 29: Very short length scales of CeO2 pair distribution functions before and after irradiation with 2.2 GeV Au ions

were slightly lower quality and the poorer resolution did not permit confident identification of oxygen dimer defects in ThO_2 after irradiation.

Interestingly, the distance of the O-O correlation (~1.45 Å) is similar to the O-O spacing of a peroxide ion (1.49 Å). The peroxide ion is a bound state of two oxygen atoms with an overall charge state of -2 [75]. These peroxide ions are predicted to be stable in CeO_2 based on several DFT studies [73, 75]. A similar PDF correlation was also observed in an MD simulation of electronically-excited, fluorite-derivative titanate pyrochlore and was attributed to O_2-like defects [85].

The presence of peroxide is notable because it enables a unique charge compensation mechanism. DFT studies have shown that the short O-O spacing and -2 overall charge of the peroxide ion causes the peroxide defect to cause less distortion to the surrounding lattice and eliminates the need for charge compensation *via* oxidation of cations [73]. The formation of peroxide ions may also facilitate the reduction of cerium atoms as the formation of peroxide can free electrons to localize on nearby cerium atoms [75]. The observation and attribution of short O-O distances to dimer and/or peroxide defects also supports the notion that oxygen interstitials largely remain in the system in clusters rather than leaving grains *via* diffusion to grain boundaries.

Raman Spectroscopy – Local Structure and Vibrational Properties

Raman spectroscopy is complimentary to PDF analysis and is a useful tool for probing short-range order and vibrational properties of materials. Raman spectroscopy is especially sensitive to the local coordination environment of cations in fluorite-structured oxide materials. Group theory predicts only one Raman-active mode for the fluorite structure (space group *Fm*-3*m*). This is the triply-degenerate F_{2g} (or equivalently, T_{2g}) breathing mode, which represents the oscillation of the oxygen cage around the central cation [86].

The T_{2g} Raman peak of pristine CeO_2 is typically centered about ~465 cm^{-1}. Measurement of unirradiated CeO_2 confirmed the presence of the T_{2g} peak at ~466 cm^{-1} and the absence of all other peaks. The Raman spectrum of CeO_2 undergoes three main changes after irradiation, all of which are illustrated in Figure 30. The most noticeable changes are the asymmetric broadening of the T_{2g} peak to the lower frequency side (feature

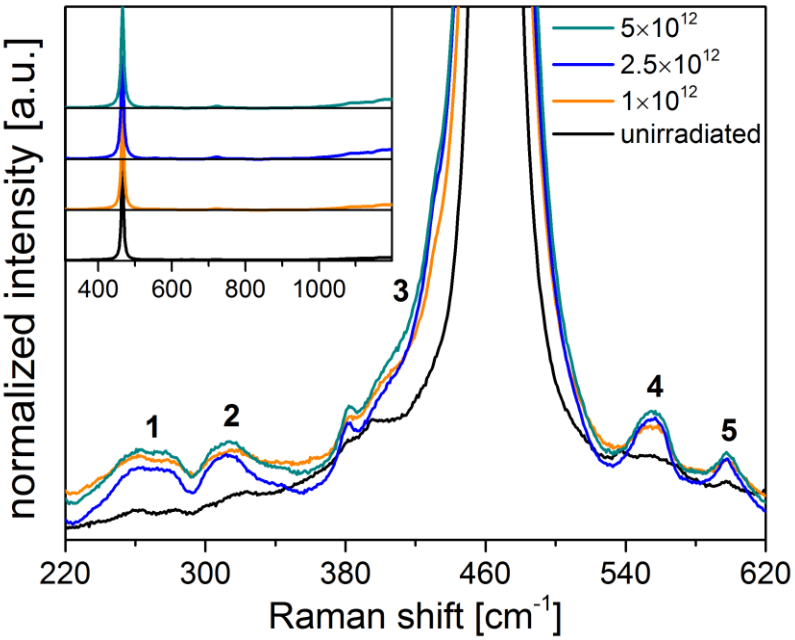


Figure 30: Magnified region of Raman spectrum of CeO_2 before and after irradiation with 1 GeV Au ions. Various defect peaks and radiation damage features are numbered (1-5). The inset shows the full-range Raman spectra. The full-range spectra show decreasing signal-to-noise ratio with increasing ion fluence

3 in Figure 30) and the decrease in the signal-to-noise ratio with increasing ion fluence (Figure 30 inset).

Asymmetric broadening to lower frequencies indicates a decreasing Ce-O force constant, which is typically concomitant with structural disorder and an increase in heterogeneous microstrain. Irradiation-induced asymmetrical broadening has been attributed to various effects ranging from Fano resonance to phonon-confinement [87, 88]. Phonon-confinement analysis shows that peak broadening is attributed to increasing defect density [88]; however, phonon-confinement analysis alone is insufficient to characterize defect morphology [87]. To this end, *ab initio* calculations can yield valuable insights. Recent DFT calculations suggest that asymmetric broadening of the F_{2g} peak occurs as a result of cerium reduction and the concomitant incorporation of oxygen vacancies [89]. A simple illustration of this is process is shown in Figure 31. Replacement of Ce^{4+} with reduced Ce^{3+} ions would result in an increase in the F_{2g} mode frequency because Ce^{3+} is larger than Ce^{4+} and the resulting Ce-O bonds will be shorter and stiffer (Figure 31b). However, DFT shows that the characteristic frequency actually decreases if cation reduction is accompanied by structural relaxation, such as volumetric swelling (Figure 31c). The coordination and characteristic frequency of the atomic arrangement in Figure 31c is similar to the coordination environment found in Ce_2O_3 [90]. The latter atomic arrangement yields the E_g mode with a characteristic frequency of ~410 cm^{-1}. It was suggested [89] based on these observations that asymmetric broadening of the CeO_2 F_{2g} peak results from a mixture of Ce_2O_3-like (E_g) and CeO_2-like (F_{2g}) vibrational modes (Figure 31d). The former is caused by the minor population of Ce^{3+} cations and the latter are caused by the main population of Ce^{4+}.

The decreasing signal-to-noise ratio at higher fluences is caused by a breakdown of selection rules caused by defect accumulation. This signal degradation is illustrated by the increasing background at high frequencies (>1000 cm^{-1}) in the normalized Raman spectra (see Figure 30 inset). Swift heavy ion irradiation also causes the emergence of several low-intensity defect bands, which are numbered in Figure 30. Many of these bands have been observed in ion-irradiated CeO_2 [60, 65, 87, 88] and CeO_2 doped with aliovalent cations [91]. Defect bands are typically attributed to complexes comprising oxygen vacancies and

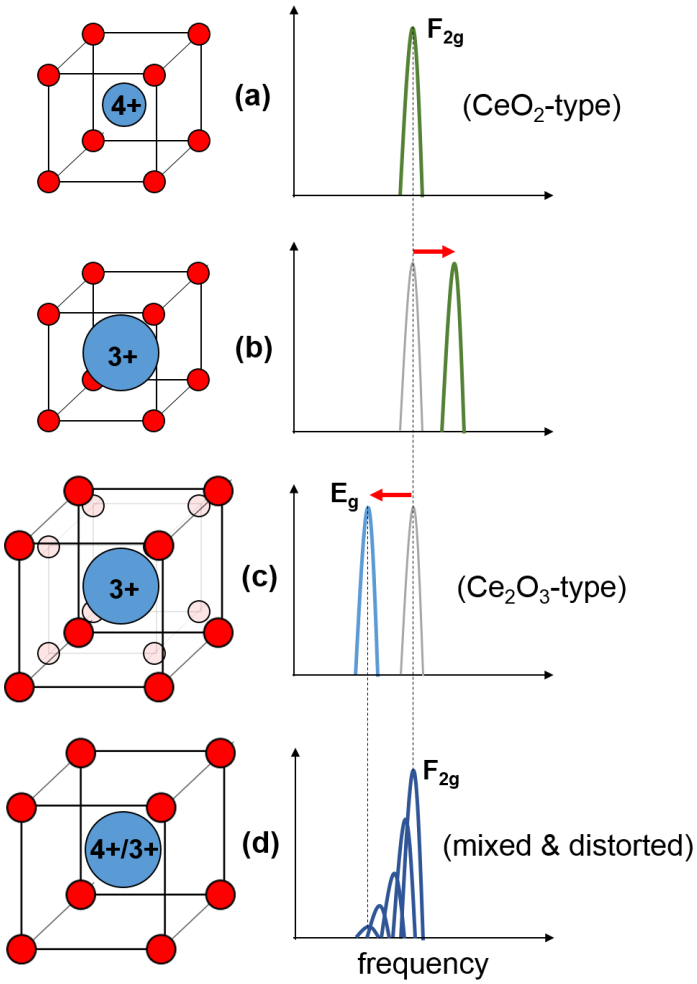


Figure 31: Schematic of F_{2g} peak modifications based on findings from reference [89]. (a) Pristine CeO_2 shows one F_{2g} peak representative of CeO_8 coordination environment. (b) Replacing Ce^{4+} with Ce^{3+} in the same environment would cause a shorter/stiffer Ce-O and corresponding increase in F_{2g} frequency. (c) Relaxing Ce^{3+} environment by swelling results in a coordination more like that of Ce_2O_3 and decrease in F_{2g} frequency. (d) Irradiation-induced swelling and partial reduction results in asymmetric broadening of F_{2g} peak to lower frequencies indicative of mostly Ce^{4+} with some Ce^{3+} in the structure

reduced Ce^{3+} cations.

DFT calculations were used to study the vibrational modes of several of these defective Ce-O arrangements [89]. A summary of these DFT results is presented in Figure 32. The figure shows that a pristine $Ce^{4+}O_8$ coordination yields the lowest vibrational frequency. $Ce^{3+}O_8$, $Ce^{3+}O_7$ and $Ce^{4+}O_7$ defect arrangements have characteristic frequencies that increase in that precise order. A combination of theoretical and experimental works suggests that the characteristic band of the $Ce^{3+}O_7$ complex appears at ~550 cm^{-1}. From these insights, the defect bands in Figure 30 labeled (4) and (5) are attributed to cerium in coordination with oxygen vacancies (*i.e.*, CeO_7 arrangements).

DFT results also suggest that defect band (1) and the small feature at ~380 cm^{-1} are also attributed to cation reduction and cations in coordination with vacancies [89]. The remaining defect band (2) located at ~300 cm^{-1} is not readily attributable to typical Ce^{3+} and oxygen vacancy defects, but the peak was previously observed in heavily-doped CeO_2 [92]. Many surface defects, such as surface and sub-surface vacancies [89] and Ce-OH complexes [93] yield bands that lie in the range 250-330 cm^{-1}. Therefore, it's possible that these types of defects contribute to the band. Alternatively, it's possible that radiation-damage and the breakdown of selection rules activates modes that are forbidden in pristine CeO_2.

Drop-Solution Calorimetry – Defect Energetics

The calorimetry measurements reported in this section were performed by Anna Shelyug at the University of California-Davis in collaboration with our research group using the identical set of samples that were used for the reported non-destructive neutron, X-ray, and Raman characterizations. The main findings are reported here because they are complimentary to the structural analysis of CeO_2 and ThO_2 reported in this dissertation. Most of the calorimetric data interpretation reported here was derived collaboratively by Anna Shelyug and myself. Additional details are available in manuscript: [80].

Calorimetry, unlike neutron, X-ray, and Raman characterization methods, is a destructive analysis technique. Calorimetry provides a means to derive the energetics of a material

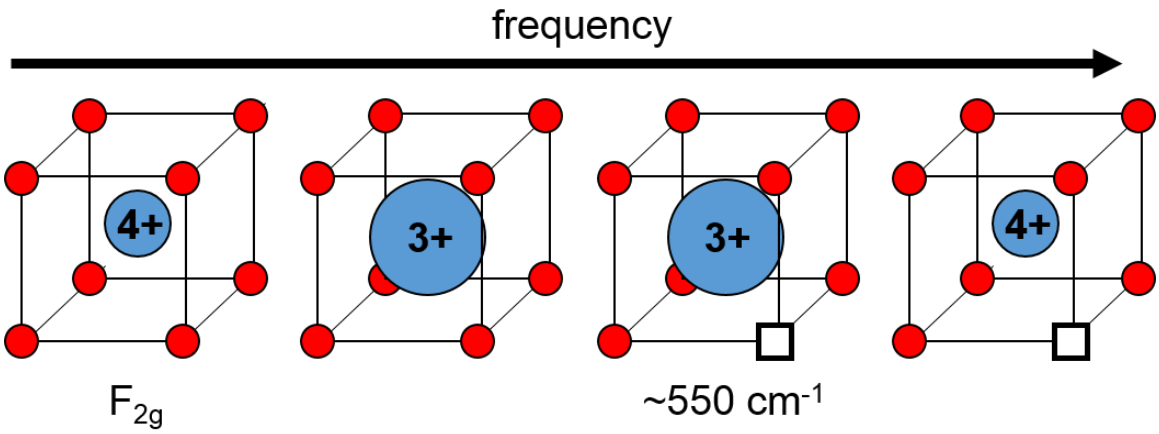


Figure 32: Relative change in defect band frequency with varying Ce-O coordination environment. The first coordination environment represents a pristine CeO_8 arrangement with a characteristic frequency of ~465 cm^{-1}. A $Ce^{3+}O_7$ arrangement has a characteristic frequency of ~550 cm^{-1}. Defect bands for $Ce^{3+}O_8$ and $Ce^{4+}O_7$ arrangements appear at lower and higher frequencies to the $Ce^{3+}O_7$ defect band, respectively. Frequency predictions based on density functional theory results from reference [89]

system, which can be used to interpret defect production and annihilation processes, as well as quantify the amount by which a material structure destabilizes after irradiation. In this regard, the information obtained from calorimetry is complimentary to structural information and can aid in bridging the gap between experimental and theoretical data.

After performing non-destructive neutron, X-ray, and Raman characterization, the irradiated and unirradiated CeO_2 and ThO_2 samples were analyzed destructively using high-temperature melt drop-solution calorimetry. For a review and description of this technique, see [94] and references therein. The primary goal of the calorimetric measurements was to measure the heat released from each sample after the sample is fully dissolved in molten sodium molybdate. The enthalpy of radiation damage was subsequently calculated using Hess's law by the expression:

$$\Delta H_{damage} = \Delta H^{unirradiated} - \Delta H^{irradiated}$$

where $\Delta H^{unirradiated}$ and $\Delta H^{irradiated}$ are the enthalpies of the drop-solution at 700 °C for the unirradiated and irradiated samples, respectively. This enthalpy of radiation damage is a measure of the amount of energetic destabilization of the structure caused by ion irradiation. Note that calorimetric studies were limited to CeO_2 owing to restrictions in handling and measuring radioactive ThO_2.

Figure 33 shows the evolution of the calculated radiation damage enthalpy for CeO_2 after irradiation with 1 and 2 GeV Au ions. The data in the figure were normalized to kJ per mole so that the measure of enthalpy in this representation is independent of sample mass. The figure shows that the radiation damage increases and then saturates at the highest ion fluences achieved. This behavior is independent of the ion energy used and appears to show Poisson-like behavior. The shape of the Poisson trend shows that radiation damage accumulates by a so-called *single-impact mechanism*. A single-impact mechanism shows a linear increase at lower fluences followed by sub-linear and saturation behavior at higher fluences. Saturation of a damage variable is often observed in materials after irradiation with swift heavy ions because of the characteristic cylindrical ion track morphology that forms in the material after dense electronic excitation.

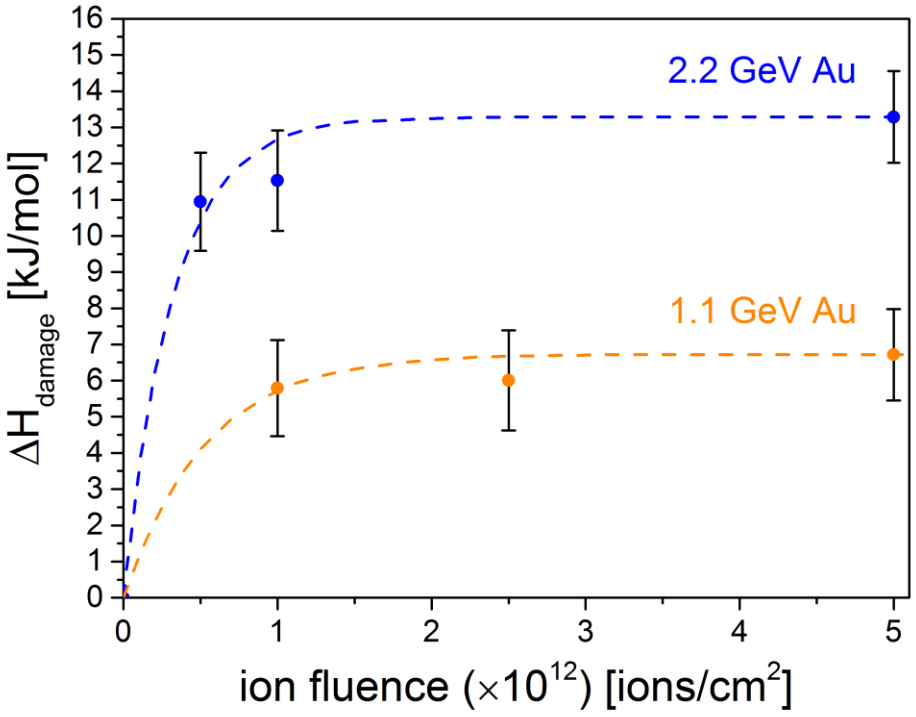


Figure 33: Change in radiation damage enthalpy with increasing ion fluence for CeO_2 before and after irradiation with 1 GeV and 2 GeV Au ions

Ion tracks in CeO_2 exhibit a unique morphology consisting of a vacancy-rich core region and an interstitial-rich halo region. Atomic displacement occurs on both cerium and oxygen sublattices, but damage is primarily concentrated on the oxygen sublattice because the lighter oxygen atoms are more susceptible to disordering [51, 52]. Analyses of heterogeneous microstrain and volumetric swelling performed in this study and in other studies [7, 66] further show that irradiation-induced microstrain saturates at much lower ion fluences (~1×10^{12} ions/cm^2) compared to volumetric swelling, which saturates at ~1×10^{13} ions/cm^2 after swift heavy ion irradiation at room temperature. These results indicate that the efficiency of the process responsible for microstrain is much higher than the efficiency for the process responsible for volumetric swelling. This premise is supported by data modeling schemes employing the single-impact model.

The single-impact model is based on the approximation that each ion-matter interaction yields a cylindrical ion track in the material and that the cross-sectional areas of the ion tracks are approximately equal to one another assuming the ion energies are approximately equal. A schematic of this is shown in Figure 34. At relatively low ion fluences, damage is approximately proportional to ion fluence because each addition ion track creates new damage (*i.e.*, defects) and there is minimal overlap of ion tracks. At the highest fluences, damage saturates because ion tracks severely overlap and damage within overlapped regions is modified in some way such that the damage production efficiency is lessened. This can occur by either defect annealing or defect clustering.

Data showing single-impact Poisson behavior are typically fit with the expression:

$$A = A_{saturation}(1 - e^{-\phi\sigma})$$

where A is the fitted parameter, $A_{saturation}$ is the saturation value of the fitted parameter, ϕ is the ion fluence, and σ is the cross-sectional area of a single ion track. Examples of commonly used damage parameters are unit cell parameters, heterogeneous microstrain, and ion track density measured by TEM. Fitting of unit cell and microstrain data of CeO_2 irradiated with 950 MeV Au ions [7] yielded ion track cross sections of 5.8 ± 0.6 nm and 8.4 ± 0.7 nm, respectively, which confirms that the efficiency (*i.e.*, damage cross-section)

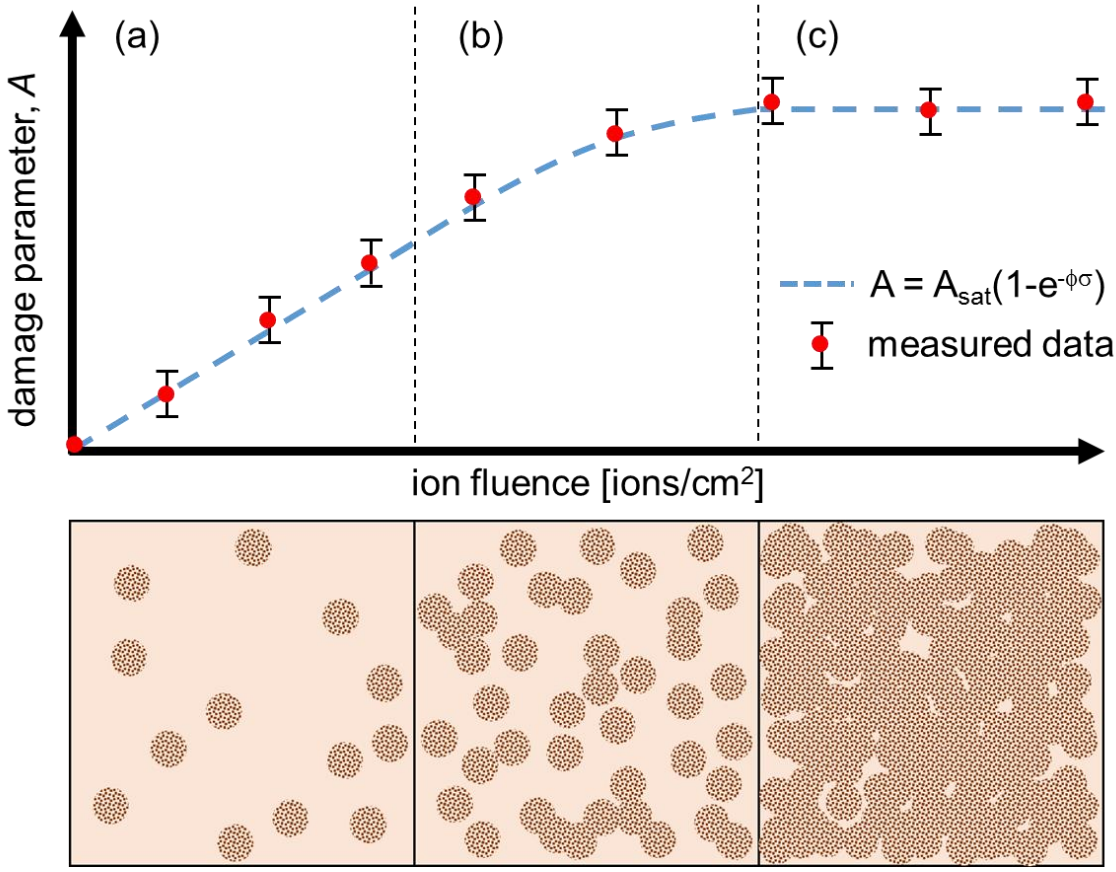


Figure 34: Schematic of single-impact model. The top panel illustrates an example of how experimental data are represented and the bottom panel shows corresponding frames of how ion tracks (darker patterned circles) are accumulated in the material (lighter matrix). At relatively low ion fluences (region *a*) the damage accumulation is approximately linear in relation to fluence because there is minimal track overlap; each ion track creates new damage. At higher fluences (region *b*) damage accumulation is sub-linear as ion tracks begin to overlap; overlapping regions do not necessarily produce new damage because defects can be annealed or cluster. At the highest fluences (region *c*) damage saturates because ion tracks severely overlap; damage production efficiency is severely lessened. Data showing single-impact Poisson behavior are typically fit with the single-impact model (blue dashed line). Common damage parameters include: unit cell parameters, heterogeneous microstrain, and ion track density

is higher (larger) for microstrain production compared to the process responsible for volumetric swelling. The calorimetric data were also fit with the single impact model (see Figure 33) in order to compare the damage enthalpy footprint with those of microstrain and the unit cell parameters. The derived effective ion track cross sectional diameters were 16.6 ± 3.2 nm and 13.8 ± 2.8 nm for the 2 and 1 GeV irradiations, respectively.

Comparison of the diameter values for 1 GeV (present study) and 950 MeV [7] irradiations shows that the effective track ion diameter for calorimetry (13.8 ± 2.8 nm) is much larger than the effective diameters for microstrain (8.4 ± 0.7 nm) and swelling (5.8 ± 0.6 nm). This suggests that drop-solution calorimetry measures the entirely of defects and microstrain created in core region, halo region, and areas surrounding each ion track. This is in contrast to the strain field, which is likely a measure of both core and halo regions, and swelling, which is likely only a measure of the core damage regions. The effective track diameters derived from calorimetric data (13-17 nm) are more in line with track diameters observed by TEM. These TEM studies show that the anion sublattice shows measurable disorder up to 8.5 nm from the ion track centers, *i.e.*, estimated track diameters are 17 nm [64].

Another observation is that the effective ion track area derived from the 2 GeV data is larger than the effective cross section from the 1 GeV data. This can be rationalized from simple kinematic considerations. Assuming head-on, elastic collisions between Au ions and electrons, higher energy ions will yield higher energy delta electrons, which can travel further distances in the material and generate defects at further distances from the ion track center. The maximum energy of a delta-electron can be calculated using the relativistic expression for maximum energy transfer between a heavy ion and electron:

$$Q_{max} = 2\gamma^2 mc^2\beta^2$$

where mc^2 is the rest-mass energy of the delta-electron, β is the ratio of Au ion velocity to the speed of light *c*, and γ is the Lorentz factor:

$$\gamma = \frac{1}{\sqrt{1-\beta^2}}$$

Lorentz factors for 1 GeV and 2 GeV Au ions can be calculated using the relativistic expression for total energy:

$$E_{total} = E_{kinetic} + E_{rest-mass}$$
$$\gamma Mc^2 = T + Mc^2$$

where *T* is the kinetic energy of the Au ion (1 GeV or 2 GeV) and Mc^2 is the rest-mass of the Au ion defined as:

$$Mc^2 = A + \Delta - 28 \times mc^2$$

where *A* is the atomic mass number and Δ is the mass difference (*i.e.*, difference between nuclide's atomic weight and its atomic mass number). Inputting the values for the $^{197}Au^{28+}$ ions used yields:

$$Mc^2 = \left(197\ a.m.u. \times \frac{931.49\ MeV}{a.m.u.}\right) - 31.17\ MeV - 28 \times 0.511\ MeV$$
$$Mc^2 = 183458.052\ MeV$$

Using this value in conjunction with the kinetic energies, *T*, yields Lorentz factors of 1.00545 and 1.0109 for 1 GeV and 2 GeV Au ions. These values yield Q_{max} values of 11.170 keV and 22.401 keV for 1 GeV and 2 GeV Au ion irradiations. The calculated Q_{max} values represent the upper limit of the delta-electron energy spectrum and the corresponding range for these energies (in CeO_2) denote the upper limit for an ion track radius in the material.

The range of delta-electrons in CeO_2 were calculated using the NIST online database ESTAR [95]. Data derived for CeO_2 using ESTAR are shown in Figure 35. The

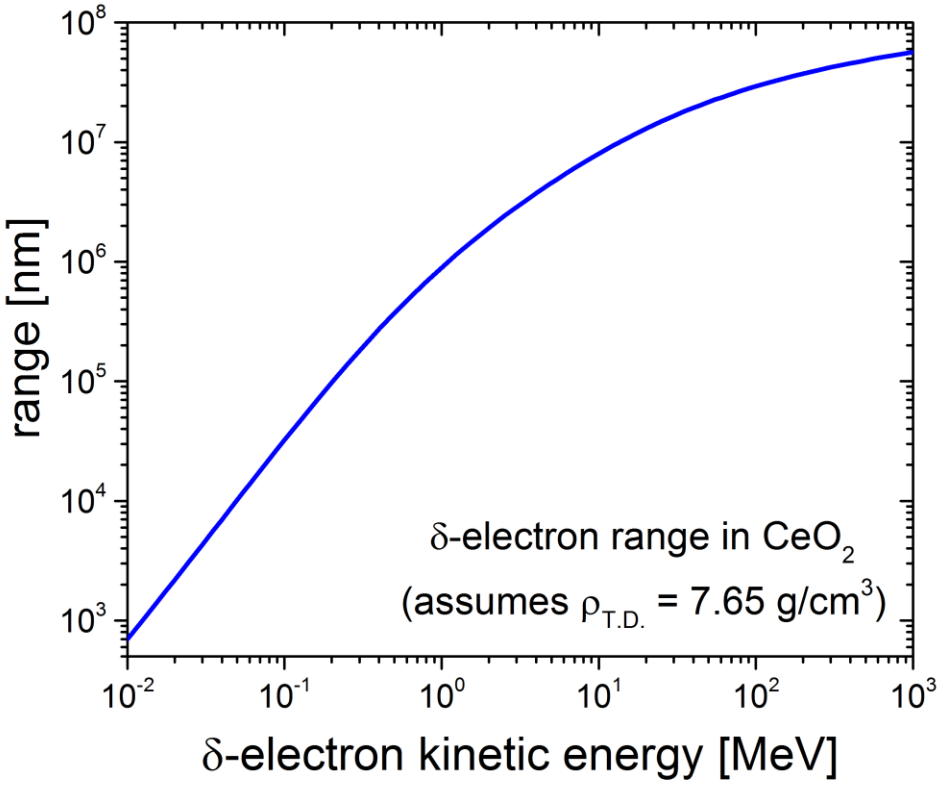


Figure 35: Range of electrons in CeO_2 as a function of electron kinetic energy. The calculation was performed with the online ESTAR database [95] and assumes a theoretical density of 7.65 g/cm^3 for CeO_2

farthest range that a delta-electron can travel in CeO_2 after an elastic collision with an Au ion of either 1 GeV or 2 GeV energy is ~840 nm or ~2650 nm, respectively. This shows that the maximum effective ion track diameter produced by 2 GeV Au ions is larger than that of 1 GeV Au ions by a factor of ~3. Assuming ion track lengths of 45 and 75 μm (*i.e.*, the sample thicknesses) for 1 and 2 GeV irradiations, the maximum effective ion track volume produced by a 2 GeV Au ion is ~16.5 times larger than the maximum ion track volume produced by 1 GeV Au ions.

The amount of energy deposited in CeO_2 by 1 GeV and 2 GeV Au ions can be calculated using the SRIM code [4]. Using these energy values in conjunction with the calculated values for the maximum ion track volumes yields an estimate for the energy density caused by 1 and 2 GeV Au ion irradiation. The calculated energy densities are 1.673 J/cm^3 and 0.1873 J/cm^3 for 1 GeV and 2 GeV irradiations, respectively. This simple estimate shows that although more energy is deposited in the material by 2 GeV Au ions (compared to 1 GeV Au ions) the energy density is drastically reduced.

Note that this gives no indication as what defects comprise the two damage regions. It's possible that damage is more severe (*i.e.*, causes volumetric swelling) within ion tracks of smaller cross-sectional area. This is the premise behind the so-called, *ion velocity effect*. Figure 33 indicates that more damage is produced by 2 GeV Au ions despite the assumption that deposited energy is more diffuse. This suggests that processes such as defect clustering and/or defect annealing are more efficient under high-density energy deposition (1 GeV irradiation) and these effects result in a smaller radiation damage enthalpy.

Defect Production Efficiency

Calorimetric measurements are often represented in normalized units of kJ/mol in order to enable direct comparison of heat measurements independent of mass. However, these values can be converted into pure energy release measurements (kJ) by taking into account the exact mass of the sample used to perform the calorimetric measurement. These pure energy measurements represent the total energy stored in the form of irradiation-induced defects and microstrain, and enable the estimation of the defect production efficiency,

which can be calculated by computing the ratio of total defect energy (*i.e.*, energy from calorimetric measurement) and total deposited energy (*i.e.*, energy from ion irradiation).

The total energy stored in the form of stable defects in units of kJ per ion track is calculated by the expression:

$$E_{defects} = \frac{H_{damage} \times \rho \times t}{m \times \phi} \left[\frac{kJ}{ion\ track}\right]$$

where H_{damage} is the measured energy associated with defects and microstrain in kJ, ρ is the density of the irradiated sample (assuming 60 % theoretical density), t is the thickness of the irradiated sample, m is the mass of the calorimetric irradiated sample, and ϕ is the ion fluence in units of ion tracks per area. The total deposited energy was calculated from the SRIM code [4] using the sample density correction described by Lang *et al*. [5]. The SRIM calculations yielded measurements of total energy deposited in the 45 and 75 μm-thick samples, assuming that the ions are cylindrical and completely pass through the samples:

$$E_{deposited} = E_{SRIM} \left[\frac{kJ}{ion\ track}\right]$$

Damage production efficiency, η, is therefore defined as:

$$\eta = \frac{E_{defects}}{E_{deposited}} \ [\%]$$

Damage production efficiency defined in this way represents the fraction of total deposited energy that results in energetic structural destabilization.

Figure 36 shows the damage production efficiency plotted against ion fluence for the two CeO_2 irradiation conditions. The figure shows that the damage production efficiency quickly decreases as the fluence increases under both 1 GeV and 2 GeV Au ion irradiation. Moreover, the gap in efficiency between the two irradiation conditions

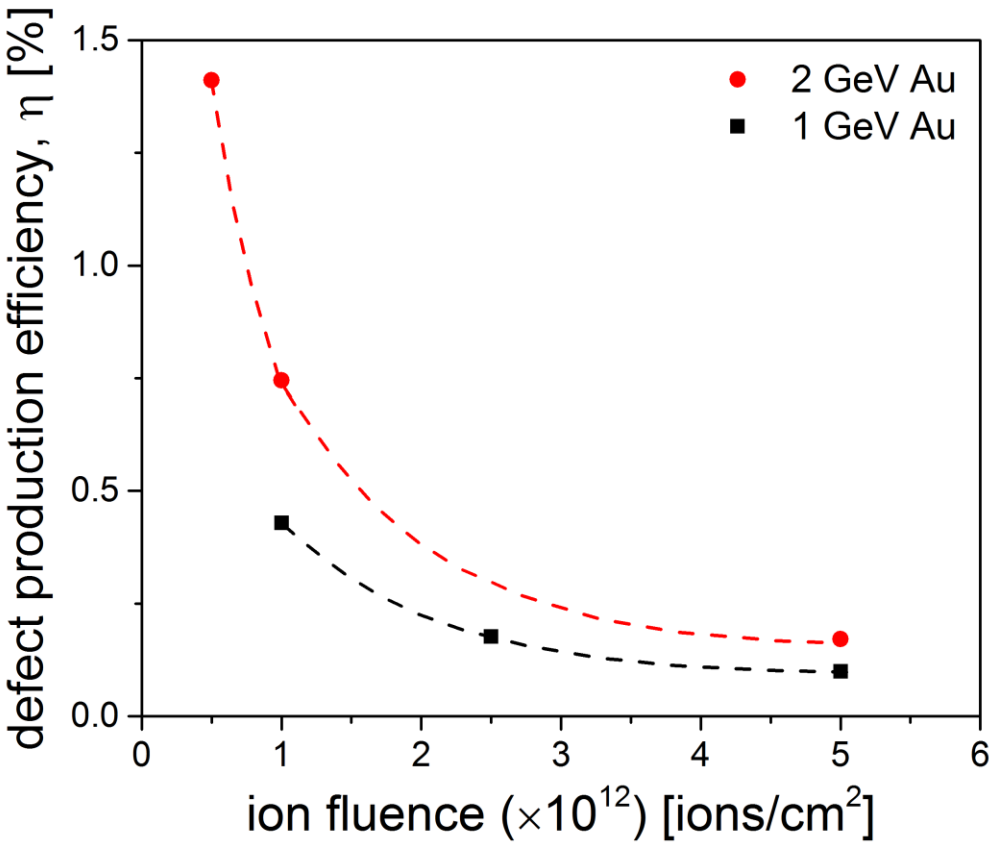


Figure 36: defect production efficiency calculated using calorimetric absolute energy measurements

decreases, and the efficiencies for both irradiation types begin to saturate after the fluence reaches 2.5×10^{12} ions/cm^2. The higher damage production efficiency of the 2 GeV irradiation is consistent with the data representation of Figure 33, which shows that the structure is more destabilized under 2 GeV Au ion irradiation compared to the 1 GeV irradiation. This indicates that the 2 GeV irradiation results in more energetic destabilization and/or results in a different type of atomic disorder (or defects) that yields a higher energy penalty.

The decrease in damage production efficiency at the higher fluences is likely attributable to the onset of severe ion track overlap in the irradiated materials (fluence regime *c* in Figure 34). TEM investigations have shown that severe overlap of ion tracks occurs at around 1.5×10^{12} ions/cm^2 in CeO_2 [54]. Studies of other material systems show that track overlap can lead to either defect annealing or defect clustering processes [96]. Track overlap in oxides likely results in defect clustering and the subsequent formation of extended defects, such as dislocation networks [97]. It's unknown if defect clusters contribute more or less to structural destabilization, but results suggest that they contribute less to energetic destabilization (*i.e.*, defect clustering is more energetically favorable than an equivalent density of isolated point defects) because agglomerate formation relieves strain caused by individual point defects.

Energy density calculations presented in the previous section demonstrate that the energy density is higher under 1 GeV irradiation compared to 2 GeV Au ion irradiation. However, the results shown in Figure 33 show that 1 GeV Au ion irradiation causes less energetic destabilization, despite the higher energy density. This indicates that higher energy densities (1 GeV case) result in more dynamic defect annealing and lower defect densities whereas lower energy densities (2 GeV case) result in less dynamic defect annealing and higher defect densities at low fluences when track overlap is minimal. This explains the results shown in Figure 36. Assuming defect production efficiency is a measure of defect *quantity*, the figure shows that more defects are produced after 2 GeV irradiation because there occurs defect annealing within atomic displacement cascades. At the higher fluences, defect clustering plays a larger role and results in a similar behavior in all materials under both types of irradiation. Defect concentrations in this high fluence

regime approach steady state because of competition between defect production and annihilation (*via* recombination or diffusion to sinks) rates.

This is further illustrated by normalizing the damage production efficiency to each ion track by dividing by the fluence. Figure 37 shows the damage production efficiency, normalized by fluence, plotted against energy deposited in the material, which is an alternative representation of fluence. The fluence was converted to energy density in order to facilitate the comparison of the data to other types of irradiations, such as femto-second laser and gamma irradiations. The figure shows similar trends as was observed for Figure 36 except that the differences at lower/higher fluences are larger/smaller. The figure clearly shows that both data sets converge at the highest fluences when defect clustering is prevalent under both irradiation conditions. This is in contrast to the low fluence data that shows that the effects of the two irradiation types are drastically different. In-cascade dynamic defect annealing is more prevalent for 1 GeV irradiation because of the higher energy density produced by ion-matter interactions.

Results and Discussion Part II: Damage Annealing

The most heavily damaged swift heavy ion-irradiated samples (5×10^{12}-1×10^{13} ions/cm^2) were annealed isochronally in order to better understand defect stability and annealing-induced modifications. Defect annealing studies ideally employ both isochronal and isothermal annealing methods because they yield insights regarding defect energetics and annealing kinetics, respectively. Experiments performed for the present study were limited to isochronal annealing investigations because of the time constraints imposed at national user facilities (synchrotron X-ray and spallation neutron sources). Studies were performed on only CeO_2, only ThO_2, or both CeO_2 and ThO_2 depending on the resources and experimental conditions available. Calorimetric studies, for example, were limited to CeO_2 because of limitations in handling radioactive ThO_2.

Neutron and X-ray Diffraction – Average Structure

All diffraction isochronal experiments followed a similar procedure. A heavily damaged CeO_2 or ThO_2 sample (5×10^{12}-1×10^{13} ions/cm^2) was characterized, heated to a temperature

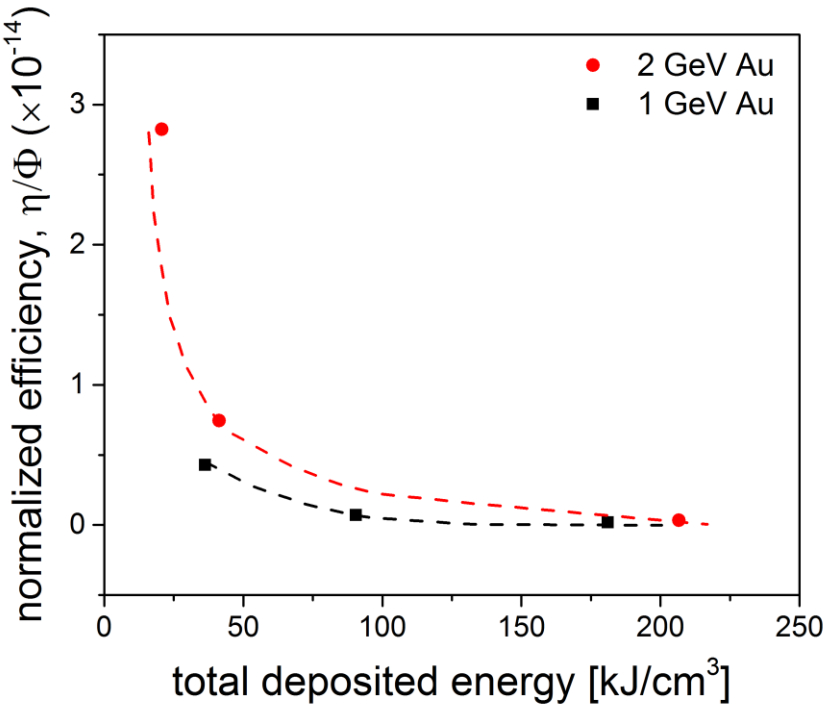


Figure 37: defect production efficiency normalized by ion fluence as a function of cumulative energy density

T_1, held at temperature for 15-20 minutes, and quenched to room temperature. After cooling to room temperature, the sample is heated to a higher temperature T_2 and the process is repeated for higher temperatures. An example schematic of a typical isochronal annealing experiment is shown in Figure 38.

Diffraction measurements performed during isochronal annealing experiments show an overall reverse of modifications observed as a result of the damage accumulation process. Annealing to higher and higher temperatures results in sharper peaks and a decrease in peak broadening. An illustration of this for swift heavy ion irradiated CeO_2 is shown in Figure 39. The sharper peaks indicate that defects are annealed, likely by Frenkel pair recombination, and more atoms return to pristine fluorite structure arrangement. The increase in peak intensity is concomitant with the decrease in peak broadening and it arises from the larger domains of pristine CeO_2 arrangements. This is a reversal from the volumetric swelling that occurs after irradiation. The illustration shown in Figure 39 is from synchrotron XRD measurements. Similar features are present in the neutron diffraction patterns (Figure 40), although the features are much subtler. The difference in peak broadening behavior is attributable to the difference in intensities between the synchrotron X-ray and spallation neutron beams and not to differences in annealing behaviors. The small sample quantity coupled with the relatively low intensity of the spallation neutron beam resulted in the neutron diffraction patterns having much worse resolution. Nevertheless, Figure 40 shows that the neutron diffraction pattern of irradiated CeO_2 exhibits shaper, more intense peaks after annealing at the highest temperatures.

A close inspection of the XRD and neutron diffraction patterns also reveals that the diffraction peaks shift slightly after annealing. The slight peaks to lower *d*-spacings (higher two-theta) mean that the unit cell parameter decreases. This is a reversal from the volumetric swelling that is observed after irradiation and it results from point defect annihilation. Rietveld refinement of the diffraction patterns yielded unit cell parameters. Figure 41 and Figure 42 show how the unit cell parameters of CeO_2 and ThO_2 evolve with increasing isochronal annealing temperature. Both cell parameters show a monotonic decrease with increasing isochronal annealing temperature. This confirms that the change in cell parameter is caused by defect annealing and not variation of temperature. High

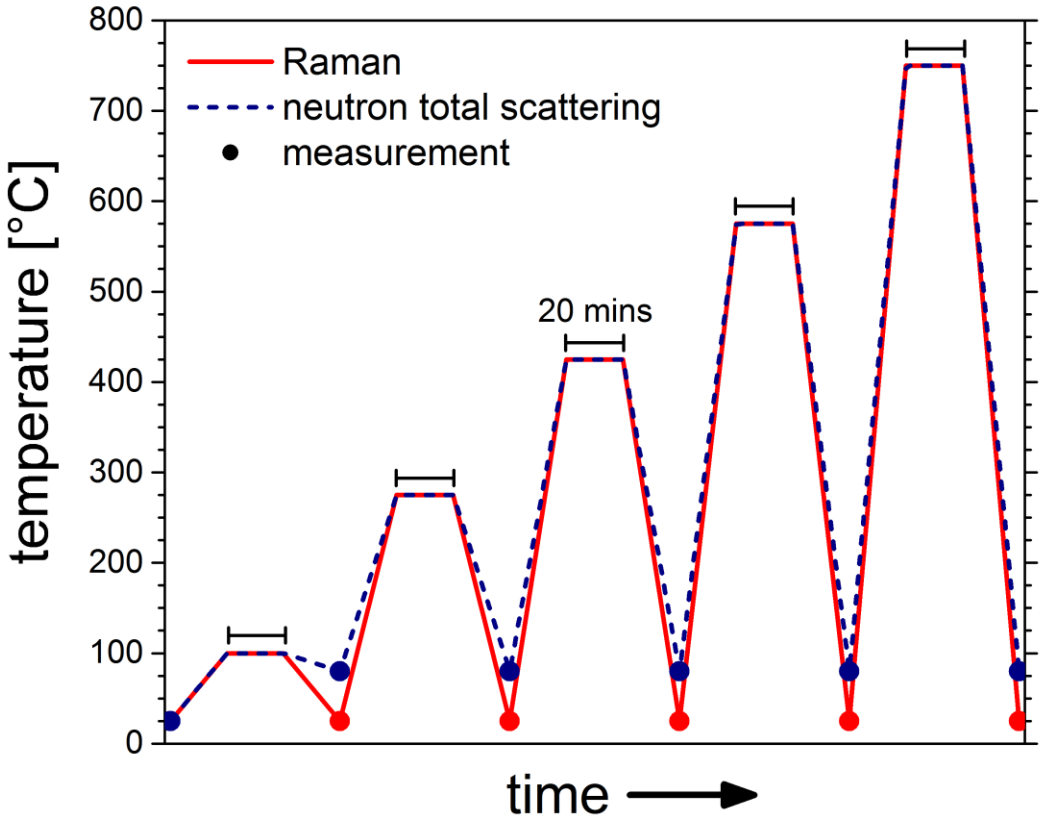


Figure 38: Example temperature profile for typical isochronal annealing experiment. Figure from reference [98]

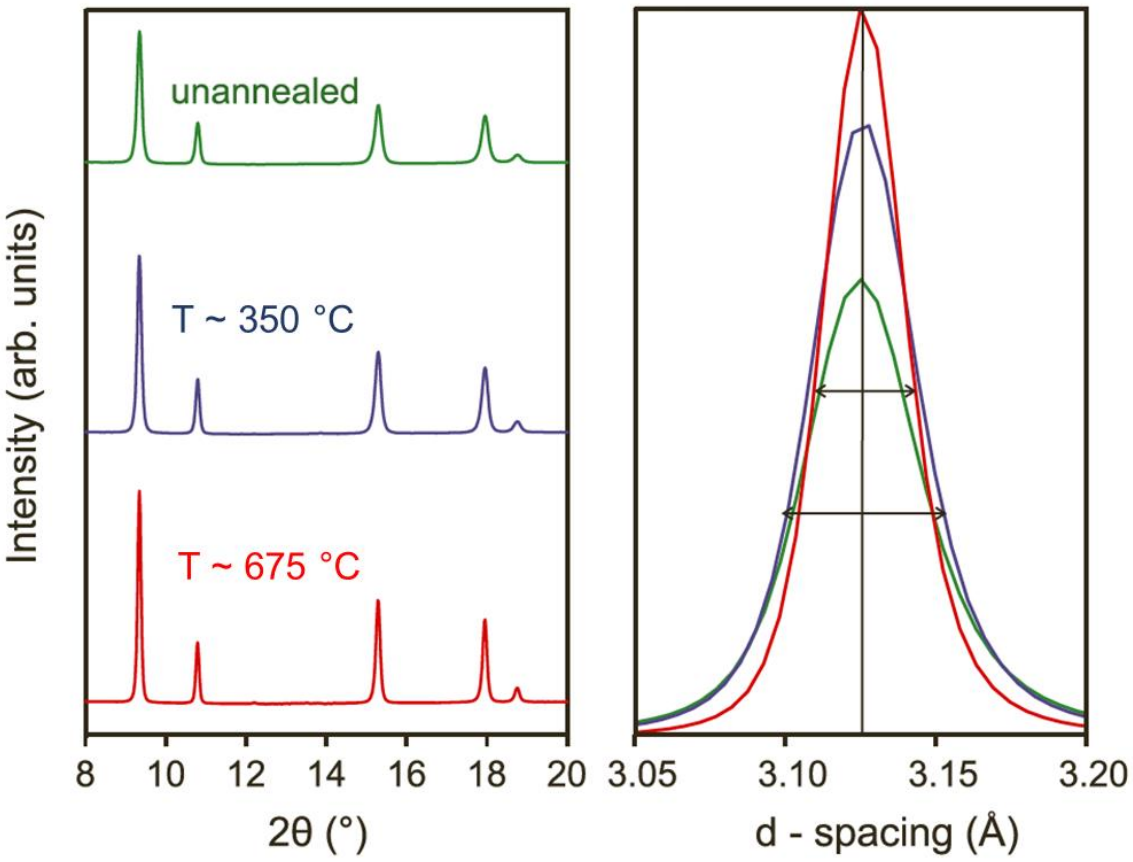


Figure 39: X-ray diffraction peaks of swift heavy ion irradiated CeO2 before and after high-temperature, post-irradiation annealing

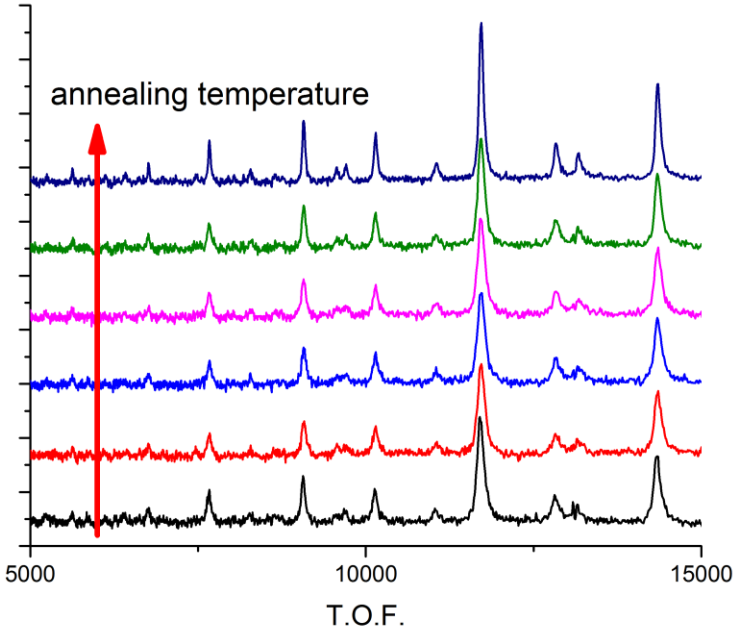


Figure 40: Evolution of neutron diffraction pattern of CeO_2 before and after post-irradiation isochronal annealing

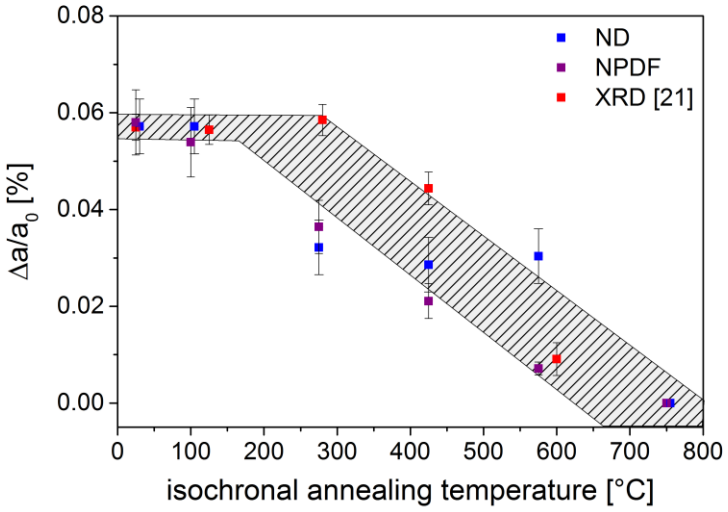


Figure 41: Fractional change of unit cell parameter of swift heavy ion-irradiated ThO2 before and after isochronal annealing. Figure from reference [98]

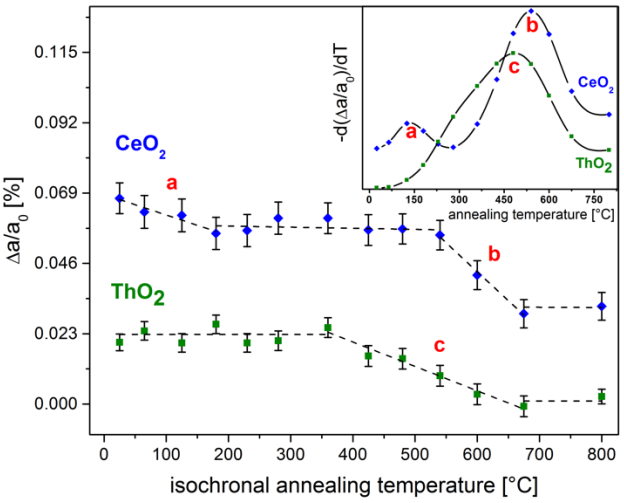


Figure 42: Fractional changes of unit cell parameters with increasing isochronal annealing temperature. The inset shows the derivative of the fractional change in unit cell parameter. Figure adapted from reference [15]

temperature would cause an increase in the unit cell parameter on account of thermal expansion.

A comparison of the different diffraction types (neutron *vs*. X-ray) in Figure 41 shows that the values derived from the two techniques are similar. There occur slight differences that are likely attributable to experimental uncertainties. Absolute values are more reliable from XRD in this case because the measurement resolution is much higher compared to that of the neutron diffraction measurements. Nevertheless, both datasets show a similar annealing process. It's important to highlight this observation because the XRD and neutron datasets shown in Figure 41 are of ThO_2 irradiated under two very different conditions, 945 MeV and 2 GeV Au ion irradiation. This means that the isochronal annealing experiment yields information about point defects and not the defect structure, which can differ drastically among the two types of irradiation conditions. Specific defects will only anneal at characteristic isochronal annealing temperatures.

Figure 42 shows data comparing the isochronal annealing behavior of swift heavy ion irradiated CeO_2 and ThO_2. The measured damage parameter in this case is the unit cell parameter, which monotonically decreases with increasing isochronal annealing temperature. The relative change in lattice parameter, $\Delta a/a_0$, was plotted instead of the actual lattice parameters because the cell parameters of CeO_2 and ThO_2 differ by approximately 0.2 Å. The dashed black lines in the figure do not represent a model and are only used to guide the eye.

The figure shows that the two irradiated materials show different annealing behavior throughout the temperature range. CeO_2 shows two large changes in $\Delta a/a_0$ compared to ThO_2, which only shows one large change. These large changes in $\Delta a/a_0$ are indicative of discrete annealing stages. The annealing stages are more easily identified in the inset of Figure 42, which shows the derivative of $\Delta a/a_0$ plotted against isochronal annealing temperature. In this representation, the discrete annealing stages are denoted by peaks. CeO_2 data shows two sharper peaks whereas ThO_2 data shows one much broader peak. This suggests that the annealing stage of ThO_2 represents various defect annealing mechanisms.

Isochronal annealing stages occurring at lower temperature are likely attributable to the annealing of oxygen-type defects because oxygen atoms are lighter and, as a result, exhibit lower energy barriers for migration compared to cation-type defects. This suggests that the first annealing stage of CeO_2 is attributed to oxygen defect annealing. More evidence for this is presented in later sections. One potential mechanism for oxygen defect annealing involves oxygen vacancy migration. The annihilation of oxygen vacancies would result in the re-oxidation of Ce^{3+} to Ce^{4+}, which would induce the decrease in unit cell parameter observed from Rietveld results. Another consequence of cation re-oxidation is a decrease of heterogeneous microstrain. The level of heterogeneous microstrain in the material would decrease following cation re-oxidation because the ionic radius of Ce^{4+} is smaller than that of Ce^{3+}.

Evidence for this decrease in heterogeneous microstrain is shown in Figure 43. The figure shows results from Williamson-Hall analysis of the diffraction data of Figure 42. Williamson-Hall analysis decouples peak broadening contributions from microstrain and crystallite size by distinguishing the $\tan(\theta)$-dependence of microstrain from the $\cos^{-1}(\theta)$-dependence of domain size [81]. Plotting $\cos(\theta)$ against $\sin(\theta)$ yields a line in which the slope is proportional to microstrain and the *y*-intercept is inversely proportional to domain size. Figure 43 shows that there are negligible changes in domain size after isochronal annealing. The changes in peak broadening are instead caused by decreases in heterogeneous microstrain. ThO_2 shows a smaller magnitude of decrease (*i.e.*, smaller change in slope) compared to CeO_2. This indicates that the microstrain is drastically decreased in CeO_2, in agreement with the proposed cation re-oxidation mechanism.

Neutron Total Scattering – Local Structure and Diffuse Scattering

Diffraction analysis is useful for monitoring changes in heterogeneous microstrain and changes in the average structure *via* changes in unit cell parameter. However, it is not able to probe short-range atomic configurations. Changes in these local configurations may indicate which defects contribute to the distinct defect annealing processes. Short range order in the irradiated materials was probed using neutron total scattering.

The total scattering pattern, $S(Q)$, comprises scattering from both Bragg and

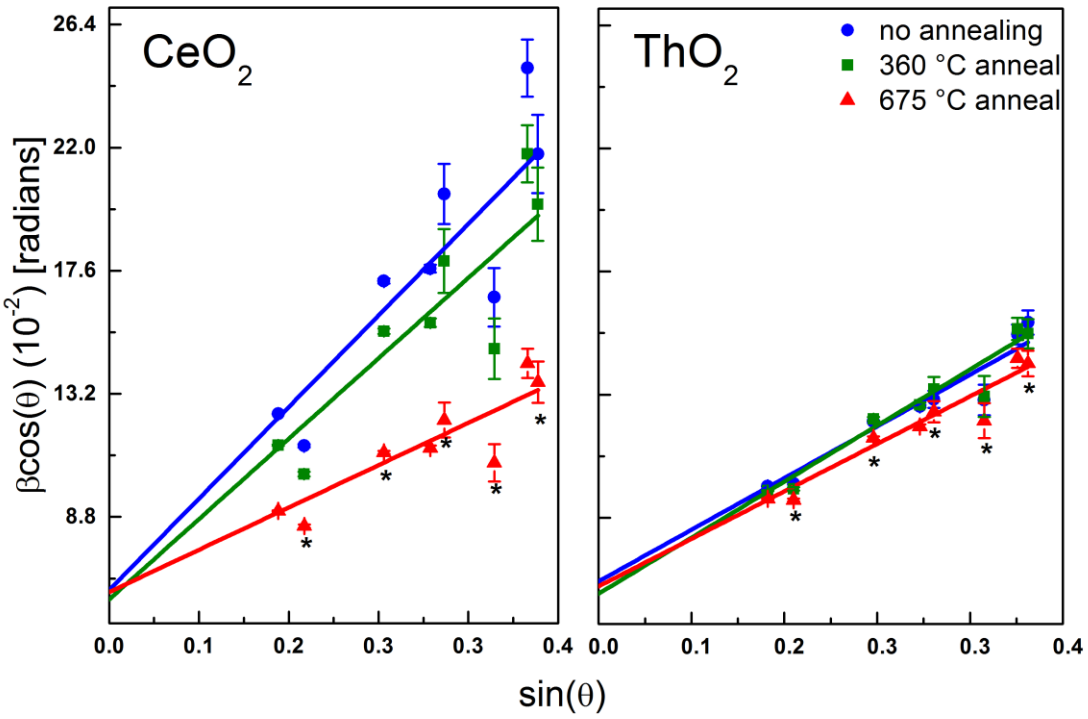


Figure 43: Williamson-Hall plots for CeO2 and ThO2 before and after post-irradiation isochronal annealing. The asterisks denote data points associated with the oxygen sublattice. These points show more scatter compared to points only associated with the cation sublattice. Figure adapted from reference [15].

diffuse components. Bragg information is equivalent to the information obtained from diffraction analysis. This is in contrast to diffuse scattering, which arises from defects and short-range atomic configurations that do not order over long length scales. Diffuse scattering in the total scattering patterns appears as broad, low-intensity peaks whereas Bragg scattering appears as sharp, high-intensity peaks.

Figure 44 shows the total scattering patterns of CeO_2 and ThO_2 before and after isochronal annealing to various temperatures. Prior to annealing, the diffuse scattering level is relatively high. The patterns are cropped to the region ~1-4 Å in order to highlight the largest changes in diffuse scattering intensity. Prior studies of reduced CeO_2 (CeO_{2-x}) have shown that the largest changes occurred in this *Q* range [77]. After isochronal annealing, the diffuse scattering level dropped to lower intensities in both materials.

A close inspection of Figure 44 reveals that CeO_2 begins to anneal at lower temperatures compared to ThO_2, which is in agreement with the unit cell parameter data shown in Figure 42. The diffuse scattering level of CeO_2 shows an abrupt drop between the 100 °C and 275 °C isochronal annealing temperatures. This is in agreement with the first annealing step observed by synchrotron XRD. Interestingly, the diffuse scattering level does not change very much after annealing to higher temperatures. This is in contrast to the ThO_2 scattering pattern, which shows a monotonic decrease from ~275 °C to at least 575 °C. The ThO_2 pattern shows an abrupt drop in scattering intensity similar to that of CeO_2 except that the drop for ThO_2 occurs at higher temperatures between 275 °C and 425 °C. Afterwards, the diffuse scattering level continues to drop until ~575 °C. After annealing at 750 °C the diffuse scattering level slightly increases. This increase in diffuse scattering is attributed to thermal diffuse scattering caused by the sample not being cooled to room temperature. Cooling rates for the vacuum furnace at the NOMAD beamline are very sluggish at lower temperatures (< 300 °C). Therefore, it's likely that the sample did not reach room temperature after heating to the highest temperature (750 °C) and this residual temperature caused the observed increase in thermal diffuse scattering. An increase in thermally-induced diffuse scattering at elevated temperatures was confirmed by additional measurements of unirradiated ThO_2. Another supporting piece of evidence for this premise is the increase in Bragg scattering.

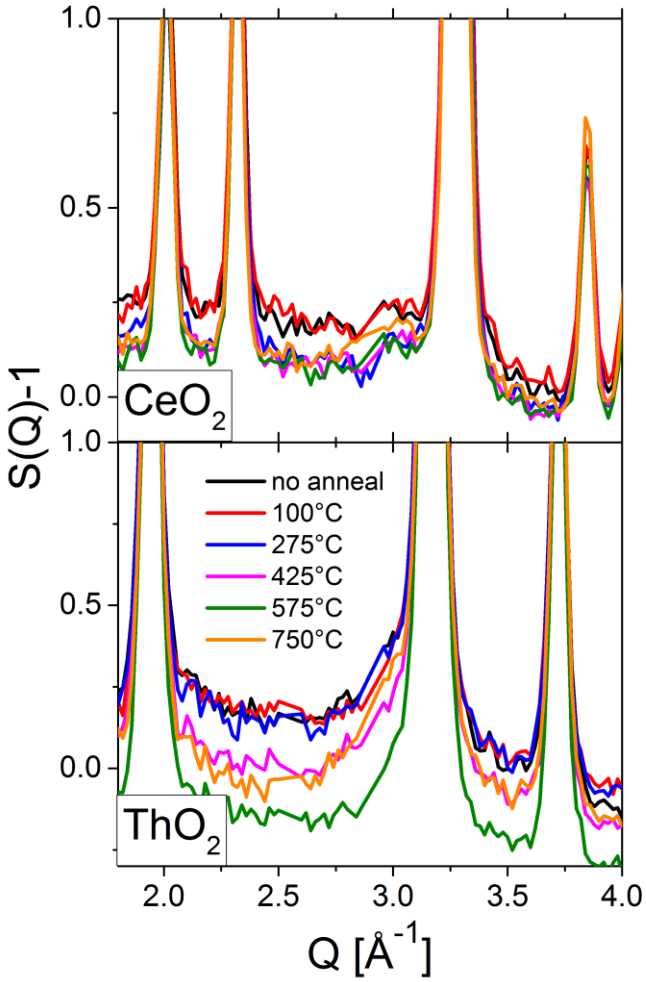


Figure 44: Total scattering functions of CeO2 and ThO2 before and after isochronal annealing to different temperatures

The total scattering patterns of ThO_2 were normalized to the third Bragg peak at ~3.7 Å in order to confirm that the sample continues to anneal above 575 °C. These normalized patterns shown in the bottom of Figure 45, compared to the S(*Q*) patterns (top), show that the intensities of the Bragg peaks continue to increase relative to the diffuse scattering after annealing at 750 °C. This suggests that the increase in diffuse scattering after 750 °C is indeed caused by thermally-induced diffuse scattering and not diffuse scattering from radiation-induced defects. The decrease in the ThO_2 diffuse scattering level occurring between ~275 °C and ~750 °C also coincides with the change in unit cell parameter observed by XRD. The change in unit cell parameter as measured by XRD begins at ~300 °C. The neutron diffuse scattering shows that the annealing initiates between 275 °C and 425 °C.

The total scattering patterns were further transformed into PDFs in order to monitor the changes in local structure before and after annealing. However, it was later discovered that the scattering measurements contained a small amount of parasitic scattering from the SiO_2 sample container. As a result, the very short-range structure of the PDFs (~1-3 Å) contained peaks corresponding to the first nearest-neighbor Si-O and O-O peaks of SiO_2 located at ~1.6 Å and ~2.6 Å, respectively. The contribution of the SiO_2 phase fraction to the total PDF was modeled by fitting a nanoparticle of SiO_2, which predominately contributes scattering intensity to low *r* regions. Refinement of the nanoparticle size resulted in an optimized nanoparticle domain size of 3 Å. This confirms that the SiO_2 phase fraction has little influence on the PDF at *r* values greater than 3 Å. Note that the small scattering contribution from SiO_2 should not significantly affect the changes observed in the total scattering patterns. The scattering is predominantly from CeO_2 or ThO_2, and the diffuse scattering analysis only relies on *relative* changes in diffuse scattering intensities from scattering patterns measured using the same sample.

Figure 46 shows how the PDF of ThO_2 evolves before and after irradiation, and before and after isochronal annealing. Structural refinement of the PDFs using the fluorite structure shows that the PDF is well modeled using the cubic fluorite structure. The difference curve has low intensity throughout the *r* range. This illustrates that the fluorite structure is fit well to the PDF at the different length scales. Surprisingly, the PDF peaks

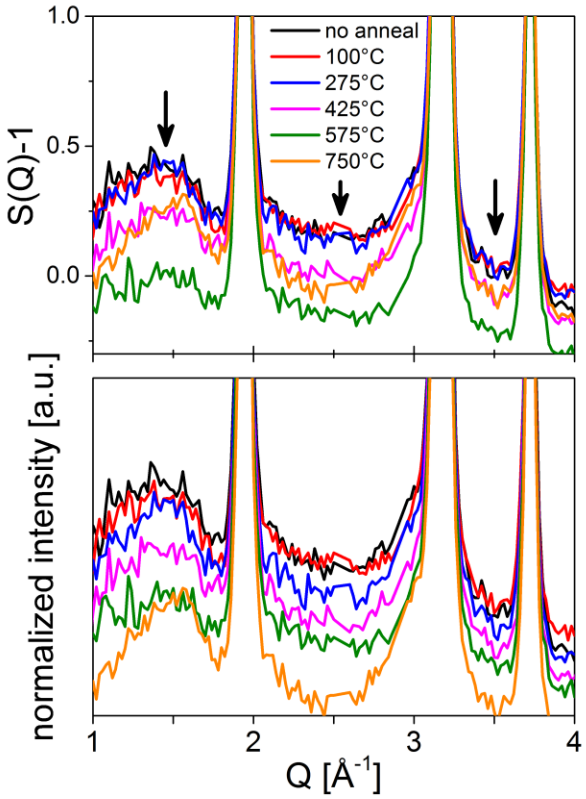


Figure 45: Total scattering functions (top) and normalized total scattering functions of ThO2 before and after isochronal annealing

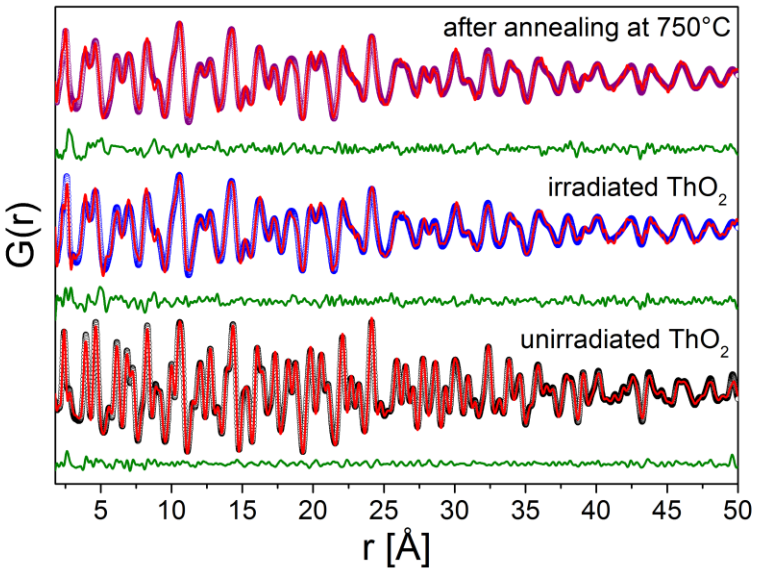


Figure 46: Pair distribution functions of swift heavy ion irradiated ThO2 before and after isochronal annealing. Figure is from reference [98]

show little difference before and after isochronal annealing. This is likely attributed to the relatively-poor resolution that resulted from using such a small sample volume in conjunction with the relatively low-intensity neutron beam. It's clear from the diffuse scattering analysis that isochronal annealing causes changes in the structure, but these changes are not immediately evident from inspection and simple refinement of the PDFs.

Raman Spectroscopy – Local Structure and Vibrational Properties

PDF analysis did not show any clear evidence for changes in the local atomic arrangements during isochronal annealing despite the obvious changes in the neutron diffuse scattering level and the XRD-based unit cell parameter measurements. As a result, Raman spectroscopy was used to probe changes in short range order *via* changes in vibrational properties. Raman spectroscopy is often equally sensitive, if not more sensitive, than PDF analysis to minor changes in local atomic arrangements. One example of this involves studies of the fluorite-derivative pyrochlore system. Raman spectroscopy was used to validate short-range Weberite-like ordering [99] that were only recently identified by structural refinement of the very short length scales of neutron PDFs [100, 101].

The Raman spectrum of swift heavy ion irradiated ThO_2 was collected before irradiation, after irradiation, and during isochronal annealing. A summary of the observed changes is shown in Figure 47. The figure shows the Raman spectrum before and after irradiation, and after isochronal annealing at the highest temperature achieved, 750 °C. The Raman spectrum of ThO_2 only contains one peak, which represents the triply-degenerate F_{2g} (or equivalently T_{2g}) vibrational mode. Immediately after irradiation with 2 GeV Au ions the Raman spectrum undergoes three main modifications: a severe decrease in the signal-to-noise ratio, asymmetric broadening of the F_{2g} peak to lower frequencies, and the emergence of a broad defect band centered about ~600 cm^{-1}. All of these features are consistent with the modifications observed after irradiation with 945 MeV Au ions [66]. Asymmetric broadening and the lower signal-to-noise ratio are consistent with the incorporation of point defects and heterogeneous microstrain. The latter causes a broader continuum of Th-O interatomic distances rather than a smaller, discrete value. This broader range of Th-O distances causes the broadening of the F_{2g} peak. The decreasing signal-to-

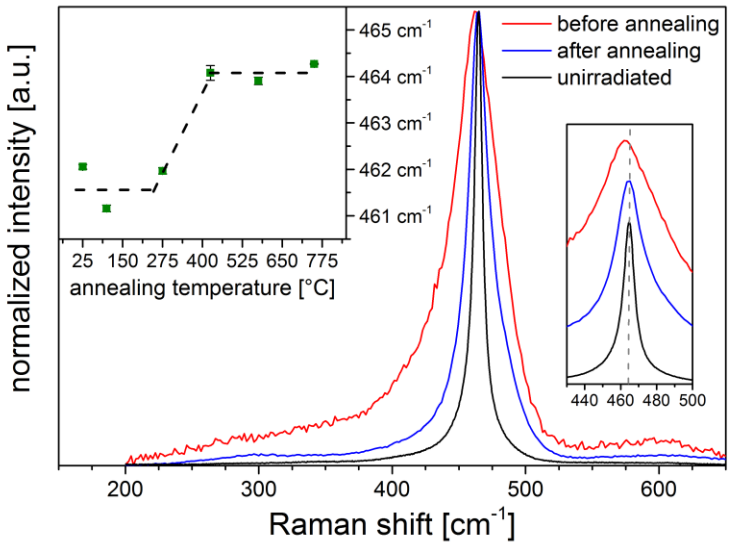


Figure 47: Raman spectrum of irradiated ThO2 before and after isochronal annealing. Inset on the left shows the evolution of the F2g peak position. Inset on the right shows a magnified view of F2g peak. Figure is from reference [98]

noise ratio is also consistent with the decreasing fluorite-structure domain size that was observed by neutron PDF analysis (Figure 26). The broad defect band at higher frequencies is likely attributable to irradiation-induced defect clusters considering the similarity of the frequency range (~550 – 620 cm^{-1}) to the range of defect complexes in CeO_2 and UO_2.

After annealing the sample to the highest isochronal annealing temperature the Raman spectrum shows a reversal of effects observed after irradiation. The normalized F_{2g} peak becomes sharper and the signal-to-noise ratio increases to the point that the broad defect band is barely detectable. A close inspection also reveals that the F_{2g} peak is blue-shifted. In order to elucidate the origin of the blue-shift, the Raman spectra were fit with Pseudo-Voight peak functions. Monitoring the evolution of the F_{2g} peak position with increasing isochronal annealing temperature revealed that the F_{2g} peak position shifts by ~2 cm^{-1} between the 275 °C and 425 °C isochronal annealing temperatures. This shift is large enough to be outside the limits of experimental uncertainty (~0.8 cm^{-1}). The characteristic temperature range for the abrupt shift in frequency coincides with the onset temperature for defect annealing as observed by XRD and neutron diffuse scattering. This suggests that the abrupt shift denotes a defect annealing stage and that the broad defect annealing stage observed for ThO_2 in Figure 42 actually comprises several distinct annealing stages that are unresolved by the lattice parameter analysis.

The F_{2g} vibrational mode represents the vibration of the oxygen cage surrounding each cation. This indicates that phonons only propagate along the oxygen sublattice. As such, changes in the characteristic F_{2g} frequency are likely attributable to changes on the oxygen sublattice. Based on this premise and reported isochronal annealing results for alpha-irradiated fluorite-structured CeO_2, UO_2, and PuO_2 [68, 102] it is proposed that the first annealing stage is attributed to the annealing of oxygen-type defects and anion Frenkel pair recombination.

In addition to the lower temperature oxygen interstitial-type defect annealing event, isochronal annealing studies report a higher-temperature cation vacancy annealing event at isochronal annealing temperatures in excess of 500 °C. A higher temperature annealing event was observed in the CeO_2 data shown on Figure 42, but no discrete high temperature annealing stage was observed for the ThO_2 data. Annealing of thorium vacancies would

also contribute to an increase in the F_{2g} signal-to-noise ratio because this annealing would result in a higher concentration of near-pristine ThO_8 arrangements. In order to test this theory, the Raman spectra were plotted in absolute scale without normalizing. This scheme was valid because Raman scattering during the annealing experiment was performed from an identical spot on the sample. Figure 48 shows the Raman spectra on an absolute scale.

Figure 48 shows that as the isochronal annealing temperature increases, the F_{2g} peak intensity increases and the peak becomes sharper. This is in agreement with the normalized data representation shown in Figure 47. Most noticeable is the very large change in peak intensity between 575 °C and 750 °C. The inset of Figure 48 shows the relative change in F_{2g} peak intensity and it is clearly seen that the intensity increases by ~125 % between 575 °C and 750 °C. For comparison, the peak intensity only increased by ~50% between 25 °C and 575 °C. It's proposed that this drastic increase in peak intensity signifies the cation vacancy annealing stage that was observed in prior studies of irradiated fluorite-structured oxides.

Differential Scanning Calorimetry – Thermodynamic Stability

The calorimetry measurements reported in this section were performed by Anna Shelyug at the University of California-Davis in collaboration with our research group using the identical set of samples that were used for the reported non-destructive neutron, X-ray, and Raman characterizations. The main findings are reported here because they are complimentary to the structural analysis of CeO_2 and ThO_2 reported in this dissertation. Most of the calorimetric data interpretation reported here was derived collaboratively by Anna Shelyug and myself. Additional details are available in manuscript: [80].

Differential scanning calorimetry (DSC) is a means to measure exothermic or endothermic events that occur during the defect annealing processes. Unlike the structural characterizations that were performed during isochronal anneals, the calorimetry measurements were performed *in situ* as the temperature was continuously increased. DSC measurements were performed in both air and argon gas atmospheres in order to elucidate the effect of environment on the defect annealing mechanisms. DSC measurements were

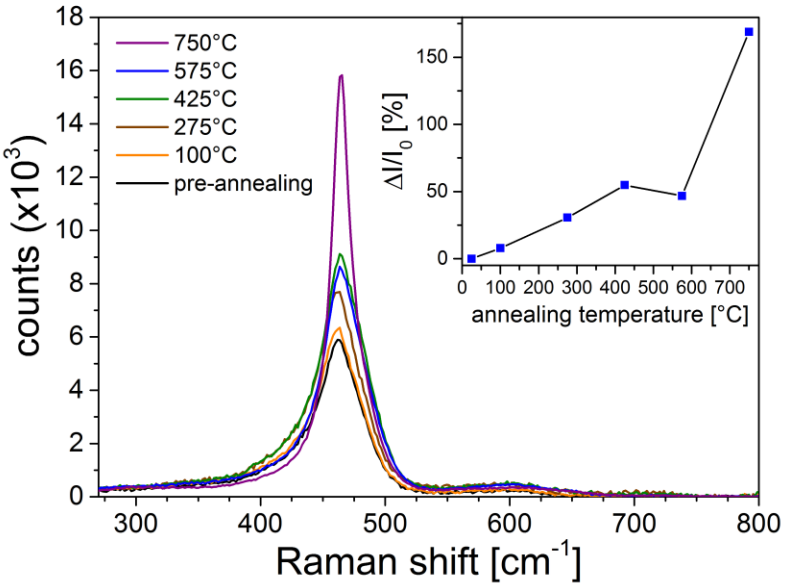


Figure 48: Evolution of Raman spectrum of irradiated ThO2 with absolute intensity. Inset shows the relative change in F2g peak intensity after annealing to different temperatures. Figure is from reference [98]

only performed on swift heavy ion irradiated CeO_2 owing to limiting regulations in handling radioactive ThO_2.

Figure 49 shows the DSC results for swift heavy ion irradiated CeO_2. The data show evidence for two distinct annealing regimes in agreement with the structural analysis results. The two annealing regimes are labeled "step 1" and "step 2" in Figure 49. The temperature ranges for the two annealing steps are ~175 – 400 °C and ~600-1000 °C. These temperature ranges are very similar with the regimes for oxygen defect and cation vacancy annealing reported elsewhere [103]. Varying the carrier gas from air to inert argon gas shows that the first annealing stage is severely suppressed in the absence of an oxygen atmosphere. This provides direct evidence that the first stage is attributed to the annealing of oxygen-type defects.

Interestingly, *in situ* thermogravimetric analysis showed that CeO_2 does not undergo a weight gain during the annealing process. This suggests that oxygen interstitials largely remain in the lattice as isolated interstitials or as small clusters rather than diffusing and leaving grains *via* grain boundaries. Because of this, it's surprising that the oxygen annealing stage is severely suppressed by the change of atmosphere. The latter suggests that the defect annealing of CeO_2 is strongly influenced by surface and sub-surface diffusion processes, which are typically much faster than intra-grain diffusion processes. This is supported by the reported catalytic efficiency of CeO_2, but it is at odds with the TGA result. The negligible weight change during annealing suggests that the stage results from the dissociation of interstitial-type oxygen clusters and the annealing of oxygen vacancies. It's possible that in the absence of oxygen in the atmosphere, distinct oxygen-type annealing stages are shifted to higher temperatures as indicated by the increased continuum region between 25 °C and 600 °C in the argon DSC data.

Conclusions and Recommendations

A combined structural and thermodynamic analysis was performed on CeO_2 and ThO_2 irradiated with swift heavy ions at room temperature in order to elucidate defect accumulation and annihilation mechanisms in fluorite-structured oxide materials. Inspection of the bulk structures using diffraction showed that energetic ion irradiation

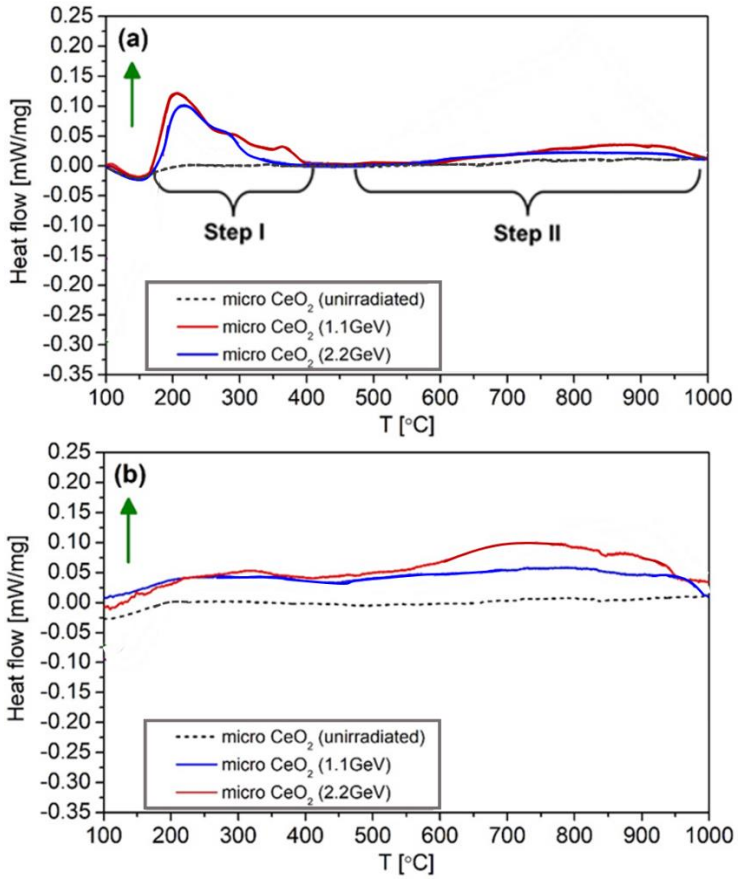


Figure 49: Differential scanning calorimetry measurements of swift heavy ion irradiated CeO_2 performed under flowing air (top) and argon gas (bottom). Positive changes in heat flow (green arrows) denote exothermic events whereas negative changes denote endothermic

caused the production of point defects and the accumulation of heterogeneous microstrain. The two materials remained crystalline and did not undergo any phase transformations after irradiation with 945 MeV, 1.1 GeV, and 2.2 GeV Au ions to fluences as high as 1×10^{13} ions/cm^2. Rietveld analysis of CeO_2 samples showed evidence of significant oxygen vacancy concentrations after irradiation.

Investigation of short-range atomic ordering was conducted using neutron total scattering, X-ray total scattering, and Raman spectroscopy. These characterization methods showed peak broadening and decreases in pair distribution function (PDF) peak intensities consistent with the incorporation of irradiation-induced heterogeneous microstrain caused by atomic displacement. Boxcar-type PDF modeling revealed that damage accumulation in CeO_2 is driven primarily by Frenkel pair production and subsequent cation reduction. Analysis of neutron PDF and Raman spectroscopy data yielded evidence for the presence of oxygen defect clusters and various defect complexes containing Ce^{3+} and vacancies after irradiation, in agreement with density functional theory (DFT) predictions. The magnitude of atomic disordering in CeO_2 saturated upon reaching a fluence of 5×10^{12} ions/cm^2.

Measurements of irradiated ThO_2 suggested different damage accumulation mechanisms. No large concentrations of oxygen vacancies were observed after irradiation in this material and the magnitude of structural disorder was much lower in comparison to CeO_2. Boxcar-type PDF analysis showed that damage accumulation in ThO_2 is strongly characterized by grain subdivision likely caused by dislocation network formation. This suggests that oxygen interstitials or clusters are more mobile in ThO_2 compared to CeO_2 and this higher mobility drives more rapid dislocation network formation. It's also proposed that the redox capability of cerium more readily enables defect clustering, which limits the mobility of oxygen interstitials and reduces the likelihood that interstitials are annihilated at grain boundaries. This was supported by the thermogravimetric analysis (TGA) results of irradiated CeO_2 that showed negligible weight gain after defect annealing at high temperature. This indicated that oxygen interstitials largely remain in CeO_2 as clustered defects and do not leave the system *via* diffusion to grain boundaries.

Drop-solution calorimetry was performed on the irradiated CeO_2 samples in order to measure energetic destabilization of the lattice caused by irradiation-induced defects.

These measurements showed that 2 GeV Au ions caused a larger magnitude of energetic destabilization than 1 GeV Au ions. The measured increase in enthalpy associated with radiation damage is shown to saturate at the highest fluences ($1\text{-}5\times10^{12}$ ions/cm^2) in agreement with measurements of heterogeneous microstrain. The saturation behavior of microstrain and radiation damage enthalpy was well described by a single-impact model for ion track formation. A comparison of effective ion track diameters from the fitted single-impact models suggests that the quantified radiation damage enthalpy is a summed measure of point defects, atomic disordering, and heterogeneous microstrain caused by ion irradiation.

Calorimetric data were also modeled assuming the homogeneous formation of cylindrical ion track structures in the bulk. This modeling resulted in an estimate for the energetic destabilization efficiency caused by swift heavy ion irradiation. Analysis showed that 2 GeV Au ions are much more efficient at destabilizing the structure compared to 1 GeV Au ions. This difference was attributed to more efficient in-cascade atomic re-combination. Relativistic kinetics calculations showed that the deposited energy density is ~9 times higher from 1 GeV Au ions compared with 2 GeV Au ions. The higher deposited energy density promotes more efficient dynamic defect annihilation, and this explains the higher saturation value for 2 GeV ion irradiation. It was observed that the efficiency of energetic destabilization saturates to a similar value for all irradiation types at higher fluences ($1\text{-}5\times10^{12}$ ions/cm^2). This saturation behavior was attributed to defect agglomeration and the onset of dislocation network formation, which dominates at high fluences and occurs in irradiated CeO_2 regardless of the ion energy used.

Defect stability and kinetics were investigated using structural and calorimetric analyses during high temperature annealing experiments. Isochronal annealing experiments performed in air atmospheres showed that the effects of ion irradiation and damage accumulation are reversed upon increasing annealing temperature. Short-range structural analyses performed with neutron PDF analysis and Raman spectroscopy did not show any drastic changes in local atomic arrangements. The largest changes were observed by bulk structure probes. Diffraction and diffuse scattering analysis showed that point defect concentrations and heterogeneous microstrain decrease with increasing isochronal

annealing temperature. Monitoring the evolution of the unit cell parameters showed CeO_2 and ThO_2 both exhibit two and one defect annealing stages, respectively, although the single annealing stage of ThO_2 appears to be a convolution of multiple annealing stages.

The first annealing stage of CeO_2 was attributed to cation oxidation ($Ce^{3+} \rightarrow Ce^{4+}$) upon observing the effect of annealing atmosphere. Differential scanning calorimetry showed that the first annealing stage is drastically suppressed upon changing the atmosphere to inert argon gas. This showed that the annealing mechanism is strongly dictated by the oxygen potential and the mechanism is likely associated with surface or near-surface diffusion. The other annealing stages were attributed to the annealing of oxygen agglomerates and the onset of vacancy migration. The onset of vacancy migration typically occurs at ~20% of the melting temperature, which corresponds to ~480 and 678 °C for CeO_2 and ThO_2, respectively.

The structural analyses indicate that the materials were irradiated within the *point defect swelling* regime where interstitials are mobile, but vacancies are immobile. Future irradiations should be performed at higher temperatures in order to evaluate the extent of radiation damage in expected operating regimes for inert matrices and nuclear fuels. It is possible that irradiations performed above the *stage III* onset temperature will result in much different irradiation-induced defects that were not observed in the present study. This study also demonstrated that defect clusters comprising oxygen interstitals, vacancies, and reduced cerium cations can form after energetic ion irradiation. These point defect clusters are analogous to oxygen defect clusters that form in hyper-stoichiometric UO_2 (UO_{2+x}). Kinetic Monte Carlo studies of defect clusters in UO_{2+x} have shown that certain cluster morphologies can exhibit very fast diffusion mechanisms and that taking these defect energetic modifications into account can drastically improve bulk diffusivity predictions. Therefore, modified migration energies of oxygen interstitial and vacancy clusters in fluorite structured oxides should be taken into account if considering materials for applications in which diffusion and ion conducting properties are important. Future studies should concentrate on identifying defect stability and migration energy trends using DFT for specific defect clusters deduced from Raman spectroscopy and neutron pair distribution function analysis, as shown here.

CHAPTER II: POINT DEFECTS IN OXIDIZED URANIUM DIOXIDE

Abstract

Atomic structures of UO_2 and $UO_{2.07}$ were experimentally characterized at room temperature and at elevated temperatures up to 1000 °C in order to elucidate relationships between stoichiometry, temperature, oxygen point defects, and phase changes. Atomic structure modifications were probed using Raman spectroscopy and neutron total scattering. Bulk phase analysis performed using neutron diffraction showed that both materials are well represented by single fluorite structure models, and both materials undergo thermal expansion as predicted by pre-established models. Detailed analysis of short-range structural features, however, revealed that the oxidized material was not a single phase compound at lower temperatures (< ~600 °C), but was instead a two-phase mixture of fluorite-type $UO_{2+x\,(s)}$ and cubic U_4O_{9-y}. Changes in various measured quantities from Rietveld refinement and pair distribution function (PDF) analysis enabled the estimation of $UO_{2+x\,(s)} + \alpha\text{-}U_4O_{9-y} \rightarrow UO_{2+x\,(s)} + \beta\text{-}U_4O_{9-y}$ and $UO_{2+x\,(s)} + \beta\text{-}U_4O_{9-y} \rightarrow UO_{2+x\,(s)}$ phase boundaries, which were in good agreement with the established uranium oxide phase diagram. Reverse Monte Carlo (RMC) modeling of neutron total scattering data was applied in order to characterize oxygen interstitial defect clusters in single-phase UO_{2+x} ($UO_{2.07}$ at 600 and 1000 °C). All RMC models were fit well to all data at all temperatures and length scales. The use of bond valence sum constraints ensured that resultant models were chemically-sensible by limiting uranium valences to expected values. Modeling of stoichiometric UO_2 revealed that no interstitial defect clusters formed, and the material remained fluorite-like up to 1000 °C. Close inspection of UO_{2+x} modeling results demonstrated that oxidation caused the formation of small oxygen defect clusters of varying size. Defect clusters comprised O-O interatomic distances as short as ~2 Å oriented along <111>-type directions. These arrangements shared similar characteristics with defect clusters predicted by density functional theory but were distinct from previously-proposed *Willis*- and *di-interstitial*-type defect clusters. Oxygen defect cluster morphology can greatly impact bulk diffusivity predictions that are critical for multiscale modeling efforts. Therefore, further work is needed in order to lift the discrepancy between experimental and computational defect structure models.

Introduction

General

Elemental uranium exhibits unique physiochemical properties that are driven in large part by the interactions of outer-shell 5*f* electrons. In contrast to the lanthanides and the heavier actinides in which electrons are more tightly bound to atomic nuclei, the lower actinides, such as uranium and plutonium, possess delocalized (itinerant) 5*f* electrons that can interact and participate in bonding. This behavior gives rise to rich yet unexpected phenomena, such as unconventional superconductivity [104, 105], and the dynamic magnetism [106] of Pu. In the presence of ligands (in complexes) or associate elements (in solid state compounds), strong electronic interactions dictate defect stability that ultimately influence important bulk physiochemical properties.

Uranium dioxide (UO_2) is the lowest thermodynamically stable end-member in the uranium oxide system at ambient conditions and finds use as the primary constituent of nuclear fuels. The prevalent use of UO_2 in nuclear fuels is attributable to attractive material properties, such as a high melting temperature, chemical inertness, and the ability of the material to accommodate extraordinary amounts of structural disorder. Beyond these attractive features, however, UO_2 remains difficult to characterize, both experimentally and theoretically.

From a computational point of view, an accurate assessment of UO_2 is challenging because of the effects of strongly correlated electrons. In strongly correlated systems, the strength of the Coulomb interaction among electrons is on the order of, or larger than, the band width of the 3*d*-, 4*f*-, or 5*f*-shells [107]. Thus, there exists a dynamic competition between electron transport and strong on-site Coulomb repulsion between 5*f* electrons. Uranium's electrons are mostly localized and the 5*f* band is narrow meaning that orbital overlap is small. This is problematic for density functional theory (DFT) modeling because first generation functionals, such as the local density approximation (LDA) or generalized gradient approximation (GGA), essentially neglect correlation effects, i.e., all electrons experience the same time- and energy independent potential. As a result, UO_2, which is experimentally characterized as an antiferromagnetic Mott insulator, can be erroneously predicted to be a ferromagnetic metal [108]. Alternative methods, such as patchwork

functionals (e.g., DFT+*U*) and hybrid functionals (e.g., *HSE*), offer promising solutions. However, factors such as anisotropic thermal conductivity [109], low-temperature Jahn-Teller distortion [110], and magnetic ordering [108] further complicate modeling efforts.

Experimental characterization is also difficult owing to factors, such as radiotoxicity and strong catalytic behavior. Indeed, one of the most challenging variables to control is the stoichiometry of uranium oxides [8, 111]. Within the domain of fuel manufacturing and post-reactor storage, the oxidation of UO_2 emerges as both a central theme and a severe limitation. The oxidation of UO_2 to U_3O_8, for example, is concomitant a ~36% increase in volume compared to UO_2. This drastic change in density is problematic because it provides a means for rupturing of the fuel rod sheath, which would result in the dispersion of volatile radioactive fission product elements into the environment. Oxidation of U^{4+} to higher charge states, e.g., U^{6+}, is also of concern because actinides of higher valence exhibit higher solubilities and mobility in groundwater [112].

From a design and engineering standpoint, material modification processes occurring on the meso- and macroscale are of primary interest, as they are most relevant to real-world reactor operation applications [113]. However, processes occurring on the atomic- to microscopic length scales contribute equally to multiscale modeling of the fuel because accurate characterization of these phenomena and underlying microstructural mechanisms yield improved thermodynamic parameters that are critical to bridging the gap between meso- and engineering scales [114-116]. In order to accurately assess and predict the evolution of fuel mechanical properties over operational (reactor) and geological (disposal) timeframes, it is critical to characterize not only prevalent defect morphology in oxidized UO_2, but also the associated defect diffusion kinetics and the role of defect agglomeration (cooperativity) in the gradually evolving $UO_2 \rightarrow U_4O_{9-y} \rightarrow U_3O_7 \rightarrow U_3O_8$ crystallographic ordering motif.

Early studies employing oxygen potential measurements concluded that oxidation of nuclear fuel in pile is negligible, and high burnup and the incorporation of fission products actually results in nuclear fuel becoming slightly *hypo*-stoichiometric (see [117-119] and references therein). This remarkable finding was attributed the incorporation of certain fission products, specifically Mo, and Zr in the fuel cladding that efficiently getter

most of the excess oxygen produced by fission. The case for Mo acting as a buffer was attributed to an apparent saturation of the oxygen potential at high burnup near the oxygen potential for the $Mo + O_2 \rightarrow MoO_2$ reaction. More recent studies, however, showed that the oxygen potential continues to increase past the potential of the Mo oxidation reaction at higher burnups (~100 MWd/kgHM) [120]. This finding indicates that oxidation is not fully buffered by Mo, as previously assumed. It was also concluded that a significant fraction (~25 %) of free oxygen was gettered by the inner surface of the Zr cladding and that the O:U ratio exhibits a radial dependence in which the O:U peaks in the colder rim region and then plummets as the distance to the clad decreases.

The main finding by Walker *et al*. [120] was that the fuel is *hypo*-stoichiometric at very high burnup (~100 MWd/kgHM), but this claim was later refuted. Spino and Peerani [121] used thermodynamic data to re-interpret available oxygen potential data for UO_2 nuclear fuel and concluded that fuel tends to oxidize, not reduce, at high burnup. The shift to a *hyper*-stoichiometric tendency was predicted to occur at ~80 GWd/tM and the maximum O:M ratio was predicted to be 2.001-2.002. The onset of *hyper*-stoichiometric tendency was attributed to saturation of oxygen uptake by the inner surface of the clad and stagnation of uptake by fission product oxidation. Recent post-irradiation examinations provide further evidence to suggest that hyper-stoichiometric U_4O_9 can actually form from fused grain boundaries in the colder rim region of nuclear fuel subjected to power transients [122]. These findings agree with observations of Walker *et al*. [120] and Riglet-Martial *et al*. [123] that indicate that oxygen is thermally transported along the temperature gradient from the hot pellet center to the relatively cold pellet periphery region. More work is clearly needed to elucidate the role and extent of UO_2 oxidation during in-pile operation, especially as it relates to transient, highly non-equilibrium conditions, in order to better predict the effects of oxygen transport on critical nuclear fuel properties, such as fission gas release, which are highly dependent on stoichiometry [124].

Overview of UO_2 Oxidation

Uranium dioxide exhibits several distinct structural and chemical modifications with increasing oxygen ingress. Although the formal terminal member in the uranium oxide

system is UO_3, the final product of UO_2 oxidation in dry air is typically U_3O_8. Between the UO_2 and U_3O_8 endmembers there exist two thermodynamically stable polymorphs: U_4O_{9-y} and U_3O_{7-y} [125]. Traditionally, the oxidation of UO_2 is characterized as a two-step mechanism involving these intermediates in the sequence [126]:

$$UO_2 \rightarrow U_4O_{9-y}/U_3O_{7-y} \rightarrow U_3O_8$$

In the first step, which involves the oxidation of nominally stoichiometric UO_2 to U_4O_{9-y}/U_3O_{7-y}, oxidation exhibits diffusion controlled kinetics with a rate dependence that yields parabolic weight gain behavior [127]. The intermediate phases form on the surface and sub-surface regions, and further oxidation is limited by oxygen diffusion through the U_4O_{9-y}/U_3O_{7-y} product layer [128].

In the second step, oxidation of U_4O_{9-y}/U_3O_{7-y} to U_3O_8 proceeds *via* a nucleation and growth mechanism, which is characterized by a sigmoidal weight gain behavior [129]. The sigmoidal behavior can be rationalized by considering the surface-to-volume (S:V) ratio [130]. At the onset of U_3O_8 formation (i.e., the flat region of sigmoid), the S:V ratio is low. When the product layer reaches a critical thickness, cracking begins. This cracking exposes fresh surfaces where U_3O_8 can nucleate; thus, cracking enhances the rate of oxidation (quasi-linear portion of sigmoid). Oxidation slows when no further cracking can occur and once nearly all of the U_3O_{7-y} has been consumed.

Several parameters are known to influence the oxidation rate of UO_2. These include: temperature, moisture, oxygen partial pressure, dopants, irradiation, material history, grain size, crystallographic orientation, and physical form (*i.e.*, powder, polycrystalline pellet, or single crystal) [131]. Chemical doping by fission products, for example, has been shown to inhibit the onset of U_3O_8. Of the other aforementioned factors, changes in temperature and oxygen partial pressure are perhaps the largest thermodynamic driving forces behind the oxidation of UO_2. Modification of these two factors results a complex phase diagram, which is rich in crystallographic phases. In the following section, the effects of temperature, oxygen partial pressure, and physical form are reviewed in the

context of defects and the evolution of the uranium oxide phase diagram. The investigation of all other parameters is deemed beyond the scope of the proposed study.

Oxygen Ingress and Defect Clustering

In the absence of external modification from pressure, fission, and/or irradiation, the most significant factors influencing the oxidation rate of UO_2 are temperature and oxygen partial pressure, P_{O2}, which is proportional to the oxygen-to-metal (O:M) ratio. There exist an excess of 15 distinct crystallographic phases in the temperature-P_{O2} phase space between the UO_2 and UO_3 endmembers, with the exact number remaining a subject of debate. It is generally understood that structural phase transformations resulting from increasing oxygen ingress are driven in large part by changes in the short-range ordering of oxygen interstitials.

In the simplest case, the oxidation of UO_2 (*i.e.*, increasing the O:U ratio) can result from the incorporation of two predominant defect types: uranium vacancies and oxygen interstitials. Despite this, numerous studies have demonstrated the propensity for the latter defect at low to moderate temperatures. The preference for oxygen interstitial defects in UO_{2+x} was experimentally confirmed by early magnetic susceptibility measurements [132]. Analyses of defect stability performed by *ab initio* and empirical simulations also support this interpretation [133-143]. For example, Bertolus *et al.* found that the formation energies for uranium interstitials and vacancies (5.36 eV and 10.43 eV, respectively) were orders of magnitude larger compared to the formation energy for oxygen interstitials (-0.05 eV) [116]. Large discrepancies are also found when comparing Schottky and anti-site defects to pure oxygen defects. Thus, it is generally understood that the oxidation of UO_2 proceeds primarily through the incorporation of oxygen interstitials with less modification occurring on the uranium sublattice.

In addition to being oxygen-mediated, the oxidation of UO_2 also occurs quite rapidly, even with minimal change in thermodynamic impulse (*e.g.*, temperature). Both experimental (see [125] and references therein) and theoretical [134, 136, 144, 145] studies have shown that the oxidation of UO_2 is an exothermic process —a property corroborated by the reported [146] pyrophoric nature of freshly reduced UO_2. Chemisorption of oxygen

on freshly reduced surfaces occurs readily even at temperatures as low as -183 °C [147, 148]. Chemisorption is predicted to saturate when each surface cation is paired with an adsorbate [147]. This is in agreement with density functional theory (DFT) surface studies that predict the formation of terminal $<U^{6+}\text{-}O^{2-}>$ bonds on UO_2 surfaces for dry oxidation [149, 150]. Upon saturation, it is proposed that excess oxygen coming in contact with UO_2 is first physically adsorbed before being chemisorbed [151].

After dissolution of oxygen, the propagation of oxygen into the bulk is suggested to proceed *via* a non-classical diffusion mechanism in which oxygen interstitials systematically diffuse into the bulk through the occupation of every third layer in the sub-surface region [152]. These experimental results, coupled with complimentary DFT insights [150], indicate that this non-classical (*i.e.*, non-exponential) diffusion originates from a unique charge transfer mechanism between cations and interstitials. Oxygen atoms in the subsurface region diffuse step-wise in order to maximize charge transfer efficiency. At every third layer, oxygen interstitials are each surrounded by ~38 nearest-neighbor uranium atoms that collectively donate a total of ~2 electrons to the interstitial [152]. Once the occupancy of oxygen interstitials at the oxidation front layer reaches ~25%, charge transfer efficiency is decreased. The decrease in charge transfer efficiency provides the thermodynamic driving force for the propagation of oxygen deeper into the bulk.

It is unclear as to what spatial extent this non-classical diffusion is valid. Anderson *et al*. identified a low-temperature (-130–50 °C) sub-surface oxidation mechanism in which the maximum oxygen uptake is approximately four times the oxygen content in the chemisorption layer [153]. Bannister estimated the maximum oxygen penetration depth for this low temperature mechanism to be ~40 Å [154]. Mass oxidation of the bulk likely requires higher temperatures where a second diffusion mechanism (with characteristic onset temperature of ~80 – 180 °C [153, 154]) is dominant. These findings illustrate how unique bonding between uranium and oxygen can dictate the incorporation and diffusion of oxygen.

In addition to altering defect kinetics, strong electronic interactions also influence the stability of defects in UO_2. The fluorite unit cell contains large octahedral holes located at (0,0,½), (0,½,0), (½,0,0), and (½,½,½) (Figure 50). Early studies predicted that oxygen

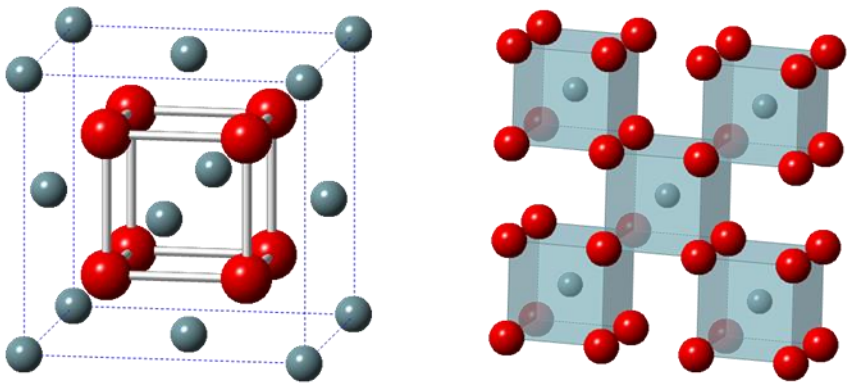


Figure 50: Crystal structure of UO2. The structure is fluorite (space group *Fm*-3*m*) and is composed of interpenetrating FCC uranium (left) and SC oxygen (right) sublattices

interstitials preferentially occupy these holes [155]; however, later studies showed that this is not the case. The earliest efforts to characterize oxygen defects in UO_2 employed reciprocal- and real-space (Fourier) analysis of neutron diffraction measurements [78, 82, 83, 156, 157]. Using hyper-stoichiometric single crystal UO_2 ($UO_{2.12}$) measured at 800 °C, Willis determined that excess oxygen in the fluorite lattice occupies two main interstitial sites. These interstitial types, termed *O*' and *O*'', are displaced by approximately 1 Å along the <110> and <111> directions, respectively, from the octahedral holes in the fluorite structure [78, 156]. This defect model was later revised to include more accurate occupation values [158] and it was found that oxygen interstitials occupy *O'* and *O''* sites in near equal concentrations.

An intuitive description of this cluster can be derived by considering the relaxation of nearby lattice oxygens. This description assumes that the structure first incorporates two *O*' interstitials at adjacent 4*b* octahedral sites in the fluorite structure. As the interstitials relax towards each other along a <110> direction, the interstitials displace two lattice oxygens on the basis of Coulomb repulsion, thus creating two vacancies [159]. The displaced lattice oxygens orient along <111> directions (*O*'' interstitials), thus yielding the so-called "Willis" or 2:2:2 defect cluster. It is now generally understood that dissolved oxygen in UO_{2+x} agglomerates to form complex defect cluster arrangements. The 2:2:2 cluster is just one of many oxygen defect clusters that have been proposed (see, for example, Figure 51). The size, geometry, and arrangement of these clusters directly impacts the phase stability of uranium oxides, and the diffusion of point defects [79, 160-162] and fission products [163-167].

Influence of Defect Clustering on Phase Stability

The temperature-composition phase diagram of the uranium oxide system can be rationalized by considering the coalescence, growth, and evolution of oxygen defect clusters. Figure 52 shows the generally accepted temperature-stoichiometry phase diagram of uranium oxide. The lowest stable end-member in the uranium oxide system under typical pressure-temperature (P-T) conditions is UO_2. As UO_2 dissolves increasing amounts of oxygen, the unit cell parameter decreases linearly with composition following Vegard's law [170, 171]. This decrease in volume with increasing atomic content indicates that the

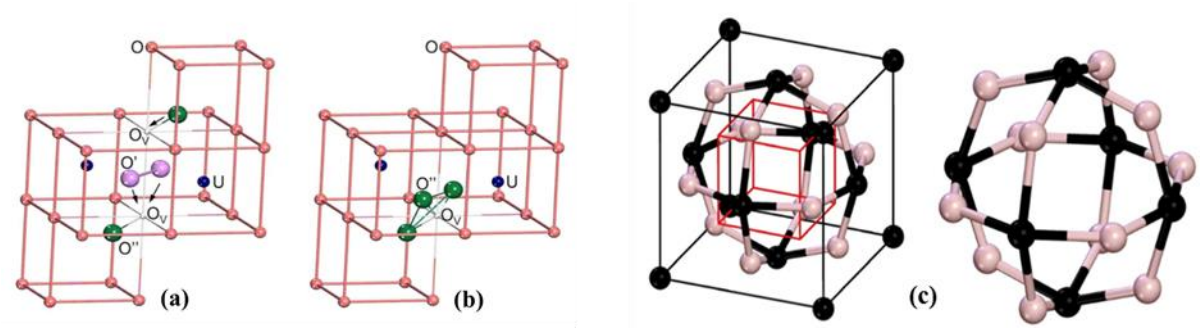


Figure 51: Various oxygen defect clusters proposed for UO2+x. (a) The 2:2:2 cluster is composed of two oxygen vacancies (Ov), two interstitials oriented along <110> (pink), and two interstitials oriented along <111> (green). (b) The split di-interstitial cluster is formed by three interstitials (*green*) sitting on a 111 plane above an oxygen vacancy. (*c*) The cuboctahedral cluster is formed by twelve oxygen interstitials (*pink*) that form a spherical-like cluster inside of the UO_2 unit cell. Figures are adapted from references [168, 169]

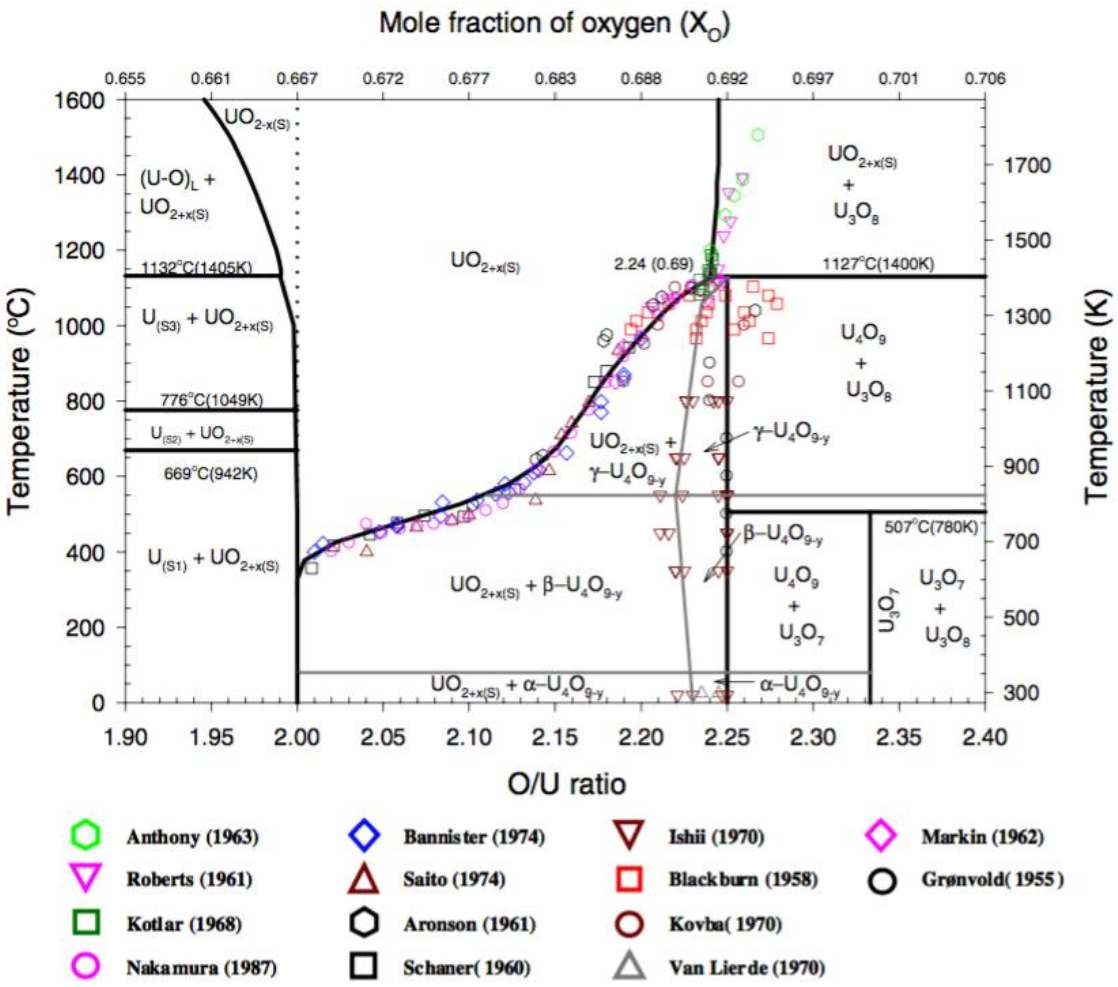


Figure 52: The temperature-stoichiometry phase diagram of uranium oxide. (figure from [173])

interaction between interstitials and the host structure is dominated by attractive chemical potentials rather than mechanical effects, which would lead to volumetric swelling [169]. This is in agreement with findings by Andersson *et al*. [172] that imply that defect stability in UO_{2+x} is a dynamic competition between hybridization, which lowers the band energy, and Coulomb repulsion among ions in the system.

Vegard's law typically fails when approaching the composition $UO_{2.125}$ [170]. The abrupt change in unit cell evolution at this composition has been attributed to the onset of dominance of the U_4O_{9-y} phase, which exists in a mixture with single-phase UO_{2+x} at low temperatures. The U_4O_9 ($UO_{2.25}$) structure is approximated as a 4×4×4 supercell of the UO_2 fluorite unit cell [174] and exhibits three unique polymorphs. The lowest temperature polymorph is rhombohedral α-U_4O_9. This phase transforms to the cubic β-phase at approximately 65°C [175-177]. The β-phase subsequently undergoes an isomorphic transition to γ-U_4O_9 at approximately 550°C [178-180]. Samples of composition U_4O_9 are nearly always non-stoichiometric and it has been suggested [181] that U_4O_9 does not actually exist and should instead be designated as U_4O_{9-y} to reflect the off-stoichiometric nature of the material. (Note: the terms U_4O_9 and U_4O_{9-y} are used interchangeably in this Dissertation).

Beyond U_4O_{9-y}, the uranium oxide system undergoes a cubic-to-tetragonal distortion to reach the composition U_3O_7. As with U_4O_9, U_3O_7 also exhibits a significant range of non-stoichiometry (U_3O_{7-y}) [182]. Early studies reported the existence of two main U_3O_7 polymorphs: α-U_3O_7 and β-U_3O_7, which differ only in *c*/*a* ratio (~0.986 and ~1.031, respectively) [183, 184]. However, the existence of the α-U_3O_7 phase has been called into question [185]. The structures of U_3O_7 and U_3O_{7-y} were reviewed quite recently. These studies suggest that U_3O_7 exhibits only one polymorph and the reported variation in *c*/*a* ratio is attributable to variations in heterogeneous microstrain, stoichiometry, and the spatial arrangement of cuboctahedral oxygen clusters [111, 182].

Further oxidation of U_3O_7 results in biphasic mixtures of U_3O_7 and U_3O_8 in which the amount of U_3O_8 increases at the expense of U_3O_7 [186]. U_3O_8 is the final product that results from the oxidation of UO_2 in dry air. Unlike U_4O_{9-y} and U_3O_{7-y}, the crystal structure of U_3O_8 is less related to its precursors because the local symmetry of U_3O_8 is not based

on the arrangement of octahedral oxygen defect clusters. The U_3O_8 structure is best described as a layered structure that results from the expansion and subsequent shear of the 111-type UO_2 planes. Instead of exhibiting an *ABCABC*... stacking sequence as in the fluorite structure, the atom planes of U_3O_8 exhibit an *AAA*… ordering pattern.

The Dilute Limit

The low O:M regime is the most relevant to in-pile fuel performance modeling because deviations from perfect stoichiometry in fuel are expected to be extremely low (2.001-2.002) at the highest burnup levels [121]. Ironically, less is known about defect cluster arrangements in this low O:M regime (UO_{2+x} for $x < 0.12$) than in the higher O:M regime (UO_{2+x} for $x > 0.12$). This is largely attributable to the diffuse and transient nature of oxygen defects in the former regime. The low O:M regime is dominated by the presence of intrinsic point defects [169] and smaller oxygen clusters, such as split di-interstitials [79, 172, 187-190] and Willis-type clusters [78, 158, 191], which are readily accommodated in the fluorite-type structure.

A growing body of theoretical models exists for oxygen defects in the low O:M regime [79, 142, 145, 168, 169, 172, 187, 189-196], but modern experimental studies remain scarce because of the need for local probe structural characterization techniques. The vast majority of modern experimental work has been performed using Raman spectroscopy [171, 197-200] and X-ray absorption fine structure (XAFS) [201, 202] techniques, which probe vibrational properties and static coordination environments, respectively. Although valuable, many Raman studies [171, 198] rely on the early defect models established by Willis owing to the difficulty in quantitatively interpreting Raman spectra without dedicated *ab initio* models. The dependence on early defect models makes these results more speculative and prone to systematic error because pre-existing defect models, such as the 2:2:2 cluster, have yet to be validated as a stable ground-state defect species by *ab initio* models.

The 2:2:2 cluster proposed by Willis remains the best candidate model for oxygen clusters in UO_{2+x} ($x < 0.12$) for several reasons. First, the model is not based on *a priori* models. The model was derived using experimental measurements of $UO_{2.12}$ at high

temperature. Second, the model is based on fundamental observations from oxygen displacements in stoichiometric UO_2. Willis accurately characterized the structure of UO_2 at room temperature [82] and elevated temperatures [83] and found that lattice oxygens in UO_2 vibrate anisotropically at high temperature. The anisotropic character of lattice oxygen displacements was used to significantly reduce the number of refinable parameters in models in order to derive the 2:2:2 stoichiometry of the Willis cluster [78]. Lastly, the model was reproducible. The 2:2:2 arrangement was experimentally observed a second time using UO_{2+x} crystals of slightly different stoichiometry (x = 2.11, 2.13) at slightly different temperature (~700°C) by Murray and Willis [159] using an analysis technique similar to the method employed by Willis in the earliest study [158].

Despite being the best experimentally-derived model, *ab initio* studies have consistently shown that 2:2:2 clusters (and similar derivatives varying only in the ratio of O'' to O' and O_v) are energetically unstable. Willis-type defect arrangements consistently dissociate into more-stable split di-interstitial clusters (and derivatives varying in the number of O'') upon relaxation despite variations in DFT methods [79, 169, 172, 189, 190, 194, 196, 203]. The instability of the Willis cluster has been attributed to the relatively open structure of the defect. The O' type interstitials are unable to displace lattice oxygens along the <111> directions which allows the O' type interstitials to relax to O'' positions [169]. One study has suggested that Willis-type clusters are instead metastable, low-energy (0.14 eV) transition states that form when split di-interstitial clusters rapidly migrate [189].

Fast migration of oxygen clusters is not limited to Willis-type clusters. Andersson *et al*. [79] showed that split di-interstitials have similar low-energy barriers (0.47 eV). Ichinomiya *et al*. [193] also showed that di-interstitial clusters have lower migration energies than mono-interstitials using temperature accelerated dynamics (TAD). The use of TAD simulations is advantageous because TAD does not require *a priori* knowledge of migration paths. Bai *et al*. [204] probed the kinetics of various cluster types (1-5 interstitials per cluster) with TAD and found that the migration paths of clusters in UO_{2+x} are complex and non-intuitive. They found that migration energy scales with cluster size as $2O_i < 3O_i < 1O_i < 5O_i < 4O_i$. By incorporating the low-energy split-di-interstitial migration mechanism, Andersson *et al*. [79] showed that kinetic Monte Carlo (kMC) diffusivity predictions more

accurately reproduced experimentally-measured diffusivity values for UO_{2+x}. Behera *et al*. [162] also performed a comprehensive study in order to determine the effect of O:M ratio and temperature on the diffusivity calculated from kMC based on DFT-derived parameters and found that the use of more-accurate di-interstitial binding energies, coupled with the lower migration energy of di-interstitial clusters, better replicated the experimentally-observed [205, 206] peak in diffusivity with increasing x in UO_{2+x}.

These results clearly demonstrate how defect cluster morphology strongly influences accurate assessment and prediction of diffusion, fission gas transport, and conductivity mechanisms of UO_2. In this study, various experimental and data modeling schemes were applied to UO_2 and $UO_{2.07}$ in an attempt to elucidate the precise morphology of oxygen defect clusters in UO_{2+x} in the low O:M regime. Experimental data are first assessed by drawing comparisons to pre-established phase diagrams and proposed defect models. A novel, unbiased defect modeling scheme is thereafter introduced and applied to the measured data.

Results and Discussion

Determination of the Oxygen-to-Metal Ratio

Accurate determination of the oxygen-to-metal (O:M) ratios of the UO_2 specimens was critical to obtaining reliable structural models. Calculation of the O:M ratios was performed by two methods. The first method was based on Vegard's law, which predicts that the lattice parameter of a solid solution mixture is proportional to a linear combination of the lattice parameters of the mixture components. Upon oxidation, the unit cell of UO_2 shrinks rather than expanding with increasing oxygen content [126, 127, 170, 171, 207, 208]. At low O:M values (< ~2.10), the decrease in unit cell parameter is approximately linear with increasing oxygen content and is therefore analogous to a Vegard-type prediction. Of the various empirical models reported for UO_{2+x}, the model of Teske *et al*. [208] was used because it has been tested and validated against thermogravimetric analysis and solid electrolyte coulometry (SEC). Teske *et al*. determined that the unit cell parameter of UO_{2+x} is correlated to the O:M ratio by the relation:

$$a = (5.4705 - 0.1306\,x)\ \text{Å}$$

where a is the unit cell parameter of UO_{2+x} and x is the degree of hyperstoichiometry in UO_{2+x}. The cell parameter method was the only means to determine the O:M ratio prior to the neutron total scattering and Raman spectroscopy experiments because there was only a limited amount of sample powder and other O:M determination methods, such as combustion analysis, are destructive. Analysis of the cell parameters based on preliminary XRD measurements performed after synthesis and fabrication of the UO_2 pellets indicated that the O:M ratios of the two UO_2 samples were 1.996(4) and 2.073(3). The unit cell parameters determined from neutron scattering experiments resulted in values of 1.995(4) and 2.068(1). It was assumed that these stoichiometries remained generally constant throughout the sample preparation process and the characterization experiments because the samples were always handled and transported in inert argon atmosphere and were heated in a vacuum furnace during the neutron scattering experiments. Comparison of the lattice parameters derived from neutron diffraction with the lattice parameters derived from XRD showed excellent agreement and provided confidence that oxidation state was preserved between sample synthesis and neutron scattering characterization.

Further validation of the O:M values was achieved by characterizing the UO_2 powders after the neutron scattering and Raman spectroscopy experiments. The second O:M determination was performed using the ignition method. The ignition method was based on ASTM C-1453-00 [11]. In this method, the oxygen content in the starting sample is calculated from the weight gain from oxygen after the starting sample is oxidized to U_3O_8. The main assumption is that the uranium content is the same in the starting (UO_2) and final (U_3O_8) products. Accurate determination of the O:M ratio using this method required quantification of impurity elements because impurity elements can also oxidize and/or out-gas, which contributes to weight changes during oxidization.

The uranium oxide samples were first weighed using a standard laboratory balance to ± 0.1 mg precision and the weights were recorded. The recorded weights from the laboratory balance were defined as the initial weights of the UO_2 samples. The samples were then oxidized to U_3O_8 by heating the powders to 900 °C and holding temperature at

900 ºC for approximately four hours. Ignition of the samples was performed under flowing synthetic air (40 mL/min) with a temperature ramp rate of 3 ºC/min using a TGA/DSC instrument. Prior to increasing the temperature during each TGA/DSC run, the weight of the powder and crucible was stabilized and tared such that the starting mass in the TGA was zero. The TGA/DSC results are summarized and illustrated in Figure 53.

The TGA results showed that both samples exhibited significant weight gains at temperatures in excess of ~350 ºC. The DSC signals confirmed that the large weight gains between ~350-550 ºC were attributable to phase transformations, which appeared as large exothermic events (peaks). Interestingly, the oxidized sample only exhibited only one exothermic large peak whereas UO_2 showed two distinct exothermic events. The two distinct exothermic events of UO_2 are indicative of the $UO_2 \rightarrow U_3O_7$ and $U_3O_7 \rightarrow U_3O_8$ phase transformations.

It was clear that the UO_{2+x} sample fully oxidized to U_3O_8 because the weight change reached steady-state after approximately 7 hours. Therefore, the exothermic event of the UO_{2+x} sample is attributable to a phase transformation to U_3O_8. However, it remains unclear as to why the first peak ($UO_2 \rightarrow U_3O_7$) is absent or drastically suppressed in the DSC measurement of UO_{2+x}. Several studies have shown that the lower temperature peak is greatly affected by sample preparation history. A large suppression of the U_3O_7 peak has been observed in other studies and was attributed to increased disorder [209], specific surface area [210], and increased oxygen content [210, 211]. It's been speculated that the presence of excess oxygen in UO_2 can delay oxidation [210] and/or suppress the $UO_2 \rightarrow U_3O_7$ oxidation step (see Appendix 12 of ref. [211]).

Spark plasma sintering (SPS) was used in the present study to produce dense pellets of UO_2. More work is needed to clarify the relationship between sample preparation methods and the evolution of the DSC signal considering that the SPS method is very unique from the referenced DSC studies of UO_2. Nevertheless, further DSC characterization is outside of the scope of the present study and the measured DSC signals were only used to confirm that the oxidation to U_3O_8 was completed. The TGA signals showed that the onset of saturation in weight gain was concomitant with the completion of the U_3O_8 exothermic event. Both signals showed a slight increase in weight gain between

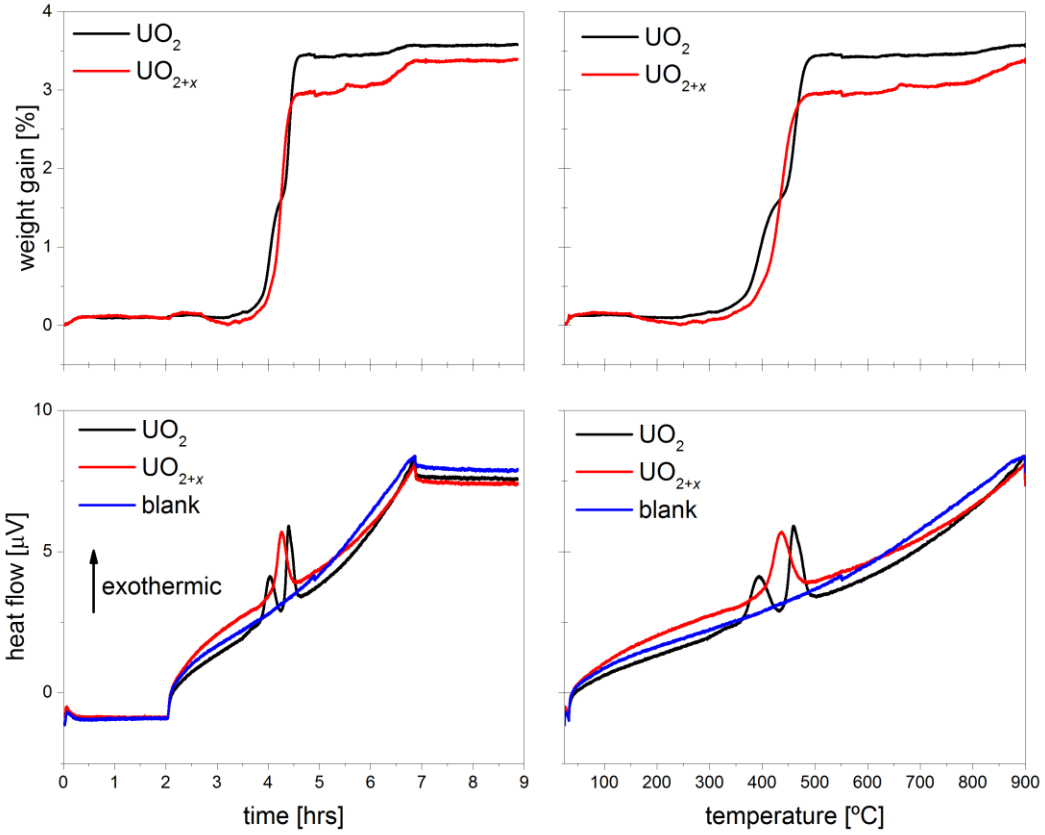


Figure 53: Summary of thermogravimetric analysis results for UO_2 and UO_{2+x} samples. Clockwise from the top left: Weight gain *versus* time, weight gain *versus* temperature, heat flow *versus* temperature, and heat flow *versus* time for both samples. The heat flow measurements are compared to a blank alumina crucible to highlight the strong exothermic peaks of the samples

the 4-hour and 7-hour marks, but both weight gains reached steady state after 7 hours in the TGA. The steady state masses were defined as the final weights of the U_3O_8 end products.

After combustion, the U_3O_8 samples were characterized in order to identify impurity elements. Impurities were detected by ICP-MS and quantified through subsequent data analysis. Twenty non-volatile impurities were quantified after being selected as the most likely candidates to be present in UO_2 [8]. The impurity search was limited to twenty on account of the limited ICP-MS resources available at the University of Tennessee and the high cost required to perform the work using facilities at other institutions. The ICP-MS results are presented in Table 3. The results represent the average of eleven ICP-MS measurements performed on various U_3O_8 samples (*i.e.*, each U_3O_8 powder was sampled several times). The results of UO_2 and UO_{2+x} samples were averaged because both materials were synthesized using the same starting material, both samples were prepared using very similar preparation methods (*i.e.*, using the same laboratory equipment), and both samples were characterized identically. As expected, the impurity concentrations were low and the impurities with the highest concentrations were metallic elements, such as Fe, Ni and Al.

The weight gains from oxidation and the impurity concentrations from ICP-MS were used to calculate the uranium contents of the samples using the equation:

$$U = \left(\frac{\left(\frac{3A}{3A + 8O} \right) \times (W - W \times N)}{I} \times 100 \right) - L$$

where U is the uranium content in weight percent, A is the atomic weight of uranium (237.98 for these samples), O is the atomic weight of oxygen (15.9994), W is the sample weight after ignition in grams, N is the total of the detected non-volatile impurities expressed in grams of oxide per gram of ignited U_3O_8, I is the sample weight in grams prior to ignition, and L is the total of the non-volatile impurities that were not detected (or lower than the detection limit) expressed as a percent. A value of 0.01 % was used for the non-

Table 3: Impurity concentrations in UO_2 samples determined by ICP-MS

element	µg element/g U_3O_8	g element/g U_3O_8	g oxide/g element	g oxide/g U_3O_8
Li	1.280864737	1.28086E-06	2.15	2.75386E-06
Mg	17.4630621	1.74631E-05	1.66	2.89887E-05
Al	10.50969048	1.05097E-05	1.89	1.98633E-05
Cr	1.995079441	1.99508E-06	1.46	2.91282E-06
Mn	1.550252128	1.55025E-06	1.58	2.4494E-06
Fe	69.07446311	6.90745E-05	1.43	9.87765E-05
Ni	10.64639053	1.06464E-05	1.27	1.35209E-05
Co	0.098390567	9.83906E-08	1.41	1.38731E-07
Cu	5.723105783	5.72311E-06	1.25	7.15388E-06
Zn	11.46314077	1.14631E-05	1.24	1.42143E-05
Zr	3.450410368	3.45041E-06	1.35	4.65805E-06
Mo	1.909183368	1.90918E-06	1.50	2.86378E-06
Cd	0.105998414	1.05998E-07	1.14	1.20838E-07
In	0.051961521	5.19615E-08	1.21	6.28734E-08
Sn	38.48192465	3.84819E-05	1.27	4.8872E-05
Ba	0.796962624	7.96963E-07	1.12	8.92598E-07
La	0.054509297	5.45093E-08	1.17	6.37759E-08
Ce	0.025438579	2.54386E-08	1.17	2.97631E-08
Gd	3.100440746	3.10044E-06	1.15	3.56551E-06
Pb	1.3040521	1.30405E-06	1.15	1.49966E-06
			sum:	0.000253401
			standard deviation:	2.37014E-05

volatile impurities that were not detected, in accordance with the recommendation in ASTM C-1453 [11]. Values for the quantified impurity elements (gram of element per gram of U_3O_8) were converted to grams of oxide per gram of U_3O_8 by multiplying each concentration with the corresponding conversion factor (g oxide/g element) shown in Table 3. The sum of the non-volatile impurities measured by ICP-MS was used as the value for *N*. The uranium content in the samples were 88.15 and 87.75 wt% uranium. The calculated O:M ratios based on ICP-MS and TGA analysis were 1.998(47) and 2.075(83). The large uncertainties in the O:M ratios largely stem from the relatively large uncertainty in weight determined from the laboratory balance (± 0.1 mg) as compared to the high precision in weight from TGA (0.01 %; approximately ± 3 µg). The O:M results from both methods are summarized in Table 4.

Pair Distribution Function Simulations

PDFs of UO_{2+x} were simulated using the PDFgui software [23] prior to performing PDF analysis in order to predict how hyper-stoichiometry and oxygen defect clustering would modify the neutron PDF of UO_2. The simulations were performed assuming neutron radiation, an *r*-spacing of 0.01 Å, Q_{damp} = 0.017659, and Q_{broad} = 0.0191822, which are all representative of data collected at the NOMAD beamline at the SNS as of August 2017. Q_{max} was set to 31.4 $Å^{-1}$ in all cases as to match the experimental value. The most commonly used Q_{max} value for standard samples at NOMAD ranges from 31.4 - 35 $Å^{-1}$. Q_{max} = 31.4 $Å^{-1}$ is an optimized value and was used to produce the experimental PDFs.

The PDF of pristine, stoichiometric UO_2 was simulated using *Fm*-3*m* space group symmetry with uranium atoms at the 4*a* site and oxygen atoms at the 8*c* site. In PDFgui, this is performed by placing a uranium atom at the origin (0, 0, 0), an oxygen atom at (¼, ¼, ¼), and populating the unit cell with *Fm*-3*m* symmetry operations. The unit cell parameter for the pristine arrangement was set equal to 5.4705 Å, as suggested by Teske *et al*. [208]. This unit cell can be imagined as a simple cube of oxygen atoms centered inside of a larger FCC cube of uranium atoms as shown in Figure 50a. In this representation, atomic displacements are more easily described with respect to the FCC uranium sublattice. In other situations, it is easier to describe atomic displacements with

Table 4: Summary of O:M values calculated

Sample Name	Method	Time of Measurement	O:M ratio
UO_2	Unit Cell Parameter	Before structural characterization	1.996(4)
UO_2	Unit Cell Parameter	During neutron characterization	1.995(4)
UO_2	ICP-MS/TGA	After structural characterization	1.998(47)
$UO_{2.07}$	Unit Cell Parameter	Before structural characterization	2.073(3)
$UO_{2.07}$	Unit Cell Parameter	During neutron characterization	2.068(1)
$UO_{2.07}$	ICP-MS/TGA	After structural characterization	2.075(83)

respect to the SC oxygen sublattice. This is accomplished by shifting the origin from (0, 0, 0) to (¼, ¼, ¼). This configuration has an oxygen atom at the center (0, 0, 0) and a uranium atom at the (¼, ¼, ¼) site. This alternative unit cell can be visualized as a 2 x 2 x 2 supercell of oxygen cubes with four uranium atoms occupying the center of four alternating oxygen cubes. This representation is similar to the schematic in Figure 50b in which uranium atoms occupy the center of alternating oxygen cubes.

The simulation of the PDF of pristine UO_2 is shown in Figure 54 alongside a histogram of the atomic distance distribution for the identical UO_2 configuration. The PDF of UO_2 only contains two features at real-space distances below ~3.5 Å. These features are the first nearest-neighbor (1-NN) <U-O> peak located at 2.37 Å and the 1-NN <O-O> peak located at 2.74 Å. Clustering of oxygen atoms in UO_{2+x} would result in peaks emerging at the lower *r* region. Therefore, various defect cluster models were tested in order to characterize the low-*r* effects of each defect cluster type on the PDF.

The first defect cluster type tested was the so-called 2:2:2 Willis cluster. This atomic arrangement was constructed following the criteria outlined in ref. [158]. In this configuration, the uranium atoms, lattice oxygens, O' interstitials, and O'' interstitials are located at the 4*a* (0, 0, 0), 8*c* (¼, ¼, ¼), (½, *y*, *y*), and (*x*, *x*, *x*) sites, respectively. The values of both *y* and *x* were first set equal to 0.11 in accordance with the values reported by Willis [158], but were later relaxed. The PDFs were simulated for UO_{2+x} where $x \sim 0.07$ in accordance with the experimental *x* value. This was accomplished in PDFgui by manually adding two interstitials into a 2×2×2 fluorite supercell. The resultant composition was not exactly $x = 0.07$, but rather: $(8\times8 + 2)/(4\times8) = 2.0625$. The multiplier (8) in the latter calculation represents the number of fluorite unit cells in the 2×2×2 supercell. The unit cell parameter was also modified with increasing hyper-stoichiometry in order to replicate the lattice contraction that occurs in UO_{2+x} with increasing oxygen ingress. The change in unit cell parameter was predicted using the linear relation described by Teske *et al*. [208]:

$$a_x = (5.4705 - 0.1306\,x)\ \text{Å}$$

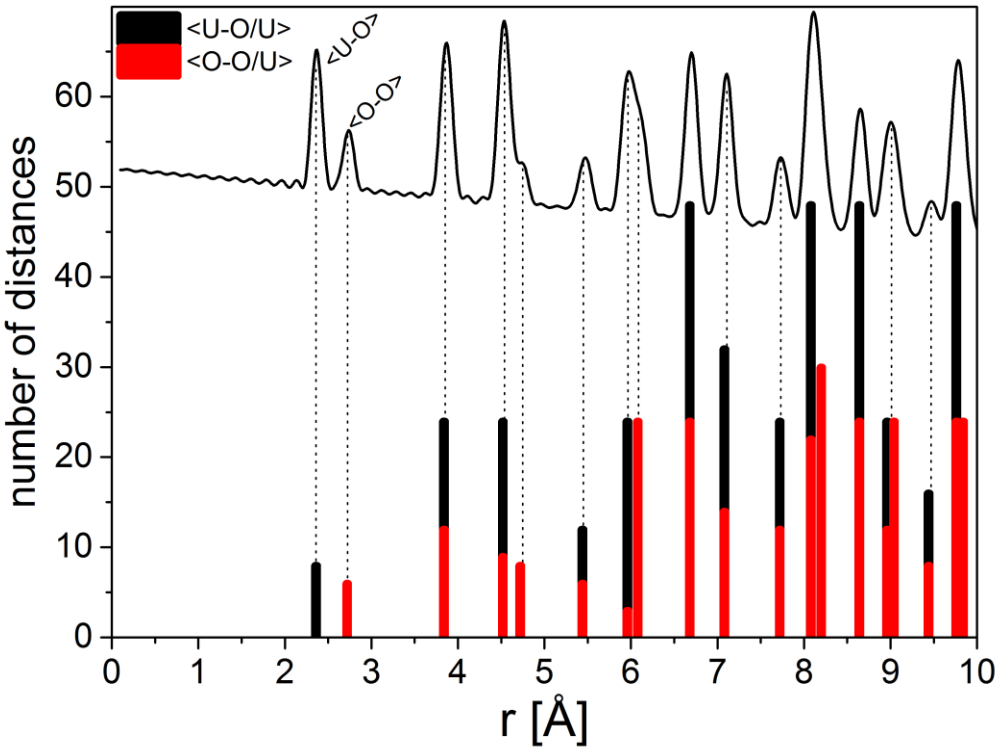


Figure 54: Simulated pair distribution function of pristine UO_2 with Qmax = 35 $Å^{-1}$

where a_x is the unit cell parameter for a certain composition of UO_{2+x}, x is the amount of hyper-stoichiometry, and 5.4705 is the unit cell parameter for stoichiometric UO_2.

Figure 55 shows the simulated PDFs for UO_{2+x} with and without oxygen interstitials in a concentration of: O:M = 2.0625. The oxygen interstitials were arranged in the form of a Willis 2:2:2 defect cluster containing 2 vacant lattice oxygen sites, 2 O'-type interstitials, and 2 O''-type interstitials. The figure shows that hyper-stoichiometry and defect clustering causes the PDF to look very similar to the defect-free PDF. Interstitials residing in special defect cluster sites do not result in additional peaks emerging and they rather contribute mostly to pre-existing peak intensities.

Calculating the PDFs for a system containing split di-interstitial defects yields very similar findings. The top panel of Figure 56 shows the calculated PDF for $UO_{2.0625}$ assuming a split di-interstitial configuration for the two foreign oxygen atoms. The figure is in agreement with the findings for the Willis cluster simulation and shows that the largest changes are predicted to be slight, relative changes in peak intensities and changes in inter-peak intensities (*e.g.*, region between 3 – 3.5 Å). Deconvolution of the PDF peaks appears critical to better understanding how clustering affects the PDF. To this end, the calculation was gradually modified in order to elucidate the precise contribution of defect clusters to overall PDF peak intensities.

Split di-interstitial defect clusters comprise three oxygen interstitials displaced equally along <111> directions from a single oxygen lattice vacancy. This distance, the distance between the vacancy and a single interstitial, was varied in order to highlight the effect of this variable on the resultant PDF. Note: the intensity contribution from the three interstitials was artificially augmented during this analysis in order to highlight small resultant changes. The effects of varying the vacancy-interstitial distance are shown in the top panel of Figure 56. The main finding is that vacancy-interstitial distance needs to lie within a precise range in order to avoid violating the minimum distance requirement, which is that no peaks should occur at r values below ~2 Å where the 1-NN U-O peak terminates. If the vacancy-interstitial distance is too small (black and red PDFs), the minimum distance requirement is violated, and if the distance is too large, the interstitials become too close to neighboring lattice oxygen atoms. A reasonable value lies in-between these extremes and

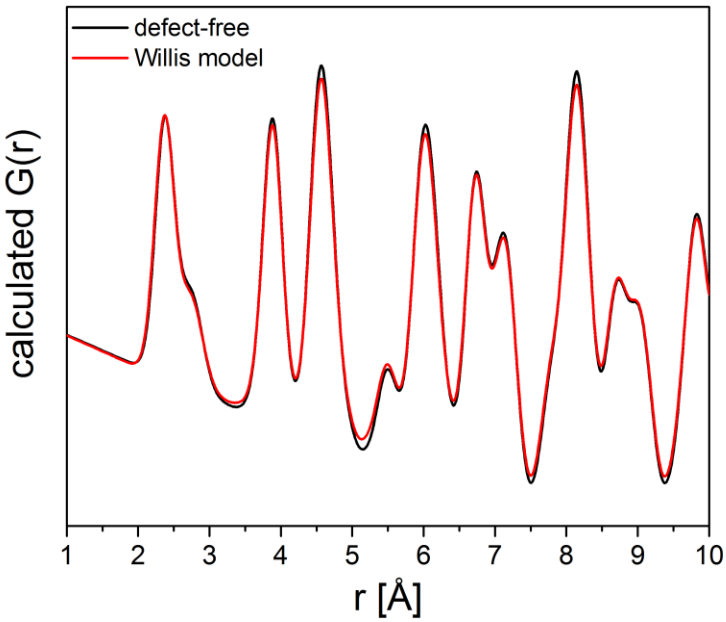


Figure 55: Calculated difference in PDF structure before (black) and after (red) including oxygen interstitials in a Willis 2:2:2 defect configuration

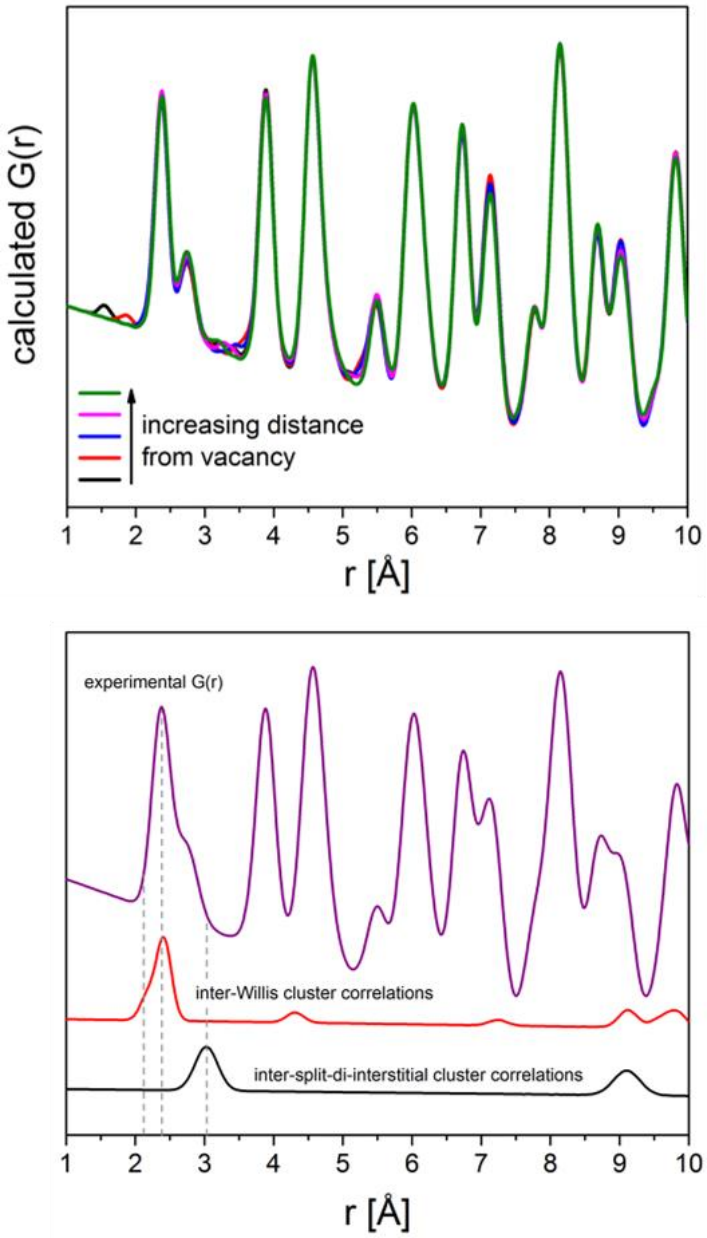


Figure 56: Calculated PDFs for $UO_{2.0625}$ assuming a split di-interstitial defect configuration (top) and the calculated inter-cluster correlations for the two proposed defect models after optimization

results in the 1-NN U-O peak gaining intensity and/or a low-*r* tail depending on the distance magnitude.

The bottom panel of Figure 56 shows the de-convoluted PDF contributions that result only from inter-cluster and intra-cluster oxygen-oxygen correlations. The figure shows that the intensity gained by the 1-NN U-O peak comes from inter-cluster correlations in the case of the Willis cluster. This is in contrast to the split di-interstitial model in which intensity gained by the 1-NN U-O peak comes from interatomic distances between interstitial oxygens and lattice oxygens. This conclusion is inferred from the fact that the first inter-cluster peak occurs at much higher *r* (~3 Å). These observations all show that the effects of interstitials and defect clustering are very small. The small changes in the PDF are mostly masked by other peaks and interpretation of interstitial clustering will rely on accurate accounting of slight, relative changes in peak intensities.

Neutron Diffraction – Average Structure

The average structures of the UO_2 samples were characterized by measuring neutron diffraction at various temperatures. A visual inspection of the diffraction patterns reveals that Bragg peaks are retained up to 1000 ºC, meaning that both UO_2 and $UO_{2.07}$ remain crystalline up to the highest temperature achieved in the present study. Rietveld refinement of the diffraction patterns confirmed that the samples exhibited the cubic fluorite structure (space group *Fm*-3*m*) at all temperatures. Figure 57 shows all neutron diffraction patterns and Rietveld refinement fits for all of the samples at various temperatures. The figure shows the fitted models (*colored curves*) overlaid on the experimental data points. The small intensities of the difference curves (*i.e.*, difference between data and fitted model) demonstrate that both samples are well represented by the fluorite structure at all temperatures.

A close inspection of the diffraction patterns reveals that the Bragg peaks of the two samples are offset in *d*-spacing. Figure 58 shows a comparison of the diffraction patterns of the two samples at the lowest and highest temperatures. The figure demonstrates that the peaks of $UO_{2.07}$ are shifted to lower *d*-spacings at all temperatures relative to the peaks of UO_2. The shift confirms that the UO_2 lattice contracts upon oxidation, which is

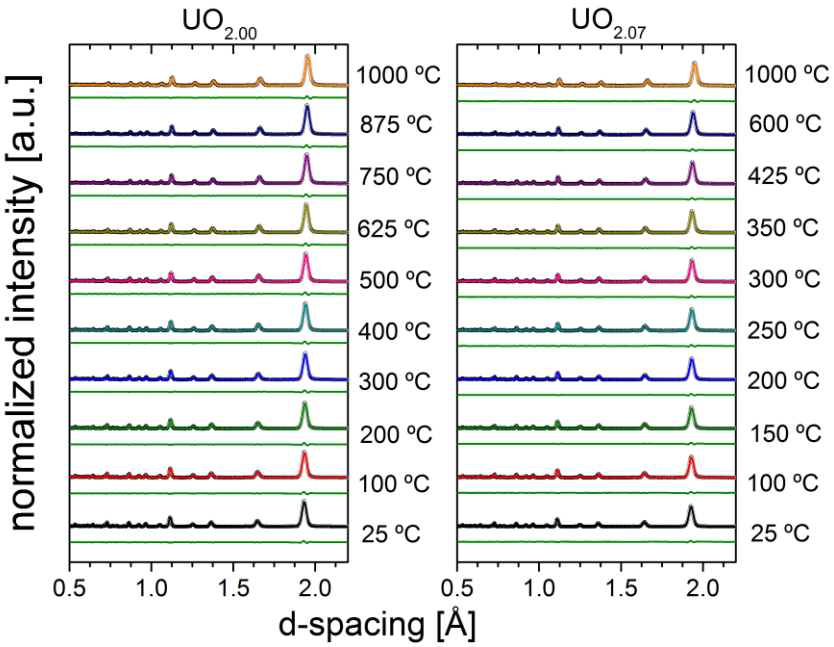


Figure 57: Neutron diffraction patterns of UO_2 and UO_{2+x} at different temperatures. Black circles represent measured data, colored lines denote the fits of the refined fluorite structure models, and the green lines signify the difference between the data and the fitted models.

consistent with previous observations [126, 170, 208]. Within each sample set, the peaks shift to higher *d*-spacings (*i.e.*, swell) with increasing temperature due to thermal expansion. Figure 58 also shows the evolution of the diffraction peaks as the temperature is increased. The peak widths broaden and the background increases with increasing temperature. The dampening of the peak intensities and the increase in background signifies an increase in atomic displacement parameters and diffuse scattering, respectively, as a result of increased thermal atomic motion. The decrease in peak intensity is more severe at the lower *d*-spacings because those peaks are more susceptible to small changes in atomic displacements.

Rietveld refinement of the diffraction patterns yielded accurate determination of the unit cell parameters. A comparison of the cell constants for the two UO_2 materials is shown in Figure 59. Additional cell parameter data from the literature were also included for comparison. Most notable from the figure is the measured value for the UO_2 sample compared to the other data sets (see Figure 59 inset). Recently, there have been attempts to determine the cell constants and fundamental properties of stoichiometric UO_2 with better precision because they are critical input data for computational modeling efforts. Leinders *et al*. [8] performed a comprehensive analysis of stoichiometric UO_2 by rigorously quantifying effects from impurities, stoichiometry, temperature, and instrumental resolution, and obtained a value of 5.47127(8) Å for the unit cell parameter at 20 ºC, which is significantly higher than the value of 5.4704 Å [207], which is the generally accepted value. The value of the lattice constant in the present study also suggests a higher value for perfectly stoichiometric UO_2 following a very similar procedure. The value at 20 °C obtained in the present study was 5.47087(13) Å when derived by extrapolation from the lattice parameter at 100 °C. A smaller value was obtained when extrapolating to 20 °C from the cell parameter value at 34 °C (the lowest temperature data point in the data set). However, the uncertainty in temperature was higher for the 34 °C data point because the thermocouples only read the temperature value of the furnace chamber. If the sample temperature was not yet at equilibrium with the furnace chamber temperature at the time of the measurement, it is possible that the temperature of the sample was actually lower than 34 °C. It was for this reason that the 100 °C data point was also referenced. The time

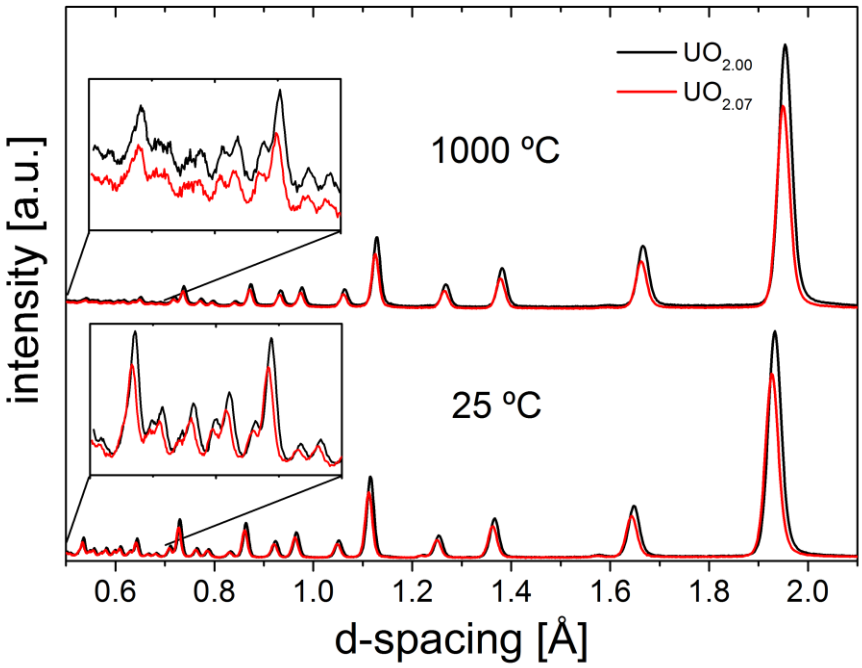


Figure 58: Comparison of neutron diffraction patterns of UO_2 and $UO_{2.07}$ measured at room temperature and 1000 ºC

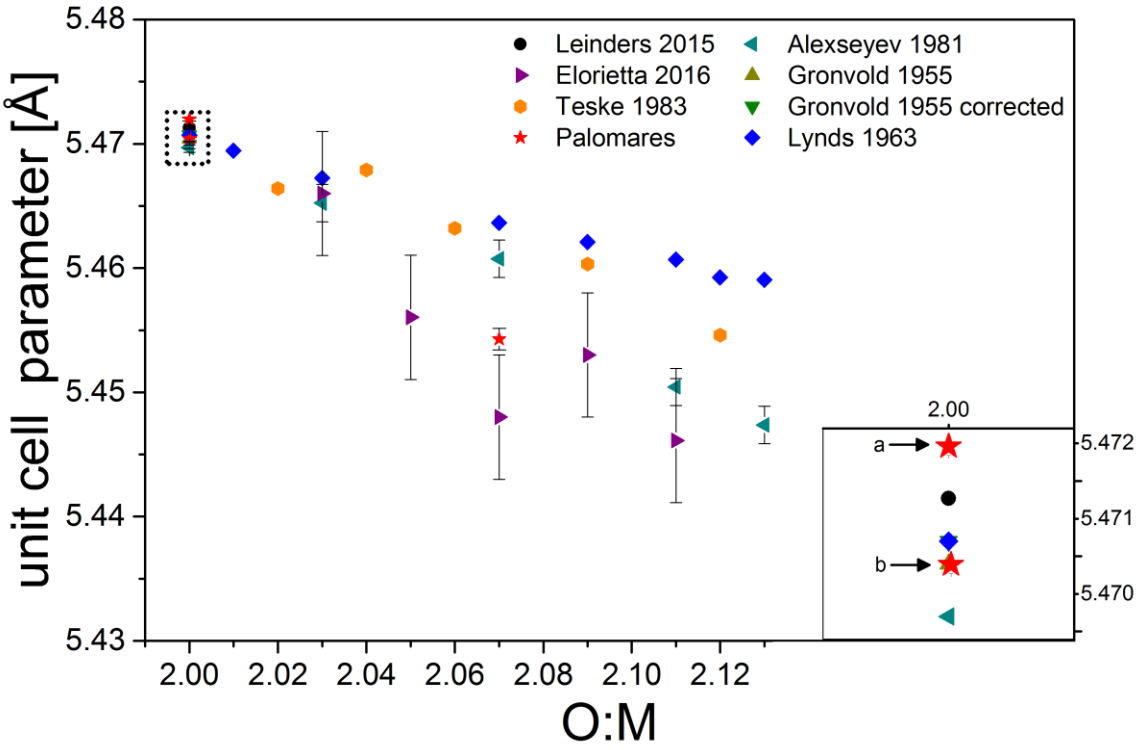


Figure 59: Comparison of uranium oxide unit cell parameters

required to obtain sample temperature equilibrium is much lower at elevated temperatures.

Temperature dependences of the atomic displacement parameters and unit cell parameters were also quantified *via* structural Rietveld refinement of the diffraction patterns. The unit cell data were plotted alongside the cubic polynomial thermal expansion recommendation presented by Martin [212], which was derived by fitting a spline function to twelve independent data sets available in the literature. The equations by Martin for the linear thermal expansion are:

$$L_T = L_{273}(9.973 \times 10^{-1} + 9.082 \times 10^{-6}T - 2.705 \times 10^{-10}T^2 + 4.391 \times 10^{-13}T^3)$$

for 273 K ≤ T ≤ 923 K (0 °C ≤ T ≤ 650 °C), and:

$$L_T = L_{273}(9.9672 \times 10^{-1} + 1.179 \times 10^{-5}T - 2.429 \times 10^{-9}T^2 + 1.219 \times 10^{-12}T^3)$$

for 923 K ≤ T ≤ 3120 K (650 °C ≤ T ≤ 2847 °C) where L_T is the sample length at temperature T in K and L_{273} is the sample length at 273 K (0 °C). Two equations were used to describe different temperature ranges in order to obtain a better overall fit to the data sets. The Martin thermal expansion prediction is often cited as the best current model for the thermal expansion of stoichiometric UO_2 [213]. Improved uncertainty values to the Martin prediction were derived by Fink [214] by incorporating information from three additional data sets that were either excluded by Martin or were unavailable when the Martin prediction was derived.

The unit cell results derived from Rietveld refinement were plotted as fractional changes in length in order to compare the data to the Martin-Fink prediction. The fractional change in length was defined as:

$$\frac{\Delta L}{L_{273}} = \frac{L_T - L_{273}}{L_{273}}$$

where L_T is the isometric unit cell length at temperature T in K and L_{273} is the isometric unit cell length at 273 K (0 °C). The value of L_{273} was determined by extrapolation from the value of L at 100 °C (373 K) using the low temperature (273 K ≤ T ≤ 923 K) instantaneous linear coefficient of thermal expansion (cte) derived by Martin [212]:

$$\alpha_P(l) = 9.828 \times 10^{-6} - 6.930 \times 10^{-10}T + 1.330 \times 10^{-12}T^2 - 1.757 \times 10^{-17}T^3$$

where T is temperature in K and $\alpha_P(l)$ is the instantaneous linear cte in K^{-1}. The value of $\alpha_P(l)$ was 9.754×10^{-6} K^{-1} for T = 100 °C.

The exact partial differential definition of the linear cte is:

$$\alpha_P(l) = \frac{1}{L}\left(\frac{\partial L}{\partial T}\right)_P \approx \frac{1}{L}\frac{\Delta \mathrm{L}}{\Delta \mathrm{T}}$$

Re-arranging this equation yields:

$$\Delta L = (L_T - L_{273}) = \alpha_P(l) \times L_T \times \Delta T = \alpha_P(l) \times L_T \times (T - 273)$$

where $\alpha_P(l)$ is the instantaneous cte at temperature T in K and T is in K. Therefore, the value of L_{273} was defined as:

$$L_{273} = L_T(l) \times \left(1 - \alpha_P(l) \times (T - 273)\right)$$

The calculated value of L_{273} using the value of $\alpha_P(l)$ mentioned above was 5.47089(13) Å based on the unit cell length measurement at 100 °C. Martin [212] also referenced a near-room-temperature cte value of 9.5×10^{-6} K^{-1}. Using this value for the cte yielded a value of L_{273} of 5.47103(13) Å. This value is only mentioned for reference and was not used in plotting and analyzing the present data.

The primary reason for using the 100 °C measurement instead of the room-temperature measurement was to improve accuracy. The lowest-temperature

measurements (denoted as either 298 K or 25 ºC) were performed at near-room temperature; however, the temperature inside the sample environments can vary up to ± 10 °C from the nominal room temperature value of 25 °C depending on the sample environment history. Background measurements were performed at elevated temperature prior to measurement of the samples, which resulted in residual heat in the sample environment at the time of loading of the UO_2 sample. Temperature readings collected during the *room-temperature* measurement indicated a value of 34(10) °C in the sample chamber. However, it's possible that the sample temperature was not yet at equilibrium with the chamber temperature. Temperature measurements were much more accurate at elevated temperatures (≥100 °C) because the furnace temperature was explicitly set during the experiment. The sample temperature was also more likely to reach equilibrium at elevated temperatures where temperature fluctuations were minor. As a result, the value of L_{273} was determined by extrapolation of the 100 ºC measurement rather than extrapolation from the ambient temperature measurement.

Figure 60 shows the measured thermal expansion data of UO_2 plotted alongside the Martin-Fink model. The figure illustrates the evolution of the theoretical sample volume with increasing sample temperature and shows that the measured thermal expansion of UO_2 was higher than the established prediction. The trend was nearly identical even when the value of L_{273} = 5.47103(13) Å was used (*not shown*). Most recently, Guthrie *et al*. [215] reported a systematic offset of UO_2 thermal expansion data to higher values relative to the Martin prediction using synchrotron XRD (see Figure 60). The data of Guthrie *et al*. were collected at higher temperatures approaching the melting point of UO_2; therefore, they are complimentary to the lower-temperature data presented here. The data of Guthrie *et al*. [215] exhibit a linear thermal expansion offset of ~0.2-0.3 % from the Martin-Fink prediction and lie on the upper bound of uncertainty. The neutron data are in agreement with the trend, as the data also lie on the upper bound of uncertainty. At higher temperatures, the data fall back to within the bounds of uncertainty of the Martin-Fink model. Guthrie *et al*. [215] attributed the higher rate of thermal expansion to the improved resolution attained when using state-of-the-art instruments, such as third-generation synchrotron sources, as compared to the measurement techniques used to derive the

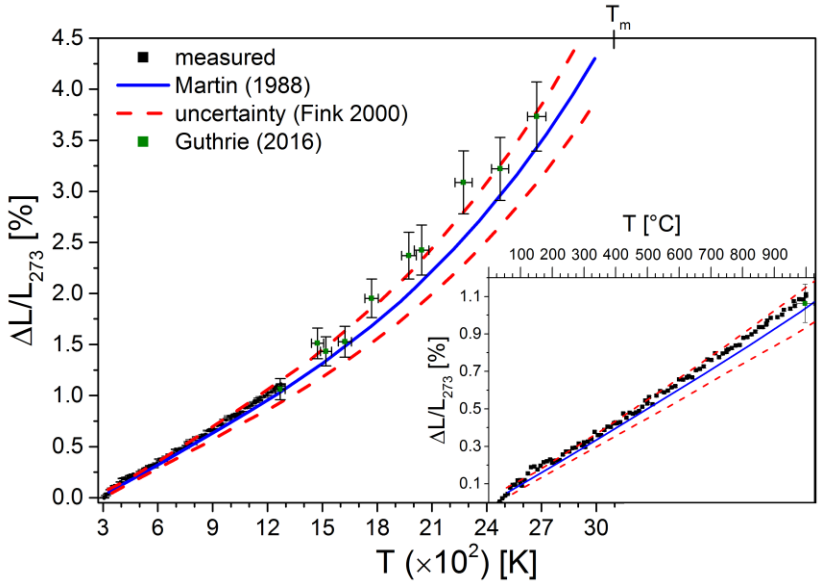


Figure 60: Measured thermal expansion of UO2

standard reference materials.

The unit cell constants were derived assuming full stoichiometry at all temperatures. In order to account for the effect of partial reduction of UO_2 to UO_{2-x} on the unit cell parameter, the Rietveld analysis was repeated with the oxygen site occupancy as an added refinement variable. The analysis showed that the maximum change in unit cell parameter at any temperature was 0.00038 Å and the refined O:M ratio at 1000 ºC was 1.96(2). Consideration of these changes yielded a negligible change to the observed offset in the linear thermal expansion.

Martin [212] also investigated the effect of hyper-stoichiometry on the thermal expansion behavior of UO_2 and concluded that the thermal expansion of UO_{2+x} is nearly identical to the thermal expansion of UO_2 for x = 0-0.13 to temperatures as high as 1247 °C. Following the procedure outlined for UO_2, the value of L_{273} was estimated to be 5.45489(89) Å assuming an identical linear cte at 100 °C as for UO_2. Figure 61 shows the measured linear thermal expansion of UO_{2+x} compared to that of UO_2. Within experimental uncertainty, the data below ~650 °C were in agreement with Martin's assessment that the thermal expansion behaviors of UO_2 and UO_{2+x} are identical. Above ~650 °C, the linear thermal expansion of UO_{2+x} was higher than that of UO_2. It was unclear if the offset in thermal expansion is temperature-dependent or athermal at higher temperatures due to the lack of data above 1000 °C. UO_{2+x} also shows higher thermal expansion compared to the Martin-Fink model.

Further information regarding the temperature evolution of the fluorite structure was obtained by inspection of the atomic displacement parameters (ADPs). The ADP, often denoted as U, represents the average atomic displacement of an atom from the ideal site of the atom in the lattice, *i.e.*, $U = \langle u^2 \rangle$, where u is an instantaneous atomic displacement distance in Angstrom. The symmetry of the fluorite structure dictates that the ADPs of uranium and oxygen are isotropic ($U_{11} = U_{22} = U_{33}$; $U_{12} = U_{13} = U_{23} = 0$). In other cases in which the structure is not fluorite, ADPs can also be modeled as anisotropic ($U_{11} \neq U_{22} \neq U_{33} \neq U_{12} \neq U_{13} \neq U_{23}$). Figure 62 shows the evolution of the UO_2 isotropic ADPs with increasing temperature. The measured ADPs of UO_2 are plotted alongside ADP values reported by Hutchings [216] and Willis [83] for comparison.

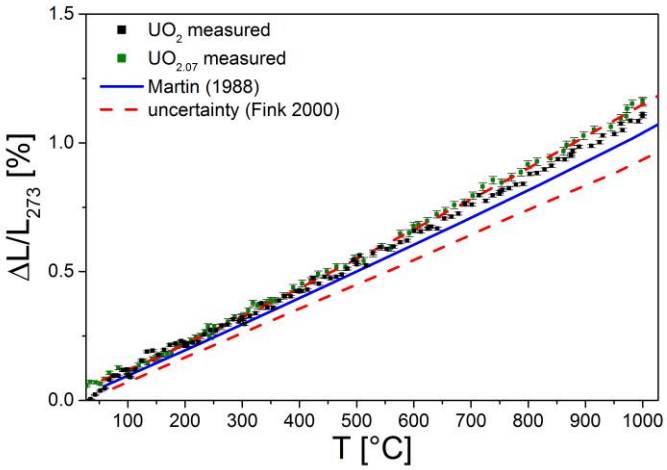


Figure 61: Comparison of thermal expansion of UO_2 and UO_{2+x}

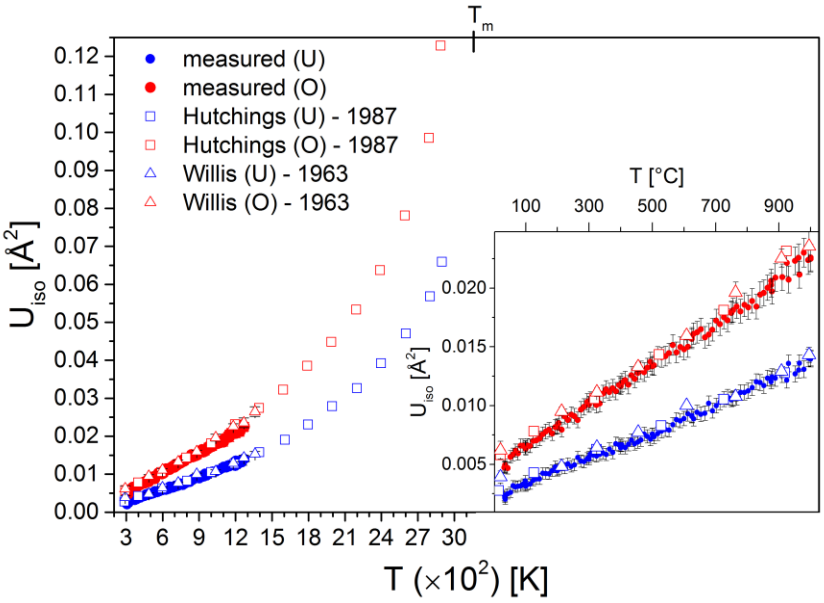


Figure 62: Evolution of the UO_2 atomic displacement parameters

The measured ADP values for both uranium and oxygen were in agreement with reported values at all temperatures within experimental uncertainty. Close agreement between the three datasets independently validated the measured temperatures [215]. Analogous to the thermal expansion behavior, the evolution of the UO_2 ADPs was different from that of UO_{2+x}, albeit at lower temperatures. A comparison of the ADPs between UO_2 and UO_{2+x} is presented in Figure 63.

The ADP values and the trends were very similar among the two materials. The ADPs of the oxidized sample were slightly offset to higher values, but were indistinguishable at most temperatures within experimental uncertainty. The largest discrepancy occurred at the lowest temperatures. Between room temperature and approximately 100 °C, the ADP values of $UO_{2.07}$ appear significantly higher than the corresponding ADPs of UO_2.

Crystallographic, *i.e.*, Rietveld, analysis determines the *distribution* of positions of atoms where the width of the distribution is defined as the ADP [217]. Therefore, an ADP comprises contributions from both static atomic displacements (*i.e.*, different atom positions) and dynamic atomic displacements (*i.e.*, thermal atomic vibration). Considering that temperature evolution of atomic vibrations is typically well-behaved near and above the Debye temperature (~125 °C for UO_2), the abrupt shifts in ADP values were attributed to changes in the quasi-static atomic arrangement. The shifts in ADP at low temperatures are attributed to the $UO_{2+x(S)}$+α-U_4O_9 → $UO_{2+x(S)}$+β-U_4O_9 phase transition, which occurs at ~80 °C (see [173] and references therein). Differential analysis of the uranium and oxygen ADPs suggest that the phase transition occurs between 75-100 °C in the $UO_{2.07}$ sample, which was in agreement with the reported temperatures. Rietveld analysis showed no indication of a secondary U_4O_9 phase in the measured diffraction patterns. This indicates that the ADP analysis is quite robust and sensitive to very small changes in atomic arrangements.

A second notable feature in Figure 63 is the decreased difference between the oxygen and uranium ADPs of UO_2 and $UO_{2.07}$ at ~600 °C. Although the changes are within experimental uncertainty, a close inspection reveals that the ADPs of both samples begin to overlap between ~600-700 °C. Analogous to the low temperature shift, the change may

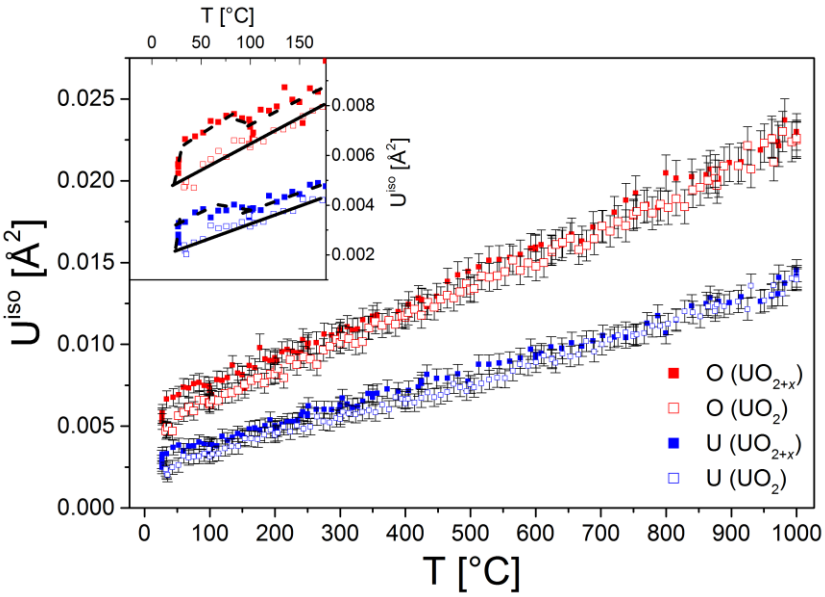


Figure 63: ADPs of UO_2 and UO_{2+x}

be attributed to the $UO_{2+x(S)}$+β-U_4O_9 → $UO_{2+x(S)}$ phase boundary. That the feature is less prominent than for the $UO_{2+x(S)}$+α-U_4O_9 → $UO_{2+x(S)}$+β-U_4O_9 phase transition indicates that thermal (*i.e.*, dynamic) contributions to the ADP are higher. Differential analysis in this case was less useful because the differences between the UO_2 and $UO_{2.07}$ data are very small. The suggested phase temperature of 600-700 °C, is higher than the transition temperature predicted for $UO_{2.07}$ [173]. A phase transition temperature of ~600 °C corresponds to an O:M ratio of ~2.12 based on the established phase diagram.

The ADPs shown in Figure 63 were derived from Rietveld refinement of two-minute measurements that were collected sequentially during the experiment. In order to obtain more accurate ADP values, only the neutron diffraction patterns from the thirty-minute measurements were used. Thirty-minute measurements were performed at room temperature and 100, 200, 300, 400, 500, 625, 750, 875, and 1000 °C for UO_2 and at room temperature, 100, 150, 200, 250, 300, 350, 425, 600, and 1000 °C for $UO_{2.07}$. The ADPs from Rietveld refinements of these data are shown in Figure 64. The data collected for 30 minutes yielded ADP values with much smaller error bars. In most all cases, the error bars in Figure 64 are no larger than the data points. Inspection of these data showed that the ADP values for both samples clearly converge above ~600 °C for both datasets. It was not possible to distinguish a finite transition temperature because the two data sets were collected at slightly different temperatures. The information in Figure 64 indicates that the transition temperature lies between 400-600 °C, as would be expected for $UO_{2.07}$.

More extensive modeling of the ADPs was performed in order to validate the apparent phase transformations. Lattice vibrations were described using both Debye and Einstein approximations. In the Debye representation, atomic vibrations are modeled as confined phonons. It follows that there is a finite number of phonon states because the phonon frequency cannot be infinite with this assumption. Analyses invoking the Debye model often cite the Debye temperature of the solid. Simply, the Debye temperature corresponds to the excitation frequency for the highest frequency mode. All modes are therefore exited at the Debye temperature. The reported Debye temperatures of UO_2 typically lie in the range between 100-125 °C (375-395 K) [83, 218, 219].

Derivation of the Debye temperature from ADPs is typically considered doubly

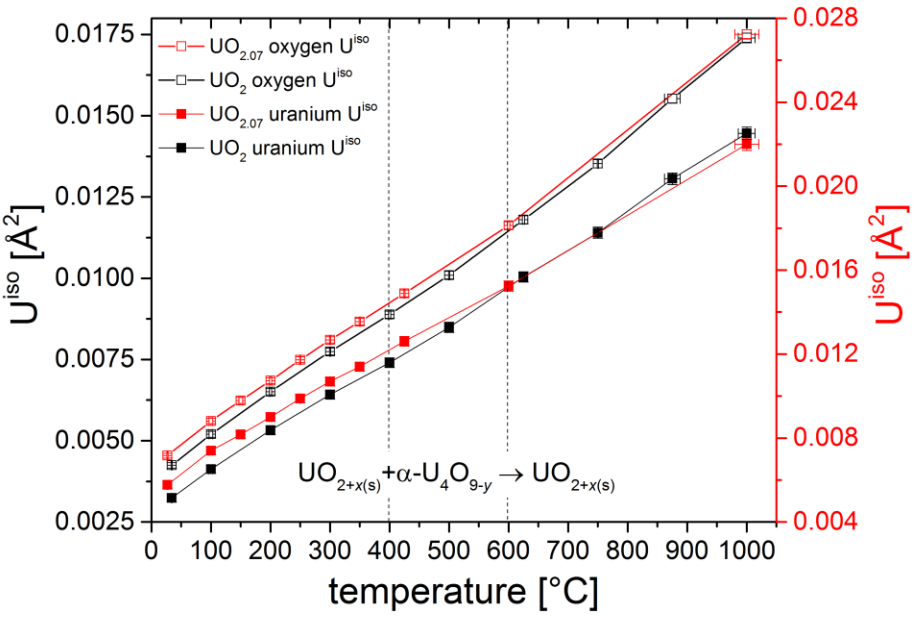


Figure 64: Temperature evolution of isotropic atomic displacement parameters of UO_2 and $UO_{2.07}$ from Rietveld refinement of high-resolution diffraction patterns

approximate because Debye theory itself is approximate and Debye theory only applies to monatomic crystals [83]. However, it's been shown that Debye theory is relatively accurate in describing well-behaved systems and simple ionic crystals. Fitting the ADPs for UO_2 using the reduced temperature, which accounts for the changing volume of the system (thermal expansion) [83], yielded a Debye temperature of ~385 K (125 °C), in agreement with reported values. Debye theory was also used to predict the temperature evolution of the ADPs. A large deviation from the Debye prediction can often indicate the presence of static atomic disorder that results from either a phase transformation or some small shift in the local arrangements of atoms.

In the Debye representation, the temperature evolution of the ADPs was calculated according to the expression:

$$\langle u^2 \rangle_T = \frac{3\,\hbar^2\,T}{M\,k_B\,\theta_D^2}\left[\varphi\left(\frac{\theta_D}{T}\right) + \frac{1}{4}\frac{\theta_D}{T}\right] + A$$

where:

$$\varphi(x) = \frac{1}{x}\int_0^x \frac{x'}{e^{x'} - 1}\,dx'$$

and where $\langle u^2 \rangle_T$ is the isotropic ADP at temperature *T*, $\hbar$ is the reduced Planck constant, *T* is temperature, *M* is the mass of the vibrating atomic species, k_B is the Boltzmann constant, θ_D is the Debye temperature of the solid, *A* is the arbitrary offset constant that accounts for intrinsic static disorder in the system. Since the ADPs are typically well behaved above the Debye temperature (100-125 °C), the Debye model was fit to the ADPs in the range 100-400 °C where no phase transformations were expected. Because of this, it was not possible to model the $UO_{2+x(S)}$+α-U_4O_9 → $UO_{2+x(S)}$+β-U_4O_9 phase transformation, which occurs at low temperature (~80 °C). However, any deviations in ADP behavior that occur at high temperature as a result of the $UO_{2+x(S)}$+β-U_4O_9 → $UO_{2+x(S)}$ phase transformation should appear as a constant offset in the *y*-axis (magnitude of ADP).

The fitting results showed that the Debye prediction is indeed capable of revealing the small change in ADP behaviors at high temperature. Figure 65 shows the ADP values of uranium and oxygen from Rietveld refinement plotted against the fitted Debye ADP prediction. The main finding was that the uranium and oxygen sublattices respond differently and at different rates to the $UO_{2+x(S)}$+β-U_4O_9 → $UO_{2+x(S)}$ phase transformation. The uranium ADPs of UO_2 and $UO_{2.07}$ showed very different behavior. The ADPs of UO_2 were well represented by the Debye model at all temperatures whereas the ADPs of $UO_{2.07}$ begin to deviate from the Debye prediction at ~400 °C.

The deviation from the Debye prediction occurs at a temperature that is near the $UO_{2+x(S)}$+β-U_4O_9 → $UO_{2+x(S)}$ phase boundary. The measured magnitudes of the high temperature (400-1000 °C) ADPs are lower than expected from the Debye prediction. This indicates that there is a change in the uranium arrangements that lowers the amount of static disorder in the material. It is certainly possible that the change is attributed to the $UO_{2+x(S)}$+β-U_4O_9 → $UO_{2+x(S)}$ phase transition because the transition results in a single phase instead of two. This would decrease the overall microstrain associated with $UO_{2+x(S)}$/β-U_4O_9 domain boundaries and the small uranium displacements that accompany the change in the local uranium environment in the β-U_4O_9 phase. The β-U_4O_9 phase exhibits cuboctahedra in the local environment and the transition between α-U_4O_9 and β-U_4O_9 phases is characterized by changes in short U-U and cuboctahedron U-O distances [220]. It's expected that a transition from the β-U_4O_9 phase to a mono-$UO_{2+x(S)}$ phase also results in changes in U-U and U-O distances.

Contrary to the $UO_{2.07}$ uranium ADP behavior, the oxygen ADPs significantly increase at high temperature. The ADP trends for both UO_2 and $UO_{2.07}$ showed a similar trend, although the deviation from the Debye prediction was clearer for the UO_2 dataset because the data points were more evenly spaced out. Both datasets indicated that the oxygen ADPs deviated from the Debye prediction above ~600 °C. Increases in static disorder (*y*-axis offsets) in both materials were attributed to increases in oxygen Frenkel defects. Analysis of the UO_2 site occupancies showed that the 8*c* site occupancy decreased beginning at 750 °C. This is precisely the temperature at which the UO_2 oxygen ADP started to deviate from the Debye prediction. Increased thermally-induced anti-Frenkel

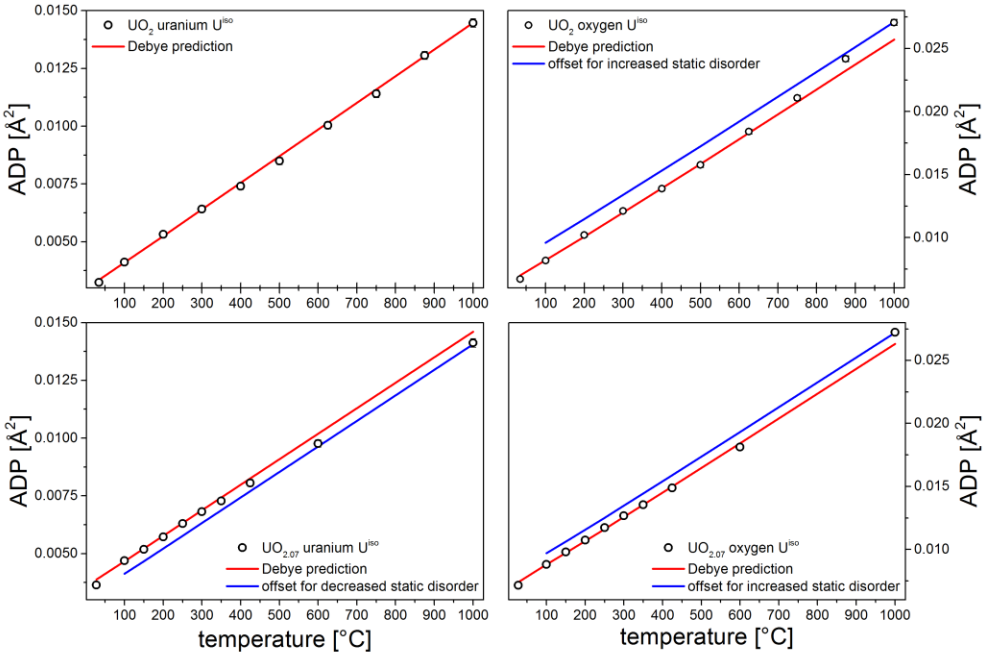


Figure 65: Comparison between Rietveld ADP values and Debye predictions

disorder is also likely for $UO_{2.07}$, as it might explain why the offset appears smaller for $UO_{2.07}$ than for UO_2. Although thermally-induced anti-Frenkel disorder occurs in both materials, the effects are more suppressed in UO_{2+x} because the system already contains an excess of oxygen, which might lead to increased anti-Frenkel recombination, whether it be correlated of uncorrelated recombination. As such, it was not possible to unambiguously determine if the deviations in oxygen ADP behaviors around 600 °C were attributed to the $UO_{2+x(S)}$+β-U_4O_9 → $UO_{2+x(S)}$ phase transition or increased anti-Frenkel disorder. The results suggest that the increase was a result of thermally-induced anti-Frenkel disorder rather than the $UO_{2+x(S)}$+β-U_4O_9 → $UO_{2+x(S)}$ phase transition.

Raman Spectroscopy – Local Structure and Vibrational Properties

Raman spectroscopy was performed in order to gauge the microscopic oxidation level of the samples and to probe local distortions caused by point defect accumulation and oxygen defect clustering. Raman spectroscopy is extremely sensitive to modifications of the oxygen sublattice because it probes atomic vibrations and associated polarization processes that are largely caused by oxygen atoms, which are much lighter and mobile in comparison to heavier uranium cations. Raman spectroscopy is oftentimes more sensitive to local oxygen sublattice disorder in fluorite-structured oxides in comparison to neutron total scattering. However, Raman spectra are much more difficult to model and interpret compared to neutron total scattering. As such, the high sensitivity of Raman spectroscopy and the modeling capability of neutron total scattering data can be quite complimentary when used in tandem.

Several particles of the two UO_2 samples were loaded into a custom-built aluminum containment box in a glove bag filled with argon gas. The sample container was sealed air-tight in the inert gas atmosphere and the Raman spectra were collected in backscattering geometry though the borosilicate glass window on the box. The Raman spectra of UO_2 are sensitive to both the excitation wavelength and laser power used. UO_2 exhibits an absorption edge at ~2 eV [221]; therefore, resonance Raman features arise when utilizing excitation sources of energies higher than 2 eV [222]. These resonance features have been attributed to forbidden Frölich LO(Γ) scattering [222]. In order to avoid the emergence of

resonance Raman features in the spectra, the samples were probed using a 785 nm (1.58 eV) red diode laser.

The Raman spectra of uranium oxides are also sensitive to the excitation laser power. Highly energetic laser radiation can oxidize UO_2 and artificially induces the appearance of defect peaks in the spectra. Correspondingly, the laser power was limited to 1 mW during the experiments. A value of 1 mW was chosen based on values of 0.5-1 mW commonly reported in the literature for UO_2 studies [171, 223, 224]. The prevention of oxidation effects in the UO_2 samples was verified during the experiments by monitoring the time evolution of the Raman measurements and confirming that the spectra did not change after repeated measurements using 1 mW laser power.

Figure 66 shows a comparison of the Raman spectra of UO_2 and $UO_{2.07}$. The spectra were both normalized relative to the highest intensity peak. The common features in both samples are the peaks at ~445 and ~1150 cm^{-1}. The peak located at ~445 cm^{-1} represents the lone Raman-active mode of UO_2. This peak is typical of fluorite-structured oxides and is attributed to the triply-degenerate T_{2g} (or F_{2g}) mode representing the vibration of oxygen atoms (with O_h symmetry) in anti-phase around the central uranium atom [197, 225-227]. The second peak at ~1150 cm^{-1} was originally attributed to electronic scattering characteristic of a $\Gamma_5 \rightarrow \Gamma_3$ crystal field transition [228-230], but has more recently been attributed to a resonance feature representing the second overtone of the α_3 LO band that appears at ~575 cm^{-1} and grows in intensity with increasing excitation energy [222]. Manara *et al*. [197] have suggested that the 1150 cm^{-1} peak can be regarded as a signature of a quasi-perfect fluorite structure due to the observation that the peak intensity diminishes with increasing oxidation level. This hypothesis was recently confirmed by a systematic Raman spectroscopy study of $UO_2 \rightarrow U_4O_9$ oxidation mechanisms [171]. The similarity in the peak at 1150 cm^{-1} before and after oxidation suggests that the $UO_{2.07}$ sample retains highly cubic character after incorporation of oxygen interstitials.

The main differences between the spectra of UO_2 and $UO_{2.07}$ are the blue-shift of the T_{2g} peak, the asymmetric broadening of the T_{2g} peak to the high frequency side, and the increase in intensity of a defect band between ~500 and 700 cm^{-1}. The shift and asymmetric broadening of the T_{2g} peak to higher frequencies with increasing O:M ratio has

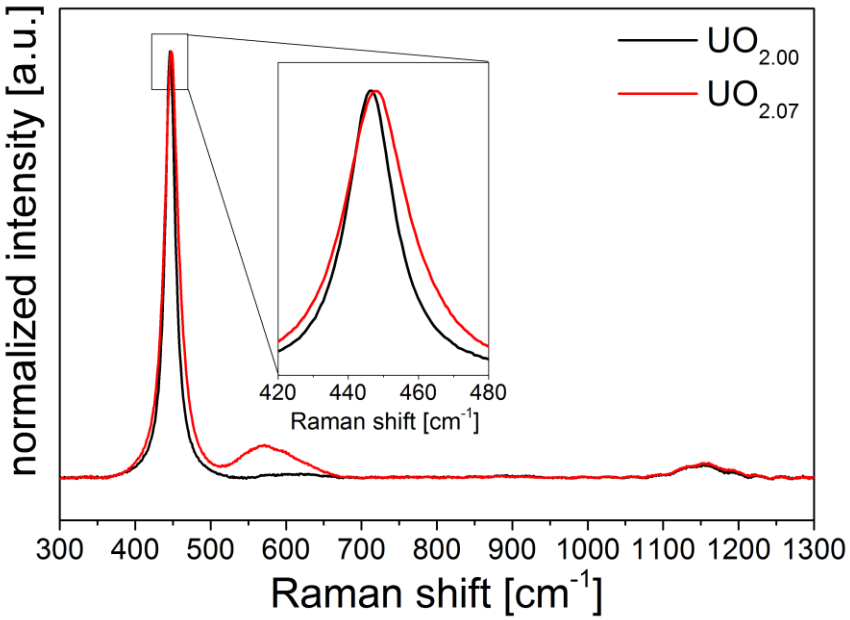


Figure 66: Comparison of Raman spectra of UO_2 and UO_{2+x}

been observed by several researchers [171, 197, 198, 200]. Intuitively, the blue-shift of the T_{2g} peak indicates that U-O bonds stiffen. Assuming the lattice retains the same dimensions or shrinks (as is the case for UO_{2+x}), the T_{2g} up-shift is in agreement with the bulk incorporation of oxygen interstitials, which results in closer atomic packing, shorter interatomic distances, and more rigid or correlated atomic motion.

He & Shoesmith [198] decomposed the asymmetric T_{2g} peak of UO_{2+x} into two peaks (a main peak at 445 cm^{-1} and a minor secondary peak at ~470 cm^{-1}) noting that the secondary peak is analogous to a defect peak in rare-earth element doped ZrO_2 that is characteristic of tetragonal symmetry. He & Shoesmith [198] correlated the secondary 470 cm^{-1} peak to the O:M ratio meaning that the asymmetric broadening of the T_{2g} peak is associated with the distortion of cubic symmetry caused by the incorporation of oxygen Frenkel defects and defect clusters. The defect band observed between ~500 and 700 cm^{-1} is often the most telling feature of UO_2 oxidation. As is common practice, the broad band was decomposed into several individual peaks.

Oxidized UO_2 typically exhibits only two peaks in this region [171, 198, 223] whereas the spectra of irradiated UO_2 [224, 231-236] and doped UO_2 [237-243] often show three or more peaks. The defect peaks are normally located at ~530, 575, and 630 cm^{-1}, but often shift depending on the O:M ratio and/or amount of lattice distortion caused by irradiation or doping. The two Raman spectra were fit with various peaks in order to de-convolute the defect band and compare the defect peak positions with the values reported in the literature. The UO_2 spectrum was only fit with one peak in order to determine the position of the peak. It was assumed that the intensity of the defect band of the UO_2 sample was negligible compared to the $UO_{2.07}$ sample. The $UO_{2.07}$ spectrum was fit following the procedure of He & Shoesmith [198] and Elorrieta *et al*. [171]. The defect band was fit with two peaks that were initially centered at 575 cm^{-1} and 630 cm^{-1}. The T_{2g} peak was only fit with one peak instead of two because the asymmetry was not strong enough to require the secondary peak at ~470 cm^{-1}. Both spectra were fit with Lorentzian peak profiles after testing confirmed that the use of a Pseudo-Voight profile (a convolution of Gaussian and Lorentzian profiles) does not significantly alter the results.

The fitting results revealed that the T_{2g} peak of the UO_2 sample was located at ~445 cm^{-1}, which is in agreement with literature values. The position of the T_{2g} of $UO_{2.07}$ was shifted by ~2 cm^{-1} to 447 cm^{-1}. A comparison of the peak widths (16.2 and 21.4 cm^{-1}) demonstrated that the peak broadened by ~30 % after oxidation. Figure 67 illustrates the peak fitting results for the $UO_{2.07}$ sample. A close inspection confirmed that the T_{2g} peak was fit well without the need for a secondary peak at ~470 cm^{-1}. The converged fit yielded defect peak position values of ~562 and ~598 cm^{-1}. Interestingly, the position of the second defect peak (denoted *D2* in Figure 67) is in very good agreement with the corresponding defect peak position of $UO_{2.07}$ measured by Elorrieta *et al*. [171]. The first defect peak (denoted *D1* in Figure 67) is also in agreement with the limited reports in the literature. Elorrieta *et al*. showed that the D1 peak shifts to lower wavenumbers with increasing oxidation level, but reported a similar central peak value of 562 cm^{-1} at a composition of $UO_{2.03}$ [171].

The D2 peak has been attributed to the distortion of the oxygen sublattice, as the peak has been shown to grow in intensity with increasing oxygen content [171, 198]. One study suggests that the peak is a signature of the cuboctohedral defect cluster based on polarization measurements [223], although the experiments were performed on U_4O_9 not UO_{2+x}. Nevertheless, the peak appears to be associated with oxygen defects of some type. Therefore, the emergence of the D2 peak in $UO_{2.07}$ is an indicator that the material contains oxygen interstitials, whether they are clustered or not. The attribution of the peak to cuboctahedra defect coordination would coincide with the expected $UO_{2+x(s)}$ + α-U_4O_9 mixture at room temperature.

The D1 peak is also typically linked to defect accumulation, although researchers have reported varying accounts of peak evolution. He & Shoesmith [198] observed a monotonic decrease in the D1 peak intensity with increasing O:M ratio whereas Elorrieta *et al*. [171] reported a relative increase in D1 peak intensity between $UO_{2.03}$ and $UO_{2.09}$, and a decrease from $UO_{2.09}$ to $UO_{2.24}$. Guimbretiere *et al*. [231] observed a simultaneous increase in the D1 and D2 peak intensities of stoichiometric UO_2 after ion irradiation and claimed that peaks are not caused by surface oxidation because the irradiation was performed under vacuum. This is in contrast to the findings of He & Shoesmith [198] in

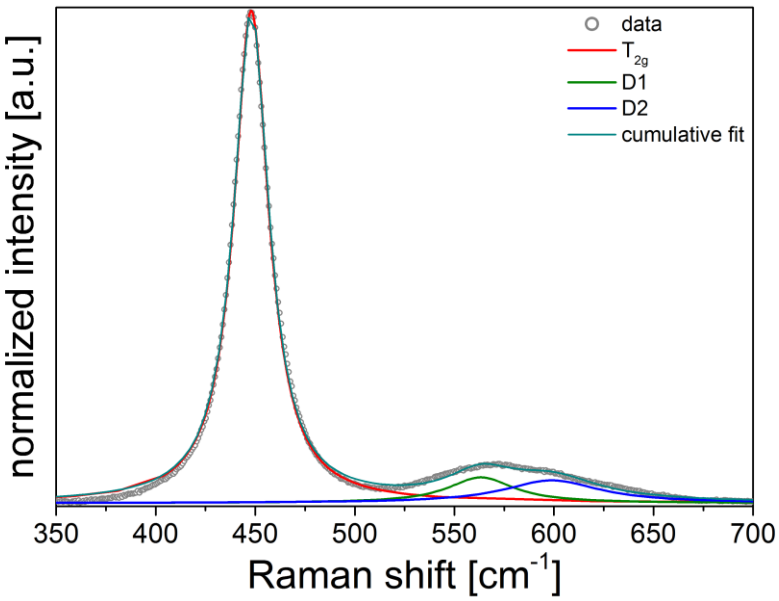


Figure 67: Peak fit of UO_{2+x} Raman spectrum

which the D1 and D2 peaks evolve in opposite directions. The D1 and D2 peaks decrease and increase with increasing O:M, respectively.

He & Shoesmith [198] noted that the frequency of the D1 peak is similar to the forbidden F_{1u} IR-active LO mode at the center of the Brillouin zone and suggested that the mode becomes active due to a localized lowering of symmetry and a breakdown of selection rules. It was further noted that the breakdown is likely induced by loss of translational symmetry at vacant oxygen sites as a result of oxygen defect clustering, and changes in local uranium coordination environments caused by oxidation [198]. What is puzzling however, is that the peak decreases in intensity with increasing O:M ratio above 2.09. This suggests that the D1 peak is a defect signature specific to the fluorite structure and that around O:M ~ 2.1, local domains of U_4O_9 begin to compete with the fluorite-type domains, which induces a decrease in D1 peak intensity. The increased intensities of D1 and D2 between UO_2 and $UO_{2.07}$ indicate that the two materials exhibit fluorite-structure character although $UO_{2.07}$ incorporates an increased amount of oxygen interstitials.

Neutron Total Scattering – Local Structure and Defect Clustering

Neutron total scattering, like diffraction, conveys information about the average structure and long-range atomic periodicity through Bragg scattering. Unlike diffraction patterns, however, total scattering functions also convey information about short-range interatomic interactions through diffuse coherent scattering. Diffuse scattering appearing in diffraction patterns is typically treated as a background artifact and is fit and subtracted from the data. In total scattering analysis, diffuse scattering is carefully treated by taking into account all sources of background scattering, *e.g.*, from sample holders and the instrument chamber, and by quantifying miscellaneous sample properties, such as multiple scattering and absorption. Assuming data are properly treated, diffuse scattering can reveal details regarding point defects and short-range ordering schemes. This can be quite complimentary to structural and vibrational properties measured by Raman spectroscopy because diffuse scattering features can be readily fit and quantified by employing pair distribution function (PDF) analysis.

The easiest means to fit and quantify structural properties from PDFs is by small-box PDF refinement. This method is similar to Rietveld analysis of diffraction data and operates as a least-squares analysis method. The starting models used for small-box refinements are typically models derived from Rietveld refinement. Fitting these average-structure models to short- and intermediate range structures, *i.e.*, the PDF, can immediately reveal how local atomic arrangements may vary from averaged atomic positions. The PDFs, $G(r)$, of UO_2 and $UO_{2.07}$ are shown in Figure 68 at various temperatures.

The PDFs represent interatomic distance maps of the measured materials. This means that each peak in the PDF comprises one or more characteristic interatomic distance in the probed structure and the position of the peak maxima denotes the mean interatomic distance for that atom pair. For example, the first two peaks in the UO_2 PDF correspond to the mean first nearest-neighbor U-O and O-O distances in the fluorite structure. These are the <111> U-O atom pairs and the <100> O-O atom pairs with atom spacings of ~2.36 and ~2.72 Å, respectively, in UO_2 at room temperature. The intensity of a single peak, or correlation, indicates the relative concentration of that unique atom pair in the material, and the width of a single correlation denotes the relative amount of deviation from the mean atom spacing value. Peak broadening can be caused by thermal disorder and/or static disorder. Peak broadening is typically quantified by the so-called atomic displacement parameter (ADP) as in Rietveld refinement.

Figure 68 shows that the PDF of UO_2 undergoes two main modifications with increasing temperature: peaks broaden and peak intensities decrease. Peak broadening and smaller peak intensities are concomitant PDF features and they indicate that there is an increase in atomic disorder. The increased atomic disorder is likely driven mostly by increased thermal disorder that follows from increasing the sample temperature. $UO_{2.07}$ undergoes very similar features. Neither of the materials show any drastic change in peak arrangements or preferential loss of peak intensity at higher r values. This demonstrates that both materials remain crystalline and do not undergo any phase transformation. It is likely that the peak positions and relative intensities vary with increasing temperature and between the two datasets (UO_2 *vs*. $UO_{2.07}$), but changes are too small to be readily observed when viewing the entirely of the PDF (0-50 Å) all at once. Changes in peak positions and

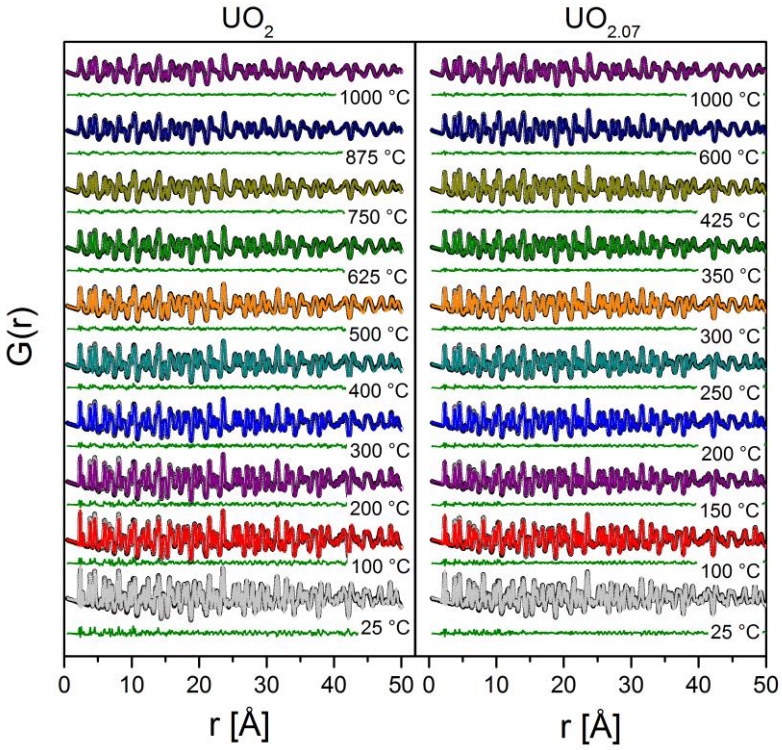


Figure 68: Small-box refinement fits to the PDFs of UO_2 (left) and $UO_{2.07}$ (right) at all temperatures

relative intensities were instead quantified using structural refinement.

All PDFs were fit with the fluorite structure model through small-box PDF refinement. The structure was relaxed and optimized by refining the unit cell parameter, the overall scale factor, and the isotropic ADPs of uranium and oxygen. All site occupancies were fixed to unity for both UO_2 and $UO_{2.07}$. Short-range interatomic correlated motion leads to preferential increase in peak intensity at lower *r* values. This correlated motion was accounted for by refining a single correlated motion parameter. The small-box refinement fit results are shown in Figure 68 alongside the PDFs. The optimized fluorite structure model fits are denoted by the colored lines overlaid on top of the measured PDFs and the difference between the PDF and the fitted PDF are illustrated by green lines below each fitted PDF.

Overall, all PDFs were fit well with the fluorite structure. This is illustrated by the relatively low intensity of the difference curves at all temperatures. The difference curve intensities are largest at the lowest temperatures. This might result from resolution effects because it is easier to fit broader peaks, such as those at high temperature, compared to sharper peaks, such as those at low temperature. Regardless, the difference between low and high temperatures is not excessively large. The quality of the fits were assessed using a goodness-of-fit parameter, R_w, defined as:

$$R_w = \sqrt{\frac{\sum_{i=1}^{n} \omega(r_i)\,[G_{obs}(r_i) - G_{calc}(r_i)]^2}{\sum_{i=1}^{n} \omega(r_i)\,G_{obs}^2(r_i)}}$$

where G_{obs} is the experimentally measured PDF, G_{calc} is the simulated PDF, and $\omega(r_i)$ is a weighting factor. Figure 69 shows the evolution of the R_w value with increasing temperature for both samples. The plot shows that the R_w value of UO_2 monotonically decreases with increasing temperature whereas the R_w value of $UO_{2.07}$ decreases and then increases abruptly between ~400-600 °C. This abrupt change in the R_w may indicate the phase transformation from the mixed $UO_{2+x\,(s)}$ + β-U_4O_{9-y} phase to single-phase $UO_{2+x\,(s)}$, which is in agreement with the phase transition boundary in the phase diagram reported by Higgs *et al*. [173]. It's unlikely that the phase transformation between $UO_{2+x\,(s)}$ + α-U_4O_{9-y}

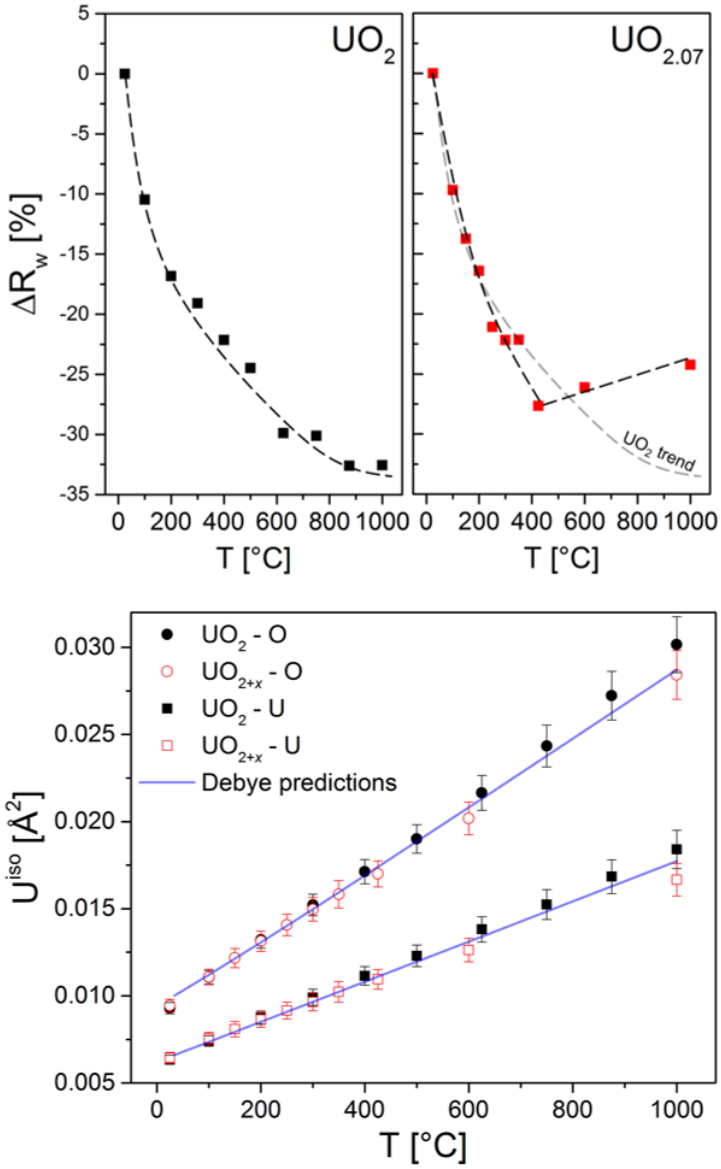


Figure 69: Comparison of small-box pair distribution function refinement results for UO_2 and $UO_{2.07}$. The top two panels show the evolution of the goodness-of-fit, R_w, with increasing temperature. The bottom plot shows the evolution of the uranium and oxygen isotropic atomic displacement parameters (ADPs; U^{iso}) with varying temperature. The ADPs are compared with predictions based on the Debye model

and $UO_{2+x\,(s)}$ + β-U_4O_{9-y} would be observed because there were no additional data points collected between 25 and 100 °C, where the phase transition is reported to occur. It's surprising that the phase transformation between ~400 – 600 °C causes an *increase* in R_w instead of a decrease. Intuitively, it would make more sense for the fluorite structure model fit to improve upon going from a two-phase mixture to a single phase. This might indicate that single-phase $UO_{2+x\,(s)}$ has a certain characteristic that is not well fit with the fluorite structural model used.

Small-box refinement showed that both materials undergo thermal expansion at higher temperatures, in agreement with the Rietveld analysis. Also in agreement with Rietveld analysis, small-box refinement showed that the isotropic ADPs of UO_2 and $UO_{2.07}$ increased with increasing temperature. The isotropic ADPs for UO_2 and $UO_{2.07}$ are shown in Figure 69. Predictions made using Debye theory are plotted alongside the data for reference. All refinements yielded uranium and oxygen ADPs that are within experimental uncertainty of the Debye model. The evolution trends for the two materials are similar to the trends derived from Rietveld refinement results, although the Rietveld ADPs had much smaller error bars. This enabled the observation of the $UO_{2+x\,(s)}$ + β-U_4O_{9-y} to single-phase $UO_{2+x\,(s)}$ phase transformation from the Rietveld ADPs alone, which was not possible here because of the larger error bars.

The results shown in Figure 69 provide confidence that the $UO_{2.07}$ data collected at 600 °C and 1000 °C represent single-phase UO_{2+x}, as expected based on the accepted phase diagram of uranium oxide. These two sets of data ($UO_{2.07}$ at 600 °C and 1000 °C) were therefore further characterized through fitting of various proposed defect structure models using small-box PDF refinement. Fitting of the two neutron PDFs was limited to the range 0-10 Å in order to emphasize modeling of the short-range structure where defect cluster signatures are most likely to be present in the PDF. A similar short-range PDF fitting procedure was performed on U_4O_9 materials and enabled the determination of short-range atomic ordering schemes in α- β- and γ-U_4O_9 phases containing octahedral defect clusters [220].

Each PDF was fit with five simple defect models and a pristine UO_2 model. The pristine UO_2 models assumed perfect stoichiometry (O:M = 2.00) and were used to gauge

the sensitivity of the small-box analysis to interstitials. For example, if a defect model fits worse or equal to the reference model then the defect model is either wrong or the fitting procedure is not sensitive enough to precisely determine the position of adventitious oxygen atoms. A description of these defect models and the notation used are summarized in Table 5.

The first three so-called *octahedral* models are based on the most simplistic assumption that adventitious oxygen occupy the large, empty octahedral cavities in the center of the fluorite unit cell. An oxygen atom located at this site would have an O-O distance equal to the 1-NN U-O distance and would therefore not violate the minimum distance requirement set by the first peak in the PDF. There are no peaks in the PDFs shorter than the 1-NN U-O peak, therefore, the 1-NN U-O distance should in theory be the shortest atom-atom distance in the material. The other two *octahedral* models incorporate relaxation modes to the octahedral interstitial model. The <110> and <111> octahedral models contain interstitials placed at sites analogous to the 48*i* and 32*f* sites, respectively, in fluorite symmetry. The <110> model enables the octahedral interstitials to relax along <110> directions whereas the <111> model enables the octahedral interstitials to relax along <111> directions.

The remaining defect models were based on leading defect model candidates reported in the literature. The so-called *Willis 2:2:2* model is based on the well-established defect cluster configuration derived by Willis from neutron diffraction studies [158]. The split di-interstitial configuration is based on models derived from computational studies [79]. The latter model is notable because it results from the DFT optimization of the Willis cluster. The Willis cluster is seemingly unstable from an energetic point of view according to DFT. All models fit well without any strongly correlated refinement parameters.

The fit results for the two datasets are shown in Figure 70. The main findings are that in both cases the octahedral interstitial model does a poor job of fitting the data and a proposed defect cluster model from the literature (*Willis 2:2:2*) yields the best fit results. It's likely that the octahedral model performs worst because atoms located at the octahedral position invoke a strong diffraction condition that would cause easily-observable peak mismatch at higher *r* values. The two octahedral interstitial model variants (<110> and

Table 5: Summary of various defect structure models fit to the local structure of the $UO_{2.07}$ PDFs

Defect model name	Model description
Octahedral	Interstitial occupies 4*b* octahedral hole at (½ ,½,½)
<110> Octahedral	Same as *Octahedral Interstitial* model but interstitials allowed to relax along <110> directions
<111> Octahedral	Same as *Octahedral Interstitial* model but interstitials allowed to relax along <111> directions
Split di-Interstitial	Three interstitials sit on a 111-plane above a vacant 8*c* oxygen site
Willis 2:2:2	Two adjacent 8*c* vacancies, one interstitial displaced along a <111> direction from each vacancy towards an empty octahedral hole, and two interstitials displaced along <110> direction from each other half-way in-between the vacancies

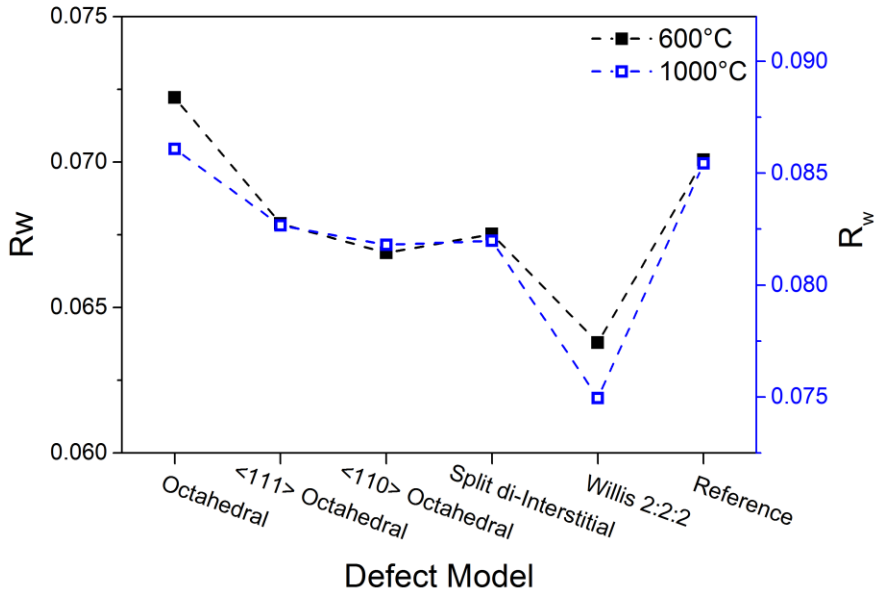


Figure 70: Comparison of goodness-of-fit parameters obtained from fitting different defect models to the PDFs of $UO_{2.07}$ at 600 and 1000 °C

<111>) likely perform better than the un-relaxed octahedral model because they disrupt or destroy this strong diffraction condition. Collectively, this indicates that a mono-interstitial model is not ideal and adventitious oxygens likely cluster, as other studies suggest.

The Willis cluster model yielded the best agreement with the data. The distorted octahedral models and the split di-interstitial model gave similar results. This may be attributable to the similarity in relaxation modes between the split di-interstitial and <111> octahedral models. Both configurations consist of oxygen interstitials relaxing along <111> directions towards neighboring lattice oxygen atoms. If this is the case, then it's surprising that the Willis cluster performs far superior. This is because the Willis cluster contains displacement modes (<111> and <110> displacements) that are found in the other models.

The Willis model success is not directly related to the <110> displacements not found in the *<111> octahedral* and *split di-interstitial* models. If this were the case, then the *<111> octahedral* model would have performed much better relative to the latter two. The success also appears not to be directly related to the presence of oxygen vacancies because the *split di-interstitial* model also contains a vacancy in close proximity to interstitials. The improved fit must be somehow related to the unique combination of these elements or perhaps the presence of multiple vacancies, especially vacancies that are in close proximity to interstitials. An improved point defect modeling scheme requires more explicit accounting of these vacancies.

To this end, the neutron total scattering data were modeled using Reverse Monte Carlo (RMC). RMC modeling lifts the stringent restriction of applying a pre-determined defect structure, such as the Willis or split di-interstitial cluster, and does not rely on explicit space group formulations. Instead, the structural model is driven purely by statistical mechanics. Rietveld analyses of the average structure are used to construct a large atomic ensemble (supercell) with atoms in pristine arrangement according to the average structure. The entropy of the supercell is thereafter maximized within a given set of constraints. In this case, the constraints are the short-range structure (PDF), intermediate-range structure (PDF), the long-range structure (diffraction pattern), minimum distance constraints (from the PDF), and soft chemical constraints (*via* the bond

valence sum method). Modeling performed in this way is unbiased by pre-established defect cluster models and derived atomic structural models are driven only by experimental data and not interatomic potentials or electronic interactions.

RMC modeling performed in this study was limited to a 10×10×10 supercell (~5.5nm×5.5nm×5.5nm), but there is technically no limit to how large a supercell can be. The main limitation for very large supercells is computational resource. 1000-unit cell ensembles were chosen because they provide a reasonable tradeoff between minimizing required computational power and optimizing counting statistics. The 1000-unit cell ensembles were also run at least 10 different times (independently) in order to avoid uniqueness issues. In each case the supercell optimization was run for at least 12 hours to enable sufficient time for changes in atomic arrangements to reach steady state. RMC simulations do not converge in the same way that a small-box least-squares PDF fit does. Rather than reach an absolute minimum, RMC simulations reach a steady state in which random atom moves that improve the fit are produced at the same rate as random atom moves that degrade the fit.

An example of the quality of the RMC fits is shown in Figure 71. The figure highlights just how well the RMC models fit the data at all length scales. RMC was used to fit the short-range (G(r)), intermediate-range (D(r)), and long-range structures (diffraction pattern) all at once such that the resultant model is self-consistent at all length scales. This method of RMC modeling has surprisingly been applied few times relative to small-box modeling. This is possibly a result of the difficulty in preparing the total scattering data for RMC analysis and the tediousness in running, processing, and analyzing such large quantities of data.

RMC boasts several advantages in comparison to small-box modeling. The first is that vacancies can be modeled explicitly by introducing pseudo-atoms with zero neutron scattering length into the supercell. This is unlike small-box modeling or Rietveld refinement in which vacancies can only be modeled implicitly through varied site occupancies. Vacancies in RMC simulations can perform functions like real atoms and can therefore be moved around the supercell with proper accounting. This explicit modeling of vacancies enables the investigation of, for example, short-range vacancy ordering, which

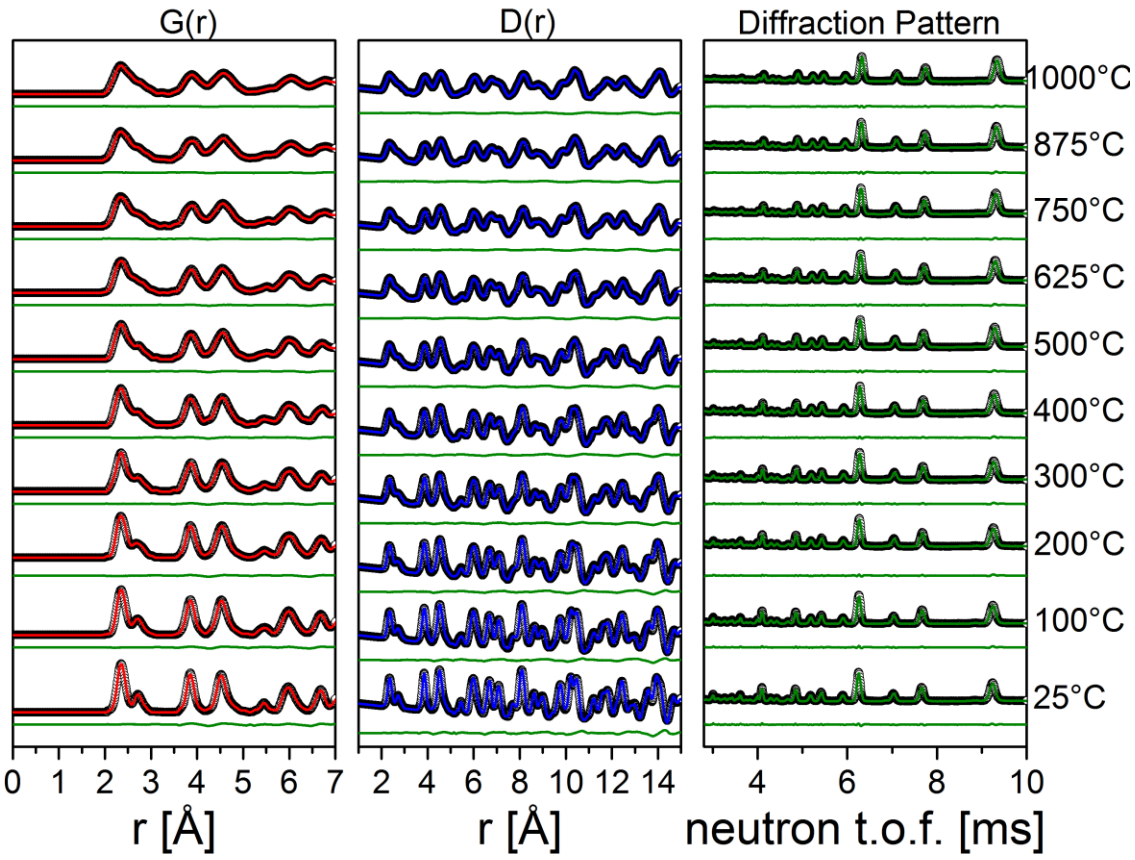


Figure 71: RMC fit results for $UO_{2.00}$ data. Experimental data are shown in black, fitted structural models are denoted by the colored lines, and the thin green lines below the data represent the difference between the data and the fitted structural models

might be associated with defect clusters. As a test, vacancies were introduced into the $UO_{2.00}$ supercells at the 4*b* octahedral site, which is normally unoccupied in the pristine fluorite structure, and the vacancies were allowed to move without restriction. Optimization of all UO_2 supercells at all temperatures showed that the vacancies remain at the octahedral sites and do not occupy any other sites, even though no restriction was placed on vacancy movement. This confirmed that modeling of vacancies in the UO_2 structure was valid and could be used for modeling $UO_{2.07}$.

Another advantage to RMC modeling is that the optimized supercell can be used to obtain partial PDFs. Inspection of the partial PDFs can reveal hidden peak splitting that might otherwise be hidden in the G(r) function, which is a convolution of all of the partial PDFs with different weighting factors. Figure 72 shows the partial PDFs alongside the overall fits to the PDFs of UO_2 at the lowest, intermediate, and highest temperatures achieved during the experiment. The overall fits to the PDFs are identical to those shown in Figure 71 and illustrate the excellent fit to the data. More importantly, the partial PDFs demonstrate that an excellent fit is obtained without any unexpected partial PDF peak splitting. The partial PDFs shown in blue, red, and green represent the U-O, O-O, and U-U partials, respectively. All partials undergo similar evolution with temperature. They all decrease in intensity and broaden. This is consistent with the derived ADPs from small-box and Rietveld refinements and demonstrates that the atoms are more disordered at higher temperature as a result of thermal vibration.

A close inspection reveals that the 1-NN U-O peak undergoes anisotropic peak broadening that is not observed much for the other peaks. This asymmetric peak character is difficult to model using simple Gaussians, which is the characteristic peak form function of neutron scattering. The inability of two Gaussians (one for 1-NN U-O and one for the 1-NN O-O peak) to characterize the asymmetric peak broadening of the first two peaks has caused some researchers to propose that the local structure of $UO_{2.00}$ at high temperature (> ~1000 °C) is not fluorite in character. One proposed explanation is that the local structure of $UO_{2.00}$ comprises two types of U-O distances, a longer and shorter U-O distance, in agreement with *Pa*-3 type symmetry, and oxygen atoms occupying (¼+*x*, ¼+*x*, ¼+*x*) sites instead of (¼, ¼, ¼) sites as in the fluorite structure [244]. This proposed model

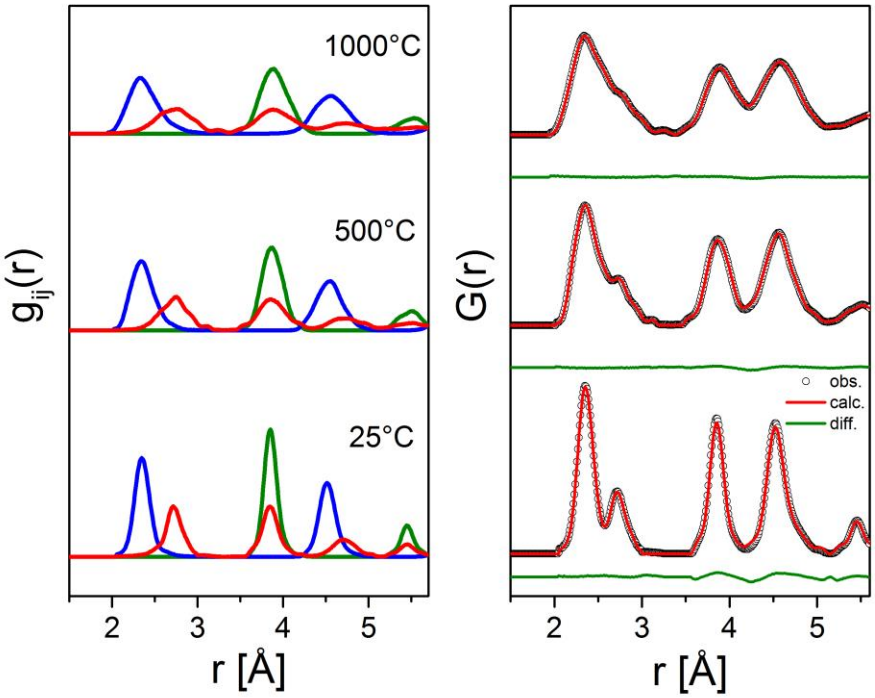


Figure 72: Partial pair distribution functions (left) and overall fit to the G(r) function for UO_2 data at 25, 500, and 1000 °C. The blue, red, and green partial PDFs represent the U-O, O-O, and U-U partials, respectively

requires that UO_6 square bipyramid polyhedra coexist alongside normal cubic UO_8 polyhedra. Fitting of this model to the neutron PDF of $UO_{2.00}$ at high temperature yielded good agreement with the data [244]. However, the results shown here suggest that the model may be too restrictive and is rather an approximation to the actual atom behavior.

The partial PDF results in Figure 72 clearly show the formation of shorter- and longer U-O distances at high temperature, but these bonds form a continuum of bond distances rather than two distinct, characteristic U-O distances (short and long). If two distinct distances were formed, then the first U-O peak would undergo peak splitting, which is not observed. This suggests that the *Pa*-3 model is merely approximating the longer U-O distances that form and the various polyhedra shapes that result from this U-O bond lengthening. The validity of the *Pa*-3 model was also tested by initializing the supercell with *Pa*-3 symmetry. Modeling results showed that this different starting configuration also converges to the same result as for the supercell initialized to *Fm*-3*m* symmetry. The ability of the RMC model to yield a continuum rather than two distinct U-O distances is likely attributable to the large simulation cell size (counting statistics) and thus the ability to model more intermediate-range interatomic interactions. A disadvantage to small-box modeling is that large simulation cells are difficult to implement without imposing space group symmetry because atomic displacements need to be imposed manually. This can become quite tedious for very large atom ensembles. As a result, local distortions are often approximated by different space group symmetries that incorporate varying types of polyhedra, like the *Pa*-3 model. The RMC model indicates that the U-O bond continuum forms as a result of intermediate-range modulations. In other words, unfavorable changes in short-range U-O coordination (caused by shorter and longer U-O distances, and/or different coordination numbers) are mitigated or cancelled out by modulations or subtle modifications at longer length scales (10-50 Å).

In fact, the preferential peak broadening to the higher *r* values can be easily explained by simple bonding arguments. The observed asymmetric broadening to higher *r* values is consistent with the expected behavior for a chemically-bonded system. Invoking a simple Lennard-Jones-type potential model, it is envisioned that increasing the temperature will increase the energy of the system (vertical axis for a plotted Lennard-

Jones-type potential). As the energy and temperature rises, atoms will tend to displace *away* from the closest neighboring atom, *i.e.*, away from the potential asymptote, to higher *r* values (longer interatomic distances) because the energy barrier is weaker in that direction. This way the minimum distance remains approximately the same and there is a larger spread of interatomic distances to higher *r* values. The resultant data for all temperatures were also consistent with interatomic distances and coordination numbers expected for UO_2. Bond valence sum analysis showed that uranium cations retain +4 valence states at all temperatures and there is no statistically-significant deviation to lower (+3) or higher (+5/+6) valence states. Oxygen atoms remain in coordination largely consistent with -2 valence states.

RMC modeling of $UO_{2.07}$ was performed in an identical manner as for $UO_{2.00}$ except that oxygen interstitials were introduced into the octahedral holes in the $UO_{2.00}$ supercells as to achieve the precise stoichiometry of O:U = 2.07. Extensive testing proved that the RMC results are independent of the starting interstitial site and the results are not overly sensitive to variations in stoichiometry. Placing interstitials at fully random sites yielded fits that converged to the same result, albeit at a slower rate. Changes in stoichiometry as large as 2.07 ± 0.04 resulted in very similar fit results, giving confidence that the presented data are quite robust. RMC modeling was only performed on the single-phase UO_{2+x} samples ($UO_{2.07}$ at 600 and 1000 °C) because oxygen interstitial positions in single phase UO_{2+x} are of more interest for nuclear fuel modeling efforts and it is more complicated to distinguish the effects of the UO_{2+x} and U_4O_9 phases when both exist in a mixed phase.

Prior to RMC modeling, the experimental PDFs of $UO_{2.00}$ and $UO_{2.07}$ were compared qualitatively in order to determine how oxidation affects the PDF. The calculated PDFs of UO_{2+x} presented in the previous Results section (section titled, *Pair Distribution Function Simulations*) showed that oxidation and defect clustering causes only very small changes in PDF peak intensities and peak widths. This was illustrated in Figure 55 and Figure 56. The experimentally measured PDFs for $UO_{2.00}$ and $UO_{2.07}$ are compared in Figure 73. The experimental PDFs are in good agreement with the simulations and show that oxidation causes only the smallest changes in PDF peak intensities (*e.g.*, second peak for ~600 °C comparison) and very small changes in peak widths (*e.g.*, low *r* boundary of

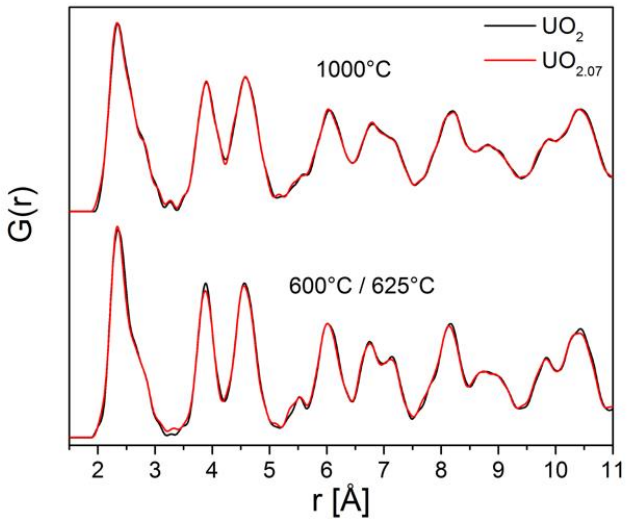


Figure 73: Direct comparison of experimental PDFs for UO_2 (black) and $UO_{2.07}$ (red) at ~600 and 1000 °C. The $UO_{2.07}$ sample was measured at 600 °C whereas the UO_2 sample was measured at 625 °C

first peak at 1000 °C). Since the differences between the PDFs are so small, defect clustering signatures will likely arise from modeling of multiple length scales (short, intermediate, and long-range) through fitting of G(r), D(r), and Bragg functions, respectively. This is because the Bragg patterns are very different while the G(r) functions are very similar. This suggests that the key to modeling defect clustering comes from either the intermediate-range structure or the unique mix of both short- and long-range structures.

The fits to the experimental G(r) function of UO_{2+x} collected at 600 and 1000 °C are shown in Figure 74. The results show that the optimized UO_{2+x} model with interstitials (*red line*) fits extremely well to the experimental G(r) function (*black circles*) at low *r* values. The very good fit is confirmed by inspection of the difference curve (*green line*), which is nearly zero throughout the *r* range shown. The fits to the D(r) functions and diffraction patterns are not presented because they are very similar to the results shown in Figure 71. That is, they show that the RMC models also fit extremely well to the data at the two temperatures investigated. This confirms that the RMC models are consistent with all length scales.

The BVS analysis results showed that uranium atoms in the model exhibit a mean valence between ~ +4–4.1 at 600 °C and the valence value drops to ~ +4 at 1000 °C. The slightly higher valence at 600 °C is consistent with the small presence of U^{5+} cations in the system that charge-compensate for the excess oxygen interstitials (x = 0.07). The smaller valence value at higher temperature likely arises from thermal expansion of the lattice. The BVS valence value is estimated based on coordination number and coordination polyhedral size. The lattice at 1000 °C is expanded much more relative to 600 °C and this extra empty space likely decreases coordination densities slightly such that the mean valence drops slightly. Nevertheless, the estimated valence values are in agreement with predictions for UO_{2+x} and show that the resultant RMC models are also chemically-sensible.

The left panel of Figure 74 shows the partial PDFs that are derived from the optimized RMC models. The partial PDFs show very similar features compared to those of $UO_{2.00}$. The U-U partial only undergoes peak broadening and a decrease in intensity. The U-O undergoes similar changes, but also shows the characteristic asymmetric peak broadening for the 1-NN U-O peak. The O-O partial of $UO_{2.07}$ shows the largest difference

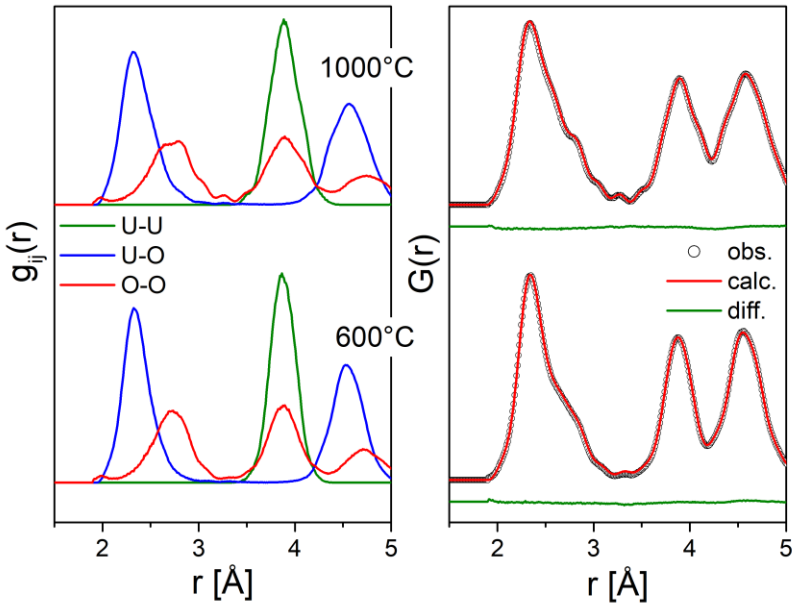


Figure 74: Comparison of RMC model fits to the G(r) function of $UO_{2.07}$ at 600 and 1000 °C (right) and the resultant partial PDFs (left)

compared with that of $UO_{2.00}$. Besides small bumps between 2.5 and 3.5 Å that may or may not be associated with Fourier termination ripples, the O-O partial of $UO_{2.07}$ shows the emergence of a small peak centered about ~2 Å. This small peak arises from short (~2 Å) O-O distances that are similar to the interstitial O'-O' distances (also ~2 Å) in the Willis cluster that was proposed based on neutron diffraction measurements [158]. Therefore, this small feature is most likely attributable to oxygen interstitials and/or interstitial clustering in UO_{2+x}.

Since the changes in the PDF and the observed clustering feature are so small, very extensive testing was performed in order to validate the data reduction and data modeling procedures. In regards to data reduction, the two biggest potential sources of uncertainty stem from inaccurate stoichiometry and the presence of Fourier ripples. Changes in stoichiometry or inaccurate attribution of $UO_{2.07}$ stoichiometry during data reduction would result mostly in changes in PDF peak intensities (*i.e.*, data scaling). As previously mentioned, testing was performed by systematically varying stoichiometry by values up to $x \pm 0.04$. This testing procedure showed that the optimized structure is only weakly affected by stoichiometry and the small peak at ~2 Å emerges from the modeling regardless of small changes in assumed stoichiometry.

It can be seen that the small peak at 2 Å emerges because of the low *r* intensity of the 1-NN U-O peak. Therefore, it was also considered that Fourier ripples might cause the 1-NN U-O peak to incorporate this low *r* 'shoulder'. In order to test this, the G(r) function of $UO_{2.07}$ was created using different values of Q_{max}. It is well known that varying the Q_{max} value for the Fourier transform will strongly modify Fourier ripples, but will modify real PDF features only very weakly or not at all. Varying the Q_{max} value from 26 to 33 $Å^{-1}$ showed that the low *r* shoulder does not move or change. This confirmed that the low *r* shoulder of the 1-NN peak is a true characteristic of the peak and is not a Fourier artifact.

The data modeling procedure was also re-visited and scrutinized. The largest sources of uncertainty from data modeling arise from constraints applied during RMC modeling. These constraints include the various datasets, BVS constraint, the presence of vacancies, and starting configuration of interstitials. The effects of the datasets were tested by systematically fitting different combinations of one, two, or all three datasets (G(r),

D(r), and diffraction pattern). All fits results showed that intensity of the O-O partial is somehow pushed to the low *r* region (2 Å), even when only fitting the diffraction pattern. Unlike the runs with G(r) and/or D(r) functions, however, the intensity in the low *r* region was not fit well. This showed that the 2 Å peak *shape* and therefore distribution of short O-O distances is dictated by the G(r) and/or D(r) functions, which convey short-range information. RMC fitting with and without BVS constraints showed that BVS constraints do not cause the 2 Å peak. This test merely showed that BVS constraints aid in making the model more chemically-sensible. The model obtained without BVS constraints showed much broader and unlikely valence distributions for both oxygen and uranium atoms. The uranium atoms had extremely varied valence values that spanned almost from +3 to +6. Uranium takes on +3 and +6 valences, but spectroscopy experiments have conclusively shown that uranium in fluorite-type oxides is typically U^{4+} or U^{5+} [245-248]. Testing also showed that supercell size (*e.g.*, 3×3×3, 5×5×5, and 10×10×10) and stoichiometry ($x \pm 0.04$) do not influence the results significantly. Lastly, testing of initial interstitial positions and incorporation of vacancies in the supercell showed that these factors do not drive the emergence of the 2 Å peak either. Having validated the reliability of the results and the presence of the small 2 Å PDF peak, the source of the peak intensity was investigated.

Bond vector analysis on the optimized supercells showed that O-O pairs that contribute to the 2 Å peak are oriented along <111>-type directions and O-O bond orientation along <100> or <110> orientations is negligible. Oxygen pair orientations are not perfectly along <111> directions, but rather deviate very slightly about perfect <111> directions owing to the inherently disordered nature of the system and the complex relaxation mechanisms involving 3+ atoms. A close inspection of the atom ensembles showed that short <111> O-O pairs result in a variety of clusters comprising 2-5 displaced oxygen atoms. Clusters containing more than 5 atoms were not observed in any of the simulation cells at any temperature. Clusters containing 4 and 5 atoms were only observed in low concentration. In both cases, the sum of 4- and 5-atom clusters contributed less than 5% to the total cluster concentration.

Figure 75 shows examples of 2-5 atom clusters observed in the simulation cells alongside the cluster size distributions calculated for both datasets from ten 16000-atom

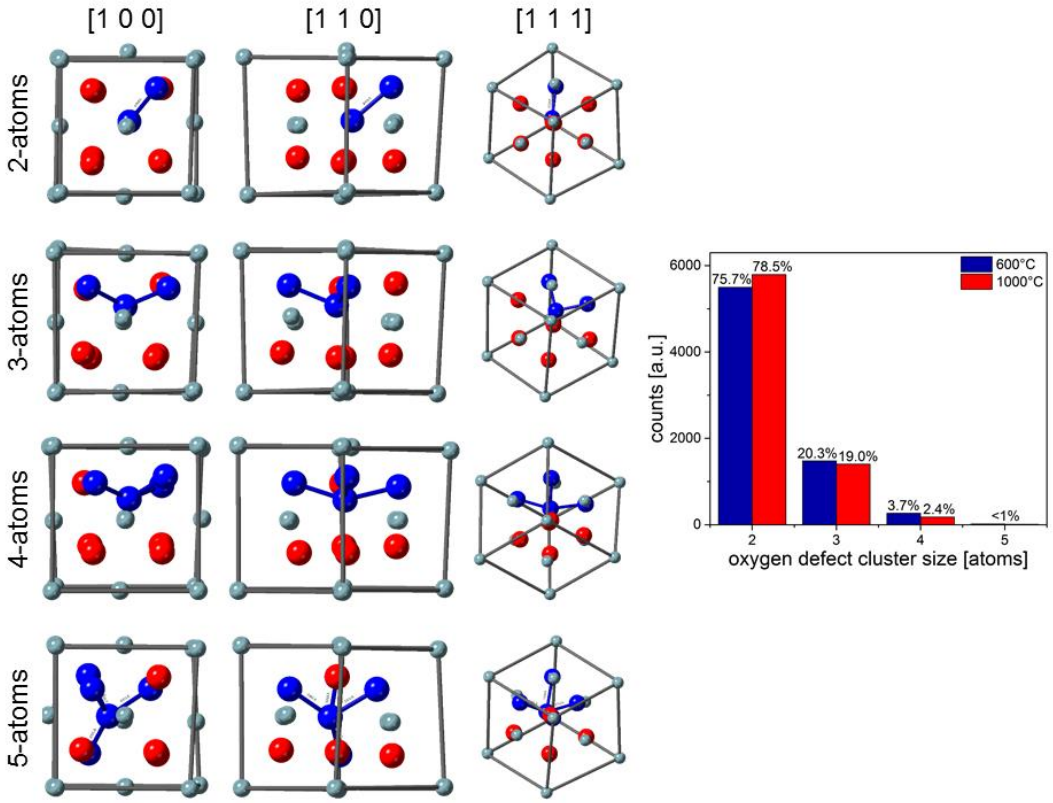


Figure 75: Examples of the various defect cluster arrangements in the optimized RMC supercells (left) and histograms of defect cluster sizes from RMC results (right). Defect cluster arrangements are shown as viewed along the three principal directions (<100>, <110>, and <111> directions). Each histogram is representative of sampling data from ten 16000-atom supercells

ensembles that were run for at least 12 hours each. The cluster illustrations are in agreement with the small-box refinement results and show that oxygen interstitials rarely occupy the centers of the unit cells, but rather displace slightly from the octahedral holes. Oxygen dimers (*i.e.*, 2-atom clusters) form when oxygen interstitials displace along <111> from the octahedral holes towards a neighboring lattice oxygen. Most dimers show that both the interstitial and lattice oxygen both are displaced from ideal sites, thus suggesting a split interstitial configuration. 3-atom clusters appear to form by a similar mechanism. An oxygen interstitial at the central octahedral hole displaces along a <110> direction and clusters with two lattice oxygens that are 1-NN to each other. The 3-atom cluster therefore resembles two individual 2-atom clusters that are bridged by the central interstitial oxygen. The O-O 'bonds' between the central interstitial and each lattice oxygen are oriented roughly along <111> directions.

4- and 5-atom clusters are extensions of the 3-atom cluster. The 4-atom cluster involves displacement of an interstitial from the octahedral site along a <111>-type direction and results in three interstitial-to-lattice oxygen pairs. Each pair is 'bonded' roughly along a <111> direction and the three lattice oxygens are separated by $a/2$ where a is the unit cell parameter. The 5-atom cluster is similar in that the 4 lattice oxygens are separated by a distance of $a/2$. As with all the other cluster types, O-O orientations between the central interstitial and the lattice oxygens are oriented along <111>-type directions.

The common feature among all defect cluster types is that all are constructed assuming only one interstitial oxygen atom. The remaining oxygen atoms in the clusters are displaced lattice oxygens. This is in contrast to the Willis and di-interstitial defects that are assembled from two nearest-neighbor oxygen interstitials. This difference in cluster building units may be attributed to interstitial concentrations. The material studied ($UO_{2.07}$) contains fewer interstitials than materials studied by Willis and Murray [78, 156-159, 249], which exhibited stoichiometries ranging from $x = 0.11$ to $x = 0.13$ for UO_{2+x}. However, DFT studies often employ 2×2×2 supercells [79, 145, 172] with two interstitials yielding a composition of $U_{32}O_{66}$ or equivalently, $UO_{2.0625}$, which is very close to the stoichiometry investigated in this study. Nonetheless, DFT cases are limited to ensembles with fewer than 100 atoms unlike RMC models that employed 16000 atoms.

Analyses also consistently show that the 2, 3, and 4 displaced lattice oxygens (for 3-, 4-, and 5-atom clusters) are all separated by minimum distances of ~a/2. This feature might be the cause for the apparent limitation in cluster size. A maximum defect cluster size of 5 atoms ensures that all interstitial-to-lattice O-O orientations are approximately along <111> directions. If more lattice atoms are added to a 5-atom cluster, the new atom(s) would make interstitial-to-lattice O-O distances less <111>-like. This suggests that the <111> O-O orientation for interstitial-to-lattice oxygens is a characteristic feature of these cluster motifs. Extensive testing of RMC parameters indicated that these <111> orientations are driven by the experimental data and not systematic artifacts from the data reduction or data modeling processes.

The cluster configurations derived from RMC models are clearly at odds with previously-proposed *Willis* and *di-interstitial*-type defect cluster models. Proposed arrangements comprise short O-O distances that are mostly aligned along <110> directions, and short vacancy-oxygen distances aligned mostly along <111>-type directions. The clusters observed in the present RMC study show that short O-O and vacancy-oxygen pairs are both aligned along <111>-type directions. The present data also show that clusters form from a single interstitial instead of two nearest-neighbor interstitials. These features likely induce the apparent limitation in cluster size. It's proposed that *di*-interstitials and *Willis*-type defect clusters may still form at higher O:M ratios when oxygen interstitial concentrations are higher and interstitials are in closer proximity to one-another, but that *Willis* and *di-interstitial* clusters do not form at lower O:M ratios. RMC results show no evidence for these types of atomic arrangements because no short O-O pairs aligned along <110>-type directions were observed. One alternative explanation for the remaining discrepancy between experiment and theory (DFT) lies with the main limitation of RMC modeling. RMC models the atomic structure whereas the DFT is a means to model electronic structures. Electronic structure modeling through RMC can only be approximated indirectly *via* use of bond valence sum constraints. It's well known that defect clustering is largely driven by a delicate balance between repulsive forces from Coulomb interactions and attractive forces derived from orbital hybridization [172]. It's therefore possible that electronic structure dictates short O-O interatomic orientations, and

this determines <110> or <111>-type orientation. The open question that remains is whether or not high entropy from elevated thermal energy is sufficient to outweigh effects electronic effects, such as orbital hybridization. A computational study of UO_{2+x} at elevated temperature suggests that electronic modifications, specifically electron transport and uranium charge flipping ($U^{4+} \leftrightarrow U^{5+}$), precedes atomic restructuring and suggests that thermally-induced entropy effects outweigh electronic effects on clustering at elevated temperatures [189]. Further work combining experimental atomic- and electronic structure modeling is needed in order to resolve the remaining discrepancy between experimental and computational observations.

Conclusions and Recommendations

Atomic structures of stoichiometric and hyper-stoichiometric UO_2 were characterized using Raman spectroscopy and neutron total scattering in order to identify point defect ordering schemes and to eliminate pre-existing discrepancies between experimental and theoretical defect structure models. Stoichiometries of the two samples were precisely determined before and after structural characterization using both lattice parameter measurements and combustion analyses. Combustion analyses were aided by impurity element measurements in order to account for weight gain effects from oxidation of impurity elements. Independent lattice parameter measurements from X-ray diffraction and neutron diffraction were in agreement with combustion analysis results and showed that the two materials possessed stoichiometries of $UO_{2.00}$ and $UO_{2.07}$.

Raman spectroscopy measurements performed at room temperature confirmed that $UO_{2.00}$ exhibited pristine atomic arrangements and negligible atomic disorder from oxidation. Similar measurements of $UO_{2.07}$ showed evidence for fluorite-structure atomic arrangements in coexistence with atomic disorder from oxidation effects. Deconvolution and peak fitting of a defect band suggested that atomic disorder was attributed to the incorporation of oxygen interstitials, possibly in defect cluster arrangements, and the subsequent breakdown of Raman selection rules.

Neutron diffraction analysis confirmed that both materials exhibited well-ordered fluorite-structure domains. Fitting of the diffraction patterns by Rietveld refinement

demonstrated that the lattice contracted upon oxidation and both materials underwent thermal expansion at rates that are in agreement, but slightly faster, than thermal expansion rates cited in the literature. The unit cell parameter and thermal expansion measurements were in agreement with recently published studies suggesting that the room-temperature unit cell parameter and thermal expansion rate of $UO_{2.00}$ are higher than previously assumed.

Detailed analysis of Rietveld refinement variables, such as temperature-dependent atomic displacement parameters (ADPs), illustrated that $UO_{2.07}$ is likely a mixture of single-phase UO_{2+x} and a U_4O_{9-y} phase below ~600 °C despite the Rietveld refinement fit result that showed that $UO_{2.07}$ is fit very well with a single fluorite structure phase and no U_4O_9-type phase. A close inspection of ADP temperature dependences indicated critical temperatures of ~100 and ~500 °C for $UO_{2+x\,(s)} + \alpha\text{-}U_4O_{9-y} \rightarrow UO_{2+x\,(s)} + \beta\text{-}U_4O_{9-y}$ and $UO_{2+x\,(s)} + \beta\text{-}U_4O_{9-y} \rightarrow UO_{2+x\,(s)}$ phase transitions, respectively. These critical temperatures were in agreement with the established uranium oxide phase diagram.

The neutron pair distribution functions (PDFs) of single-phase $UO_{2.07}$ (UO_{2+x}) at 600 and 1000 °C were modeled by both small-box and reverse Monte Carlo (RMC) methods. Small-box refinement of the PDFs showed that the Willis 2:2:2 cluster model fits the local structure of $UO_{2.07}$ the best for data collected at both 600 and 1000 °C. This was in contrast to RMC models that suggested the presence of isolated, distorted, octahedral-type interstitials. RMC models, unlike small-box models, were in agreement with data at all length scales (diffraction pattern, D(r), and G(r)) and were more chemically-sensible owing to the use of bond valence sum constraints. RMC models suggested that interstitials were too diffuse in $UO_{2.07}$ to form Willis- or di-interstitial-type clusters. Rather, isolated interstitials formed small clusters comprising 1-4 displaced lattice oxygens and a single oxygen interstitial displaced from the octahedral site and oriented along a <111>-type direction in respect to the displaced lattice oxygens. Future work combining experimental atomic- and electronic structure modeling is needed in order to resolve the remaining discrepancy between experimental and computational observations.

CHAPTER III: POINT DEFECTS IN RARE-EARTH-ELEMENT-DOPED URANIUM DIOXIDE

A version of this dissertation chapter is presented in an unpublished manuscript by Sarah Finkeldei, Raul I. Palomares, Angela Baena, Joerg Neuefeind, Maik Lang, and Felix Brandt. The manuscript is currently in preparation for submission to a scientific peer-review journal.

S.F. and F.B. conceived of the experiments; S.F. and A.B. prepared the samples; R.I.P., S.F., and J.N. performed the neutron scattering and Raman spectroscopy experiments; R.I.P. and S.F. performed analysis and interpretation of the experimental data; S.F. wrote the manuscript with input from all co-authors.

Abstract

Rare earth elements, such as Nd, are readily soluble in the UO_2 fluorite structure and can form a diverse array of solid solutions. This doping process occurs naturally in nuclear fuel during in-pile operation, as rare earth elements have a relatively high fission yield. Rare earth oxide additives can also be incorporated by design during fuel fabrication as a strategy to improve reactor efficiency and to mitigate deleterious features, such as fission gas release. Studies have shown that rare earth elements significantly influence electrochemical properties of UO_2 and can even modify oxidation kinetics. This study investigated atomic structure modifications in UO_2 before and after doping with Nd in order to identify potential defect clustering signatures. Structural changes were characterized using a combination of neutron total scattering and Raman spectroscopy. Analyses revealed that small loadings of Nd cause local atomic distortions in the very short range structure (< 10 Å) of the UO_2 materials. Small-box modeling of neutron pair distribution functions showed that these distortions were consistent with extremely small (< 1 Å) atomic relaxations. The magnitude of atomic relaxation was weakly correlated with the amount of loading at very low doping levels and suggested that distortions in local arrangements were caused by differences in U and Nd coordination environments. Preliminary reverse Monte Carlo modeling confirmed this and showed direct evidence for oxygen vacancy clustering that was formerly predicted by density functional theory studies. Trapping of oxygen vacancies in clusters influences both oxygen vacancy and

interstitial migration. Therefore, these defect clustering schemes must be taken into account in order to better predict corrosion kinetics of spent nuclear fuel.

Introduction

Doping of UO_2 with additives is a useful strategy for improving the properties of UO_2-based nuclear fuel. Oxide additives comprising Nb, V, Ti, Cr, Al, and Nd are shown to improve the sintering properties of UO_2 during pellet fabrication and often result in higher pellet densities and larger grain sizes [250, 251]. Larger UO_2 grain sizes often suppress fission gas release and can mitigate the onset of grain subdivision, so-called *rim structure*, compared to UO_2 fuels of finer grain structures, when irradiated to similar burnup levels [251]. Oxide additives such as Er_2O_3 and Gd_2O_3, which are strong neutron absorbers, can also be mixed into UO_2 in order to indirectly improve reactor efficiency. This is accomplished through the strategic placement of spiked fuel bundles in different areas of the reactor core. The effects are often flatter and more optimized power profiles that improve overall efficiency and lifetime of nuclear fuel [252].

Chemical doping of UO_2 nuclear fuel also occurs naturally during the course of operation as uranium fissions. Besides volatile fission products (*e.g.*, Xe and Kr), noble metals (*e.g.*, Ru and Rh), and elements forming separate oxides (*e.g.*, Ba and Cs), one of the largest fission product groups are the rare earth and actinide elements that are soluble in the UO_2 fluorite structure [253]. The interplay of these elements in the UO_2 matrix is of great interest because the incorporation of rare earth elements increases the oxygen potential of the material [254]. Oxygen potential and oxidation rate in turn greatly affect key engineering properties, such as fission gas retention [124].

Rare earth elements, such as Nd and La, are incorporated into the fluorite lattice at the 4*a* cation site. It's often assumed, based on diffraction phase analysis, that rare earth dopants and host uranium atoms form a perfect fluorite structure solid solution. This is unlikely however because uranium and rare earth elements differ in chemistry. Rare earth dopants like Nd are trivalent whereas uranium often takes on +4 and +5 valence states in cubic fluorite-type structures [246, 255]. This difference in cation chemistry is often accompanied by variations in local coordination. Trivalent dopants in oxides are often

surrounded by fewer oxygen atoms and exhibit distorted coordination environments, such as distorted mono-capped polyhedra [100], which are quite different from that of perfectly cubic UO_8 units. This stark difference in expected coordination environments suggests that structural modulations occurring at intermediate-range length-scales (10-50 Å) hold the key to understanding how distorted local environments result in bulk, averaged fluorite structures.

The accommodation of distorted local units appears to be related to the ability of the fluorite structure to exhibit strong phase stability from room temperature up to the melting temperature, even under large deviations from perfect stoichiometry. This unique feature is quite evident for rare-earth element (REE)-doped UO_2, as these materials can be either *hypo*-stoichiometric, stoichiometric, or *hyper*-stoichiometric. Resultant stoichiometry of rare earth element-doped UO_2 is strongly dependent on fabrication history, such as sintering atmosphere and quenching rate. Doped oxides that are fully *hypo*-stoichiometric and perfectly stoichiometric represent materials in which charge compensation for trivalent REE dopants is fully compensated by oxygen vacancies and uranium oxidation ($U^{4+} \rightarrow U^{5+}$), respectively. Doped oxides, like pure UO_2, can also incorporate adventitious oxygen leading to the formation of $REE_xU_{1-x}O_{2+y}$–type phases [256, 257].

Elucidating the exact mechanisms for REE incorporation can lend valuable information for better understanding the behavior of soluble fission products in UO_2. Studies often emphasize the effects of REE doping on short-range defect structures because this behavior is strongly tied to defect energetics and can influence diffusion properties. For example, REE dopants often attract oxygen vacancies (O_v) and form REE-O_v defect complexes that trap vacancies and inhibit vacancy migration [258, 259] . This decrease in available oxygen vacancies can influence electrochemical reactivity, which is a key factor in predicting fuel corrosion behavior [239]. Prevalent clustering of vacancies is also thought to inhibit oxygen interstitial migration [258] and interstitial accommodation mechanisms in the fluorite structure. The latter claim is based on Raman spectroscopy and X-ray diffraction observations showing that REE-doped UO_2 can sometimes bypass U_4O_9 formation during oxidation from UO_2 to U_3O_8 [238]. Further evidence suggests that doping

influences phase stability and can cause unexpected phase separation at lower temperatures [260-263].

This study investigates the effects of Nd^{3+}-doping on the structure of UO_2. This study is the first part of an ongoing research plan that will incorporate an increasing amount of elements, such as noble metal precipitates (so-called ε-particles), into UO_2 materials in order to better emulate spent fuel and to identify the effects of these foreign additives on corrosion susceptibility. Emphasis is placed on characterizing short-range atomic ordering schemes through the use of local structural probes, such as Raman spectroscopy and neutron total scattering. Reverse Monte Carlo modeling introduced in Chapter II of this Dissertation is applied to the Nd-doped UO_2 data and preliminary results and recommendations are presented.

Results and Discussion

Neutron Diffraction – Average Structure

All samples were studied using neutron diffraction in order to characterize average structure modifications and to confirm that all materials exhibit the cubic fluorite structure after chemical doping. At first glance, all materials showed peaks consistent with the fluorite structure. Rietveld refinement of the neutron diffraction patterns confirmed this and showed that there is no evidence of secondary phases and phase separation. If secondary phases form as a result of atomic immiscibility, they are below or very near the limit for detection. Figure 76 shows the Rietveld refinement results undoped UO_2 and UO_2 with the highest Nd doping level. The comparison shows that both diffraction patterns are in good agreement with the fitted fluorite structural model and both show very similar features. The background level of the $Nd_{0.133}U_{0.867}O_{2\pm y}$ diffraction pattern is similar to that of the undoped sample. This is somewhat surprising because local structural disorder typically causes an increase in diffuse scattering, which appears as an increase in background (*i.e.*, decreasing signal-to-noise ratio) in the diffraction pattern. The lack of strong diffuse scattering, even for the highest doped specimen, suggests that all samples exhibit well-ordered fluorite-type domains. The diffraction patterns of all of the other UO_2 and Nd-doped UO_2 samples are not shown for brevity, but they all exhibited very similar

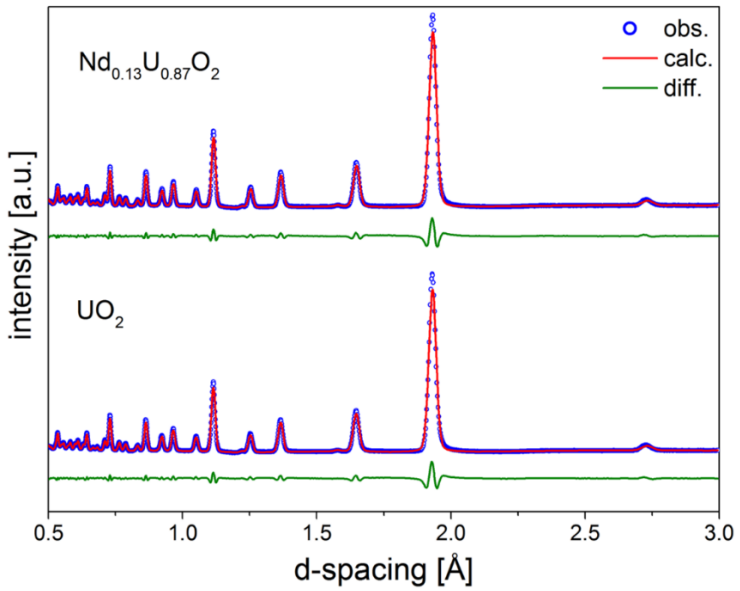


Figure 76: Comparison of neutron diffraction patterns of undoped UO_2 (bottom) and Nd-doped UO_2 with the highest Nd loading (top). Both diffraction patterns were fit with the cubic fluorite structure. Both materials are composed of a single cubic phase

features and were also fit very well with fluorite structure models.

Besides phase analysis, Rietveld refinement is also useful for extracting structural parameters, such as unit cell parameters, atomic site occupancies, and atomic displacement parameters (ADPs). All diffraction patterns were fit with a fluorite structure model assuming a completely random solid-solution, *i.e.*, uranium and neodymium atoms are randomly distributed among the lone 4*a* cation site and oxygen atoms occupy the lone 8*c* anion site in the fluorite structure (space group *Fm*-3*m*). The unit cell parameters derived from Rietveld full profile refinement are shown in Figure 77 plotted against Nd content, *x*, in atomic fraction. The data are plotted alongside various cell parameter evolution models referenced in [264]. The trend line labeled, $Nd_xU_{1-x}O_{2-y}$, represents the evolution of the cell parameter when charge compensation for Nd^{3+} dopants is fulfilled fully by oxygen vacancies. This line therefore represents fully reduced samples. The trends labeled $Nd_xU_{1-x}O_2$ (U^{5+}) and $Nd_xU_{1-x}O_{2-y}$ (U^{6+}) are cell parameter relationships calculated for systems in which charge compensation for Nd^{3+} dopant atoms is fully fulfilled by oxidation of uranium from U^{4+} to U^{5+} and U^{6+}, respectively.

The latter is quite unlikely for these samples doped with low concentrations of Nd considering the very different cation coordination geometry required for U^{6+} cations. The prevalent formation of U^{6+} in the fluorite structure would likely trigger a phase transformation to an orthorhombic-type structure like U_3O_8 in which U^{6+} is more easily accommodated. Experimental evidence for this comes from studies of the Zr-U-O system in which a U:Zr ratio of 2:1 resulted in a transformation from the fluorite structure to an orthorhombic *Cmcm*-type structure with approximately equal concentrations of U^{4+} and U^{6+} [265]. Theoretical studies [266] have also shown that the disproportionate reaction, $U^{6+} + U^{4+} \rightarrow 2U^{5+}$, is energetically favorable and thus U^{5+} is preferred over U^{6+} in the fluorite structure. The relationship for $Nd_xU_{1-x}O_{2-y}$ (U^{6+}) was thus plotted for reference, but it is noted that cell parameters in this regime are likely attributable to mixed contributions from vacancies and U^{5+} cations, *i.e.*, a linear combination of $Nd_xU_{1-x}O_{2-y}$ (charge compensation from vacancies) and $Nd_xU_{1-x}O_2$ (U^{5+}) (charge compensation from $U^{4+} \rightarrow U^{5+}$ oxidation).

One advantage of using neutron diffraction as opposed to X-ray diffraction is the

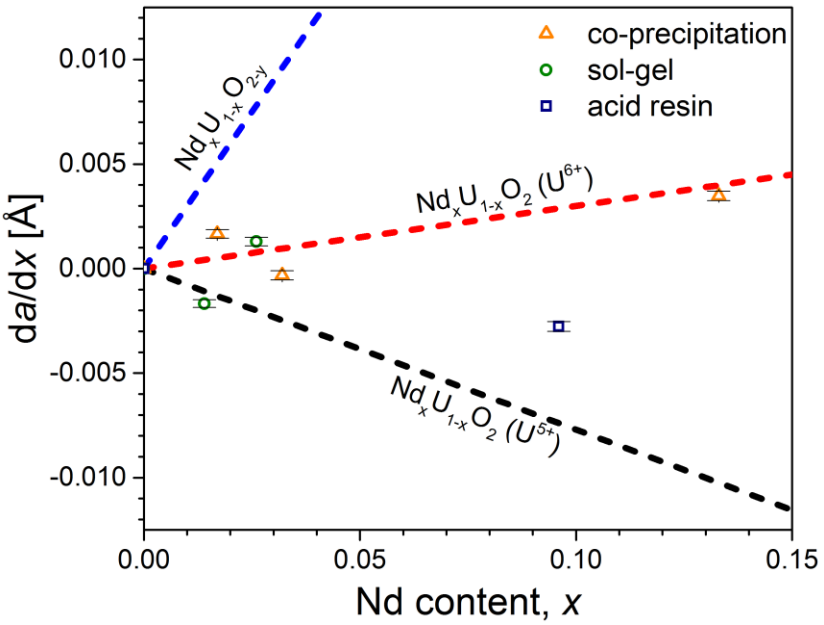


Figure 77: Evolution of unit cell parameters of UO_2 and Nd-doped UO_2 samples with varying Nd content

increased sensitivity to the oxygen sublattice. This sensitivity permits the refinement of the oxygen 8*c* site occupancy, which is a measure of the oxygen vacancy concentration in the system. The refined site occupancy values for all samples are shown in Figure 78. A site occupancy value of 1 would indicate that the 8*c* oxygen site is 100% occupied and there are nearly no oxygen vacancies in the system. The refinement results show that all samples have 8*c* site occupancy values less than 1, indicating the presence of vacancies. Surprisingly, all samples except for $Nd_{0.133}U_{0.867}O_{2\pm y}$ show similar occupancy values within experimental uncertainty. The site occupancy value of $Nd_{0.133}U_{0.867}O_{2\pm y}$ is ~0.01 (1%) less than the other samples. The large discrepancy between the value for the $Nd_{0.133}U_{0.867}O_{2\pm y}$ sample and the others is likely attributable to the reported miscibility gap of Nd-doped UO_2 at room temperature [260-263].

Biphasic mixtures have been observed in UO_2 specimens doped with ~6–25 atom percent Nd [263]. Interestingly, reported observations show that both phases exhibit fluorite structure characteristics with no evidence for Nd_2O_3 formation. Initial observations suggested that the miscibility gap results from non-homogeneous Nd distributions and the production of Nd-rich and less Nd-rich areas. Reported Raman results suggest that the two phases represent sub-stoichiometric $Nd_xU_{1-x}O_{2-y}$ and stoichiometric $Nd_xU_{1-x}O_{2.00}$ phases in which charge compensation of Nd^{3+} is achieved through the incorporation of oxygen vacancies and oxidized U^{5+} cations, respectively [262]. This was supported by diffraction data showing that one phase (presumably $Nd_xU_{1-x}O_{2-y}$) shows an expected linear change in cell parameter with Nd content whereas the second phase (presumably $Nd_xU_{1-x}O_{2.00}$) shows a non-linear change. Charge compensation of Nd^{3+} by both vacancies and U^{5+} cations is very likely for the present samples based on Figure 77.

If the miscibility gap of Nd-doped UO_2 occurs for compositions with ~6-25 atom percent as reported, then the $x = 0.096$ sample in the present study should also exhibit non-linear behavior relative to lower dopant levels, as shown for $x = 0.133$. This is was not observed and suggests that the miscibility gap may be suppressed or manipulated by employing different synthesis routes. The $x = 0.096$ sample was produced by an acid resin synthesis route unlike the other samples that were produced by co-precipitation and sol gel synthesis methods. Further systematic study of acid resin samples is needed in order to

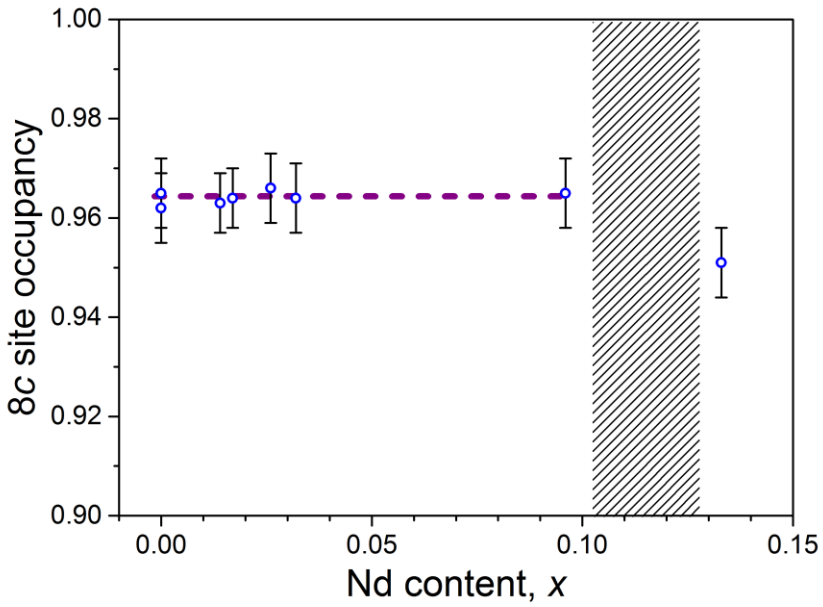


Figure 78: Refined 8*c* site occupancy values vs. Nd content in the UO_2 samples

elucidate the effect of synthesis route on miscibility or immiscibility behavior. The relatively low 8*c* site occupancy value of $Nd_{0.133}U_{0.867}O_{2\pm y}$ might represent the average of the 8*c* occupancy values of the vacancy- and U^{5+}-rich phases that are indiscernible from Rietveld analysis. For example, if it is assumed that the U^{5+}-rich phase has a site occupancy value of 1.00, then the occupancy value of the vacancy-rich phase would be 0.94 in order to yield the average value of ~0.97 that is observed for $Nd_{0.133}U_{0.867}O_{2\pm y}$.

Further evidence supporting the presence of a miscibility gap is given by the atomic displacement parameters (ADPs). The ADPs represent the spatial average of instantaneous atomic displacements from the pristine 4*a* and 8*c* atomic coordinates. The symmetry of the fluorite structure dictates that the ADPs of cations and anions are isotropic. The ADP of a certain Wyckoff site can therefore be visualized as a sphere whose diameter represents the magnitude of the instantaneous atomic displacements for that Wyckoff site. It's noted that both static and dynamic disorder can contribute to the ADP. ADPs typically increase with temperature owing to an increase in thermal disorder. However, very small static displacements from pristine Wyckoff sites can also be incorporated in the ADP sphere. A system possessing small static displacements caused by atomic restructuring (*e.g.*, phase transformations) will yield ADPs that are unusually large.

An unusual change in the overall ADP evolution is clearly seen for the Nd-doped samples. Figure 79 shows that ADPs for the 8*c* oxygen site and the 4*a* mixed U/Nd cation site for all samples. The figure shows that at low dopant levels, the trend is as expected. All samples were measured at room temperature and atoms should therefore have similar thermal ADP contributions. Any increase in the ADPs should arise from static atomic displacement, *i.e.*, disorder. The data show that this is indeed true. The change in the magnitude of the cation ADP is negligible, in agreement with the understanding that disorder primarily occurs on the oxygen sublattice due to the high energy penalty associated with cation defects compared to anion defects. The change in the oxygen ADP, however, shows a gradual increase with increasing dopant concentration. The trend shows that the level of doping is correlated with the level of atomic disorder on the anion sublattice. The data also show that a large change occurs between the last two data points. This is in agreement with the site occupancy data and suggests that there is a miscibility

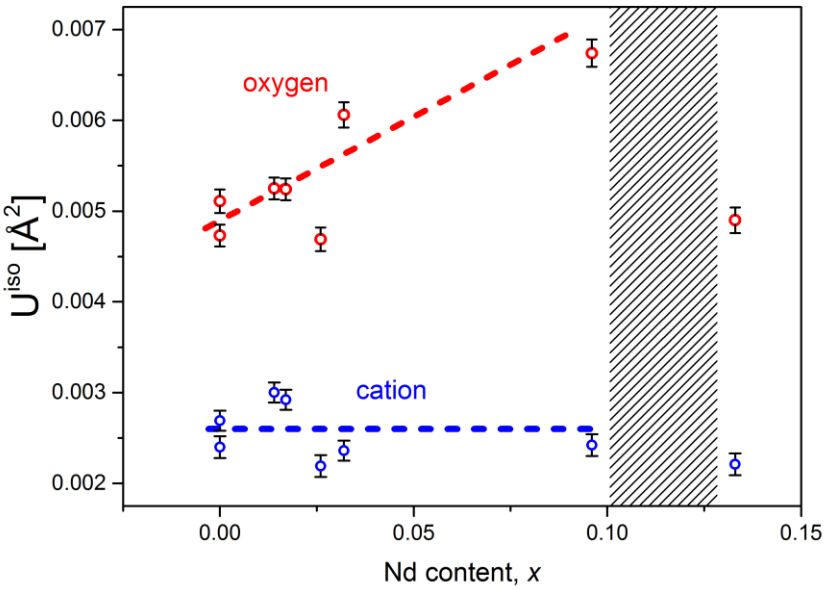


Figure 79: Change in isotropic atomic displacement parameters of the oxygen and cation sites with varying Nd concentration

gap above ~10 atom% Nd. The phase transformation into well-ordered vacancy-rich and U^{5+}-rich domains likely occurs to relieve internal strain. The well-ordered nature of the two types of domains, which are both fluorite structure domains, would result in a decrease in the ADP value because there is a large decrease in static atomic disorder within the two domains.

Raman Spectroscopy – Local Structure and Vibrational Properties

Raman spectroscopy is extremely sensitive to small changes in vibrational properties and is therefore a useful tool for probing the effects of dopant Nd^{3+} cations. The coordination environments of trivalent and tetravalent cations are usually quite different and should therefore exhibit characteristic vibrational signatures. These signatures can be used to characterize the evolution of short range ordering with increasing Nd content.

UO_2 only exhibits one Raman-active vibrational mode. This mode is the triply-degenerate T_{2g} mode which represents the breathing mode of UO_8 coordination environment. Figure 80 shows the Raman spectra for all undoped and doped UO_2 samples. The figure shows the T_{2g} mode is indeed present for all materials at ~445 cm^{-1}. Besides the T_{2g} mode, the spectra show that increasing the Nd loading level causes the emergence of a defect feature in the frequency range ~480–650 cm^{-1}. Similar features have been observed in many ThO_2 [267] CeO_2 [91] and UO_2 [237-239, 241-243, 262, 263] compounds doped with trivalent ions and are attributed to various defect complexes and anion substructure modifications.

Systematic studies have shown that the broad defect structure between ~480 and ~650 cm^{-1} comprises three distinct defect bands located about ~540, ~575, and ~620 cm^{-1} [238]. Following the notation of Lee *et al*. [239], the defect bands are hereafter referred to as the α, β, and γ peaks, respectively. The α band at ~540 cm^{-1} has been attributed to oxygen vacancies based on similar observations in rare-earth element doped CeO_2 [268]. These interpretations are supported by *ab initio* investigations of anion-deficient, isostructural CeO_2 [89]. The clearest evidence comes from studies of UO_2 doped with Th^{4+}. Thorium only exhibits the tetravalent state in the oxide form; therefore, there is no need to charge compensate Th^{4+} dopant atoms with oxygen vacancies. Raman studies of U-Th-O

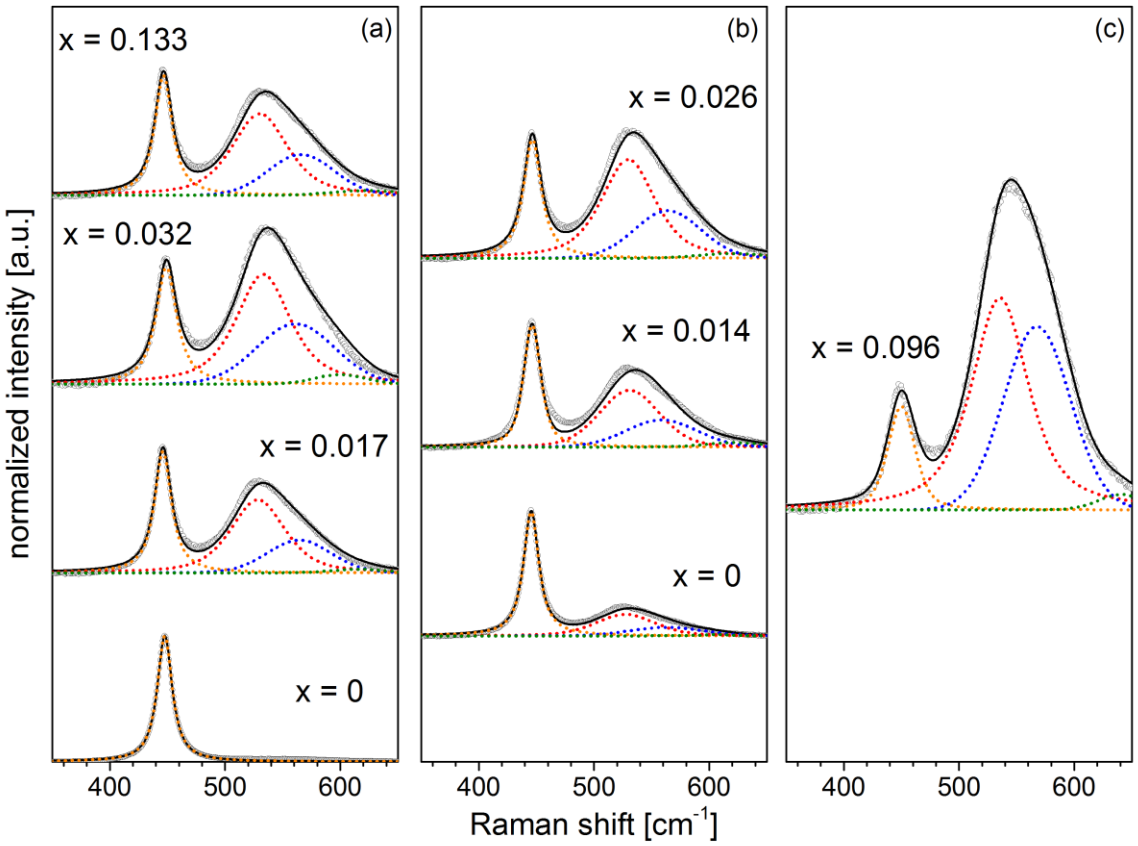


Figure 80: Raman spectra of UO2 and Nd-doped UO2 samples prepared by (a) co-precipitation, (b) sol gel, and (c) acid resin synthesis routes. The values of *x* denote the loading level of Nd in atomic fraction (*e.g.*, *x* = 0.017 is equivalent to 1.7 atom% Nd). The data are shown as grey circles and the colored dotted lines represent fitted peaks. The black lines show the overall fit of the peaks to the data

compounds revealed no evidence of a defect band at ~540 cm^{-1} [267], which suggests that the peak is indeed associated with vacancy complexes.

The higher frequency β and γ bands at ~575 and ~620 cm^{-1} have been attributed to the normally forbidden longitudinal optical (LO) T_{1u} vibrational mode and the presence of secondary U_4O_9-type atomic ordering with a characteristic A_{1g} stretch mode, respectively. Both features were observed in Raman studies of oxidized uranium oxide (U_4O_9) [223]. It's assumed that the LO mode is made Raman-active by structural disorder, in this case point defects, which causes a breakdown of Raman selection rules [222]. The γ peak has also been observed in hypo-stoichiometric Zr^{4+}-doped $Ce^{4+}O_2$ compounds and was attributed to the ZrO_8 complex because Ce^{4+} and Zr^{4+} have different ionic radii [242].

All Raman spectra were fit with four pseudo-Voight peaks in order to extract the defect band properties and to evaluate the evolution of the bands with increasing doping level. Figure 81 shows the evolution of the defect peak areas with increasing doping level. In each case, the defect band peak areas were normalized to the area of the F_{2g} peak to enable direct comparison between the different measurements. The figure shows that the defect peaks grow approximately linearly with increasing doping level below approximately 10 atom% Nd. Above this threshold, there is a drastic drop in defect band intensity. The drastic drop between x = 0.096 and x = 0.133 coincides with the aforementioned miscibility gap in Nd-doped UO_2 at room temperature.

The trend observed for the α-peak indicates that the oxygen vacancy concentration gradually increases with increasing dopant level up to the approximate composition $Nd_{0.1}U_{0.9}O_{2\pm y}$. Upon reaching ~10 atom% Nd, there is a large decrease in the α-peak area ratio. A similar drop in peak area ratio was reported for stoichiometric Gd-doped UO_2 samples [243], but was not observed for hypo-stoichiometric Gd-doped UO_2 samples [239]. This suggests that excess oxygen may be needed in order to trigger the phase separation into vacancy-rich and U^{5+}-rich phases. In the hypo-stoichiometric samples, all of the charge compensation for Nd^{3+} is produced by vacancies; therefore, the area of the α-peak is expected to increase linearly with the dopant concentration.

The β and γ peaks also show a gradual increase and an abrupt drop at ~10 atom% Nd. The increase in β area correlates with an increase in atomic disorder on the anion

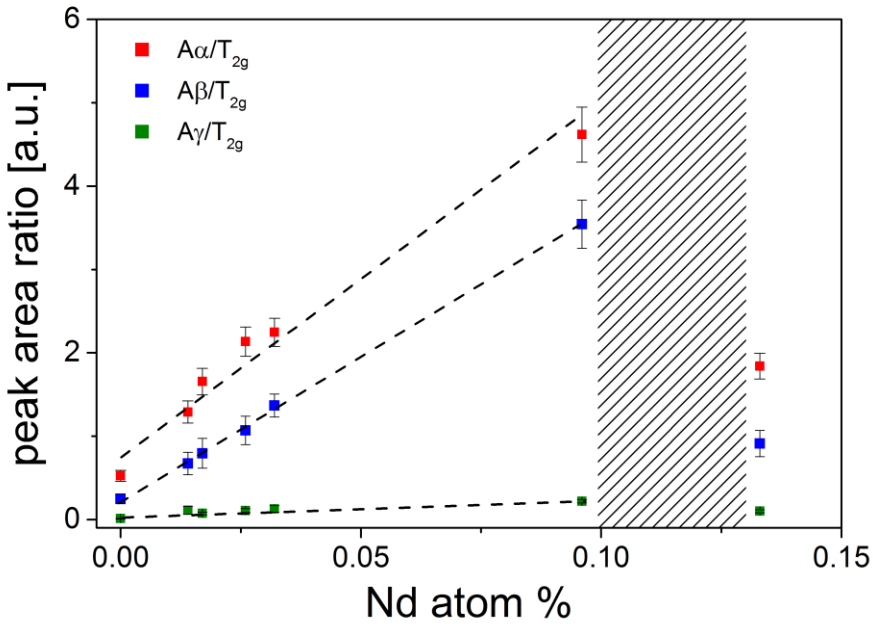


Figure 81: Change in normalized peak areas with increasing Nd doping level. Peak areas were derived by peak fitting of the defect bands in the Raman spectra. The shaded region highlights the large discontinuity between the last two data point sets and the dashed lines are included to guide the eye

sublattice, which promotes a breakdown of Raman selection rules and the activation of the LO mode. This is in agreement with the Rietveld refinement results that showed increasing oxygen ADPs with increasing dopant concentration. The area of the γ peak is the smallest of all the defect bands, but it shows a small increase nonetheless. Although the γ peak has been attributed to MO_8 arrangements [242], there is overwhelming evidence from studies of uranium oxides to suggest that the peak is instead associated with either U_4O_9 formation [238] or the formation of cuboctahedral interstitial oxygen arrangements [223], which are vital building blocks to the U_4O_9 structure [220]. The low intensity of the γ peak in all Raman spectra suggests that the materials exhibit strong fluorite structure characteristics, which is in agreement with the Rietveld refinement results.

Neutron Pair Distribution Function Analysis – Local Structure

Neutron diffraction analysis showed that the average structures of all samples are cubic and Rietveld refinement confirmed the preservation of well-ordered fluorite-type domains after doping. However, both Rietveld and Raman analysis results showed evidence for atomic disordering, primarily on the anion sublattice. Neutron pair distribution function (PDF) analysis was employed in order to better probe these anion substructure modifications through inspection of short range atomic ordering.

Figure 82 shows the PDFs for all doped and undoped samples measured at room temperature. The PDFs are cropped from 2-5 Å to highlight the short range structure of the materials. Each peak in the PDF corresponds to one or more characteristic interatomic distance in the material. The first and second peaks in this case correspond to the first nearest-neighbor (1-NN) cation-oxygen and oxygen-oxygen distances, respectively. After that, the peaks begin to overlap and large peaks comprise multiple atomic correlations. For example, the third peak in the PDF is attributed to the second nearest-neighbor (2-NN) oxygen-oxygen and the 1-NN cation-cation distances.

The PDFs exhibit sharp peaks and there is no large systematic change in peak position or peak intensities. This is in agreement with the diffraction data and shows that the materials are highly crystalline and ordered even at the shortest length scales. The minor ripples between ~3-3.5 Å are attributed to Fourier ripples and not actual interatomic

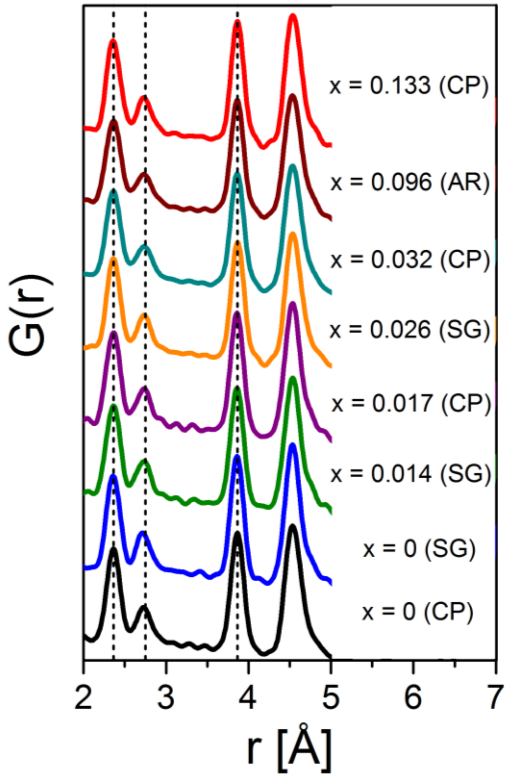


Figure 82: Neutron pair distribution functions of all undoped and Nd-doped UO_2 samples

distances. Fourier ripples arise from the truncation of the *Q* range prior to performing the Fourier transform to obtain the PDFs. At a glance, the changes in the PDF are very subtle and barely discernable. The largest changes appear to occur to the second peak. This is not surprising because this peak is attributed to oxygen-oxygen correlations. This agrees with the diffraction and Raman analysis results showing that most modifications occur on the oxygen sublattice. Small-box structural refinement was applied in order to better characterize these subtle changes to the PDFs.

Small box refinement is very similar to Rietveld refinement in that it is a least-squares fitting procedure. A simple atom ensemble containing 4 cations and 8 anions was first constructed. Afterwards, the PDF is simulated and the model was modified until the simulated PDF better matched the experimentally measured PDF. The starting model was a fluorite structure model based on the Rietveld refinement results, *i.e.*, the average structure. The symmetry was set to *Fm*-3*m* and the unit cell parameters, site occupancy values, and ADPs were copied from the Rietveld refinement results. The PDF conveys information about the short and intermediate-range structure. Therefore, by fitting the average structure model to the PDF in this way, one can immediately observe the differences between the average structure and the shorter range structure.

The initial average structure fits, sometimes called *GSAS fits*, were quite poor. It is possible that was due to resolution effects. For example, it is well known that the extent of *Q*-range truncation during the Fourier transform affects the lattice parameter conveyed by the PDF [269] and the PDF is affected by correlated motion among atoms. The latter is modeled using a correlated motion parameter implemented in the small-box refinement procedure. However, there is no equivalent parameter in Rietveld refinement and this parameter must be estimated at the start of the small-box refinement procedure. In order to obtain a better representation of the actual structure, the initial average structure models were optimized by relaxing the lattice parameters, atomic displacement parameters, overall scale, and correlated motion parameter. An example of a relaxed structure fit to a PDF is shown in Figure 83.

The relaxed structure fit to the entire PDF is illustrated by the purple line. The residuals, plotted as a green line, showed similar behavior for all samples. All difference

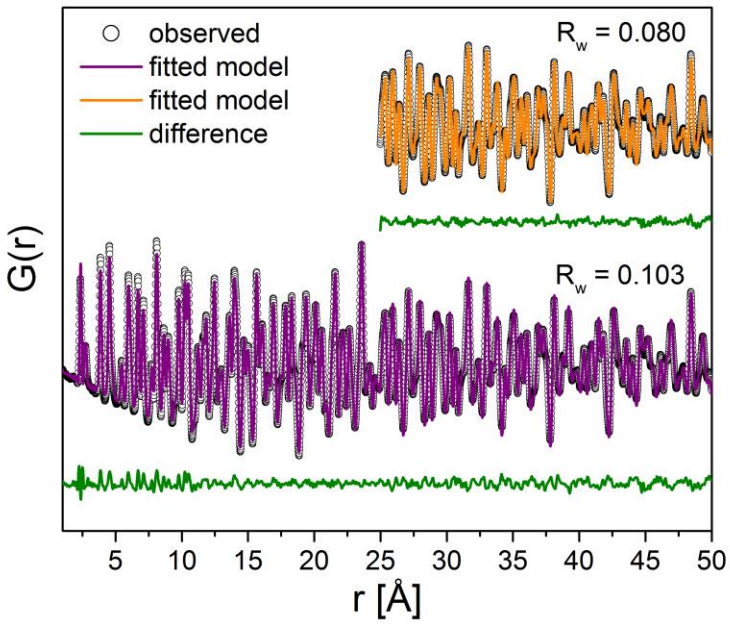


Figure 83: Comparison of small-box modeling fit results for the full-range pair distribution function (purple) and for a cropped range (yellow). The cropped PDF corresponds to an R_{min} value of 25 Å whereas the full range PDF corresponds to an R_{min} value of 1 Å. The R_w values listed represent the weighted goodness-of-fit of the fluorite structure model fitted to the data

curves showed high intensity in the low (~0-15 Å) and high (~30-50 Å) *r* regions, and lower intensity in the intermediate *r* region (~15-30 Å). This dumbbell-type shape is characteristic of a discrepancy between short and long range structures. When the short and long range structures are different the program cannot fit the entire PDF well. The program will attempt to fit both the short and long range structures equally well and this results in the program fitting the intermediate region the best and the short and long-range structures slightly worse.

A powerful technique capable of determining the cross-over region between the unique short- and average structures is the so-called boxcar fitting method. In this method, the goodness-of-fit, R_w, is monitored as the structure is sequentially refined over different *r* ranges. The goodness-of-fit parameter is defined as:

$$R_w = \sqrt{\frac{\sum_{i=1}^{n} \omega(r_i)\,[G_{obs}(r_i) - G_{calc}(r_i)]^2}{\sum_{i=1}^{n} \omega(r_i)\,G_{obs}^2(r_i)}}$$

where G_{obs} is the experimentally measured PDF, G_{calc} is the simulated PDF, and $\omega(r_i)$ is a weighting factor. Since the high *r* region is more representative of the average structure than the low *r* region, the upper bound to the *r* range was fixed and the lower bound to the fitted *r* range was varied. Fitting regions with different r_{min} values in this way enables one to vary the contribution of the short range structure to the fitted *r* region. For example, the regions $25 < r < 50$ Å, $12 < r < 50$ Å, and $0 < r < 50$ Å have the least, more, and most contributions from short range ordering.

The results from boxcar fitting are presented in Figure 84. The figure shows the relative change of the R_w values with varying r_{min}. All samples show similar long-to-short range structure crossover points at ~15 Å. This indicates that the effects of local structural distortions caused by point defects and dopant Nd^{3+} cations only extend up to ~15 Å. Beyond this point, the effects diminish and are essentially averaged out either by structural modulations or some other mechanism. Another notable feature in Figure 84 is that the undoped reference samples also show long-to-short range crossover behavior. This may be due to slight oxidation of the samples, as the oxygen content was not controlled during

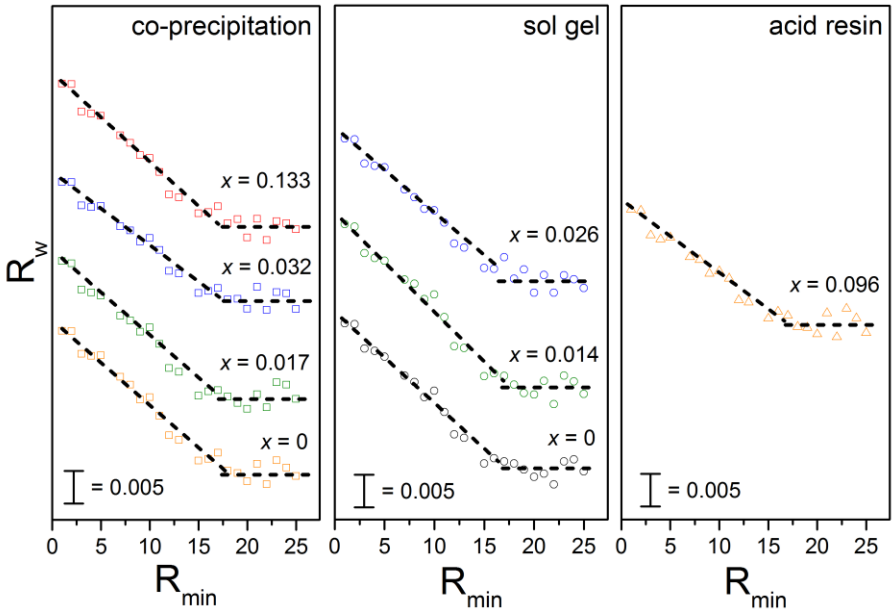


Figure 84: Relative change in goodness-of-fit value, R_w, with varying R_{min} value. Note: the data are offset along the *y*-axes. The R_{min} value denotes the lower bound to the fit range for the small-box PDF modeling. The R_{max}, or upper bound to the fit range, was always fixed at 50 Å. The results are separated based on the synthesis route labeled at the top right. The *x* values denote the atomic fraction of Nd in the system and the scale bars show the magnitude for $R_w = 0.005$

synthesis. Oxidation of UO_2 to UO_{2+x} leads to the accumulation of oxygen interstitials in the lattice. Oxygen interstitials in UO_{2+x} are known to agglomerate and form various types of defect clusters that distort the anion sublattice.

Having estimated the domain size of the short-range defect structure, the PDFs were closely inspected in order to identify the features contributing to discrepancies between the fitted model and the data. Figure 85 shows an example of this short-range analysis for the samples prepared by the co-precipitation method. The fit results showed excellent agreement within the range 0-15 Å, making it difficult to interpret small discrepancies. To this end, the error bars of the PDFs were plotted alongside the difference curves in order to identify discrepancies that are statistically significant, *i.e.*, the intensity of the difference curve exceeds the limits of experimental uncertainty.

Plotting the bounds of uncertainty showed that the discrepancy is associated with the 1-NN cation-oxygen peak. This peak is attributed to both U-O and Nd-O distances and suggests that local distortions in Nd-doped UO_2 arise from the different coordination environments of U^{4+}, U^{5+}, and Nd^{3+}. There is no observable correlation between the magnitude of distortion and the doping level. The magnitude of distortion is largest for the samples doped with 1.7 and 13.3 atom% Nd and smallest for the undoped sample and the sample doped with 3.2 atom% Nd. All samples show at least a small amount of distortion indicating that peak broadening is caused by both U^{5+} and Nd^{3+} cations. In the undoped case, the small amount of distortion can only be attributed to U^{5+} and oxygen interstitials. In the doped samples, the local distortion can be attributed to U^{5+}, oxygen interstitials, Nd^{3+}, and oxygen vacancies. Oxygen interstitials are typically associated with U^{5+} (see for example ref. [172]) whereas oxygen vacancies have a tendency to cluster with trivalent cations [259].

Figure 77 shows that the sample doped with 1.7 atom% Nd likely contains the highest concentration of oxygen vacancies. If this is true then this suggests that vacancies cause larger distortion than interstitials, U^{5+}, and Nd^{3+} cations. This assumption is made by comparison of RE-399 and RE-415. Sample RE-399 is more oxidized (*i.e.*, has more oxygen and U^{5+}) and contains more Nd^{3+} based on Figure 77, yet it shows a lower magnitude of distortion compared to RE-415. This implies that the distortion of the 1-NN

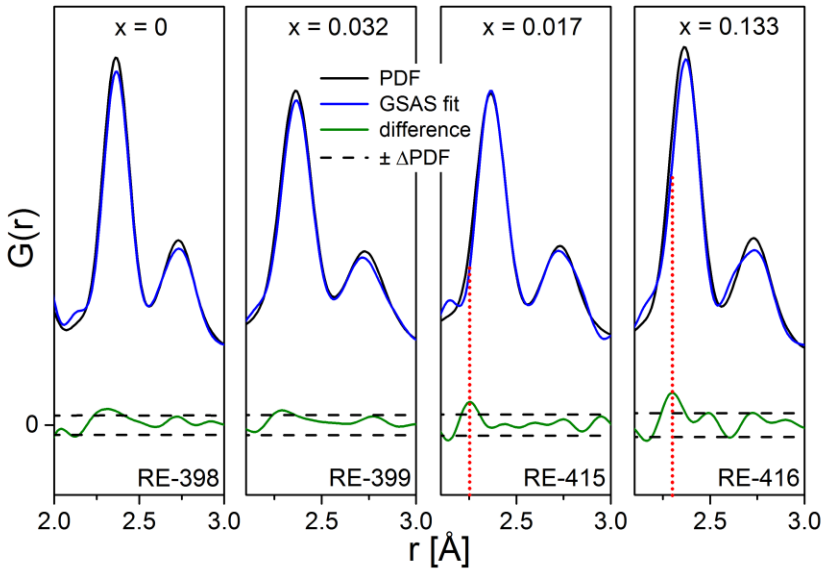


Figure 85: Small-box pair distribution function modeling results for the co-precipitation samples. The *x* values at the top denote the atomic fraction of Nd in the samples and the name at the bottom right denotes the sample name. The PDFs were initially fit with the average structure model derived from Rietveld refinement of the neutron diffraction patterns.

cation-oxygen peak is more influenced by the presence of vacancies. This notion is supported by effective size arguments. Calculations based on systematic analysis results of rare-earth element doped UO_2 showed that the effective radius of an oxygen vacancy in these systems is ~1.5 Å and ~10% larger than the calculated radius of an O^{2-} ion [264]. The larger effective size of oxygen vacancies are likely to induce more microstrain and distortion in the short-range structure.

The attribution of fitted fluorite structure model discrepancies to oxygen vacancies and the incorporation of U^{5+} and Nd^{3+} indicates that short range distortions are merely caused by small atomic relaxations. This is best illustrated using the structural model shown in Figure 86. Using the tetrahedral-coordination polyhedron of oxygen, it is expected that the replacement of the central anion with a vacancy will induce some sort of relaxation to the neighboring cations as a result of Coulomb repulsion (this is schematically illustrated using green arrows in Figure 86). The exact mode of atomic relaxation is unknown, cannot be conclusively determined from small-box modeling, and likely varies depending on the type of cations (U^{4+}, U^{5+}, Nd^{3+}) that surround the anion. However, small-box modeling can be used to estimate the average *magnitude* of atomic relaxation. This information can be valuable for estimating the difference in effective size between Nd^{3+} and uranium coordination environments, and identifying possible correlations between relaxation magnitude and variables such as doping level.

The magnitude of atomic relaxation was estimated using small-box PDF refinement by first fitting simple fluorite structures (space group *Fm*-3*m*) with mixed 4*a* cation sites. The fluorite structure models were optimized and then converted to *P*1 symmetry such that the atom positions were made variable. The 4 mixed-occupancy cation sites at (0,0,0), (½,½,0), (½,0,½), (0,½,½) were thereafter displaced along either positive or negative <111> directions, *i.e.*, towards or away from the anion site at (¼,¼,¼), in order to simulate atomic relaxation of cations that would occur if the anion was replaced with a vacancy. The magnitudes of displacement for all 4 cation sites were made equivalent to avoid over-parameterization of the so-called *relaxation* model. Vacancies were simulated by setting a lower 8*c* site occupancy value. The lower 8*c* site occupancy was determined from the Rietveld refinement results.

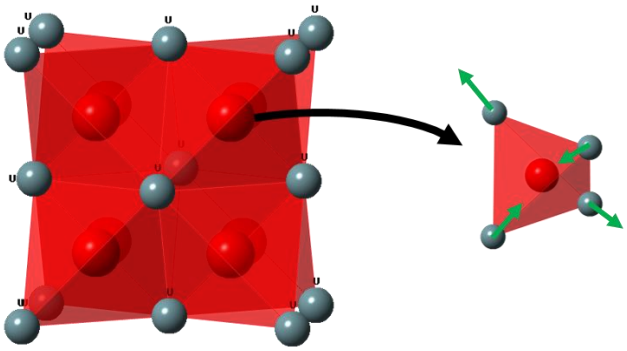


Figure 86: The unit cell of the fluorite structure (left). The unit on the right shows the tetrahedral coordination environment of a single oxygen atom. The green arrows show schematically how the local coordination environment was disturbed in order to fit 'relaxation' models to the PDFs. Different relaxation models with different displacement directions and magnitudes were used

The magnitude of atomic relaxation was estimated using small-box PDF refinement by first fitting simple fluorite structures (space group *Fm*-3*m*) with mixed 4*a* cation sites. The fluorite structure models were optimized and then converted to *P*1 symmetry such that the atom positions were made variable. The 4 mixed-occupancy cation sites at (0,0,0), (½,½,0), (½,0,½), (0,½,½) were thereafter displaced along either positive or negative <111> directions, *i.e.*, towards or away from the anion site at (¼,¼,¼), in order to simulate atomic relaxation of cations that would occur if the anion was replaced with a vacancy. The magnitudes of displacement for all 4 cation sites were made equivalent to avoid over-parameterization of the so-called *relaxation* model. Vacancies were simulated by setting a lower 8*c* site occupancy value. The lower 8*c* site occupancy was determined from the Rietveld refinement results.

Several relaxation models were fit to the data. The different models (models 1-7) represent different atomic relaxation modes. For example, model 1 involves 1 cation relaxing towards the anion site, model 2 involves 2 cations relaxing towards, etc. Models 5-7 represented some cations relaxing towards and other away from the anion site. These different models are not meant to describe the actual geometry of atomic ordering in the UO_2 samples, but rather they were used to optimize the relaxation models as much as possible without over-parameterizing the refinements. The goal of these refinements was to estimate the magnitude of atomic relaxation and not determine the actual mode of relaxation. The PDF relaxation model refinements contained only 3 refineable parameters: overall scale, correlated motion parameter, and the atomic relaxation distance. The lattice parameter and ADPs were fixed to the optimized values from fitting of the unperturbed *Fm*-3*m* model to the same *r* range.

A visual representation of the refinement procedure is shown in Figure 87. The figure shows the evolution of the R_w value with varying relaxation distance for the different relaxation models attempted. The overall minimum in R_w determines the best fit model and the optimal relaxation distance for the cations. In the example shown, the last 2 models fit the data the best and the relaxation distance is less than 1 Å. The fit results from the fitting of all models to each sample PDF are shown presented in Figure 88. The results show that a highly distorted coordination environment gives the best fit results for all samples.

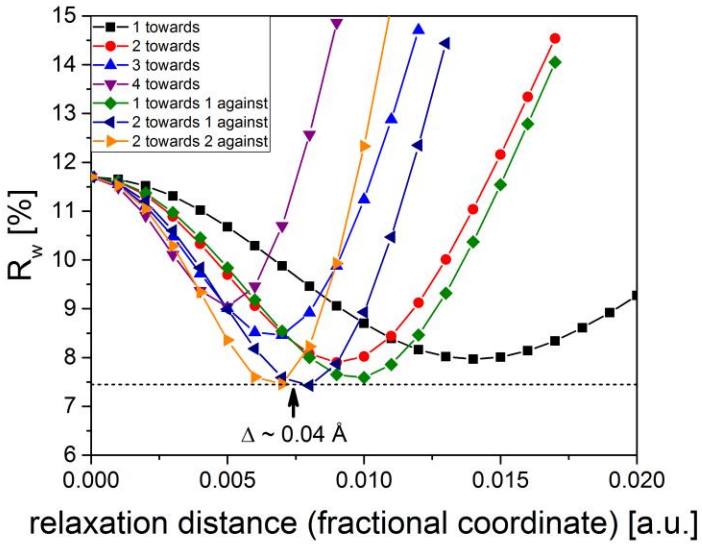


Figure 87: Illustration of minimization scheme for fitting so-called relaxation models to the neutron pair distribution functions (PDFs). Various models were fit to each PDF until the minimum R_w value was attained. The lowest R_w value among the different models corresponds to the model that best fit the data. The location of the minimum also yields the optimal atomic relaxation distance for the model of interest

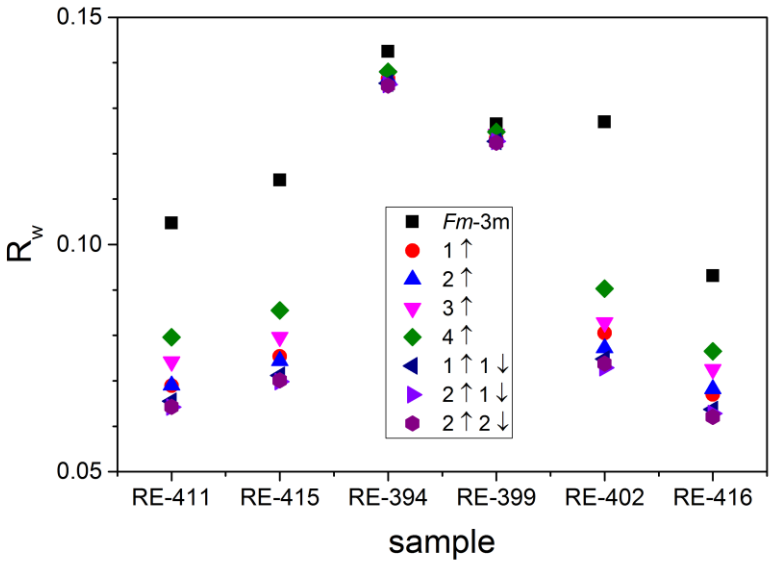


Figure 88: Results from fitting various so-called *relaxation* models to the pair distribution functions of Nd-doped UO_2 samples. The R_w is the fit agreement value. The black points represent results for fitting an unperturbed fluorite structure model. The other points represent models with a varying number of cation sites relaxed either towards (↑) or away (↓) from the neighboring anion site. All samples were best fit with relaxation model 7

The aim of fitting relaxation models was to improve the fit to the 1-NN PDF correlation. However, the improvement in the fits extended far beyond the 1-NN peak. An illustration of this is shown in Figure 89. This figure shows a comparison of the fits for the undistorted fluorite structure model and the best fit relaxation model (model 7 in Figure 88). The comparison shows that the improvement of the fit at low *r* (2-3 Å) is matched by an improvement of the fit to the higher *r* region plotted (8-11 Å). The improvement of the fit is clearly seen by comparing the green difference curves. This improvement to the fit at higher *r* was unexpected and demonstrates that very short (< 1 Å) atomic relaxation distances can yield pronounced changes in the overall PDF peak intensities in the intermediate-range region.

As previously mentioned, the various relaxation models are not meant to accurately describe modes of atomic relaxation, but rather gauge the magnitude of atomic relaxation caused by chemical doping. Atomic relaxation is likely caused by the incorporation of point defects, such as oxygen vacancies, that can induce Coulombic attraction/repulsion and/or changes in the local coordination environments of cations. The difference in charge state between Nd^{3+} and U^{4+} cations would suggest that Nd cations are under-coordinated with anions compared to U cations. For example, Nd^{3+} in Nd_2O_3 exists in 7-fold coordination. It follows that vacancies in the fluorite structure would tend to cluster around Nd^{3+} cations, as suggested by computational studies [258].

If Nd^{3+}, U^{4+}, and U^{5+} cations do indeed exhibit different coordination within a nominally fluorite structure and local distortions are caused by the effective size difference between the two unique coordination environments, then the magnitude of atomic relaxation should correlate with Nd content. The optimized atomic relaxation distance for each sample is shown in Figure 90. The data in the figure are plotted against Nd content and the data for the different data sets are differentiated in order to avoid potential systematic bias from the different preparation methods. The data show that at very low dopant concentrations, the magnitude of atomic relaxation is approximately linearly correlated with Nd content. It's possible that the magnitude of distortion saturates at higher Nd concentrations (see, *e.g.*, co-precipitation method data). Another explanation is that the data at higher Nd concentrations are more influenced by uranium oxidation to U^{5+} and this

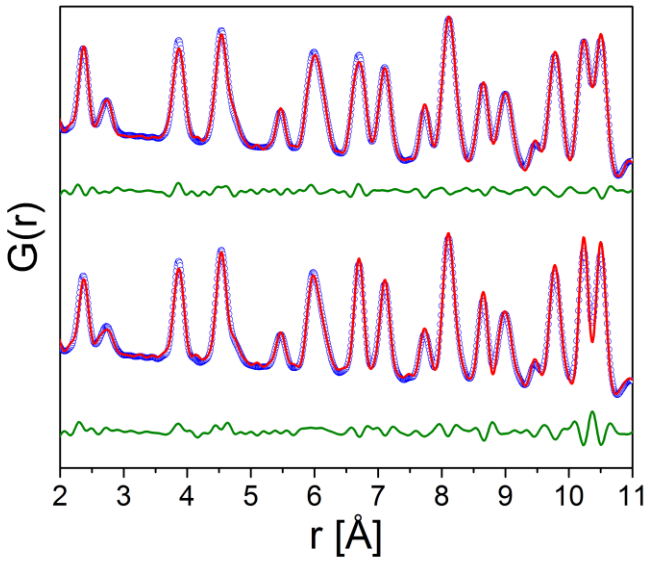


Figure 89: Visual comparison of PDF fits for unperturbed *Fm*-3*m* model (bottom) and relaxation model 7 (top). The relaxation model better models the short-range distortion and also surprisingly better fits higher *r* regions as well (8-10 Å)

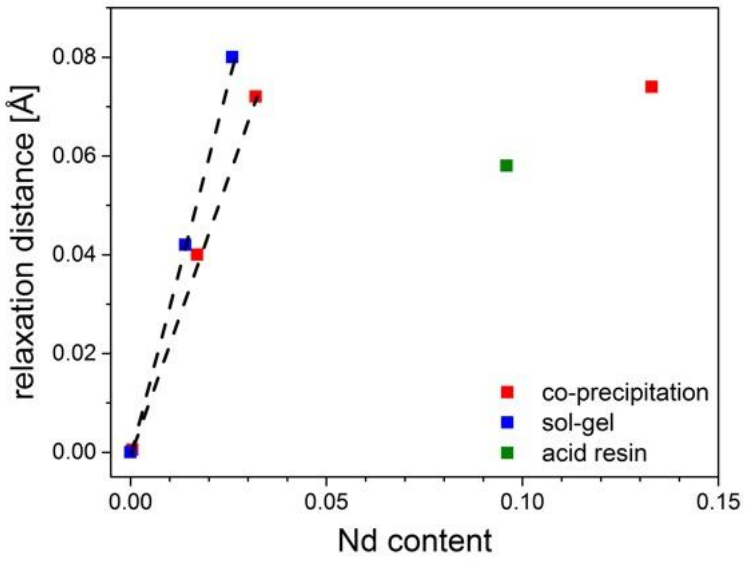


Figure 90: Optimized atomic relaxation distance *versus* Nd content in the UO_2 samples

skews the linear trend.

Uranium can exhibit +3, +4, +5, and even +6 valence states, although the U^{6+} state is not likely in the fluorite structure due to the very different coordination geometry required. Uranium oxide compounds containing U^{3+} are also rare. Therefore, it is generally accepted that the uranium oxide samples incorporate mostly U^{4+} and U^{5+} cations. This notion is supported by both computational [145] and experimental spectroscopic investigations [245, 248]. Uranium in the +5 charge state would tend to be over-coordinated compared to U^{4+} assuming a simple ionic model and assuming that the system generally follows Pauling's rules. The incorporation of large quantities of Nd^{3+} and U^{5+} would lead to competing effects that may initiate saturation behavior. Future investigation of purely hypo-stoichiometric samples (*i.e.*, no U^{5+} content) are needed in order to determine if the magnitude of atomic relaxation is linearly correlated with trivalent dopant concentration. Comparing the different synthesis methods shows that the two methods with the most data points (co-precipitation and sol gel methods) have similar trends at the low Nd concentration regime. This, however, is only a general observation because there exist only very few data points in the data set.

Reverse Monte Carlo Modeling – Defect Clustering

The main observations derived from small-box PDF modeling are: (1) the incorporation of point defects in UO_2 results in local structural distortions with domain sizes of ~15 Å, (2) localized distorted domains are likely caused by very short (< 1 Å) atomic relaxation, and (3) the magnitude of atomic displacement is weakly correlated to Nd content. One potential explanation for the latter two observations is that short-range atomic relaxation is caused by differences in Nd^{3+}, U^{4+}, and U^{5+} coordination environments. In order to test this theory, the most highly distorted sample was modeled using reverse Monte Carlo.

Reverse Monte Carlo (RMC) modeling is unique from small-box modeling in that it can be used to model neutron total scattering data using large atom ensembles. Ensembles in the present work typically comprised 12000-16000 atoms or ~1000 unit cells. Small-box modeling requires prior planning and manual manipulation of the model whereas the RMC model only relies on general constraints such as minimum distance limits and bond

valence sum requirements. In this regard, RMC is quite complimentary to small-box modeling and can be used to test models that are not biased by the user. Atomic displacements within the supercell are dictated by statistical mechanics, *i.e.*, RMC simulations aims to maximize entropy within reasonable constraints.

The RMC simulations were driven by three different data sets. These were the diffraction pattern, the normal PDF D(r) function, and the radial distribution or G(r) function. The diffraction pattern was used to convey the long-range structural information, the D(r) function was used to primarily convey intermediate range information (up to ~15 Å), and the G(r) function was used to convey short-range and coordination information. Another advantage to RMC modeling is that the modeling can explicitly handle vacancies. Vacancies in the supercell are represented by spheres with zero scattering power. The incorporation of vacancies is advantageous because it enables the investigation of vacancy ordering schemes.

The sample doped with the highest Nd concentration (x = 0.133) and the corresponding co-precipitation, undoped UO_2 sample were the only ones modeled. RMC modeling was not extended to the other data sets for lack of resources. The present work therefore represents a proof-of-concept study and not a comprehensive investigation. The stoichiometry of the undoped UO_2 sample was fixed at $UO_{2.00}$, as UO_{2-x} is not thermodynamically stable. Extensive testing showed that small deviations of x in UO_{2+x} (up to 0.05) do not significantly affect RMC results. The stoichiometry of the Nd-doped UO_2 sample was fixed based on the neutron diffraction Rietveld refinement results. In other words, the oxygen content was determined by the refined 8*c* site occupancies and the Nd concentration of the doped sample was determined based on the synthesis value (x = 0.133). This procedure was previously used for fluorite-structured CeO_{2-x} and yielded reasonable results [77]. Besides the obvious constraints of fitting the diffraction pattern, D(r), and G(r), the data were also constrained using distance of closest approach and bond valence sum (BVS) constraints. The distance of closest approach requirement was based on the first peak in the PDFs. The BVS constraint was included in order to incorporate chemical information. Extensive testing of RMC with BVS constraints has shown that BVS

parameters yield structures that are more chemical sensible, especially for ionic oxide materials [270].

A summary of RMC fitting results for undoped UO_2 are shown in Figure 91. The figure shows the fit to the diffraction pattern and PDFs. The fits to all three datasets representing three unique interatomic distance ranges (short, intermediate, and long) are quite reasonable. Therefore, the final atomic arrangement is consistent with all length-scales. The BVS results show that uranium and oxygen atoms have mostly +4 and -2 valence states, which is as expected for nominally stoichiometric UO_2. A closer inspection of the peaks in the diffraction pattern and the PDFs show that peaks are relatively sharp and intense. This indicates that atoms are generally well-ordered in the lattice.

This is confirmed by inspection of the output supercell. Projections along the [100], [110], and [111] planes are shown in Figure 92. The images show that atomic displacement is relatively small and there aren't any large concentrations of point defects. This is in contrast to results for Nd-doped UO_2, which are more disordered. Regardless, the final RMC model was consistent with all length scales. The fit to the D(r) is slightly worse, but this is attributed to instrumental resolution and not the model, *i.e.*, the fit worsens as a function of *r*. This was confirmed by subsequent tweaking of the D(r) resolution function.

The most promising feature from the RMC fitting of $Nd_{0.133}U_{0.867}O_{2\pm y}$ was the BVS result shown in Figure 93. BVS analysis shows that the uranium and oxygen atoms take on +4 and -2 valence states, as for UO_2, but Nd^{3+} maintains a valence less than +4. This is critical because it indicates that the final model is both chemically sensible, *i.e.*, the mean Nd valence is close to +3, and the overall structure remains fluorite-like, *i.e.*, it is consistent with the diffraction data. The mean valence of Nd is not perfectly +3, but slightly higher. Nd cations are likely unable to maintain a preferred +3 valence owing to the cubic symmetry of the fluorite structure. Cations in the fluorite structure normally have 8-fold coordination, so the Nd cations are accommodated by clustering with oxygen vacancies, as suggested thermodynamically and computationally.

A clear illustration of this is shown in Figure 94. The partial PDFs in the figure show that the intensity of the Nd-Va partial is much larger than the U-Va partial, which confirms that oxygen vacancies are preferentially located near Nd cations compared to U

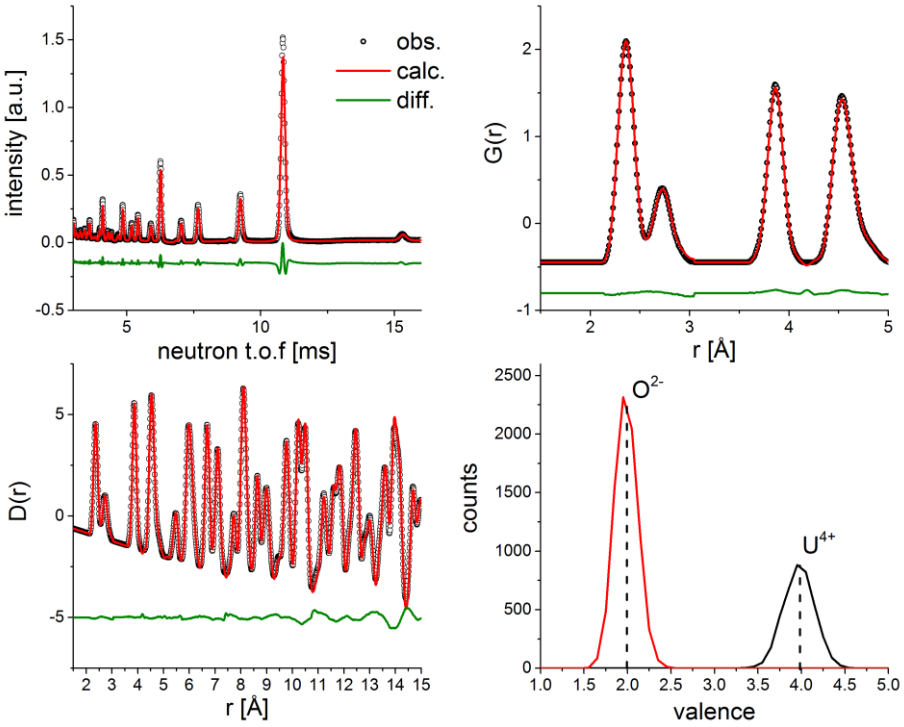


Figure 91: Summary of RMC modeling results for undoped UO_2 synthesized by the co-precipitation method. Clockwise from top left: the model fit to the diffraction pattern, the fit to the G(r) function, the bond valence sum parameter for the output atom ensemble, and the fit to the D(r) function

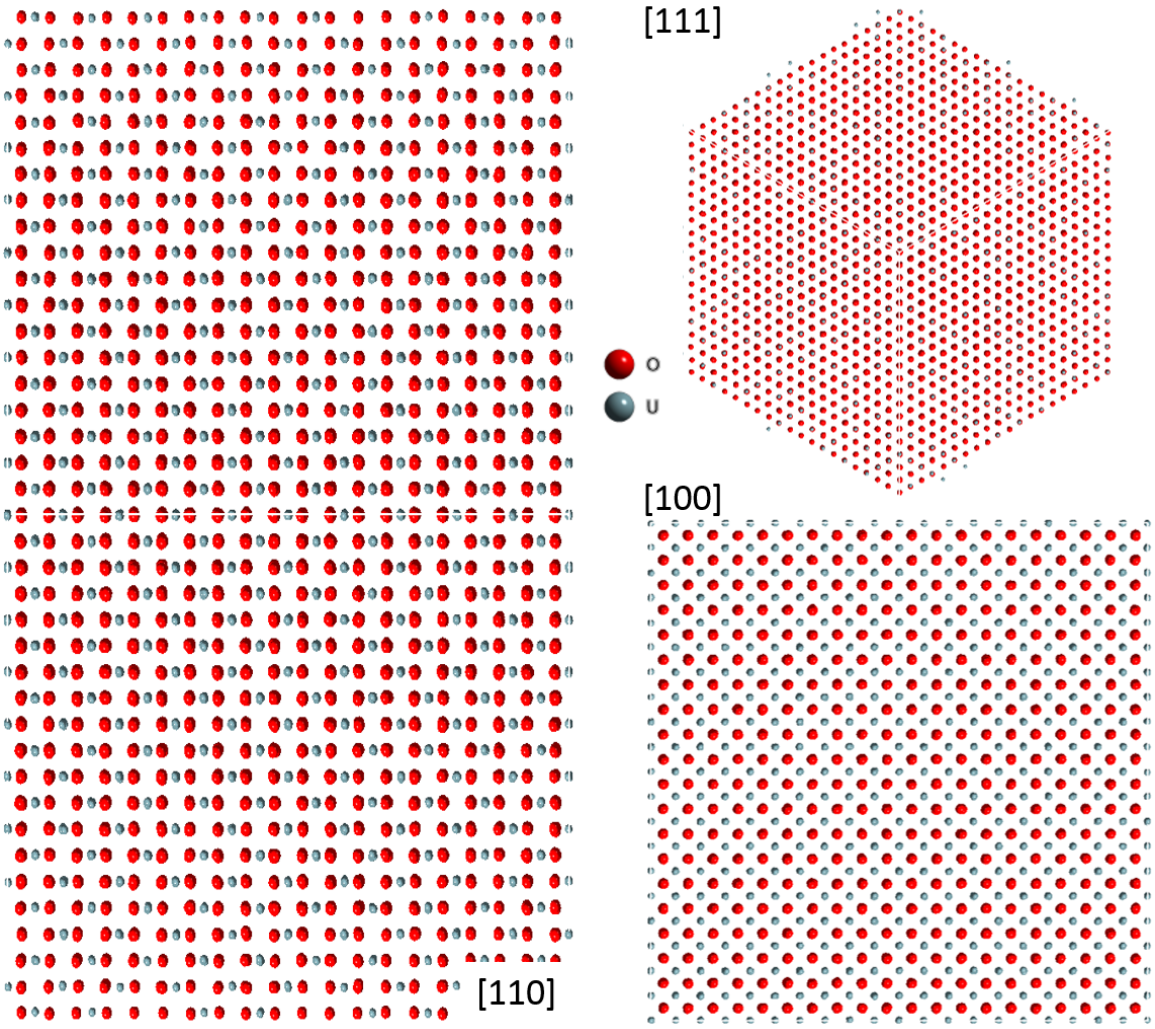


Figure 92: Final atomic supercell arrangement for UO_2 from reverse Monte Carlo modeling

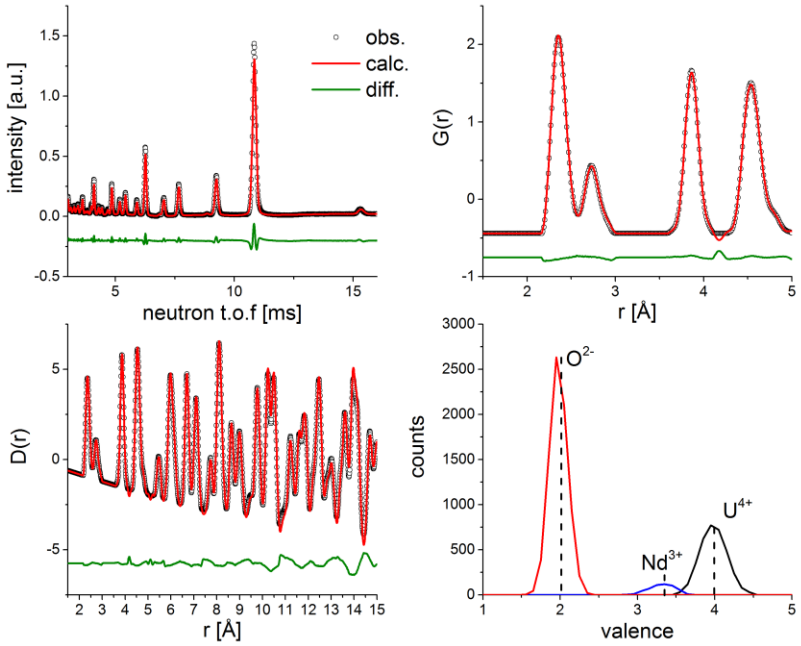


Figure 93: Summary of RMC modeling results for $Nd_{0.133}U_{0.867}O_{2\pm y}$. Clockwise from top left: RMC model fit to the diffraction pattern, fit to G(r), BVS analysis results, and fit to the D(r)

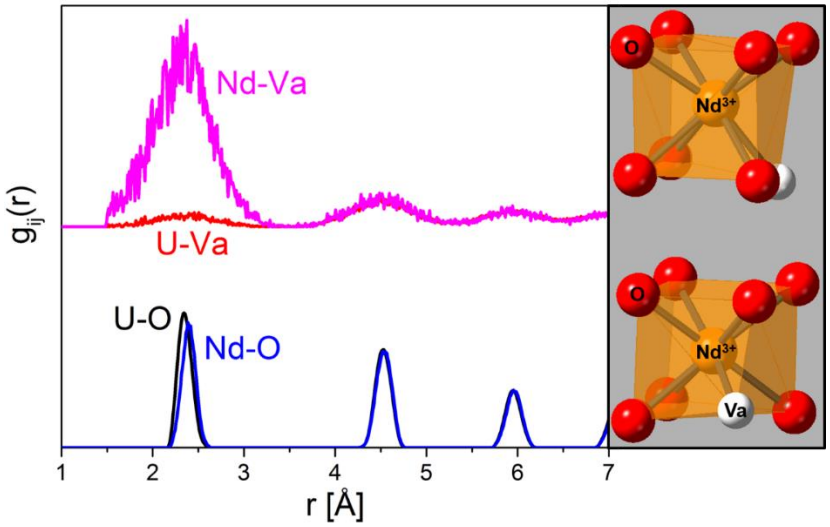


Figure 94: Various partial pair distribution functions derived from RMC model of $Nd_{0.133}U_{0.867}O_{2\pm y}$ (left) and two examples of Nd-O polyhedra from the RMC supercell output (right)

cations. The mean 1-NN Nd-O distance is also slightly longer than the mean 1-NN U-O distance, in agreement with predictions for ionic radii. The image on the right shows two isolated Nd-O polyhedral from one of the output supercells. Both polyhedra show Nd in 7-fold coordination with an oxygen vacancy in coordination where the 8th oxygen atom typically resides. This coordination is analogous to the distorted mono-capped octahedral coordination found in some complex oxides.

Conclusions and Recommendations

Atomic structure modifications in UO_2 were studied before and after incorporation of Nd^{3+} dopant ions in order to identify trends in point defect accumulation. Changes in atomic arrangements were probed using neutron total scattering and Raman spectroscopy. Bulk phase analysis performed using neutron diffraction showed that chemical doping did not result in phase transformations and all materials exhibited cubic, fluorite structures. This implied that trivalent Nd dopant elements were soluble in the UO_2 matrix and were readily accommodated at the 4*a* cation site in the fluorite structure. Rietveld refinement showed that all materials comprise highly ordered crystalline domains.

Quantification of unit cell parameters revealed that the samples are only partially hypo-stoichiometric. This indicated that charge compensation for Nd^{3+} is fulfilled by a combination of oxygen vacancies and uranium oxidation ($U^{4+} \rightarrow U^{5+}$). Oxygen atomic displacement parameters and oxygen 8*c* site occupancies from neutron diffraction analysis and integrated defect peak areas from Raman spectroscopy analysis showed large discrepancies in trends between the sample with the highest Nd concentration (13 atom%) and the other samples. This was attributed to a miscibility gap at ~10 atom% Nd. Evidence for a miscibility gap was likely not observed from diffraction analysis because immiscibility results in two fluorite-type phases with very similar diffraction peak positions.

Small-box modeling of neutron pair distribution functions revealed the presence of short-range (< 10 Å) atomic structure distortions in both doped and undoped UO_2 samples. These distortions were attributed to defect clusters composed of oxygen interstitials and oxygen vacancies (O_v). Fitting distorted fluorite structure atomic arrangements

demonstrated that observed local distortions can be accurately described by employing very short (< 1 Å) atomic relaxations. These atomic relaxations were attributed to point defects, such as oxygen defect clusters, and differences in U^{4+}/U^{5+} and Nd^{3+} coordination environments.

This theory was tested by employing reverse Monte Carlo (RMC) modeling of the neutron total scattering data in order to explicitly model oxygen vacancies. Preliminary RMC fitting results showed that the resultant Nd-UO_2 model was consistent with the experimental data at all length scales. The resultant model was also chemically-sensible as estimated valence values for U and Nd were approximately +4 and +3.5, respectively. A close inspection of the optimized atomic ensembles showed that the difference in valence arises from differences in local coordination environments. Oxygen vacancies illustrated a tendency to cluster with Nd^{3+} cations and form distorted local polyhedra. These findings were consistent with Nd^{3+}-O_v clustering schemes implied from Raman spectroscopy and reported density functional theory predictions. Trapping of oxygen vacancies in clusters influences both oxygen vacancy and interstitial migration. Therefore, these defect clustering schemes must be taken into account in order to better predict corrosion kinetics of spent nuclear fuel.

CONCLUSIONS

Point defect accumulation, ordering, and annihilation mechanisms in fluorite structured oxides, such as CeO_2, ThO_2, and UO_2, were experimentally investigated using a variety of atomic structural characterization methods. Analyses showed that swift heavy ion irradiation, oxidation, and chemical doping all induced the formation of point defects that were readily accommodated within the cubic, fluorite structures. Most extrinsic point defects formed small defect clusters comprising multiple oxygen interstitials and/or vacancies. The use of local structure probes and atomic structure modeling enabled the observation of bound oxygen dimers, split interstitials, and trivalent atom-vacancy complexes after irradiation, oxidation, and doping, respectively. Computational studies reported in the literature demonstrate that these small defect clusters can enable very rapid diffusion pathways. Experimentally observed defect cluster configurations in the present study must therefore be taken into account in future studies in order to better predict bulk properties, such as oxygen diffusivity values, which are critical for development of advanced fast ion conducting oxide materials and for improvement of multiscale nuclear fuel modeling efforts.

REFERENCES

1. Yao, T., et al., *Grain growth and pore coarsening in dense nano-crystalline UO2+x fuel pellets.* Journal of the American Ceramic Society, 2017. **100**(6): p. 2651-2658.
2. Lang, M., et al., *Characterization of ion-induced radiation effects in nuclear materials using synchrotron X-ray techniques.* Journal of Materials Research, 2015. **30**(9): p. 1366-1379.
3. Luther, E., et al., *Microstructural Characterization of Uranium Oxide.* Transactions of the American Nuclear Society, 2011. **104**(Nuclear Fuels and Materials): p. 257-258.
4. Ziegler, J.F., M.D. Ziegler, and J.P. Biersack, *SRIM - The stopping and range of ions in matter (2010).* Nuclear Instruments & Methods in Physics Research Section B-Beam Interactions with Materials and Atoms, 2010. **268**(11-12): p. 1818-1823.
5. Lang, M.I., et al., *Swift heavy ion-induced phase transformation in Gd2O3.* Nuclear Instruments & Methods in Physics Research Section B-Beam Interactions with Materials and Atoms, 2014. **326**: p. 121-125.
6. Palomares, R.I., et al., *Defect accumulation in swift heavy ion-irradiated CeO2 and ThO2.* Journal of Materials Chemistry A, 2017. **5**(24): p. 12193-12201.
7. Tracy, C.L., et al., *Redox response of actinide materials to highly ionizing radiation.* Nat Commun, 2015. **6**: p. 6133.
8. Leinders, G., et al., *Accurate lattice parameter measurements of stoichiometric uranium dioxide.* Journal of Nuclear Materials, 2015. **459**: p. 135-142.
9. Horwitz, E.P., et al., *Separation and preconcentration of uranium from acidic media by extraction chromatography.* Analytica Chimica Acta, 1992. **266**(1): p. 25-37.
10. Quemet, A., et al., *Analysis of twenty five impurities in uranium matrix by ICP-MS with iron measurement optimized by using reaction collision cell, cold plasma or medium resolution.* Talanta, 2012. **99**(Supplement C): p. 207-212.
11. International, A., *Standard Test Method for the Determination of Uranium by Ignition and the Oxygen to Uranium (O/U) Atomic Ratio of Nuclear Grade Uranium Dioxide Powders and Pellets*. 2011, ASTM: West Conshohocken, PA.
12. Park, C., et al., *New developments in micro-X-ray diffraction and X-ray absorption spectroscopy for high-pressure research at 16-BM-D at the Advanced Photon Source.* Review of Scientific Instruments, 2015. **86**(7): p. 072205.
13. Bassett, W.A., *High pressure-temperature aqueous systems in the hydrothermal diamond anvil cell (HDAC).* European Journal of Mineralogy, 2003. **15**(5): p. 773-780.
14. Bassett, W.A., et al., *A New Diamond-Anvil Cell for Hydrothermal Studies to 2.5 Gpa and from - 190-Degrees-C to 1200-Degrees-C.* Review of Scientific Instruments, 1993. **64**(8): p. 2340-2345.
15. Palomares, R.I., et al., *In situ defect annealing of swift heavy ion irradiated CeO2 and ThO2 using synchrotron X-ray diffraction and a hydrothermal diamond anvil cell.* Journal of Applied Crystallography, 2015. **48**: p. 711-717.

16. Prescher, C. and V.B. Prakapenka, *DIOPTAS: a program for reduction of two-dimensional X-ray diffraction data and data exploration.* High Pressure Research: An International Journal, 2015.
17. Toby, B.H. and R.B. Von Dreele, *GSAS-II: the genesis of a modern open-source all purpose crystallography software package.* Journal of Applied Crystallography, 2013. **46**(2): p. 544-549.
18. Juhas, P., et al., *PDFgetX3: a rapid and highly automatable program for processing powder diffraction data into total scattering pair distribution functions.* Journal of Applied Crystallography, 2013. **46**: p. 560-566.
19. Neuefeind, J., et al., *The Nanoscale Ordered MAterials Diffractometer NOMAD at the Spallation Neutron Source SNS.* Nuclear Instruments and Methods in Physics Research Section B: Beam Interactions with Materials and Atoms, 2012. **287**: p. 68-75.
20. Toby, B., *EXPGUI, a graphical user interface for GSAS.* Journal of Applied Crystallography, 2001. **34**(2): p. 210-213.
21. Keen, D., *A comparison of various commonly used correlation functions for describing total scattering.* Journal of Applied Crystallography, 2001. **34**(2): p. 172-177.
22. Syassen, K., *DATLAB, version 1.29*. MPI/FKF: Stuttgart, Germany.
23. Farrow, C.L., et al., *PDFfit2 and PDFgui: computer programs for studying nanostructure in crystals.* Journal of Physics-Condensed Matter, 2007. **19**(33).
24. Matthew, G.T., et al., *RMCProfile: reverse Monte Carlo for polycrystalline materials.* Journal of Physics: Condensed Matter, 2007. **19**(33): p. 335218.
25. Gagne, O.C. and F.C. Hawthorne, *Comprehensive derivation of bond-valence parameters for ion pairs involving oxygen.* Acta Crystallographica Section B, 2015. **71**(5): p. 562-578.
26. Trovarelli, A., et al., *The utilization of ceria in industrial catalysis.* Catalysis Today, 1999. **50**(2): p. 353-367.
27. Montini, T., et al., *Fundamentals and Catalytic Applications of CeO2-Based Materials.* Chemical Reviews, 2016. **116**(10): p. 5987-6041.
28. Beie, H.J. and A. Gnörich, *Oxygen gas sensors based on CeO2 thick and thin films.* Sensors and Actuators B: Chemical, 1991. **4**(3): p. 393-399.
29. Goodenough, J.B., *Oxide-Ion Electrolytes.* Annual Review of Materials Research, 2003. **33**(1): p. 91-128.
30. Tuller, H.L., *Mixed ionic-electronic conduction in a number of fluorite and pyrochlore compounds.* Solid State Ionics, 1992. **52**(1): p. 135-146.
31. Popel, A.J., et al., *The effect of fission-energy Xe ion irradiation on the structural integrity and dissolution of the CeO2 matrix.* Journal of Nuclear Materials, 2017. **484**(Supplement C): p. 332-338.
32. Yablinsky, C.A., et al., *Characterization of swift heavy ion irradiation damage in ceria.* Journal of Materials Research, 2015. **30**(9): p. 1473-1484.
33. Aidhy, D.S., D. Wolf, and A. El-Azab, *Comparison of point-defect clustering in irradiated CeO2 and UO2: A unified view from molecular dynamics simulations and experiments.* Scripta Materialia, 2011. **65**(10): p. 867-870.

34. Kim, H.S., et al., *Applicability of CeO2 as a surrogate for PuO2 in a MOX fuel development.* Journal of Nuclear Materials, 2008. **378**(1): p. 98-104.
35. Tabakova, T., et al., *Pure hydrogen production on a new gold–thoria catalyst for fuel cell applications.* Applied Catalysis B: Environmental, 2006. **63**(1–2): p. 94-103.
36. IAEA, *Thorium Fuel Cycle - Potential Benefits and Challenges TECDOC-1450.* 2005: Vienna, Austria.
37. Ashley, S.F., et al., *Thorium fuel has risks.* Nature, 2012. **492**: p. 31.
38. Weber, W.J., et al., *The role of electronic energy loss in ion beam modification of materials.* Current Opinion in Solid State and Materials Science, 2015. **19**(1): p. 1-11.
39. Itoh, N. and A.M. Stoneham, *Excitonic model of track registration of energetic heavy ions in insulators.* Nuclear Instruments & Methods in Physics Research Section B-Beam Interactions with Materials and Atoms, 1998. **146**(1-4): p. 362-366.
40. Klaumunzer, S., *Thermal-Spike Models for Ion Track Physics: A Critical Examination*, in *Ion Beam Science: Solved and Unsolved Problems*, P. Sigmund, Editor. 2006, The Royal Danish Academy of Sciences and Letters: Copenhagen. p. 293-328.
41. Fleischer, R.L., P.B. Price, and R.M. Walker, *Ion Explosion Spike Mechanism for Formation of Charged-Particle Tracks in Solids.* Journal of Applied Physics, 1965. **36**(11): p. 3645-3652.
42. Toulemonde, M., E. Paumier, and C. Dufour, *Thermal spike model in the electronic stopping power regime.* Radiation Effects and Defects in Solids, 1993. **126**(1-4): p. 201-206.
43. Toulemonde, M., C. Dufour, and E. Paumier, *Transient thermal process after a high-energy heavy-ion irradiation of amorphous metals and semiconductors.* Physical Review B, 1992. **46**(22): p. 14362-14369.
44. Itoh, N., et al., *Making tracks: electronic excitation roles in forming swift heavy ion tracks.* Journal of Physics-Condensed Matter, 2009. **21**(47).
45. Medvedev, N.A., et al., *Early stage of the electron kinetics in swift heavy ion tracks in dielectrics.* Physical Review B, 2010. **82**(12).
46. Lipp, V.P., et al., *Kinetics of propagation of the lattice excitation in a swift heavy ion track.* Nuclear Instruments & Methods in Physics Research Section B-Beam Interactions with Materials and Atoms, 2011. **269**(9): p. 865-868.
47. Osmani, O., et al., *Energy dissipation in dielectrics after swift heavy-ion impact: A hybrid model.* Physical Review B, 2011. **84**(21).
48. Kluth, P., et al., *Fine Structure in Swift Heavy Ion Tracks in Amorphous SiO(2).* Physical Review Letters, 2008. **101**(17).
49. Tracy, C.L., et al., *Phase transformations in Ln2O3 materials irradiated with swift heavy ions.* Physical Review B, 2015. **92**(17): p. 174101.
50. Lang, M., et al., *Structural modifications of Gd(2)Zr(2-x)Ti(x)O(7) pyrochlore induced by swift heavy ions: Disordering and amorphization.* Journal of Materials Research, 2009. **24**(4): p. 1322-1334.

51. Takaki, S., et al., *Structure of ion tracks in ceria irradiated with high energy xenon ions.* Progress in Nuclear Energy, 2016. **92**: p. 306-312.
52. Takaki, S., et al., *Atomic structure of ion tracks in Ceria.* Nuclear Instruments & Methods in Physics Research Section B-Beam Interactions with Materials and Atoms, 2014. **326**: p. 140-144.
53. Zhang, Y., et al., *The effect of electronic energy loss on irradiation-induced grain growth in nanocrystalline oxides.* Physical Chemistry Chemical Physics, 2014. **16**(17): p. 8051-8059.
54. Sonoda, T., et al., *Electronic excitation effects in CeO2 under irradiations with high-energy ions of typical fission products.* Nuclear Instruments & Methods in Physics Research Section B-Beam Interactions with Materials and Atoms, 2006. **250**: p. 254-258.
55. Ishikawa, N., et al., *Study of structural change in CeO2 irradiated with high-energy ions by means of X-ray diffraction measurement.* Nuclear Instruments & Methods in Physics Research Section B-Beam Interactions with Materials and Atoms, 2008. **266**(12-13): p. 3033-3036.
56. Ohno, H., et al., *Study on effects of swift heavy ion irradiation in cerium dioxide using synchrotron radiation X-ray absorption spectroscopy.* Nuclear Instruments & Methods in Physics Research Section B-Beam Interactions with Materials and Atoms, 2008. **266**(12-13): p. 3013-3017.
57. Sonoda, T., et al., *Clarification of the properties and accumulation effects of ion tracks in CeO2.* Nuclear Instruments & Methods in Physics Research Section B-Beam Interactions with Materials and Atoms, 2008. **266**(12-13): p. 2882-2886.
58. Iwase, A., et al., *Study on the behavior of oxygen atoms in swift heavy ion irradiated CeO2 by means of synchrotron radiation X-ray photoelectron spectroscopy.* Nuclear Instruments & Methods in Physics Research Section B-Beam Interactions with Materials and Atoms, 2009. **267**(6): p. 969-972.
59. Kinoshita, M., et al., *Recovery and restructuring induced by fission energy ions in high burnup nuclear fuel.* Nuclear Instruments & Methods in Physics Research Section B-Beam Interactions with Materials and Atoms, 2009. **267**(6): p. 960-963.
60. Ohhara, K., et al., *Oxygen defects created in CeO2 irradiated with 200 MeV Au ions.* Nuclear Instruments and Methods in Physics Research Section B: Beam Interactions with Materials and Atoms, 2009. **267**(6): p. 973-975.
61. Zhang, Y., et al., *Structural modification of nanocrystalline ceria by ion beams.* Physical Chemistry Chemical Physics, 2011. **13**(25): p. 11946-11950.
62. Shimizu, K., et al., *Change in magnetic properties induced by swift heavy ion irradiation in CeO2.* Nuclear Instruments and Methods in Physics Research Section B: Beam Interactions with Materials and Atoms, 2012. **286**: p. 291-294.
63. Chen, W.-Y., et al., *Characterization of dislocation loops in CeO2 irradiated with high energy Krypton and Xenon.* Philosophical Magazine, 2013. **93**(36): p. 4569-4581.
64. Yasuda, K., et al., *Defect formation and accumulation in CeO2 irradiated with swift heavy ions.* Nuclear Instruments & Methods in Physics Research Section B-Beam Interactions with Materials and Atoms, 2013. **314**: p. 185-190.

65. Grover, V., et al., *Effect of grain size and microstructure on radiation stability of CeO2: an extensive study.* Physical Chemistry Chemical Physics, 2014. **16**(48): p. 27065-27073.
66. Tracy, C.L., et al., *Defect accumulation in ThO2 irradiated with swift heavy ions.* Nuclear Instruments & Methods in Physics Research Section B-Beam Interactions with Materials and Atoms, 2014. **326**: p. 169-173.
67. Chute, J.H., *Direct observation of fission fragment damage in some ceramic oxides.* Journal of Nuclear Materials, 1967. **21**(1): p. 77-87.
68. Weber, W.J., *Alpha-Irradiation Damage in Ceo2, Uo2 and Puo2.* Radiation Effects and Defects in Solids, 1984. **83**(1-2): p. 145-156.
69. Douglass, D.L. and S.E. Bronisz, *Alpha Particle Irradiation Damage in ThO2.* Journal of the American Ceramic Society, 1971. **54**(3): p. 158-161.
70. Keller, C., *BINARY AND TERNARY OXIDES, HYDROXIDES AND HYDROUS OXIDES, PEROXIDES, PHOSPHATES AND ARSENATES A2 - BAILAR, J.C*, in *Comprehensive Inorganic Chemistry*, H.J. EmelÉUs, R. Nyholm, and A.F. Trotman-Dickenson, Editors. 1973, Pergamon: Oxford. p. 219-276.
71. Zeng, Y., S. Kaytakoglu, and D.P. Harrison, *Reduced cerium oxide as an efficient and durable high temperature desulfurization sorbent.* Chemical Engineering Science, 2000. **55**(21): p. 4893-4900.
72. Pakarinen, J., et al., *Annealing-induced lattice recovery in room-temperature xenon irradiated CeO2: X-ray diffraction and electron energy loss spectroscopy experiments.* Journal of Materials Research, 2015. **30**(9): p. 1555-1562.
73. Middleburgh, S.C., G.R. Lumpkin, and R.W. Grimes, *Accommodation of excess oxygen in fluorite dioxides.* Solid State Ionics, 2013. **253**: p. 119-122.
74. Xiao, H.Y., Y. Zhang, and W.J. Weber, *Stability and migration of charged oxygen interstitials in ThO2 and CeO2.* Acta Materialia, 2013. **61**(20): p. 7639-7645.
75. Iwasawa, M., et al., *First-principles study on cerium ion behavior in irradiated cerium dioxide.* Journal of Nuclear Materials, 2009. **393**(2): p. 321-327.
76. Mamontov, E. and T. Egami, *Structural defects in a nano-scale powder of CeO2 studied by pulsed neutron diffraction.* Journal of Physics and Chemistry of Solids, 2000. **61**(8): p. 1345-1356.
77. Hull, S., et al., *Oxygen vacancy ordering within anion-deficient Ceria.* Journal of Solid State Chemistry, 2009. **182**(10): p. 2815-2821.
78. Willis, B.T.M., *Positions of oxygen atoms in UO2.13.* Nature, 1963. **197**(486): p. 755-&.
79. Andersson, D.A., et al., *Role of di-interstitial clusters in oxygen transport in UO2+x from first principles.* Physical Review B, 2009. **80**(6).
80. Shelyug, A., et al., *Energetics of defects produced by highly ionizing radiation in fluorite structured CeO2.* in preparation, 2018.
81. Williamson, G.K. and W.H. Hall, *X-ray line broadening from filed aluminium and wolfram.* Acta Metallurgica, 1953. **1**(1): p. 22-31.
82. Willis, B.T.M., *Neutron Diffraction Studies of the Actinide Oxides. I. Uranium Dioxide and Thorium Dioxide at Room Temperature.* Proceedings of the Royal

Society of London A: Mathematical, Physical and Engineering Sciences, 1963. **274**(1356): p. 122-133.
83. Willis, B.T.M., *Neutron Diffraction Studies of the Actinide Oxides. II. Thermal Motions of the Atoms in Uranium Dioxide and Thorium Dioxide between Room Temperature and 1100 $^\circ$.* Proceedings of the Royal Society of London A: Mathematical, Physical and Engineering Sciences, 1963. **274**(1356): p. 134-144.
84. Muhich, C.L., *Re-Evaluating CeO2 Expansion Upon Reduction: Noncounterpoised Forces, Not Ionic Radius Effects, Are the Cause.* The Journal of Physical Chemistry C, 2017. **121**(14): p. 8052-8059.
85. Xiao, H.Y., et al., *Electronic excitation induced amorphization in titanate pyrochlores: an ab initio molecular dynamics study.* Scientific Reports, 2015. **5**: p. 8265.
86. Keramidas, V.G. and W.B. White, *Raman spectra of oxides with the fluorite structure.* The Journal of Chemical Physics, 1973. **59**(3): p. 1561-1562.
87. Costantini, J.-M., et al., *Raman spectroscopy study of damage induced in cerium dioxide by swift heavy ion irradiations.* Journal of Applied Physics, 2017. **122**(20): p. 205901.
88. Graham, J.T., Y. Zhang, and W.J. Weber, *Irradiation-induced defect formation and damage accumulation in single crystal CeO2.* Journal of Nuclear Materials, 2018. **498**: p. 400-408.
89. Schilling, C., et al., *Raman Spectra of Polycrystalline CeO2: A Density Functional Theory Study.* The Journal of Physical Chemistry C, 2017.
90. Avisar, D. and T. Livneh, *The Raman-scattering of A-type Ce2O3.* Vibrational Spectroscopy, 2016. **86**: p. 14-16.
91. Guo, M., et al., *UV and Visible Raman Studies of Oxygen Vacancies in Rare-Earth-Doped Ceria.* Langmuir, 2011. **27**(7): p. 3872-3877.
92. Fornasiero, P., et al., *Redox Behavior of High-Surface-Area Rh-, Pt-, and Pd-Loaded Ce0.5Zr0.5O2Mixed Oxide.* Journal of Catalysis, 1999. **182**(1): p. 56-69.
93. Murgida, G.E. and M.V. Ganduglia-Pirovano, *Evidence for Subsurface Ordering of Oxygen Vacancies on the Reduced ${\mathrm{CeO}}_{2}(111)$ Surface Using Density-Functional and Statistical Calculations.* Physical Review Letters, 2013. **110**(24): p. 246101.
94. Navrotsky, A., *Progress and New Directions in Calorimetry: A 2014 Perspective.* Journal of the American Ceramic Society, 2014. **97**(11): p. 3349-3359.
95. Berger, M.J., et al., *ESTAR, PSTAR, and ASTAR: Computer Programs for Calculating Stopping-Power and Range Tables for Electrons, Protons, and Helium Ions (version 1.2.3).* 2005, National Institute of Standards and Technology: online.
96. Williams, J.S., *Ion implantation of semiconductors.* Materials Science and Engineering: A, 1998. **253**(1): p. 8-15.
97. Debelle, A., et al., *Lattice strain in irradiated materials unveils a prevalent defect evolution mechanism.* Physical Review Materials, 2018. **2**(1): p. 013604.
98. Palomares, R.I., et al., *Thermal defect annealing of swift heavy ion irradiated ThO2.* Nuclear Instruments and Methods in Physics Research Section B: Beam Interactions with Materials and Atoms, 2017. **405**: p. 15-21.

99. Tracy, C.L., et al., *Role of composition, bond covalency, and short-range order in the disordering of stannate pyrochlores by swift heavy ion irradiation.* Physical Review B, 2016. **94**(6): p. 064102.
100. Shamblin, J., et al., *Probing disorder in isometric pyrochlore and related complex oxides.* Nat Mater, 2016. **15**(5): p. 507-511.
101. Shamblin, J., et al., *Similar local order in disordered fluorite and aperiodic pyrochlore structures.* Acta Materialia, 2018. **144**(Supplement C): p. 60-67.
102. Weber, W.J., *Thermal Recovery of Lattice-Defects in Alpha-Irradiated Uo2 Crystals.* Journal of Nuclear Materials, 1983. **114**(2-3): p. 213-221.
103. Matzke, H., *Atomic transport-properties in UO2 and mixed oxides (U, PU)O2.* Journal of the Chemical Society-Faraday Transactions Ii, 1987. **83**: p. 1121-&.
104. White, B.D., J.D. Thompson, and M.B. Maple, *Unconventional superconductivity in heavy-fermion compounds.* Physica C-Superconductivity and Its Applications, 2015. **514**: p. 246-278.
105. Saxena, S.S., et al., *Superconductivity on the border of itinerant-electron ferromagnetism in UGe2.* Nature, 2000. **406**(6796): p. 587-592.
106. Janoschek, M., et al., *The valence-fluctuating ground state of plutonium.* Science Advances, 2015. **1**(6).
107. Anisimov, V. and Y. Izyumov, *Electronic Structure of Strongly Correlated Materials*. 1 ed. Springer Series in Solid-State Sciences. 2010: Springer-Verlag Berlin Heidelberg. XIII, 291.
108. Wen, X.-D., et al., *Effect of spin-orbit coupling on the actinide dioxides AnO(2) (An=Th, Pa, U, Np, Pu, and Am): A screened hybrid density functional study.* Journal of Chemical Physics, 2012. **137**(15).
109. Gofryk, K., et al., *Anisotropic thermal conductivity in uranium dioxide.* Nature Communications, 2014. **5**.
110. Faber, J., G.H. Lander, and B.R. Cooper, *Neutron-diffraction study of UO2 - observation of an internal distortion.* Physical Review Letters, 1975. **35**(26): p. 1770-1773.
111. Leinders, G., et al., *Low-Temperature Oxidation of Fine UO2 Powders: A Process of Nanosized Domain Development.* Inorganic Chemistry, 2016. **55**(8): p. 3915-3927.
112. Ewing, R.C., *Long-term storage of spent nuclear fuel.* Nat Mater, 2015. **14**(3): p. 252-257.
113. Gaston, D.R., et al., *Physics-based multiscale coupling for full core nuclear reactor simulation.* Annals of Nuclear Energy, 2015. **84**: p. 45-54.
114. Stanek, C.R. *Nuclear Energy Advanced Modeling and Simulation (NEAMS) Program Update*. 2016; Available from: https://www.energy.gov/sites/prod/files/2016/07/f33/NEAMS_forNEAC-vFINAL2%20(002).pdf.
115. Tonks, M.R., et al., *Mechanistic materials modeling for nuclear fuel performance.* Annals of Nuclear Energy, 2017. **105**: p. 11-24.
116. Bertolus, M., et al., *Linking atomic and mesoscopic scales for the modelling of the transport properties of uranium dioxide under irradiation.* Journal of Nuclear Materials, 2015. **462**: p. 475-495.

117. Matzke, H., *Oxygen potential measurements in high burnup LWR U02 fuel.* Journal of Nuclear Materials, 1995. **223**(1): p. 1-5.
118. Matzke, H., *Oxygen potential in the rim region of high burnup UO2 fuel.* Journal of Nuclear Materials, 1994. **208**(1): p. 18-26.
119. Park, K., M.-S. Yang, and H.-S. Park, *The stoichiometry and the oxygen potential change of urania fuels during irradiation.* Journal of Nuclear Materials, 1997. **247**: p. 116-120.
120. Walker, C.T., et al., *On the oxidation state of UO2 nuclear fuel at a burn-up of around 100MWd/kgHM.* Journal of Nuclear Materials, 2005. **345**(2): p. 192-205.
121. Spino, J. and P. Peerani, *Oxygen stoichiometry shift of irradiated LWR-fuels at high burn-ups: Review of data and alternative interpretation of recently published results.* Journal of Nuclear Materials, 2008. **375**(1): p. 8-25.
122. Desgranges, L., et al., *Experimental evidence of the formation of a new chemical phase in a power ramped UO2 nuclear fuel.* Journal of Nuclear Materials, 2015. **457**(Supplement C): p. 246-251.
123. Riglet-Martial, C., et al., *Experimental evidence of oxygen thermo-migration in PWR UO2 fuels during power ramps using in-situ oxido-reduction indicators.* Journal of Nuclear Materials, 2016. **480**(Supplement C): p. 32-39.
124. Lawrence, G.T., *A review of the diffusion coefficient of fission-product rare gases in uranium dioxide.* Journal of Nuclear Materials, 1978. **71**(2): p. 195-218.
125. Burns, P.C. and G.E. Sigmon, eds. *Uranium: Cradle to Grave*. Mineralogical Association of Canada Short Course. Vol. 49. 2013.
126. Aronson, S., R.B. Roof, and J. Belle, *Kinetic Study of the Oxidation of Uranium Dioxide.* The Journal of Chemical Physics, 1957. **27**(1): p. 137-144.
127. Blackburn, P.E., J. Weissbart, and E.A. Gulbransen, *Oxidation of Uranium Dioxide.* The Journal of Physical Chemistry, 1958. **62**(8): p. 902-908.
128. Einziger, R.E., et al., *Oxidation of spent fuel in air at 175 to 195°C.* Journal of Nuclear Materials, 1992. **190**: p. 53-60.
129. McEachern, R.J., *A review of kinetic data on the rate of U3O7 formation on UO2.* Journal of Nuclear Materials, 1997. **245**(2): p. 238-247.
130. Quémard, L., et al., *On the origin of the sigmoid shape in the UO2 oxidation weight gain curves.* Journal of the European Ceramic Society, 2009. **29**(13): p. 2791-2798.
131. McEachern, R.J. and P. Taylor, *A review of the oxidation of uranium dioxide at temperatures below 400°C.* Journal of Nuclear Materials, 1998. **254**(2–3): p. 87-121.
132. Arrott, A. and J.E. Goldman, *Magnetic Analysis of the Uranium-Oxygen System.* Physical Review, 1957. **108**(4): p. 948-953.
133. Petit, T., et al., *Point defects in uranium dioxide.* Philosophical Magazine Part B, 1998. **77**(3): p. 779-786.
134. Crocombette, J.P., et al., *Plane-wave pseudopotential study of point defects in uranium dioxide.* Physical Review B, 2001. **64**(10): p. 104107.
135. Morelon, N.D., et al., *A new empirical potential for simulating the formation of defects and their mobility in uranium dioxide.* Philosophical Magazine, 2003. **83**(13): p. 1533-1550.

136. Freyss, M., T. Petit, and J.-P. Crocombette, *Point defects in uranium dioxide: Ab initio pseudopotential approach in the generalized gradient approximation.* Journal of Nuclear Materials, 2005. **347**(1–2): p. 44-51.
137. Gupta, F., G. Brillant, and A. Pasturel, *Correlation effects and energetics of point defects in uranium dioxide: a first principle investigation.* Philosophical Magazine, 2007. **87**(17): p. 2561-2569.
138. Yun, Y.S. and W.W. Kim. *First Principle Studies on Electronic and Defect Structures of UO₂, ThO₂, and PuO₂*. in *Proceedings of the KNS spring meeting*. 2007. Korea, Republic of: KNS.
139. Nerikar, P., et al., *Energetics of intrinsic point defects in uranium dioxide from electronic-structure calculations.* Journal of Nuclear Materials, 2009. **384**(1): p. 61-69.
140. Dorado, B., et al., *Stability of oxygen point defects in UO2 by first-principles DFT plus U calculations: Occupation matrix control and Jahn-Teller distortion.* Physical Review B, 2010. **82**(3).
141. Crocombette, J.-P., D. Torumba, and A. Chartier, *Charge states of point defects in uranium oxide calculated with a local hybrid functional for correlated electrons.* Physical Review B, 2011. **83**(18): p. 184107.
142. Geng, H.Y., H.X. Song, and Q. Wu, *Theoretical assessment on the possibility of constraining point-defect energetics by pseudo phase transition pressures.* Physical Review B, 2013. **87**(17): p. 174107.
143. Emerson, V., et al., *DFT + U investigation of charged point defects and clusters in UO 2.* Journal of Physics: Condensed Matter, 2014. **26**(32): p. 325501.
144. Korzhavyi, P.A., et al., *Oxidation of plutonium dioxide.* Nat Mater, 2004. **3**(4): p. 225-228.
145. Andersson, D.A., et al., *Density Functional Theory Calculations of UO2 Oxidation: Evolution of UO2+x, U4O9-y, U3O7, and U3O8.* Inorganic Chemistry, 2013. **52**(5): p. 2769-2778.
146. Grenthe, I., et al., *Uranium*, in *The Chemistry of the Actinide and Transactinide Elements*, L.R. Morss, N.M. Edelstein, and J. Fuger, Editors. 2006, Springer Netherlands: Dordrecht. p. 253-698.
147. Roberts, L.E.J., *The oxides of uranium. Part V. The chemisorption of oxygen on UO2 and on UO2-ThO2 solid solutions.* Journal of the Chemical Society (Resumed), 1954(0): p. 3332-3339.
148. Ferguson, I.F. and J.D.M. McConnell, *Heat of Adsorption of Oxygen on Uranium Dioxide at -183° C.* Proceedings of the Royal Society of London. Series A, Mathematical and Physical Sciences, 1957. **241**(1224): p. 67-79.
149. Skomurski, F.N., et al., *Corrosion of UO2 and ThO2: A quantum-mechanical investigation.* Journal of Nuclear Materials, 2008. **375**(3): p. 290-310.
150. Chaka, A.M., et al., *Density-functional theory investigation of oxidative corrosion of UO2.* Computational and Theoretical Chemistry, 2012. **987**: p. 90-102.
151. Ferguson, I.F. and J.D.M. McConnell, *Heat of Adsorption of Oxygen on Uranium Dioxide at -183 degrees C.* Proceedings of the Royal Society of London. Series A. Mathematical and Physical Sciences, 1957. **241**(1224): p. 67.

152. Stubbs, J.E., et al., *UO2 Oxidative Corrosion by Nonclassical Diffusion.* Physical Review Letters, 2015. **114**(24): p. 246103.
153. Anderson, J.S., L.E.J. Roberts, and E.A. Harper, *The oxides of uranium. Part VII. The oxidation of uranium dioxide.* Journal of the Chemical Society (Resumed), 1955(0): p. 3946-3959.
154. Bannister, M.J., *The storage behaviour of uranium dioxide powders — review article.* Journal of Nuclear Materials, 1968. **26**(2): p. 174-184.
155. Alberman, K.B. and J.S. Anderson, *The oxides of uranium.* Journal of the Chemical Society (Resumed), 1949(0): p. S303-S311.
156. Willis, B.T.M., *Point Defects in Uranium Dioxide.* Proceedings of the British Ceramic Society, 1964. **1**(1): p. 9-19.
157. Willis, B.T.M., *Structures of UO2, UO2+x and U4O9 by neutron diffraction.* Journal De Physique, 1964. **25**(5): p. 431-441.
158. Willis, B.T.M., *Defect structure of hyper-stoichiometric uranium-dioxide.* Acta Crystallographica Section A, 1978. **34**(JAN): p. 88-90.
159. Murray, A.D. and B.T.M. Willis, *A neutron-diffraction study of anion clusters in non-stoichiometric uranium-dioxide.* Journal of Solid State Chemistry, 1990. **84**(1): p. 52-57.
160. Poulesquen, A., L. Desgranges, and C. Ferry, *An improved model to evaluate the oxidation kinetics of uranium dioxide during dry storage.* Journal of Nuclear Materials, 2007. **362**(2–3): p. 402-410.
161. Matzke, H., *On uranium self-diffusion in UO2 and UO2+x.* Journal of Nuclear Materials, 1969. **30**(1): p. 26-35.
162. Behera, R.K., et al., *Diffusion of oxygen interstitials in UO2+x using kinetic Monte Carlo simulations: Role of O/M ratio and sensitivity analysis.* Journal of Nuclear Materials, 2016. **472**: p. 89-98.
163. Govers, K., et al., *Molecular dynamics simulation of helium and oxygen diffusion in UO2 +/- x.* Journal of Nuclear Materials, 2009. **395**(1-3): p. 131-139.
164. Geng, H.Y., et al., *Interplay of defect cluster and the stability of xenon in uranium dioxide from density functional calculations.* Physical Review B, 2010. **82**(9): p. 094106.
165. Andersson, D.A., et al., *U and Xe transport in UO2 +/- x: Density functional theory calculations.* Physical Review B, 2011. **84**(5).
166. Hong, M., et al., *Solubility and clustering of ruthenium fission products in uranium dioxide as determined by density functional theory.* Physical Review B, 2012. **85**(14): p. 144110.
167. Liu, X.Y., D.A. Andersson, and B.P. Uberuaga, *First-principles DFT modeling of nuclear fuel materials.* Journal of Materials Science, 2012. **47**(21): p. 7367-7384.
168. Geng, H.Y., et al., *Stability mechanism of cuboctahedral clusters in UO(2+x): First-principles calculations.* Physical Review B, 2008. **77**(18).
169. Geng, H.Y., et al., *Ab initio investigation on oxygen defect clusters in UO2+x.* Applied Physics Letters, 2008. **93**(20): p. 201903.
170. Lynds, L., et al., *X-Ray and Density Study of Nonstoichiometry in Uranium Oxides*, in *Nonstoichiometric Compounds*. 1963, AMERICAN CHEMICAL SOCIETY. p. 58-65.

171. Elorrieta, J.M., et al., *A detailed Raman and X-ray study of UO2+x oxides and related structure transitions.* Physical Chemistry Chemical Physics, 2016.
172. Andersson, D.A., et al., *Cooperativity among defect sites in AO(2+x) and A(4)O(9) (A=U,Np,Pu): Density functional calculations.* Physical Review B, 2009. **79**(2).
173. Higgs, J.D., et al., *Kinetics of precipitation of U4O9 from hyperstoichiometric UO2+x.* Journal of Nuclear Materials, 2007. **366**(3): p. 297-305.
174. Belbeoch, B., C. Piekarski, and P. Perio, *Structure de U4O9.* Acta Crystallographica, 1961. **14**(8): p. 837-843.
175. Belbeoch, B., J.C. Boivineau, and P. Perio, *Changements de structure de l'oxyde U4O9.* Journal of Physics and Chemistry of Solids, 1967. **28**(7): p. 1267-1275.
176. Naito, K., et al., *X-ray study on a phase transition of U4O9.* Solid State Communications, 1967. **5**(5): p. 349-352.
177. Tateno, J., *Change of the dielectric constant at the phase transition in U4O9.* Solid State Communications, 1970. **8**(13): p. 1043-1045.
178. Blank, H. and C. Ronchi, *Electron diffraction of U4O9.* Acta Crystallographica Section A, 1968. **24**(6): p. 657-666.
179. Naito, K., T. Tsuji, and T. Matsui, *An electrical conductivity and X-ray study of a high-temperature transition in U4O9.* Journal of Nuclear Materials, 1973. **48**(1): p. 58-66.
180. Grønvold, F., et al., *Thermodynamics of the UO2+x phase I. Heat capacities of UO2.017 and UO2.254 from 300 to 1000 K and electronic contributions.* The Journal of Chemical Thermodynamics, 1970. **2**(5): p. 665-679.
181. Lierde, W.V., J. Pelsmaekers, and A. Lecocq-Robert, *On the phase limits of U4O9.* Journal of Nuclear Materials, 1970. **37**: p. 276-285.
182. Leinders, G., et al., *Assessment of the U3O7 Crystal Structure by X-ray and Electron Diffraction.* Inorganic Chemistry, 2016.
183. Hoekstra, H.R., A. Santoro, and S. Siegel, *The low temperature oxidation of UO2 and U4O9.* Journal of Inorganic and Nuclear Chemistry, 1961. **18**: p. 166-178.
184. Westrum, E.F. and F. Grønvold, *Triuranium heptaoxides: Heat capacities and thermodynamic properties of α- and β-U3O7 from 5 to 350°K.* Journal of Physics and Chemistry of Solids, 1962. **23**(1): p. 39-53.
185. Rousseau, G., et al., *A detailed study of UO2 to U3O8 oxidation phases and the associated rate-limiting steps.* Journal of Nuclear Materials, 2006. **355**(1-3): p. 10-20.
186. Desgranges, L., et al., *Neutron Diffraction Study of the in Situ Oxidation of UO2.* Inorganic Chemistry, 2009. **48**(16): p. 7585-7592.
187. Andersson, D.A., et al., *Stability and migration of large oxygen clusters in UO2+x: Density functional theory calculations.* Journal of Chemical Physics, 2012. **136**(23).
188. Crocombette, J.-P., *Influence of charge states on energies of point defects and clusters in uranium dioxide.* Physical Review B, 2012. **85**(14): p. 144101.
189. Wang, J., R.C. Ewing, and U. Becker, *Average structure and local configuration of excess oxygen in UO2+x.* Scientific Reports, 2014. **4**.

190. Brincat, N.A., et al., *Computer simulation of defect clusters in UO2 and their dependence on composition.* Journal of Nuclear Materials, 2015. **456**: p. 329-333.
191. Yakub, E., C. Ronchi, and D. Staicu, *Computer simulation of defects formation and equilibrium in non-stoichiometric uranium dioxide.* Journal of Nuclear Materials, 2009. **389**(1): p. 119-126.
192. Geng, H.Y., et al., *Point defects and clustering in uranium dioxide by LSDA+U calculations.* Physical Review B, 2008. **77**(10).
193. Ichinomiya, T., et al., *Temperature accelerated dynamics study of migration process of oxygen defects in UO2.* Journal of Nuclear Materials, 2009. **384**(3): p. 315-321.
194. Chen, Y., et al., *First principles modeling of stability mechanism of nonstoichiometric uranium dioxide.* Computational Materials Science, 2010. **49**(4, Supplement): p. S364-S368.
195. Geng, H.Y., et al., *First-principles study on oxidation effects in uranium oxides and high-pressure high-temperature behavior of point defects in uranium dioxide.* Physical Review B, 2011. **84**(17).
196. Raoul, N.-H., K. Matthias, and P. Andreas, *Effects of stoichiometry on the defect clustering in uranium dioxide.* Journal of Physics: Condensed Matter, 2015. **27**(45): p. 455401.
197. Manara, D. and B. Renker, *Raman spectra of stoichiometric and hyperstoichiometric uranium dioxide.* Journal of Nuclear Materials, 2003. **321**(2–3): p. 233-237.
198. He, H. and D. Shoesmith, *Raman spectroscopic studies of defect structures and phase transition in hyper-stoichiometric UO2+x.* Physical Chemistry Chemical Physics, 2010. **12**(28): p. 8108-8117.
199. He, H., Z. Qin, and D.W. Shoesmith, *Characterizing the relationship between hyperstoichiometry, defect structure and local corrosion kinetics of uranium dioxide.* Electrochimica Acta, 2010. **56**(1): p. 53-60.
200. Lu, J.-b., G. Li, and S.-l. Guo, *Raman and Infrared Spectra of Non-Stoichiometry Uranium Oxides.* Spectroscopy and Spectral Analysis, 2014. **34**(2): p. 405-409.
201. Conradson, S.D., et al., *Charge distribution and local structure and speciation in the UO2+x and PuO2+x binary oxides for x <= 0.25.* Journal of Solid State Chemistry, 2005. **178**(2): p. 521-535.
202. Conradson, S.D., et al., *Local structure and charge distribution in the UO2-U4O9 system.* Inorganic Chemistry, 2004. **43**(22): p. 6922-6935.
203. Govers, K., et al., *Comparison of interatomic potentials for UO2. Part I: Static calculations.* Journal of Nuclear Materials, 2007. **366**(1–2): p. 161-177.
204. Xian-Ming, B., et al., *Migration mechanisms of oxygen interstitial clusters in UO 2.* Journal of Physics: Condensed Matter, 2013. **25**(1): p. 015003.
205. Contamin, P., J.J. Bacmann, and J.F. Marin, *Autodiffusion de l'oxygene dans le dioxyde d'uranium surstoechiometrique.* Journal of Nuclear Materials, 1972. **42**(1): p. 54-64.
206. Marin, J.F. and P. Contamin, *Uranium and oxygen self-diffusion in UO2.* Journal of Nuclear Materials, 1969. **30**(1): p. 16-25.

207. Gronvold, F., *High-temperature X-ray study of uranium oxides in the UO2-U3O8 region.* Journal of Inorganic & Nuclear Chemistry, 1955. **1**(6): p. 357-370.
208. Teske, K., H. Ullmann, and D. Rettig, *Investigation of the oxygen activity of oxide fuels and fuel-fission product systems by solid electrolyte techniques. Part I: Qualification and limitations of the method.* Journal of Nuclear Materials, 1983. **116**(2): p. 260-266.
209. Furuichi, R., T. Ishii, and T. Nakane, *Thermoanalytical study on the oxidation of uranium dioxides derived from uranyl nitrate, uranyl acetate and ammonium diuranate.* Thermochimica Acta, 1979. **33**(Supplement C): p. 51-67.
210. Augusto Guisard Restivo, T. and S. Luiza Silva, *Specific surface area determination by TG/DSC.* Thermochimica Acta, 1999. **328**(1): p. 47-53.
211. LLC, W.E.C., *Development of LWR Fuels with Enhanced Accident Tolerance - Final Technical Report*. 2015.
212. Martin, D.G., *The thermal expansion of solid UO2 and (U, Pu) mixed oxides — a review and recommendations.* Journal of Nuclear Materials, 1988. **152**(2): p. 94-101.
213. AGENCY, I.A.E., *Thermophysical Properties Database of Materials for Light Water Reactors and Heavy Water Reactors*. IAEA TECDOC Series. 2006, Vienna: INTERNATIONAL ATOMIC ENERGY AGENCY.
214. Fink, J.K., *Thermophysical properties of uranium dioxide.* Journal of Nuclear Materials, 2000. **279**(1): p. 1-18.
215. Guthrie, M., et al., *Thermal expansion in UO2 determined by high-energy X-ray diffraction.* Journal of Nuclear Materials, 2016. **479**: p. 19-22.
216. Hutchings, M.T., *High-temperature studies of UO2 and ThO2 using neutron-scattering techniques.* Journal of the Chemical Society-Faraday Transactions Ii, 1987. **83**: p. 1083-1103.
217. Dove, M.T., M.G. Tucker, and D.A. Keen, *Neutron total scattering method.* European Journal of Mineralogy, 2002. **14**(2): p. 331.
218. Fritz, I.J., *Elastic properties of UO2 at high pressure.* Journal of Applied Physics, 1976. **47**(10): p. 4353-4358.
219. Dolling, G., R.A. Cowley, and A.D.B. Woods, *THE CRYSTAL DYNAMICS OF URANIUM DIOXIDE.* Canadian Journal of Physics, 1965. **43**(8): p. 1397-1413.
220. Desgranges, L., et al., *Structural Changes in the Local Environment of Uranium Atoms in the Three Phases of U4O9.* Inorganic Chemistry, 2016.
221. Schoenes, J., *Electronic transitions, crystal field effects and phonons in UO2.* Physics Reports, 1980. **63**(6): p. 301-336.
222. Livneh, T. and E. Sterer, *Effect of pressure on the resonant multiphonon Raman scattering in ${\mathrm{UO}}_{2}$.* Physical Review B, 2006. **73**(8): p. 085118.
223. Desgranges, L., et al., *Raman spectrum of U4O9: a new interpretation of damage lines in UO2.* Journal of Raman Spectroscopy, 2012. **43**(3): p. 455-458.
224. Desgranges, L., et al., *What Can We Learn From Raman Spectroscopy on Irradiation-Induced Defects in UO2?* JOM, 2014. **66**(12): p. 2546-2552.
225. Marlow, P.G., J.P. Russell, and J.R. Hardy, *Raman scattering in uranium dioxide.* Philosophical magazine; a journal of theoretical, experimental and applied physics, 1966. **14**(8): p. 409-410.

226. Allen, G.C., I.S. Butler, and T. Nguyen Anh, *Characterisation of uranium oxides by micro-Raman spectroscopy.* Journal of Nuclear Materials, 1987. **144**(1–2): p. 17-19.
227. Palacios, M.L. and S.H. Taylor, *Characterization of Uranium Oxides Using in Situ Micro-Raman Spectroscopy.* Applied Spectroscopy, 2000. **54**(9): p. 1372-1378.
228. Schoenes, J., *Recent spectroscopic studies of UO2.* Journal of the Chemical Society, Faraday Transactions 2: Molecular and Chemical Physics, 1987. **83**(7): p. 1205-1213.
229. Blumenröder, S., et al., *Light scattering in heavy fermion compounds.* Journal of Magnetism and Magnetic Materials, 1988. **76-77**(Supplement C): p. 331-334.
230. Graves, P.R., *Raman Microprobe Spectroscopy of Uranium Dioxide Single Crystals and Ion Implanted Polycrystals.* Applied Spectroscopy, 1990. **44**(10): p. 1665-1667.
231. Guimbretiere, G., et al., *Determination of in-depth damaged profile by Raman line scan in a pre-cut He2+ irradiated UO2.* Applied Physics Letters, 2012. **100**(25).
232. Desgranges, L., et al., *Annealing of the defects observed by Raman spectroscopy in UO2 irradiated by 25 MeV He2+ ions.* Nuclear Instruments and Methods in Physics Research Section B: Beam Interactions with Materials and Atoms, 2014. **327**: p. 74-77.
233. Onofri, C., et al., *Evolution of extended defects in polycrystalline UO2 under heavy ion irradiation: combined TEM, XRD and Raman study.* Nuclear Instruments and Methods in Physics Research Section B: Beam Interactions with Materials and Atoms, 2016. **374**: p. 51-57.
234. Guimbretière, G., et al., *In situ Raman monitoring of He2+ irradiation induced damage in a UO2 ceramic.* Applied Physics Letters, 2013. **103**(4): p. 041904.
235. Guimbretière, G., et al., *Characterization of Nuclear Materials in Extreme Conditions: Raman Spectroscopy Approach.* IEEE Transactions on Nuclear Science, 2014. **61**(4): p. 2045-2051.
236. Jegou, C., et al., *Raman micro-spectroscopy of UOX and MOX spent nuclear fuel characterization and oxidation resistance of the high burn-up structure.* Journal of Nuclear Materials, 2015. **458**(Supplement C): p. 343-349.
237. Lebreton, F., et al., *Peculiar Behavior of (U,Am)O2−δ Compounds for High Americium Contents Evidenced by XRD, XAS, and Raman Spectroscopy.* Inorganic Chemistry, 2015. **54**(20): p. 9749-9760.
238. Talip, Z., et al., *Raman and X-ray Studies of Uranium–Lanthanum-Mixed Oxides Before and After Air Oxidation.* Journal of the American Ceramic Society, 2015. **98**(7): p. 2278-2285.
239. Lee, J., et al., *Raman study on structure of U1−yGdyO2−x (y=0.005, 0.01, 0.03, 0.05 and 0.1) solid solutions.* Journal of Nuclear Materials, 2017. **486**: p. 216-221.
240. He, H., et al., *Characterization of the influence of fission product doping on the anodic reactivity of uranium dioxide.* Canadian Journal of Chemistry, 2007. **85**(10): p. 702-713.

241. Razdan, M. and D.W. Shoesmith, *The Electrochemical Reactivity of 6.0 wt% Gd-Doped UO2 in Aqueous Carbonate/Bicarbonate Solutions.* Journal of The Electrochemical Society, 2014. **161**(4): p. H225-H234.
242. Razdan, M. and D.W. Shoesmith, *Influence of Trivalent-Dopants on the Structural and Electrochemical Properties of Uranium Dioxide (UO2).* Journal of The Electrochemical Society, 2014. **161**(3): p. H105-H113.
243. Liu, N., et al., *Influence of Gd Doping on the Structure and Electrochemical Behavior of UO2.* Electrochimica Acta, 2017. **247**(Supplement C): p. 496-504.
244. Desgranges, L., et al., *What Is the Actual Local Crystalline Structure of Uranium Dioxide, UO2? A New Perspective for the Most Used Nuclear Fuel.* Inorganic Chemistry, 2016.
245. Leinders, G., et al., *Evolution of the Uranium Chemical State in Mixed-Valence Oxides.* Inorganic Chemistry, 2017.
246. Butorin, S.M., et al., *Characteristics of chemical bonding of pentavalent uranium in La-doped UO2.* Chemical Communications, 2017. **53**(1): p. 115-118.
247. Butorin, S.M., et al., *Probing Chemical Bonding in Uranium Dioxide by Means of High-Resolution X-ray Absorption Spectroscopy.* The Journal of Physical Chemistry C, 2016.
248. Kvashnina, K.O., et al., *Chemical State of Complex Uranium Oxides.* Physical Review Letters, 2013. **111**(25): p. 253002.
249. Willis, B.T.M., *Crystallographic studies of anion-excess uranium oxides.* Journal of the Chemical Society, Faraday Transactions 2: Molecular and Chemical Physics, 1987. **83**(7): p. 1073-1081.
250. AGENCY, I.A.E., *Advanced Fuel Pellet Materials and Fuel Rod Design for Water Cooled Reactors*. IAEA TECDOC Series. 2010, Vienna: INTERNATIONAL ATOMIC ENERGY AGENCY.
251. Arborelius, J., et al., *Advanced Doped UO2 Pellets in LWR Applications.* Journal of Nuclear Science and Technology, 2006. **43**(9): p. 967-976.
252. Hesketh, K., *2.16 - Burnable Poison-Doped Fuel A2 - Konings, Rudy J.M*, in *Comprehensive Nuclear Materials*. 2012, Elsevier: Oxford. p. 423-438.
253. Kleykamp, H., *The chemical state of the fission products in oxide fuels.* Journal of Nuclear Materials, 1985. **131**(2): p. 221-246.
254. Une, K. and M. Oguma, *Oxygen potentials of (U,Nd)O2 ± x solid solutions in the temperature range 1000–1500°C.* Journal of Nuclear Materials, 1983. **118**(2): p. 189-194.
255. Bès, R., et al., *Charge compensation mechanisms in U1-xGdxO2 and Th1-xGdxO2-x/2 studied by X-ray Absorption Spectroscopy.* Journal of Nuclear Materials, 2017. **489**: p. 9-21.
256. Zhang, L. and A. Navrotsky, *Thermochemistry of rare earth doped uranium oxides LnxU1−xO2−0.5x+y (Ln = La, Y, Nd).* Journal of Nuclear Materials, 2015. **465**: p. 682-691.
257. Zhang, L., et al., *A combined calorimetric and computational study of the energetics of rare earth substituted UO2 systems.* Acta Materialia, 2015. **97**: p. 191-198.

258. Solomon, J.M., A. Navrotsky, and M. Asta, *Energetics and defect clustering trends for trivalent rare earth cations substituted in UO2.* Journal of Nuclear Materials, 2015. **457**: p. 252-255.
259. Solomon, J.M., et al., *Computational study of the energetics and defect clustering tendencies for Y- and La-doped UO2.* Acta Materialia, 2014. **78**: p. 282-289.
260. Dottavio, G., et al., *Characterising the U–Nd–O miscibility gap by an experimental and a theoretical approach.* Journal of Nuclear Materials, 2015. **458**(Supplement C): p. 394-405.
261. Dottavio, G., et al., *Existence of a miscibility gap in uranium neodymium oxide materials used as nuclear fuels simulants.* Progress in Nuclear Energy, 2014. **72**(Supplement C): p. 22-26.
262. Desgranges, L., et al., *Miscibility Gap in the U–Nd–O Phase Diagram: a New Approach of Nuclear Oxides in the Environment?* Inorganic Chemistry, 2012. **51**(17): p. 9147-9149.
263. Desgranges, L., et al., *Evidence of a Biphasic Domain in the UO2-Nd2O3 Diagram at Room Temperature: a Proof for a Miscibility Gap in UO2-Nd2O3 Phase Diagram ?* Solid State Phenomena, 2011. **172-174**.
264. Ohmichi, T., et al., *On the relation between lattice parameter and O/M ratio for uranium dioxide-trivalent rare earth oxide solid solution.* Journal of Nuclear Materials, 1981. **102**(1): p. 40-46.
265. Sali, S.K., et al., *Oxidation/reduction studies on ZryU1-yO2+x and delineation of a new orthorhombic phase in U-Zr-O system.* Journal of Solid State Chemistry, 2008. **181**(8): p. 1859-1866.
266. Catlow, C.R.A., *Point Defect and Electronic Properties of Uranium Dioxide.* Proceedings of the Royal Society of London A: Mathematical, Physical and Engineering Sciences, 1977. **353**(1675): p. 533-561.
267. Rao, R., et al., *Raman Spectroscopic Investigation of Thorium Dioxide–Uranium Dioxide (ThO2–UO2) Fuel Materials.* Applied Spectroscopy, 2014. **68**(1): p. 44-48.
268. McBride, J.R., et al., *Raman and x-ray studies of Ce1−xRExO2−y, where RE=La, Pr, Nd, Eu, Gd, and Tb.* Journal of Applied Physics, 1994. **76**(4): p. 2435-2441.
269. Qiu, X., et al., *Reciprocal-space instrumental effects on the real-space neutron atomic pair distribution function.* Journal of Applied Crystallography, 2004. **37**(1): p. 110-116.
270. Norberg, S.T., M.G. Tucker, and S. Hull, *Bond valence sum: a new soft chemical constraint for RMCProfile.* Journal of Applied Crystallography, 2009. **42**(2): p. 179-184.

VITA

Raul Irvin Palomares was born on January 8 near Atlanta, GA. As an undergraduate, he worked as a research assistant at the Nuclear Engineering Teaching Laboratory (NETL) at the University of Texas at Austin Pickle Campus. He graduated with a Bachelor of Science (B.S.) degree in Physics with an emphasis on nuclear engineering and radiation physics from the University of Texas at Austin in May 2013. He began graduate studies in nuclear engineering at the University of Tennessee in August 2013. He earned a Doctor of Philosophy (Ph.D.) degree in Nuclear Engineering in the spring of 2018. His undergraduate and graduate work has resulted in two first-author technical reports, four first-author peer-review journal articles, and several other peer-review journal articles as a co-author.